Understanding Extrudate Swell: From Theoretical Rheology to Practical Processing

ROBERTSON, BENJAMIN

Understanding Extrudate Swell: From Theoretical Rheology to Practical Processing

Ben Robertson
Department of Chemistry
Durham University

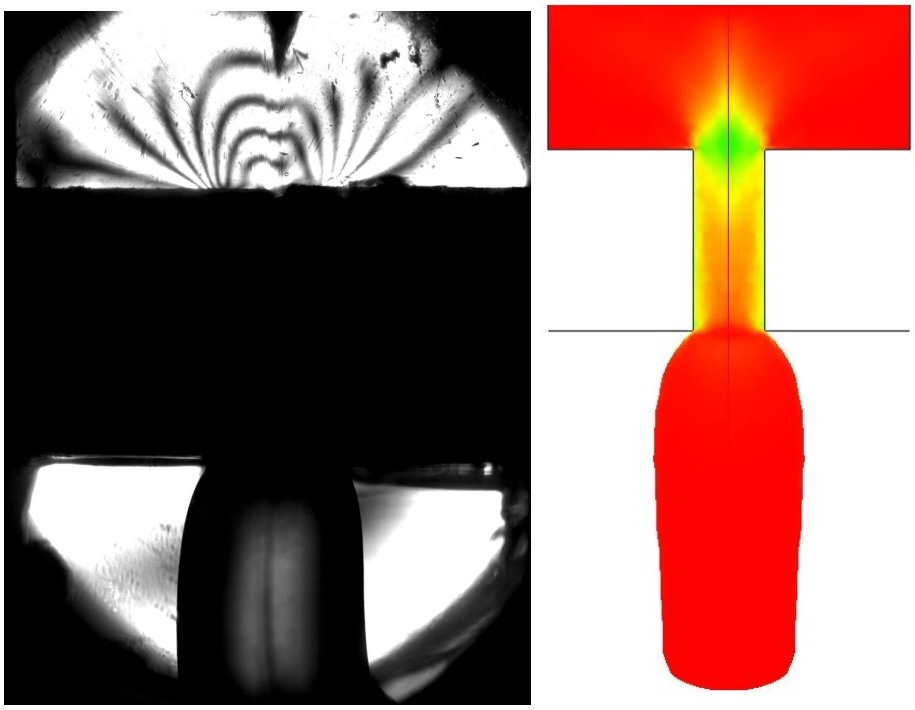

A thesis submitted for the degree of Doctor of Philosophy
December 2018

Durham University

Abstract

This thesis focusses on the measurement and prediction of extrudate (or die) swell of molten polymers. The overall aim of this work is to understand extrudate swell for complex, industrially relevant systems. This is performed by first understanding the causes of swelling for well defined, monodisperse polymers at a molecular level. The systems are then gradually built up in complexity from bidisperse to very polydisperse and/or branched samples. At each stage predictions for extrudate swell are obtained using the *flowSolve* fluid dynamics package combined with a molecular constitutive equation and are compared to extrusion experiments using a novel Multi-Pass-Rheometer setup. The effects of both molecular weight and temperature can be ignored when shear rates are scaled by Rouse Weissenberg number as extrudate swell is a chain stretch controlled phenomenon. For monodisperse systems theoretical predictions using the Rolie-Poly constitutive equation match experimental results up to a W_R=7 above which simulations over-predict swelling ratios. This is justified in this work using reduction of monomeric friction at high deformation rates.

Extrudate swell of polydisperse polystyrenes is successfully predicted up to high Weissenberg numbers using the Rolie-Double-Poly equation when combined with monomeric friction reduction. A slight under-prediction is seen at low Weissenberg number where the chain stretch times of long polymer chains are increased by dilution with shorter chains. Qualitatively correct but quantitatively poor predictions are obtained for highly polydisperse polyethylenes where the low shear extrudate swell is under-predicted.

Branched polymers behave differently experimentally to linear samples, exhibiting extrudate swell below the Rouse time of the polymer backbone. A small amount of branching increases swelling ratios versus the linear case but moderate increases in branching above this point have little effect on the experimentally observed swelling ratios. Significantly branched polyethylenes swell more than this, especially at high shear rates. There is a similar trend in simulated results using the XPP model but only a partial agreement between simulated and experimental extrudate swell is observed.

Contents

Table of Abbreviations

Abbreviation	Expansion
BOB	Branch On Branch theory
CCR	Convective Constraint Release
CLF	Contour Length Fluctuations
CR	Constraint Release
FE	Finite Extensibility
FENE	Finitely extensible Non-linear Elastic
GLaMM	Graham, Likhtman and Milner McLeish model
GPC	Gel Permeation Chromatography
HDPE	High Density PolyEthylene
K-BKZ	Kaye-Bernstein,Kearsley,Zapas model
LCB	Long Chain Branch(ing)
LDPE	Low Density PolyEthylene
LVE	Linear Viscoelastic Envelope
MPR	Multi Pass Rheometer
μPP	Microscale Polymer Processing
PCN	Primitive Chain Network
PTT	Phan-Thien-Tanner model
RDP	Rolie-Double-Poly equation
Rolie-Poly	Rouse LInear Entangled POLYmer theory
SER	Sentmanat Extensional Rheometer
WLF	Williams-Landau-Ferry Equation
XPP	eXtended Pom-Pom model

Table of Symbols

Symbol	Definition
α	XPP anisotropy parameter
β	CCR parameter
$\dot{\gamma}$	Shear rate
$\gamma(t)$	Rheometer oscillation strain at time t
γ_0	Strain amplitude
ΔP	Pressure drop
ϵ	Hencky strain
ζ	Monomeric friction coefficient
ζ_{min}	Minimum allowed value for monomeric friction reduction coefficient
ζ_f	Monomeric friction reduction coefficient
η_0	Polymer melt viscosity
κ	Velocity gradient
λ	Chain stretch
λ_{max}	Maximum chain stretch (finite extensibility)
μ	*flowSolve* solvent viscosity
ω	Oscillation frequency
ρ	Density
σ	Polymeric stress
τ	Shear stress, generally at a die wall
τ_b	Backbone relaxation time
τ_d	Reptation time
τ_e	Entanglement time
τ_r	Rouse reorientation time
τ_R	Rouse time
τ_s	Stretch relaxation time

Symbol	Definition
θ	The die exit angle
ϕ	Volume fraction
ϕ_{dil}	Effective dilution
a	Tube diameter
$\mathbf{A}$	Auxiliary Rolie-Poly orientation tensor
$\mathbf{A}_{ij}$	Rolie-Poly sub-orientation for element i coupled with element j
$\mathbf{A}_i$	Total Rolie-Poly orientation for element i
B	Swelling ratio, defined as D/d_0
b	Statistical step length
C_∞	Polymer backbone characteristic ratio
c_ν	Constraint release scaling term
C_1	WLF horizontal shift factor
C_2	WLF horizontal shift factor
C_3	WLF vertical shift factor
D	Extrudate diameter
$\mathbf{D}$	Rate of deformation tensor
d_0	Diameter of extrusion die
D_B	Distance below the die the maximum swelling ratio occurs
Đ	(poly)Dispersity
e	Contraction ratio at die entry
f	Material elasticity parameter
$F(\lambda)$	Finite extensibility function
f_{ns}	First non-solvent element $= lastfast + 1$
$fastfactor$	*flowSolve* criterion for dynamically working out fast modes
$firstStretch$	The fastest Rolie-Poly element treated using the stretch Rolie-Poly equation
g	Acceleration due to gravity (9.81 mm s^{-2})
G'	Storage modulus
G''	Loss modulus
G_{entry}	Relaxation modulus at a die entry
G_{exit}	Relaxation modulus at a die exit
G_0	Plateau modulus $G_0 = \frac{4}{5}G_e$
G_e	Entanglement modulus
G_i	The relaxation modulus of simulation mode i

Symbol	Definition
I	Identity matrix
k_B	Boltzmann constant
l	Die length
l	Monomer bond length
l	Sample length
l_0	Sample length upon loading
$lastfast$	The last simulation mode included in the solvent viscosity
m	Fitting parameter for *Tanner* theory
m	Mass of polymer
M_{mon}	Monomer weight
M_{poly}	Polymer molecular weight
M_e	Entanglement molecular weight
M_n	Number average molecular weight
M_w	Weight average molecular weight
max_{len}	The maximum allowed length of a simulation triangle side
n	Number of backbone bonds
N	Degree of polymerisation
N_1	First normal stress difference
N_A	Avogadro's constant
p	Flow pressure
$p, \mu(t), R(t)$	GLaMM theory terms
q	Number of 'Pom-Pom' arms
Q	Volume flux into a capillary
R	Gas constant
$\langle R \rangle$	Mean end-to-end distance
$\langle R^2 \rangle$	Mean square end-to-end distance
$\mathbf{R}(s,t)$	Tube trajectory tensor
r_{cap}	Capillary radius
r_{entry}	Radius of a flow entry line
r_p	Piston radius $\equiv r_{\text{entry}}$
s	tube co-ordinate
$\mathbf{S}$	Pom-Pom orientation tensor
S_{xx}, S_{yy}	Orientation is the xx or yy directions respectively

Symbol	Definition
S_c	Critical orientation value for onset of monomeric friction reduction
$surface$	*flowSolve* Surface tension term
T	Temperature
$\overline{T}$	Average value of quantity or tensor T
$\overset{\nabla}{\boldsymbol{T}}$	The Upper Convected Maxwell derivative of tensor
t	Time
t_{dump}	Time between writing of simulation output files
t_{max}	Maximum simulation run time
t_{real}	Real (non-simulation) flow time
t_{stop}	Time after which the simulation flow input is stopped
t_{strain}	*flowSolve* internal time scale
T_0	WLF reference temperature
T_g	Glass transition temperature
T_m	Melting temperature
$timestep$	Strain time per simulation step
$unit_{\text{length}}$	*flowSolve* internal length unit
v	Flow velocity
v_{inp}	Flow input velocity
v_p	Piston velocity $\equiv v_{\text{inp}}$
W_d	Reptation Weissenberg number
w_j	Weight fraction of chains j
W_R	Rouse Weissenberg number
Z	Number of entanglements per polymer chain=M_W/M_e
Z_{eff}	Effective (diluted) number of entanglements per chain

Statement of Copyright

Acknowledgements

Adequately thanking everyone who has helped me whilst completing my PhD would require far too many pages so I will try to be brief.
To my supervisors, Richard, Tom and Ian. Thank you for all the helpful meetings, your enthusiasm for polymers, allowing me to go to all corners of the world and for reading many a paper or thesis draft. I couldn't have done this without your supervision.
To Mum, Dad, Grandma and Judith. For your love, support, encouragement, food and your many fun scientific questions I am forever grateful.
I thank my SOFI CDT cohort. You have all supported me with help, advice, discussion, fun and laughter throughout the last 4 years and I hope we all stay in touch!
Thank you Rahul for agreeing to live with me for three and a half years and being a great flatmate. Sometimes we even saw each other.
Thanks to my many friends at St Nic's church, especially my TAP group. My PhD would not have been possible without you all helping me through so many prayers and so much fellowship (i.e. cake). I will miss you all.
To the Thompson group past and present: Arron, Vicki, Elise, James, Ophelie, Colin, Matt, Rebecca, Carl, Steve, Dave. Thank you for office/tea-time chat, discussions and practical help. Some of it was about science. Special thanks to Steve, Carl and Dave for teaching me all I know about rheology, both experiment and theory. This isn't goodbye, just an extended TGOT.
Thanks as well to Dr Tim Nicholson for hosting me down in Queensland and teaching me the inner workings of *flowSolve*.
To Matilda, for the gift of hydraulic oil, freely given.
Thanks to everyone at DUHWS for walking with me up many a mountain and thus keeping me sane through 8 years in Durham. Thanks for the adventures, and I'll see you on the fells sometime!
The greatest thanks of all go to the awesome God who has made all of this possible. As a rheologist I have to say that all mountains do indeed flow before the LORD.

Chapter 1

Summary

This thesis aims to understand the extrudate swell of complex industrial polymer formulations. This work does not follow much previous literature in choosing a polydisperse, semi-crystalline polyethylene to study. Instead, for the first time, in Chapter 4, monodisperse melts of linear polystyrene are used. In these systems rheological features are sharp, unaltered by polydispersity, which makes them ideal for investigating the effects of a range of constitutive and geometrical parameters on extrudate swell. Chain stretch and orientation are used to describe how the flow conditions at different points along an extrusion die effects extrudate swell. Experimental and simulated values of extrudate swell are presented and compared. The well controlled, monodisperse samples are available only in small quantities, therefore the Multi-Pass Rheometer, with its small sample volume, is used for small-scale experiments. An extension to the existing Rolie-Poly model in the form of monomeric friction reduction is introduced to improve agreement with experiments. Secondly, in Chapter 5, a bidisperse system is investigated as a first approximation to a polydisperse melt. This provides a first look at how polydispersity will affect extrudate swell whilst still within a well-defined system. Moving up in complexity, moderately polydisperse systems are studied and simulated using the Rolie-Double-Poly equation set before moving onto some industrial, very significantly polydisperse materials in Chapter 6. These systems allow investigation of the effect of molecular weight distribution on swelling ratios as well as test the limits of the polydisperse theories. In Chapter 7 sets of polyethylene samples with controlled molecular weight and well defined degrees of long chain branching are used to show how branching affects the extrudate swell whilst still allowing resolution of molecular detail. Firstly, Chapters 2 and 3 describe previous work on extrudate swell, background to the constitutive equations and a description of the experimental techniques used.

Chapter 2

Introduction

This section describes the background to this thesis. Firstly in Section 2.1 the previous work and theories underlying extrudate swell are explained. Secondly, in Section 2.2 the relevant background behind polymer dynamics and some constitutive equations are described. Thirdly, Sections 2.3 and 2.4 describe the background behind the computational and experimental apparatus.

2.1 Extrudate Swell

Extrudate swell is a long-standing problem in industrial extrusion. The phenomenon was originally called 'die swell' after the extrusion dies used as inserts in industrial extrusion equipment. In very early work it was called the 'Barus effect'[1] but this term is no longer used except in use of a B value to describe swelling. In this work it is referred to as extrudate swell in recognition that it will occur on any form of extrusion process, not just that involving a die. A schematic description is shown in Figure 2.1. In short, when a viscoelastic melt flows through a pipe and emerges from a contraction it swells outwards. The extrudate thus has a larger diameter than the original extrusion pipe. The industrial problem occurs when a specific extruded product shape is required. A die cannot be chosen of the same shape as the desired product as extrudate swell will deform the flow after the die into a different shape. Careful die design is therefore required to ensure a specific polymer at a specific set of flow conditions meets the minimum criteria for a product shape. Extrudate swell is caused, in part, by stresses relaxing at the die exit.[2] If the swelling is not understood these stresses may be 'trapped in' to the final product, causing weaknesses within the product. An understanding of the causes of extrudate swell

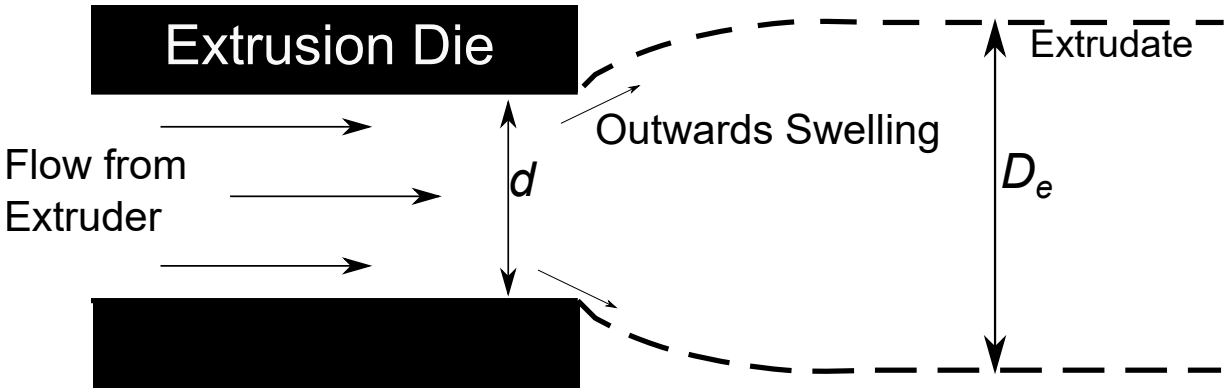

Figure 2.1: Schematic diagram describing the phenomenon of extrudate swell

and ways of predicting its effects has therefore long been sought after.

2.1.1 Theoretical Prediction of Swelling

Attempts to predict extrudate swell date back to approximately the 1970s with the theory of Tanner.[3] This theory assumed that extrudate swell was a consequence of elastic recovery of a fluid element at the die exit as in Figure 2.2.

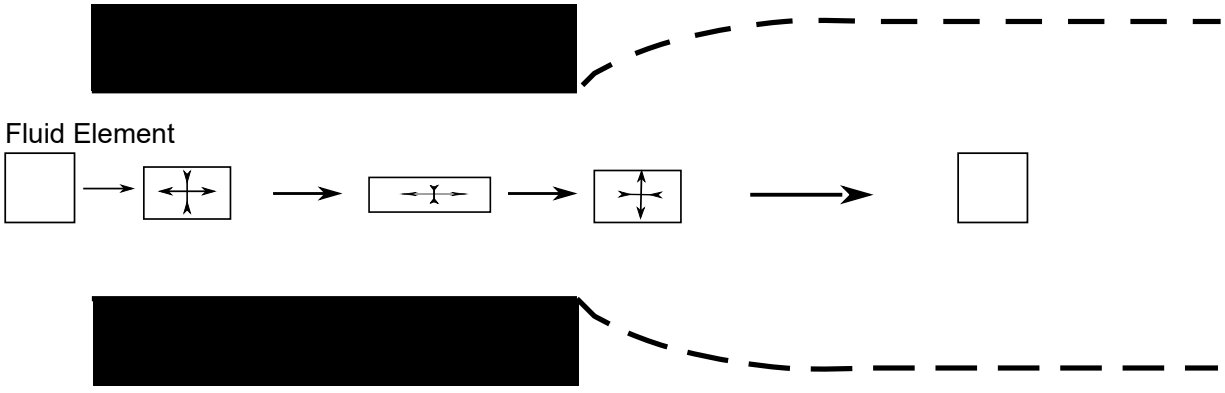

Figure 2.2: Deformation of a fluid element along and after an extrusion die. The element goes from undeformed before the die to elongated in the flow direction within the die before relaxation occurs perpendicular to the flow direction after the die exit.

If stresses are solved over the deforming fluid element a general relationship is obtained:

$$B = \frac{D_e}{d} = \sqrt[6]{1 + f^2/2}$$
$$\text{where} \tag{2.1}$$
$$f = \left(\frac{N_1}{2\tau}\right)_w$$

D_e is the diameter of the extrudate, d is the die diameter (shown on Figure 2.1) and the B value (or swelling ratio) is the ratio of the two. N_1 and τ are respectively the normal stress difference and shear stress at the die wall. This theory produced reasonable predictions for some experimental measurements although failed to predict the well known condition that extrudate swell ratios tend towards 1.1 for Newtonian flow, compared to the value of 1 that would indicate no swelling. Tanner therefore introduced a correction factor of 0.1 to give the equation:

$$B = 0.1 + \left(1 + \frac{1}{2}\left(\frac{N_1}{2\tau}\right)_w^2\right)^{\frac{1}{6}} \tag{2.2}$$

The correction factor is purely added to match experimental data and has no physical basis from the elastic recovery arguments used in the theory derivation. Indeed, this factor was later revised to 0.13 to give better agreement [4] and is altered to 0.2 in the case of slit (rather than capillary) dies.[5] This indicates the slightly arbitrary nature of these predictions. Prediction of the Newtonian value of swelling is difficult using elastic recovery arguments as all stresses should have relaxed by the die exit.[6] The theory above has been useful and is widely accepted despite the fact that it misses various factors:

- Die Entry effects are ignored. Upstream stresses at a die entry are ignored, assuming homogeneous flow. Effectively, the die length l is infinite.
- Die Exit effects are ignored. The die exit is assumed to be simply a removal of the boundary provided by the die wall. In reality, an exit corner results in an extensional flow at the exit point (extensional pull-off) which will affect the stress state at the exit.
- A single relaxation time is assumed. The material is assumed to relax at one relaxation time only, rather than having multiple modes of relaxation as exist in polymer melts.
- A B value is the only output value. A single swelling ratio is only partially useful,

distances taken to relax and an extrudate profile would also be beneficial.

- There are no allowances made for effects such as gravity, surface tension or cooling of the extrudate that will cause the extrudate profile to differ for a practical extrusion into cold air.

Tanner later edits the equation to replace the factor $\frac{1}{2}$ by a variable parameter $\frac{4-m}{m+2}$ which reduces to Equation 2.2 for m=2. The fitting parameter m=2 results in an over-prediction in swelling although using m=3.8 has been shown to produce better agreement to experimental data.[7] In [8], Guillet *et al* investigated the effects of upstream contractions on swelling. They extended the formula of Tanner, adding a factor representing the stress built up at the die entry and taking into account relaxation along the die.

$$B = \left(\frac{e^3(G_{\text{exit}}) + e(G_{\text{ent}} + G_{\text{exit}})}{G_{\text{exit}} + e(G_{\text{ent}} + G_{\text{exit}})} \right)^{\frac{1}{6}} \tag{2.3}$$

e is the contraction ratio at the die entry, G_{ent} is the relaxation modulus at the die entry and G_{exit} is the relaxation modulus at the die exit. The longer the residence time within the die, the lower the exit modulus and thus the lower the extrudate swell. This simple theory, combined with Equation 2.2, gave the correct trend in swelling ratios with die length; a decrease in swelling with increasing $l:d$ ratio. It also correctly captured the decrease in extrudate swell with increasing die residence time,[9] implying that the important factor is the time, relative to a polymer relaxation time, available for stress to relax within the die. The long die residence times were achieved either via low shear rates or by long die lengths (at constant $l:d$). The trend was that at short residence times B increased rapidly whilst at long times it tended towards a constant value of 1.1-1.4 depending on shear rate. This value depended greatly upon the entry contraction ratio, which increased the narrower the capillary (the greater the contraction ratio). This was stated to be due to the differing normal stress difference at the die exit. Similarly, maximum, high shear values varied rapidly, being up to 2.45 for short capillaries but 1.65 for long and wide capillaries. The capillary diameter, contraction ratio and $l:d$ ratio must all be taken into account when comparing any values of extrudate swell. The polymers used in [9] were high and low density polyethylenes and polystyrene. The swelling ratios were generally lower for polyethylenes than for polystyrene with very little difference between HDPE and LDPE. This may be due to the significantly shorter relaxation times for polyethylenes compared to polystyrene. Swelling ratios for orifice dies (with no capillary or a very short capillary) have been found to be 66% higher than for dies with long $l:d$ ratios.[10] Liang

[11] described another model for predicting extrudate swell based on the die exit pressure drop:

$$B = [1 + (\frac{3\Delta P_{\text{exit}}}{\tau_w})^2]^{\frac{1}{4}} \tag{2.4}$$

This expression matched experimental data well at high shear rates but greatly under-predicted swelling at low shear rates. It therefore fails to capture the effect of polymer viscoelasticity on swelling. The same group later found a linear dependence of swelling on wall shear stress:[12]

$$B = f_0 + f_1\tau_w \tag{2.5}$$

The constants f_0 and f_1 are material specific elasticity parameters and are fitted to data for each material. Later papers add a second order term $f_2\tau_w^2$.[13] This equation is not predictive, rather is used to extract material parameters from experimental data.

For Newtonian flows, extrudate swell can be analysed in terms of the Reynolds number of the flow.[14] At low Reynolds numbers (laminar flow) the extrudate swell is $\sim 1.1 - 1.2$, but at high Reynolds number, the extrudate swell is lower and necking is exhibited, where there is an initial expansion out of the die but the flow later contracts. At higher Reynolds number, B becomes less than 1, so the fluid contracts upon exiting the die. This behaviour will not be the same for non-Newtonian, polymeric systems. This is explained in terms of the inertia of the flow; the flow will move forwards out of the die faster than the internal stresses can relax. At low speeds, the stresses have ample time to relax and extrudate swell is slightly higher. At very high speeds extrudate swell will be 'delayed'.[15] Here, the extrudate emerges from the die faster than it can relax outwards. Swelling does not start at the die exit, rather beginning a short way from the die exit, expanding gradually to the same maximum swelling ratio as if swell had occurred instantaneously.

A way of predicting extrudate swell more faithfully to the underlying physics is to use a constitutive equation and a fluid dynamics package. In 2015 Konaganti *et al* [16] used the PolyFlow package[1] to investigate the effect of a series of constitutive equations on predictions of extrudate swell. They used both integral models, such as K-BKZ and differential models such as Phan Thien Tanner (PTT). Overall all these models correctly predicted the change in extrudate swell as a function of shear rate but the integral models over-predicted swelling ratios and the differential models under-predicted them. Konaganti *et al* showed that this was due to memory effects from the die entry. The parameters for both models derived from linear and non-linear rheological fits, therefore

[1]This is a commercial CFD Package, found at https://www.ansys.com/en-gb/products/fluids/ansys-polyflow

it seemed that the differences in swelling ratio predictions came from a difference in the model within the solver used rather than a parametrisation error. Material data on the HDPE were missing, including molecular weight distribution data and structural (branching) information, therefore it is not possible to say if the under-prediction was inherent in the differential model based methods used in their work and in this thesis. Kim used a similar set of equations to investigate the effect of die $l:d$ ratio on capillary flow.[17] Longer dies had a smaller die entry pressure drop and a more stable flow at the die entry but the effect on swelling was not investigated. The different constitutive equations predicted significantly different swelling ratios, with PTT fitting extrudate swell well and the Pom-Pom model for branched polymer melts under-predicting the swelling significantly. Ganvir *et al* performed simulations using a Lagrangian-Eulerian solver and the PTT [18] and the eXtended Pom-Pom (XPP) models.[19] They found good agreement with experimental data for linear, low density polyethylene and the PTT model while the XPP model gave reasonable predictions for a branched polyethylene at high temperatures. The high temperature was required due to the non-isothermal extrusion. Slow relaxation modes within the polyethylene mean that stress takes a long time to relax. If the extrudate cools below either its glass transition or melting temperature within this time the swelling will cease and swelling ratios will be lower than predicted. The extrusion conditions are therefore very important in measuring extrudate swell.

2.1.2 Experimental Extrusion Measurements

Practically, previous measurements have used a capillary rheometer to obtain the controlled shear rates required. A schematic of the setup is shown in Figure 2.3. The die can be changed to allow for a variety of different geometries. The length l and diameter d of the die can be changed, the entry angle into the die can be altered and the die material can be varied. The setup generally involves vertical extrusion downwards into air. To obtain an accurate measurement of extrudate swell; surface tension, gravity and thermal effects must be either eliminated or corrected for. The extrudate will minimise surface energy, therefore surface tension will favour an almost spherical extrudate rather than a long and thin one. Gravity will pull the extrudate down, causing necking or die contraction. Temperature effects are less certain. If extrudate cools it will contract thermally, causing die contraction. However, the extrudate may also expand due to temperature differences between the outside and inside of the extrudate and thus differences in polymer relaxation times. Cooling below a glass transition temperature (T_g) will completely arrest swelling

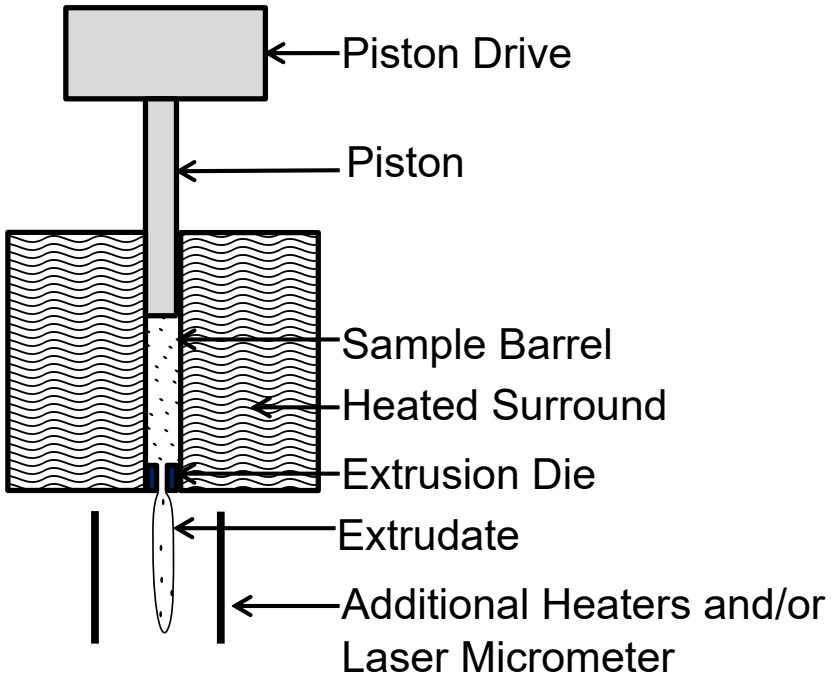

Figure 2.3: A schematic diagram of a capillary rheometer

whereas cooling below a melting temperature (T_m) may cause other effects such as changes in volume associated with changes in crystallinity. Temperature differences will result in three stages of extrudate swell with increasing time:[20]

1. An initial rapid expansion out of the die.

2. A contraction due to temperature differences between the extrudate and surrounding medium.

3. A steady state flow where the extrudate is 'frozen'

Eliminating temperature dependence can be done by annealing into a hot medium. This can be into hot air [20, 21] or into a hot oil bath as in [22]. The advantage of the hot oil bath was that gravity could also be eliminated by choosing an oil of the same density as the extrudate. The extrudate could therefore be measured for a very long period of time without cooling or sagging, and the steady state flow for polyethylenes observed. In non-isothermal cases measurements can be carried out by annealing the extrudate. This involves taking a sample of the extrudate and heating it up above the glass transition temperature then waiting for any internal stresses to relax. The advantage of this method is that all stresses in the sample completely relax. This is useful in samples

in which rapid cooling outside the die would cause crystallisation, trapping stress inside the crystal, thus distorting extrudate swell data. The disadvantage of this method is that it is difficult to measure change in extrudate swell over time and that measured diameters must be corrected for thermal expansion/cooling. For example, in [23] the polymer used was polypropylene which crystallises upon cooling to room temperature. Annealing the samples resulted in an increase in B by $\sim$0.1 and correcting for a change in density with temperature increased B by a further 0.1. This is equivalent to an increase of 30-35% in swelling ratio. A similar comparison for polystyrene only resulted in a 5-6% increase, highlighting the difference between crystalline and non-crystalline polymers. The annealing temperature can have a small effect on B,[24] so care must be taken to relax all samples the same amount. Polymers extruded at temperatures close to their glass transition will have more trapped in stress than those extruded at high temperatures. This is a problem for most commercial polymers, which are glassy or crystalline at room temperature. One study on polybutadiene [25] (which is molten at room temperature) showed that the effect of gravity was small for high molecular weight samples and that extrusion into a medium such as oil or water resulted in an increase in swelling ratios versus extrusion into air. It is therefore best not to use of an oil bath for extrusion even if it eliminates the gravity effects for low viscosity samples. Heating the extrudate below the die so extrusion is isothermal as in [21] is preferable. The simplest way to minimise gravity effects is to remove the extrudate as soon as it is extruded. This was done in [23] both as a way to minimise gravity and to obtain samples for later measurement. Another way is to use a high viscosity sample, i.e. with a high molecular weight, which minimises the relative effect of gravity on the overall stress state of the sample.[24]

In 1998, Yang *et al* investigated the effect of molecular weight on extrudate swell.[26] They found an increase in swelling ratio with increasing dispersity but, crucially, found that both the time dependent swell during annealing and ultimate (fully annealed) extrudate swell was molecular weight independent when rescaled by polymer relaxation time. The polymer relaxation times were not calculated directly, rather being taken from the relative viscosities of each sample at a constant stress. This study also found a general decrease in swelling with increasing die length, but also a decrease in swelling with the addition of slip at the die exit, showing that extrudate swell depends on both die entry and exit effects.

It is necessary to account for differences in the stress-state of the sample across the extruder, not only considering shear at the die wall but extension at the die entry and exit. Working out the molecular reasons for these differences will provide a better understanding

of the polymer physics underlying extrudate swell.

2.2 Polymer Physics

An isolated or unentangled polymer chain consisting of n bonds of length l will not have an end-to-end distance equal to its contour length, nl. Instead it will assume a random Gaussian coil formation with an end to end distance $R \propto \sqrt{n}l$. This is due to the increased entropy of the chain when it takes up a disordered, random coil conformation. The polymer will have an average end to end distance $\langle R \rangle = \sqrt{C_\infty n}l$. C_∞ is a measure of the stiffness of the polymer backbone. The two polymers used in this work are polyethylene and polystyrene, having C_∞ of 6.8 and 9.85 respectively. [27, 28]. Instead of using monomer numbers the statistical step length b is used. A chain can be said to consist of N freely jointed segments of length b. $b = \sqrt{\langle R^2 \rangle / N}$ where N is the degree of polymerisation. If one were to stretch out the polymer chain towards its finite extensibility (approximately the contour length) it would relax back towards its Gaussian coil configuration due to an entropic spring force (according to the Rouse model). This time taken to relax back will increase with molecular weight of the polymer and also the viscosity of any surrounding media.[27]

$$\tau_r \propto \frac{\eta_0 M_{\text{poly}}}{\rho RT} \tag{2.6}$$

The reorientation time, τ_r is not to be confused with the Rouse time τ_R in the next section although is related. For a polymer melt, the viscosity η_0 is given by:

$$\eta_0 = \frac{b^2 \zeta \rho N_A M_{\text{poly}}}{36 M_{\text{mon}}^2} \tag{2.7}$$

ζ is a monomeric friction coefficient, ρ is the melt density, N_A is Avogadro's number, M_{mon} is the monomer weight and M_{poly} is the polymer weight. An important scaling to note here is that when Equation 2.7 is substituted into Equation 2.6 the Rouse reorientation time is proportional to the molecular weight squared.

2.2.1 Tube Theory of Polymer Melts

The above scaling of viscosity being proportional to molecular weight is not universally valid. In the melt, above a critical molecular weight the viscosity increases as $M_w^{\sim 3.4}$ and the polymer melt must be thought of as entangled. These entanglements act like temporary

cross-links, preventing polymer chains from freely relaxing via Rouse motion. This critical molecular weight is approximately 2-3 times the molecular weight between entanglements, M_e. To consider accurately the motion of an entangled polymer chain within a melt of other polymer chains not only the individual motions of our test chain must be considered but also the motion of all chains around it and how all the chains interact with each other. The relaxation methods available are described using tube theory. The tube theory of polymer dynamics was first developed by Doi and Edwards [29] and hinges on the idea that a polymer chain can be thought of as kept within a constraining tube made up of all surrounding chains, shown in Figure 2.4 a).

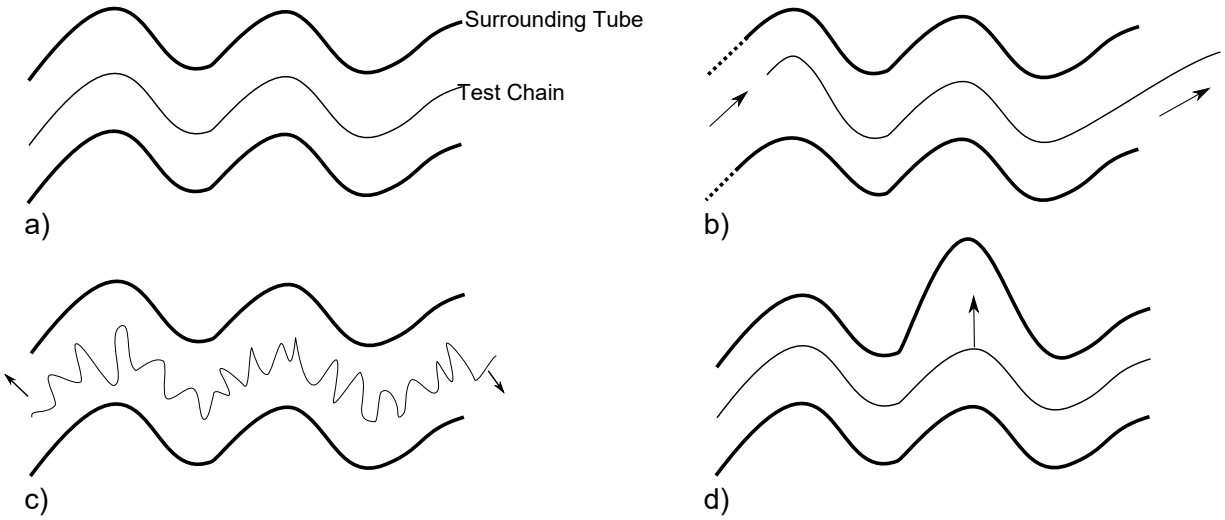

Figure 2.4: Relaxation processes available to a test chain within the tube theory. a) describes a polymer chain constrained within a tube, b) describes reptation motion, c) describes Rouse motion and d) shows a constraint release event.

The test chain is considered as being made up of individual entanglement segments of molecular weight M_e. The number of entanglements per chain is given by the parameter Z, calculated using $Z{=}M_w/M_e$. Each entanglement relaxes individually on a timescale governed by the equilibration time (also called entanglement time), τ_e. This timescale is calculated using Equation 2.8.

$$\tau_e = \frac{\zeta a^2 M_e}{3\pi^2 k_B T M_{mon}} \tag{2.8}$$

ζ is the monomeric friction coefficient, a is the tube diameter, M_{mon} is the monomer molecular weight, and k_BT is the thermal energy at a temperature T.

The tube constrains the test chain so that it can only relax an applied deformation

by escaping the constraints of its tube. It can do this by reptation motion, Rouse motion and tube constraint release, defined below:

1. Reptation Motion.
   The simplest way that a tube segment can escape its tube is via curvilinear diffusion along the tube direction. As the chain ends of a tube reptate, they will escape the tube, and thus effectively forget the constraints the tube applied. A new, relaxed tube segment is created at one end of the chain and tube constraints are lost at the other end. This is illustrated in Fig 2.4 b). This process occurs on a time-scale governed by the reptation time, τ_d. The subscript d here refers to the alternative term *disengagement time*. This is the average time taken for a tube segment to completely move out of its constraining tube.

2. Rouse motion.
   In the previous point it was assumed that the polymer backbone is rigid and only able to move along its own length. In reality however, the constraining tube diameter is much greater than the monomer diameter and thus the polymer chain can be assumed to be Gaussian within its tube. The conformation of the chain is constantly changing due to Brownian motion. These motions allow relaxation of stress within a single entanglement segment and allow relaxation of chain stretch, which distorts the chain from a Gaussian configuration. Nearer the ends of the tube, Rouse motion can cause chain ends to escape the tube and thus create new tube segments. This is called primitive path (or contour length) fluctuation (CLF) and is shown in Figure 2.4 c). This process is governed by the Rouse time τ_R as well as higher frequency Rouse processes.

3. Constraint Release.
   The constraining tube is not fixed, rather being made up of a network of entangled chains which are also relaxing via reptation and curvilinear Rouse motion. Constraint release occurs where surrounding chains relax so as to remove a tube constraint on our test chain. (Figure 2.4 d)) The motion of the test chain is less hindered by the tube and it relaxes faster.

When under flow a polymer chain will be both stretched and oriented by the flow. Chain orientation involves the individual tube segments described above being aligned with the flow direction. Relaxation of this orientation requires the polymer chain to forget the constraints imposed by the oriented tube. This is governed by the reptation time, τ_d.

Chain stretch involves the individual monomers becoming aligned with each other within the tube, and ceasing to occupy a random walk orientation within the tube. The extreme value of this stretch would imply that the monomers were all perfectly aligned with each other and the chain would have length Nl where N is the number of monomers in the chain and l is the length of a monomer unit. Relaxation of the stretch requires local motion of individual segments within the tube via Rouse motion and is thus governed by the Rouse time, τ_R. These processes are described in Fig 2.5.

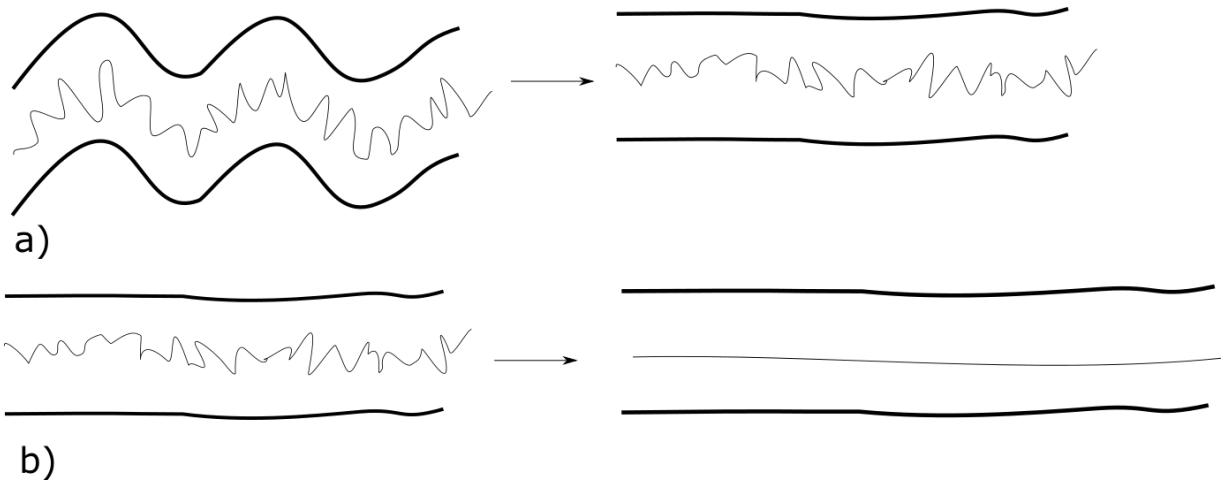

Figure 2.5: Deformation of a chain under flow. a) describes chain orientation whereas b) describes chain stretch.

Constraint release when under flow is replaced by *convective* constraint release (CCR). Tube constraints are released, not by thermal fluctuations, but by the imposed flow field removing the surrounding chains.

A flow can be made non-dimensional using these relaxation times. For a shear flow with shear rate $\dot{\gamma}$ the rates can be made non-dimensional via Weissenberg numbers:

$$\begin{aligned} W_d &= \dot{\gamma}\tau_d \\ W_R &= \dot{\gamma}\tau_R \end{aligned} \tag{2.9}$$

Above the reptation Weissenberg number W_d, chains are beginning to be oriented by a flow field and above the Rouse Weissenberg number W_R chains begin to become stretched.

2.2.2 The Rolie-Poly Equation for Linear Melts

The original Doi-Edwards formulation of the tube model works well (with adaptations) for linear flows and oscillatory shear experiments.[30] However, in non-linear flows there are problems in which unphysical phenomena are observed above the reptation Weissenberg number. Milner *et al*[30] corrected for this in the region $\tau_d < \dot{\gamma} < \tau_R$. They describe in detail the motion of a 'tube trajectory' tensor as a function of time t and distance along a tube s: $\mathbf{R}(s,t)$. This theory includes DOI-Edwards terms for relaxation and also CCR and Rouse motion terms. Their theory was later incorporated by a more comprehensive model by Graham, Likhtman, Milner and McLeish,[31] abbreviated to GLaMM. This equation set includes reptation, constraint release, CCR and CLF as previously but allows for chain stretching (i.e. where relaxation of chains within the tube is not instantaneous). The equation set is complex and involves separate differential terms for many different modes of chain relaxation as well as an integral equation for the overall polymeric stress. The advantage of this model over previous theories is that good predictions for start-up shear experiments over a very wide range of shear rates (both above and below W_d and W_R) are obtained. Predictions in extensional flow were limited by the lack of a correction for finite extensibility of chains. The start-up shear and extensional tests referred to here are commonly used for testing these constitutive equations. The experiment (generally a constant deformation rate) is started at time t=0 and the change in shear/extensional viscosity measured as a function of time from this point. This test allows transient data on the sample to be measured and may also allow a steady state viscosity to be measured at a specific deformation rate.

The major problem for utilisation of the full GLaMM model in flow computation is the complexity and relative computational intractability of solving an integral equation over a discrete mesh for thousands of time steps. Likhtman *et al* therefore introduced a single mode differential form called the Rolie-Poly model by removing the dependence of the stress on tube co-ordinate 's' and producing simple forms for chain retraction and CCR.[32] The term Rolie-Poly stands for 'Rouse Linear Entangled Polymer'. The equation they obtained (Equation 2.10) contains terms for convection, reptation, Rouse and CCR motions respectively.

$$\frac{d\sigma}{dt} = \kappa\cdot\sigma + \sigma\cdot\kappa^T - \frac{1}{\tau_d}(\sigma - I) - \frac{2(1-\sqrt{3/\mathrm{trace}(\sigma)})}{\tau_R}\left(\sigma + \beta\left(\frac{\mathrm{trace}(\sigma)}{3}\right)^{\delta}(\sigma - I)\right) \quad (2.10)$$

β describes the level of constraint release. I is the identity matrix and σ is the polymeric

stress. δ is a fitting parameter, always taken as -0.5 to match the full GLaMM theory. β=1 matches the predictions of the full theory although Likhtman *et al* found that β=0.5 better fit the steady shear data. This theory can be used in single or multi-mode forms to describe different relaxation processes. The Rolie-Poly model has been used in a variety of flow simulations; predicting stress birefringence and pressure drops for industrial samples within constriction flows,[33, 34] stress birefringence for monodisperse samples in a flow cell experiment [35] and extrudate swell.[36] In [37], stress birefringence and pressure drops in constriction flow are predicted well at low speeds for monodisperse polymers. The use of monodisperse polystyrenes allowed the separate effects of orientation and stretch above reptation and Rouse Weissenberg numbers respectively to be seen. Predictions started to become inaccurate slightly above W_R=1. The model has been extended to take into account finite extensibility effects [38, 39] where improved predictions of shear and extensional flow are obtained versus the infinitely extensible equation. Various other improvements to the model have been proposed and will be discussed in later sections. The Rolie-Poly equation described above gives a single tensorial differential equation for use in a flow solving package:[32]

$$\overset{\triangledown}{\boldsymbol{\sigma}} = \frac{(\boldsymbol{\sigma} - \mathbf{I})}{\tau_d} - \frac{2}{\tau_R}\left(\frac{\lambda - 1}{\lambda}\right)\boldsymbol{\sigma} - \frac{2\beta}{\tau_R}\left(\frac{\lambda - 1}{\lambda}\right)(\boldsymbol{\sigma} - \mathbf{I}) \tag{2.11}$$

$\boldsymbol{\sigma}$ is the polymeric stress tensor, $\mathbf{I}$ is the identity matrix, λ is the chain stretch and β is the convective constraint release (CCR) parameter.The chain stretch is calculated from the stress using: $\lambda = \sqrt{\text{trace}(\boldsymbol{\sigma}/3)}$. This definition of the stretch is the main difference from the original form in Equation 2.10 along with the omission of δ as a variable parameter. Introduced here is the upper convected Maxwell derivative, $\overset{\triangledown}{\boldsymbol{\sigma}}$. This notation removes the flow induced stress terms from the sum and will be used for various equation sets in this thesis.[2]

$$\overset{\triangledown}{\boldsymbol{\sigma}} = \frac{d\boldsymbol{\sigma}}{dt} - \boldsymbol{\kappa}\boldsymbol{\sigma} - \boldsymbol{\sigma}\boldsymbol{\kappa}^T \tag{2.12}$$

where $\boldsymbol{\kappa}$ is the velocity gradient tensor. The first term in Equation 2.11 describes the relaxation of orientation on the timescale of the reptation time. The second term describes relaxation of chain stretch on the timescale of the Rouse time. The third term describes relaxation of stress due to constraint release, happening on the Rouse relaxation timescale.

[2]In the simulations we use here the flow terms are included in the Lagrangian method used and therefore the UCM form is used.

Finite extensibility

Equation 2.11 presumes that chain stretch can increase infinitely. In reality however, chains can only extend to their contour length without breaking. In particular, the polystyrenes used within this work have a low finite extensibility. In addition, the further a chain is perturbed from its Gaussian coil conformation (stretched) the greater the spring force that is trying to reduce the stretch. A spring force, $F(\lambda)$, will restore chains to equilibrium. This is generally presumed to follow the form of the inverse Langevin function. The inverse Langevin function must be approximated in order to be tractable, and here the Pade approximation is used:

$$F(\lambda) = \left(\frac{\lambda_{\max}^2 - \lambda^2/3}{\lambda_{\max}^2 - \lambda^2}\right)\left(\frac{\lambda_{\max}^2 - 1}{\lambda_{\max}^2 - 1/3}\right) \tag{2.13}$$

Incorporating finite extensibility into the standard Rolie-Poly equation set gives:[38]

$$\overset{\nabla}{\mathbf{A}} = -\frac{1}{\tau_d}\left(\mathbf{A} - \lambda^2\mathbf{I}\right) - \frac{2}{\tau_R}\left(F(\lambda) - \frac{1}{\lambda}\right)\mathbf{A} - \frac{2\beta}{\tau_R}\left(F(\lambda) - \frac{1}{\lambda}\right)\frac{F(\lambda)}{\lambda}\left(\mathbf{A} - \frac{1}{F(\lambda)}\mathbf{I}\right) \tag{2.14}$$

At low chain stretch values $F(\lambda) \to 1$ and relaxation rates are unchanged. As λ increases $F(\lambda) \to \infty$. The tensor $\mathbf{A}$ is a chain orientation tensor and is related to the overall chain stress via the modulus G in Equation 2.15.

$$\boldsymbol{\sigma} = G \cdot F(\lambda) \cdot \mathbf{A} \tag{2.15}$$

This 'single mode' approach may work for monodisperse linear polymers but most real melts have a spectrum of relaxation processes due to higher frequency Rouse modes of chains or due to polydispersity incorporating additional relaxation times. The Rolie-Poly model used in this work is a multi-mode version in which the stress contributions of several independent modes are summed to give an overall polymeric stress. In this case, high frequency modes (where chain stretch can be assumed to relax very quickly) are approximated using the non-stretch Rolie-Poly equation, Equation 2.16.

$$\overset{\nabla}{\mathbf{A}} = \frac{(\mathbf{A} - \mathbf{I})}{\tau_d} - \frac{2}{3}\left(\text{trace}(\boldsymbol{\kappa} \cdot \mathbf{A})\right)\left(\mathbf{A} + \beta(\mathbf{A} - \mathbf{I})\right) \tag{2.16}$$

The orientation values from all modes are then summed up to give a single stress as before. For n modes:

$$\boldsymbol{\sigma} = \sum_{i=1}^{n}(G_i \cdot F(\lambda_i) \cdot \mathbf{A}_i) \tag{2.17}$$

2.2.3 Rolie-Double-Poly for Bidisperse Blends

Although the Rolie-Poly equation can be used with multiple stretching modes as an attempt to model bidisperse or polydisperse samples the simple summation of elements means that the each stretching term is mathematically uncoupled from all others. For polydisperse systems it is not correct to consider molecular weight fractions as uncoupled. To this end Boudara *et al* developed the Rolie-Double-Poly equation sets described in this section.[40, 41] Consider a short chain s and a long chain l with Rouse times $\tau_{R,s}$ and $\tau_{R,l}$, reptation times $\tau_{d,s}$ and $\tau_{d,l}$ and volume fractions ϕ_s and $\phi_l = 1 - \phi_s$. The total Rolie-Poly stress is the sum of the stresses of short and long chains.

$$\boldsymbol{\sigma} = G_0 \cdot (\phi_s \cdot F(\lambda_s) \cdot \mathbf{A}_l + \phi_l \cdot F(\lambda_l) \cdot \mathbf{A}_l) \tag{2.18}$$

G_0 is the plateau modulus of the material, as taken from the linear rheological data.The $\mathbf{A}$ tensors describe the orientation of each chain and $F(\lambda)$ is the finite extensibility function for each chain defined in the previous section. As in the Rolie-Poly equation, $\lambda_s = \sqrt{\frac{\text{trace}(\mathbf{A}_s)}{3}}$. The average orientations of each chain are given by:

$$\begin{aligned} \mathbf{A}_l &= \phi_l \cdot \mathbf{A}_{ll} + \phi_s \cdot \mathbf{A}_{ls} \\ \mathbf{A}_s &= \phi_s \cdot \mathbf{A}_{ss} + \phi_l \cdot \mathbf{A}_{sl} \end{aligned} \tag{2.19}$$

The coupled orientation terms are worked out using a form similar to the Rolie-Poly equation. For the ll and ss terms:

$$\overset{\nabla}{\mathbf{A}}_{ss} = -\frac{1}{\tau_{d,s}}(\mathbf{A}_{ss} - \mathbf{I}) - \frac{2}{\tau_{R,s}}\frac{\lambda_s - 1}{\lambda_s}F(\lambda) \cdot \left[\mathbf{A}_{ss} + \frac{\beta}{\lambda_s}(\mathbf{A}_{ss} - \mathbf{I})\right] \tag{2.20}$$

As previously, β is the CCR coefficient. The ll and ss terms simply describe the relaxation of chains due to entanglements with themselves. For a blend there are also cross coupling terms in which short chains are entangled with long ones and long chains are coupled with short ones. For the sl and ls terms the equation is slightly more complex:

$$\begin{aligned} \overset{\nabla}{\mathbf{A}}_{sl} = &-\frac{1}{\tau_{d,s}}(\mathbf{A}_{sl} - \mathbf{I}) - \frac{2}{\tau_{R,s}}\left(\frac{\lambda_s - 1}{\lambda_s}\right)F(\lambda_s)\mathbf{A}_{sl} \\ &-\frac{1}{\tau_{d,l}}(\mathbf{A}_{sl} - \mathbf{I}) - \frac{2\beta}{\lambda_s\tau_{R,l}}\left(\frac{\lambda_l - 1}{\lambda_l}\right)F(\lambda_l)(\mathbf{A}_{sl} - \mathbf{I})) \end{aligned} \tag{2.21}$$

The indices can be reversed for the ls term. Here, instead of the standard Rolie-Poly terms, there is a coupled CCR term which describes the rate of constraint release for short chains entangled with long chains.

Boudara used these equations to predict extensional and shear flow for a series of bidisperse polyisoprene blends. The predictions of extensional flow were good, but over-predicted extensional viscosities under high shear rates. In [41] a second set of similar equations (Symmetric RDP) were developed which utilised reduced computation time by making sl terms equal to ls terms. This produced similar results for extension and shear, but in reducing the number of matrix elements to be calculated should reduce computation time, especially in complex flows or in the polydisperse case where there are many more cross terms.

2.2.4 Rolie-Double-Poly for Polydisperse Melts

The form of this Rolie-Double-Poly (RDP) equation set is simply an extension of the bidisperse equation set discussed previously.[40] Consider a series of Rolie-Poly elements, each with a reptation time, τ_d, a stretch relaxation time, τ_R and a weighting, ϕ where $\sum \phi$=1. The overall polymeric stress may then be calculated using:

$$\boldsymbol{\sigma} = G_0 \cdot \sum_{i=f_{\text{ns}}}^{n} \phi_i \cdot F(\lambda_i) \cdot \mathbf{A}_i \tag{2.22}$$

$\mathbf{A_i}$ is the total orientation of element i, λ_i is the chain stretch of element i, calculated using $\lambda_i = \sqrt{\text{trace}(\mathbf{A}_i/3)}$ in the same way as with monodisperse Rolie-Poly and f_{ns} is the index of the first non-solvent mode in the simulation. The orientation on an element is the sum of the orientations of element i coupled with all other elements, j:

$$\mathbf{A}_i = \sum_{j=1}^{n} \mathbf{A}_{ij} \cdot \phi_j \tag{2.23}$$

where the orientation on element i due to coupling to element j is given by:

$$\begin{aligned} \overset{\nabla}{\mathbf{A}}_{ij} = &-\frac{1}{\tau_{d,i}}(\mathbf{A}_{ij} - \mathbf{I}) - \frac{2}{\tau_{S,i}}\left(\frac{\lambda_i - 1}{\lambda_i}\right) F(\lambda_i)\mathbf{A}_{ij} \\ &-\frac{1}{\tau_{d,j}}(\mathbf{A}_{ij} - \mathbf{I}) - \frac{2\beta}{\lambda_i \tau_{S,j}}\left(\frac{\lambda_j - 1}{\lambda_j}\right) F(\lambda_j)(\mathbf{A}_{ij} - \mathbf{I}) \end{aligned} \tag{2.24}$$

The first line in Equation 2.24 is similar to the standard Rolie-Poly terms for chain orientation and stretch for chain i. The second line contains coupling terms due to relaxation of j chains. The second term is the rate of CCR in the i chains taking into account the stretch in both i and j chains. Boudara used these equations to predict polydisperse polystyrene melts of dispersities of 1.8 and 2.3. Here, the extension hardening was reasonably accurately predicted, and the differences in this extension hardening between the two dispersities predicted but the linear viscoelastic prediction was incorrect in both cases, resulting in viscosities which were too high. Overall the model seems to give good predictions for mildly polydisperse melts especially given its simplicity. Boudara did not perform any flow simulations using these equations, so this thesis is the first time these equations have been used in such simulations.

2.2.5 Pom-Pom Equation for Branched Polymers

It is often required to simulate branched polymers for which the earlier methods of relaxation are no longer relevant. The Pom-Pom polymer is a model branched system, consisting of a backbone with a branch point at each end of the backbone and some number of dangling arms attached to each branch point.[42] In this case, reptation of the polymer along its backbone tube is no longer possible at short timescales as this would require retraction of all branch arms into the backbone tube; an entropically unfavourable process. In the case of short branch arms contour length fluctuations are very significant. The branch arms are so mobile that the chain ends are effectively unconstrained by a tube and thus relax very quickly. The backbone relaxation time is much longer and requires the backbone to relax via Rouse motion whilst still maintaining the arm constraints. The exact relaxation processes available to a branched polymer therefore depends on the relative sizes of the backbone and branch arms as well as the number of arms and branch points. It is possible to assume that the branch arms relax fast compared to the backbone and thus the polymeric stress at a wide range of timescales comes from the backbone.

Figure 2.6 shows the Pom-Pom polymer; a polymer with 2 branch points and with q branches on each. As the backbone is stretched tension is built up. This produces a restoring spring force pulling the chain ends together into a a random coil configuration. Large chain stretch values would result in high restoring forces and would thus cause branch points to be pulled back into the crossbar tube. (Figure 2.7) The dynamics of this 'branch point retraction' mean that the maximum chain stretch is therefore equal to q. This is implemented via a hard cut-off, where the chain stretch $\lambda \leq q$.

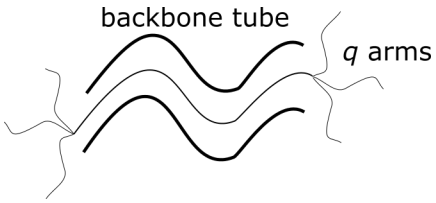

Figure 2.6: Schematic diagram of the Pom-Pom polymer

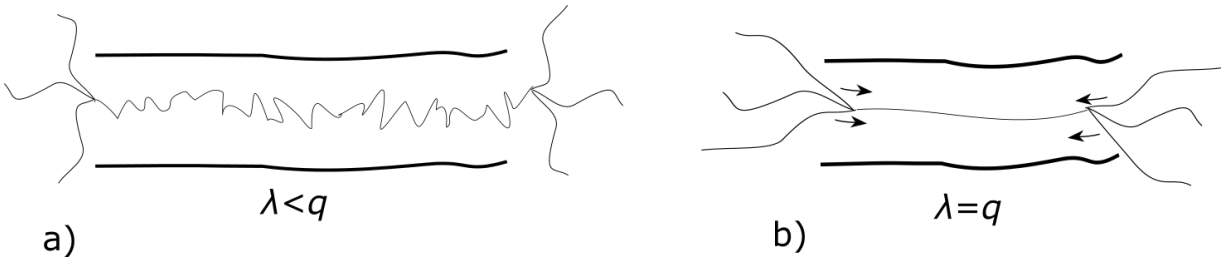

Figure 2.7: a) orientation and b) stretch of the Pom-Pom polymer for a chain stretch λ and a number of arms $q = 3$

The full model involves a integral formalism but was approximated into a differential form (Equation 2.25) to aid computation.

Pom-Pom Equation Set

Two separate components are present in the Pom-Pom set; orientation and stretch. For chain orientation, the simple form of Equation 2.25 is used:[42, 43]

$$\begin{aligned} \overset{\nabla}{\mathbf{A}} &= -\frac{1}{\tau_b}\left(\mathbf{A} - \boldsymbol{I}/3\right) \\ \mathbf{S} &= \mathbf{A}/\mathrm{trace}(\mathbf{A}) \end{aligned} \tag{2.25}$$

τ_b is the backbone orientation time. The tensor $\mathbf{S}$ describes the chain orientation and is calculated from the auxiliary tensor $\mathbf{A}$ which is used for the calculations. $\mathbf{S}$ will increase in magnitude from 0 to 1 as the chains become more oriented. The orientation term does not depend on the backbone stretch. The stretch is calculated via a second differential equation, Equation 2.26

$$\frac{d\lambda}{dt} = \lambda\boldsymbol{\kappa} : \mathbf{S} - \frac{1}{\tau_S}(\lambda - 1) \tag{2.26}$$

τ_s is the stretch relaxation time. The finite extensibility is then applied via:

$$\text{if}(\lambda > q) : \lambda = q \tag{2.27}$$

The stretch is influenced by the chain orientation via the primary flow term. The stretch relaxation time is generally not given explicitly, rather being defined as a ratio of τ_b to τ_S. The overall polymeric stress is calculated from both the stretch and orientation. As with the Rolie-Poly model this single mode model is extended to a multi-mode model by summing up stress contributions for each mode.

$$\boldsymbol{\sigma} = \sum_{i=1}^{n} \left(3 \cdot G_i \cdot \lambda_i^2 \cdot \mathbf{S}_i\right) \tag{2.28}$$

Although the Pom-Pom model was designed using a simple molecular architecture it has been found that describing a wide range of branched polymers using the multi-mode Pom-Pom idea results in qualitatively accurate predictions for a variety of more complex branched architectures.

Additions to the Pom-Pom model

Multiple additions to this model have been proposed such as drag-strain coupling [44] to avoid the hard cut-off in stretch but the only one incorporated within *flowSolve* is the correction for reversing flows:[45]

$$\frac{1}{\tau_b} = \begin{array}{l|l} \dfrac{1}{\tau_b} & \lambda > 1 \\ \dfrac{1}{\tau_b} + \dfrac{\dot{\lambda}}{\lambda} - (\boldsymbol{\kappa} : \mathbf{S}) & \lambda < 1 \end{array} \tag{2.29}$$

This correction corrects for the idea that for when a flow is reversed, e.g. at the die exit, the tube surrounding a polymer chain may relax backwards faster than the chain itself. This would mean that polymer chain ends would become unconstrained by the original constraining tube and thus new tube segments would be created around the chain, aiding backbone relaxation.

Previous Work

McLeish *et al* [43] and Inkson *et al* [46] described the predictions of the model in steady state flow and the effect of different parameter sets on start-up shear and extensional predictions. The differential form of Pom-Pom was developed for ease of use in programs such as *flowSolve* for modelling polymers under flow in arbitrary geometries and has been successful in modelling such flows in numerous studies. Bishko [42] described modelling a contraction geometry and in [47], described the use in an early incarnation of *flowSolve*. Use of the Pom-Pom model to predict stress birefringence is common, in [48] it was predicted for linear, polydisperse polystyrenes up to high flow speeds in an constriction flow. This shows the usefulness of the Pom-Pom model, that it is able to cope with linear and branched architectures simply by changing the input parameters. A problem with the model here was that it did not predict the flow instabilities that occurred at high flow rates but stable flow was predicted well. The model has been used to predict novel flow features for branched polyethylenes, including stress fangs below an upstream contraction [45] but fails to predict the formation of 'W cusps' in cross-slot flow,[49] showing that the model still lacks some of the physics needed to model flow of highly branched polymers at high extensional rates.

2.2.6 The XPP Model for Branched Polymers

The eXtended Pom-Pom model (XPP model) [50] was designed to fix some of the deficiencies of the original Pom-Pom model, namely the lack of a second normal stress difference and the unphysical hard cut-off in stretch caused by Equation 2.27. It was also designed to be easier to compute in finite element type solvers.

Rather than using the $\mathbf{A}$ tensor and dividing by its trace the XPP model uses the orientation tensor, $\mathbf{S}$ for the orientation evolution equation. Equation 2.25 becomes 2.30:

$$\overset{\nabla}{\mathbf{S}} + 2[\mathbf{D} : \mathbf{S}] \cdot \mathbf{S} = -\frac{1}{\lambda^2 \tau_b} \left(3\alpha\lambda^4 \mathbf{S} \cdot \mathbf{S} + (1 - \alpha - 3\alpha\lambda^4 \text{trace}(\mathbf{S} \cdot \mathbf{S})) \cdot \mathbf{S} - \frac{1-\alpha}{3} \cdot \mathbf{I} \right) \quad (2.30)$$

Here, α is a material dependent anisotropy parameter and $\mathbf{D} = \frac{1}{2}(\boldsymbol{\kappa} + \boldsymbol{\kappa}^T)$, the rate of deformation tensor. The removal of the finite stretch condition means that the q finite stretch is implemented by the XPP stretch equation:

$$\begin{aligned} \frac{d\lambda}{dt} &= \lambda \mathbf{D} : \mathbf{S} - \frac{1}{\tau_S'}(\lambda - 1) \\ \tau_S' &= \tau_S \exp\left(-\frac{2}{q}(\lambda - 1)\right) \end{aligned} \tag{2.31}$$

In effect, rather than a hard cut-off in stretch at q the model reduces τ_S the closer λ gets to q. Stretch therefore relaxes exponentially faster as it increases. It does not relax instantaneously however, for example if q=5 and λ=q, τ_S is reduced to around 20% of its equilibrium value. For fast enough flows stretch may still be built up above this point and λ may thus significantly exceed q.

2.3 The *flowSolve* Fluid Dynamics Package

The *flowSolve* package was developed in Leeds by the μPP microscale polymer processing project.[3] It has been adapted to include the Rolie-Poly and Pom-Pom models for simulating polymer flows. It has most often been used alongside the Multi-Pass Rheometer (MPR) to test the Pom-Pom model with regards to stress birefringence,[37, 49] although there are studies using the Rolie-Poly model.[48] Some very limited prior work exists with regards to the Pom-Pom model in free-surface flow.[51]

2.3.1 Finite Element Analysis

The program uses the finite element method; rather than attempting to solve the constitutive equation over a continuum, the region to be simulated is split up into a number of discrete elements where the flow field variables (e.g. pressure p, stress σ and velocity v) will be calculated.

The basic theory is that the flow field is calculated from the overall stress using mass and momentum conservation:

$$\begin{aligned} \nabla \cdot v &= 0 \\ \nabla \cdot \sigma &= \nabla \cdot p - \mu \cdot \nabla^2 \cdot v \end{aligned} \tag{2.32}$$

v is the flow velocity at a specific point, σ is the (polymeric) stress, calculated using a constitutive equation and μ is a solvent viscosity term, calculated by *flowSolve* for each

[3] This was an EPSRC funded project from 2001-2009. The website for this project is no longer available but some information is available at http://polymerprocess.org/

simulation. Considering a triangular finite element as in Figure 2.8:

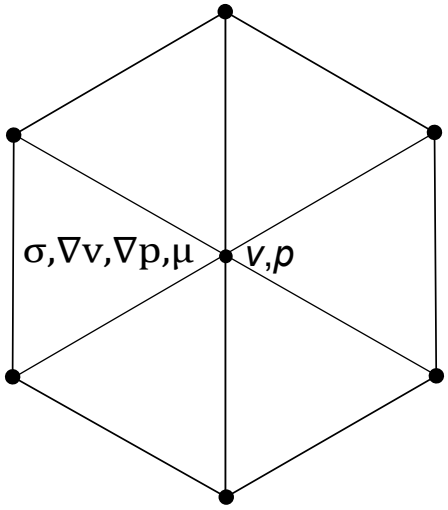

Figure 2.8: A series of finite elements in a hexagonal mesh arrangement. Each triangle vertex is a mesh point.

Each point has a velocity and pressure value. These are used to calculate velocity gradients and stresses for each triangle. To calculate the velocity at a specific point these equations are integrated over all surrounding triangles with respect to the triangle areas. Overall, this is formed into a large matrix problem for coupling of n_{tri} triangles with $n_{\text{tri}}-1$ other triangles. This is called a sparse matrix problem, as most triangles are not adjacent and thus do not contribute to the overall problem. To avoid computational artefacts based on the order in which the matrix problem is solved, it must be iterated until the solution converges. This can take some considerable time.

2.3.2 Flow Solving Routine

A basic flowchart describing the solver routine is shown in Figure 2.9. At the start of a simulation, a finite element mesh must be generated. This consists of a series of points in a hexagonal arrangement connected into a mesh of triangles. The triangular mesh arrangement is used because it readily allows a continuous deformation of the mesh throughout a simulation. A deformed triangle can still be calculated using the same equations as an undeformed one. A rectangular mesh however takes a lot more work to keep solvable as mesh elements deform. Each mesh point has a velocity applied to it which changes at each time step. Each triangle element has a velocity gradient across it as well as a stress tensor and a pressure term. This allows Equations 2.32 to be solved for each

triangle and thus velocities and velocity gradients changed due to the viscoelastic stress. A basic flow diagram can be constructed for the simulation steps:

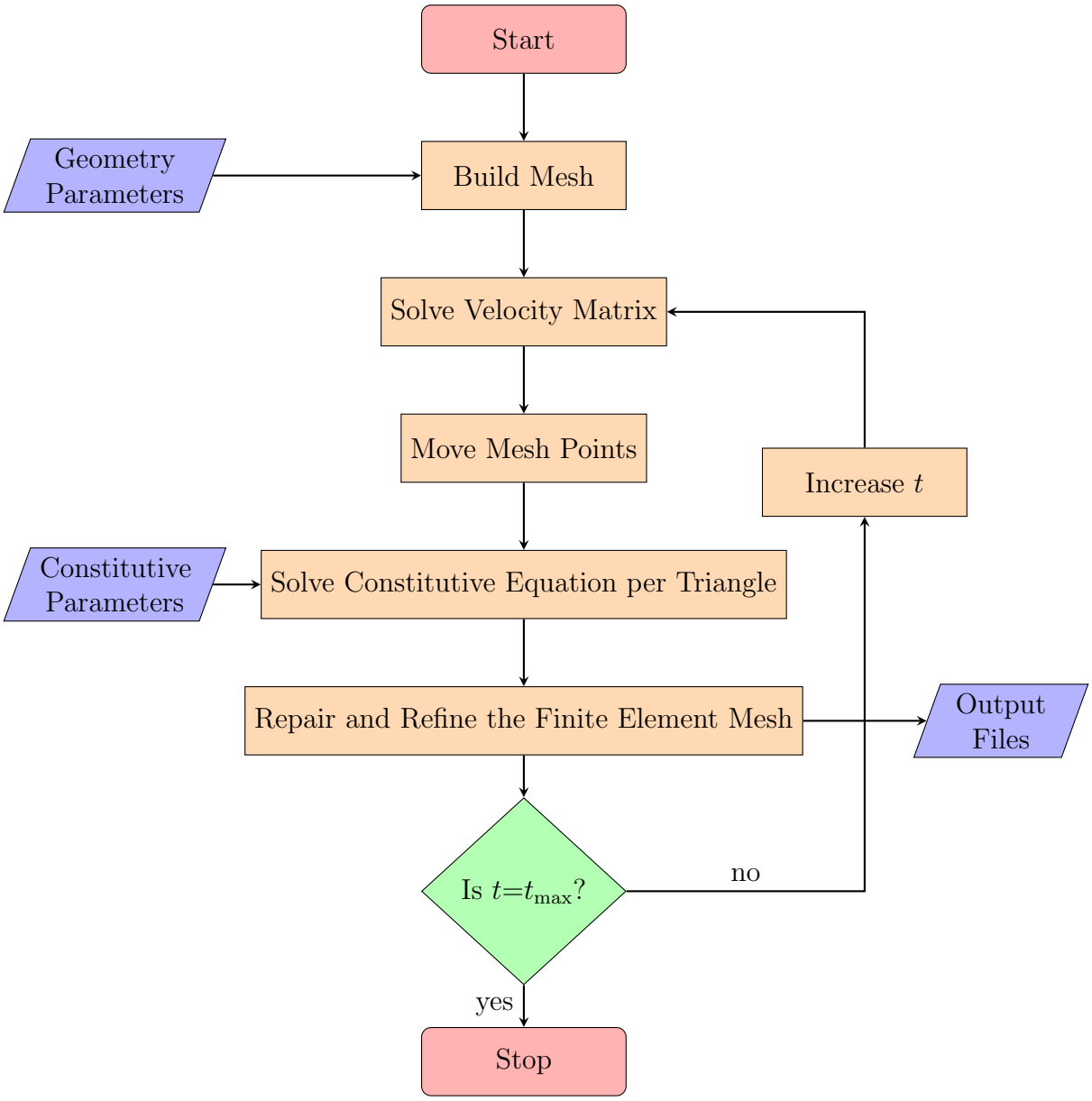

Figure 2.9: Flowchart indicating the computational method of *flowSolve*

The process behind solving of velocity gradients and movement of mesh points is not discussed further here as it has not been changed or altered within this work. Further information can be found in [47]. These steps take up the vast majority of the simulation run time. The solving of the constitutive equation is discussed in Sections 2.3.5 and 3.3.

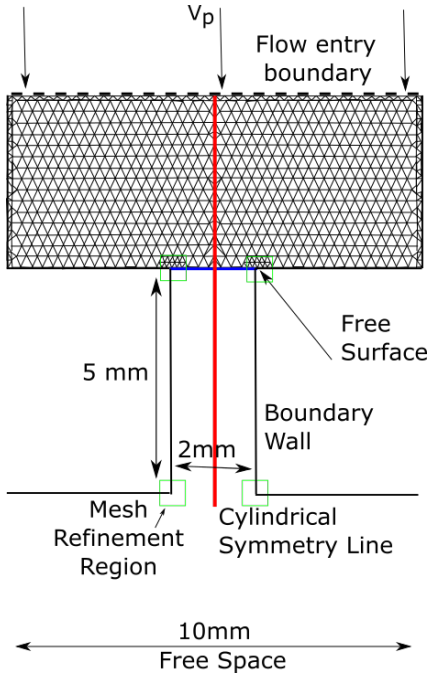

Figure 2.10: A schematic diagram of the initial *flowSolve* geometry used in extrusion simulation.

The specific parts of the mesh refinement procedure changed in this work as well as the geometry and constitutive parameter requirements are discussed below.

2.3.3 Geometry Input File Specification

An example *flowSolve* input file is given as an Appendix. The geometry which this file describes is shown in Figure 2.10.

Four separate boundary types are defined in this diagram:

1. Flow entry boundary. This is where mesh points enter the simulation. All points are defined as having an initial downwards entry velocity, v_{inp}. These points are not moved throughout the simulation and the velocity is only used for calculating the velocity gradient across the entry triangles.

2. Boundary wall. This defines the edge of the simulation area and is treated as having a no-slip boundary condition. Any point at a boundary wall has a zero velocity both tangential to and perpendicular to the wall direction and thus cannot move.

3. Mirror boundary. This defines a line of symmetry within the simulation. Use of a mirror line will greatly reduce the simulation time in geometries where symmetry exists. The tangential velocity of points on a mirror line is zero but points can move along it once fixed there.

4. Free Surface. This describes the interface between inner points (which are free to move in response to an applied velocity gradient) and the medium into which the polymer is flowing. This free-surface will have a pressure applied across it and may also have a surface tension term. These terms are used in the "Solve Velocity Matrix" step to influence the effect of applied triangle stress on the forwards free surface velocity. The pressure term in any surface triangles is replaced by an isotropic surface pressure, formed from the surface tension and any applied pressure term.

For completeness, two other boundary types are possible:

5. Flow exit. This is where points leave the simulation. As a mesh point passes across this line it is removed from the simulation and triangles it is part of also deleted. An exit velocity may also be defined so that points are pulled out of the simulation area.

6. Slip Boundary. This is the same as the Boundary wall above except that points are allowed to move along the wall once placed there. This wall has a slip length, s defined as the distance behind the wall at which the perpendicular velocity of a point would become zero. The larger the slip length the closer the slip point velocity to the centre-line flow velocity.

The simulation may also have gravity enabled or disabled. This applies a downwards force mg to any free surface points. The mass is worked out from the simulation area and a defined density.

A simulation may either be axial or planar. In a planar simulation the flux across an input line is $v_{\text{inp}} r_{\text{entry}}$ in units of mm^2 s^{-1}. In an axial simulation the flux is $\pi r^2_{\text{entry}} v_{\text{inp}}$ in units of mm^3 s^{-1}. The strain rate terms are also evaluated differently depending upon the run mode selected. To avoid having to divide by length units later the v_{inp} and r values are divided by a $unit_{\text{length}}$ value of 1 mm to ensure all lengths henceforth are in internal *flowSolve* units. Similarly, all timescales below are in reduced units of strain. $t_{\text{strain}} = \frac{t_{\text{real}}}{v_{\text{inp}}}$. Therefore, for a fixed time, a fixed volume of polymer will have passed through the entry line regardless of the value of v_{inp}.

2.3.4 Mesh Refinement Procedure

In order to generate the hexagonal mesh shown in Figure 2.10 a triangle length-scale is used. This is the maximum triangle length, max_{len}. This determines the largest triangle side allowable in the initial mesh. For later mesh refinement a max_{area} is calculated and used to determine if a triangle must be re-meshed. In Figure 2.10 and in general here, max_{len}=0.3. This may not be refined enough for simulation of special points of particular interest, for example around the extruder entry and exit. It is possible to define a mesh refinement region around these areas. Within a refinement region, the max_{len} parameter is halved, leading to a significant increase in the number of triangle elements, shown in Fig 2.11.

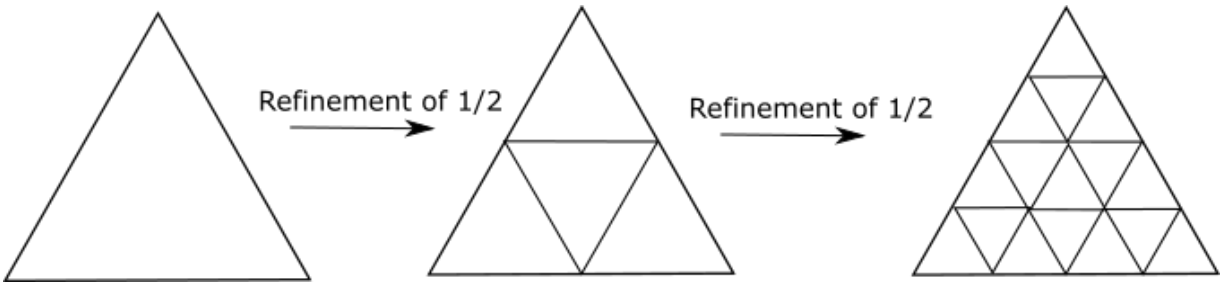

Figure 2.11: Two successive mesh refinements by a factor 1/2 on a triangle element

A mesh refinement of 1/2 will result in a doubling of the number of mesh points to solve velocities for but a quadrupling of the number of triangle elements. A further mesh refinement of 1/2 will result in 16× the triangles and 5× the mesh points. It is important therefore to choose a sufficiently coarse mesh to allow the simulation to be tractable but still maintain enough triangles to allow enough detail to be captured. The time taken to solve the finite element matrix problem scales with order n_{tri}^2 therefore significant time savings can be obtained by using a coarser mesh.

It is convenient to think of the triangle as equilateral for this diagram, however triangles will deform significantly as they move throughout the simulation geometry. The finite element solver works best when the grid is regular, therefore it will become necessary to reconnect triangles as the simulation progresses. Two examples of when this is necessary are shown in Figure 2.12. In a), point 4 has accelerated, for example at a die entry region or die exit *corner*. This means that $\triangle$045 and $\triangle$034 have become oversized. In this case, if $area_{\text{tri}} > max_{\text{area}}$, a new point is placed at the centre of the triangle and the stress divided between the three resulting triangles. In b), point 4 has decelerated,

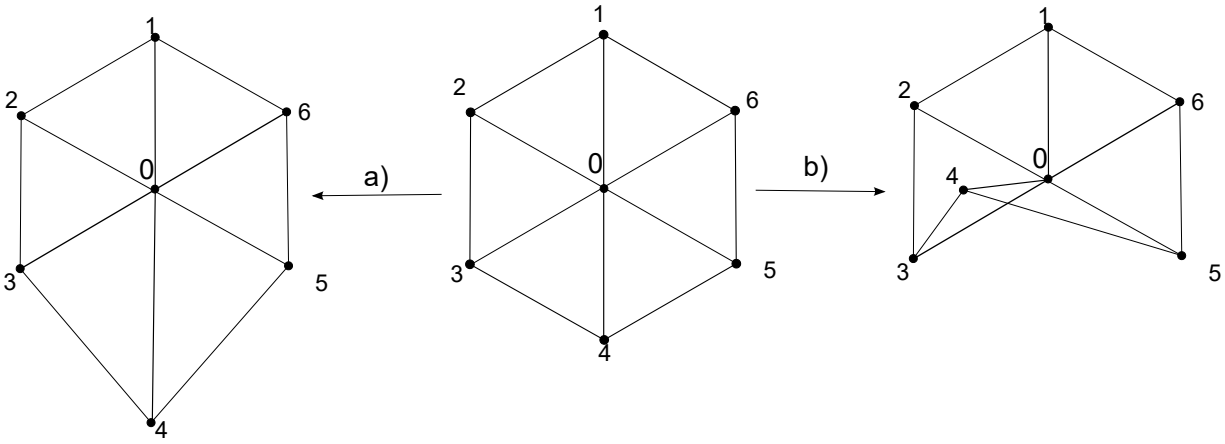

Figure 2.12: Two examples of 'unacceptable' mesh deformations during a simulation. The overall flow direction is downwards but point 4 is moving at a different velocity to the other points. In a) Point 4 has accelerated and in b) Point 4 has decelerated relative to its neighbours.

possibly after a die exit. An extreme case of this is where the velocity of point 4 changes sign and thus the point is labelled a *flipping vertex*. In either case, $\triangle 034$ has become negative. The connections of point 4 must be changed so as to maintain an acceptable mesh geometry. *flowSolve* will not allow this process to occur indefinitely, and will stall if over 100 negative triangles or flipping vertices occur during a simulation run. A special case of mesh refinement occurs at the exit corner of an extruder where the flow can round the corner, described in Figure 2.13. As the flow field rounds a corner there will come a

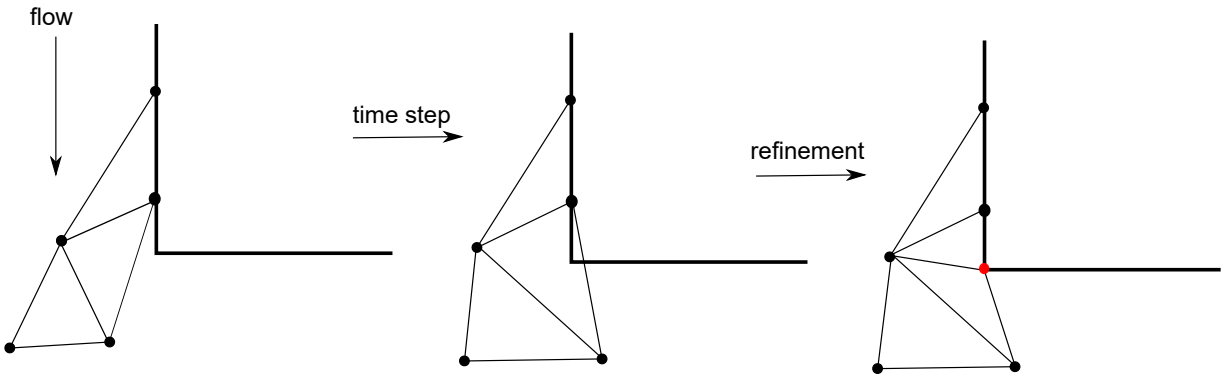

Figure 2.13: Mesh refinement around a die exit corner. The red point is a 'special' corner point.

point where a triangle element overlaps a geometry corner. This will result in inaccurate treatment of this corner and may lead to meshing errors as points can leave the geometry

at such corners. For this thesis the code has been updated[4] to create a special point at the overlapped corner and split the single triangle into two corner triangles. The special point (highlighted on the figure) is designed to deal with the exit singularity. In essence, the point is included in the *Solve Velocity* and *Update Constitutive Equation* steps but is excluded from the *Move Points* step from Figure 2.9. Thus, the velocity gradients across corner exit triangles are calculated as if the corner were not present but the exit point is consistent with the no-slip condition of the boundary wall.

2.3.5 Constitutive Parameters

Various constitutive equations are available in *flowSolve*:

- Power-law (where the power may be 1 for Newtonian fluids)
- Cross Model
- Oldroyd-B
- FENE (Finitely Extensible Non-linear Elastic)
- Single-mode Pom-Pom
- Multi-mode Pom-Pom
- XPP
- Rolie-Poly
- 2 Mode Rolie-Double Poly
- Multi-mode Rolie-Double-Poly

The Rolie-Poly and Pom-Pom equations used in this work take as a minimum input a series of Maxwell modes in ascending order of increasing τ_d. This comprises of a sequence of relaxation time-scales $\tau_{d,i}$ and a weighting term G_i which describes how the orientation of chains describes by mode i contributes to the overall stress term. In solving the Rolie-Poly equation, the Maxwell modes form a series of Rolie-Poly elements, for which various additional parameters are required:

[4]These modifications were made by the author with assistance from Dr Tim Nicholson

- $lastfast$ - *flowSolve* requires a background 'solvent' viscosity to be defined within the simulations. This solvent viscosity is used in Equation 2.32 to solve the velocity gradients. It is worked out from any 'fast' elements within the parameter set. Any elements up to and including the $lastfast$ element are defined as solvent and are not resolved using the constitutive equation.

- $fastfactor$ - This can be stated as alternative to $lastfast$ and is used for calculating the $lastfast$ for the specific simulation run. An element i is fast if $\tau_{d,i} v_{\text{inp}} > 10^{-fastfactor}$. $fastfactor$ is, by default, 2.

The solvent viscosity is worked out from any fast element using the equation:

$$\mu = \sum_{i=1}^{lastfast} G_i \tau_{d,i} \tag{2.33}$$

where i=1 is the fastest (smallest τ_d) element in the simulation

- $firstStretch$ - This is the first element which is resolved using the full stretching Rolie-Poly equation, Equation 2.14. Any element between $lastfast$ and $firstStretch$ is resolved using the non-stretch equation, Equation 2.16.

- if($i > firstStretch$) a τ_R, or Rouse relaxation time for the element.

- $surface$ - This is the surface tension term which acts across the free surface.

In the case of a non-isothermal simulation additional constitutive parameters must be added:

- WLF shift parameters, T_0, C_1, C_2.

- A freeze temperature (below which μ is set to 10^{10}).

- Heat flux across the free surface.

- Thermal conductivity.

- Heat capacity.

2.3.6 General Parameters

Various simulation specific parameters must be defined once the constitutive parameters have been defined:

- *timestep* This parameter relates the τ values to the time-scale of the simulation to be run. In order for the relaxation processes to be resolved the *timestep* should be smaller than the relaxation time of the first (fastest relaxing) slow element. A smaller *timestep* will result in a slower simulation run.
- t_{max} This is the length of time that the simulation will be run for.
- t_{stop} After this time v_{inp} is set to 0 but the simulation continues to run to allow stress relaxation.
- t_{dump} This is the time interval between the simulation producing each output file.

flowSolve allows simulation of a larger array of flow geometries and constitutive equations, and so is a powerful tool in simulation in the complex flows. The adaptability of the underlying code for new geometries and equations makes it perfect for use in this thesis.

2.4 The Multi-Pass Rheometer

2.4.1 History

The Multi-Pass Rheometer (MPR) was first developed in Cambridge[5] in the 1990s [52] for use as a high pressure, high shear rate rheometer, possibly for use on a process line. [53] The original MPR1 consisted of a simple capillary test section, from which pressure drops across the capillary could be obtained via pressure transducers in the top and lower sections (Figure 2.14)

Subsequent versions of the MPR have replaced the single capillary test section with an adjustable optical set-up. This allowed visualisation of the flow in geometries which could mimic real process flows but on small-scale volumes of material. The MPR3 had an attached X-ray apparatus to perform scattering experiments under flow.[54, 55, 56] The version used in this work is the MPR4, described in more detail below.

[5]The current pages on MPRs can be found at https://www.ceb.cam.ac.uk/research/services/rheology-centre/cambridgempr and at https://www.stratatec.co.uk/products/laboratory-solutions/multi-pass-rheometer if a sales pitch is desired.

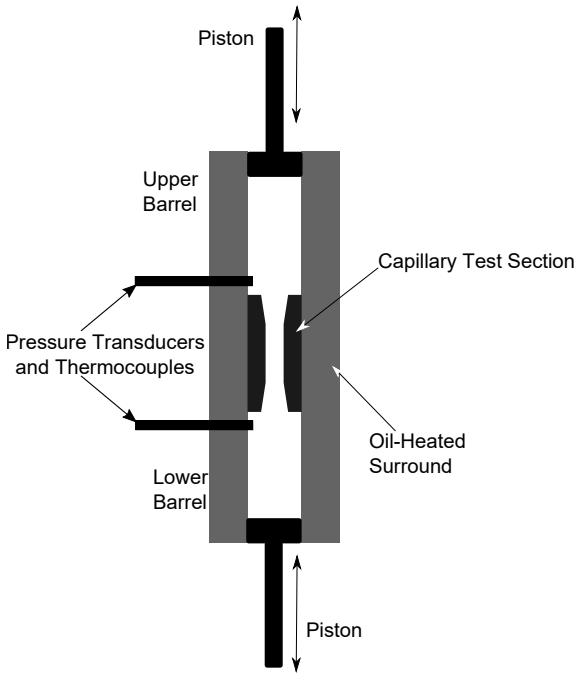

Figure 2.14: Schematic diagram of the original Multi-Pass Rheometer. Redrawn from [53].

2.4.2 Geometry

The MPR4 consists of two barrels connected by a central test section. The upper barrels are 40 mm long and 10 mm in diameter. In theory the length and diameter could be adjusted to meet a specific need, however the standard measurements are kept to in this work. A 10 mm diameter brass piston is inserted into both the upper and lower barrel. The pistons can be extended to push a sample into the test section. The test section used is designed to allow optical imaging of the sample in addition to rheological measurements. Two geometry pieces are screwed front and back into the test section and two quartz windows inserted left and right so as to slot exactly into the geometry pieces. A variety of quartz window lengths can be accommodated, shorter windows giving a test section depth of 10 mm or longer windows to give a depth of 1 mm. A 10 mm depth means that 3D effects within the test section can be ignored whilst still requiring a small sample volume to fill. One advantage of the MPR is its versatility. It can be run with many different geometries and many different run modes depending upon the physical property it is required to measure. Possible test pieces include;

- Contraction-expansion. The test pieces are inserted so as to leave a central slit through which the sample can be pushed. This allows visualisation of stresses within

the channel flow and at the entry and exit to the channel.

- Cross-slot. This test section allows extensional flow to be visualised. A sample is pushed into the geometry from the top and bottom and out of the sides. In addition to the upper and lower chambers the cross-slot has two chambers to the front and back. This means that polymer can be pushed through the section and out of the sides without leaving the MPR. A 'slave' piston driven by nitrogen pressure is used to force the sample back though the section into the barrels once the test is complete, allowing multi-pass operation.

- Tape extruder. This geometry allows extrusion of a polymer tape outside of the MPR. A narrow slit is cut in the front of the special section so that when polymer is forced into the geometry it can escape into the surrounding air and either pulled off or left to extrude.

- Capillary. The slit of the test section is replaced with a cylindrical capillary. This is particularly useful for use with axisymmetric simulations. No stresses can be visualised within the channel although they may be visible at the entry or exit of the capillary.

The sample is illuminated from the side by a 514 nm light source. The light is passed between two lenses to focus it onto the viewable area then through a linear polariser and a $^1/_4$ wave plate. These are angled at 45° to each other so as to circularly polarise the light beam. The beam then passes through the sample. At this point the polarisation of the light beam is altered by any stress present in the sample. The light is then detected by a camera fitted with a circular polariser. The stress is visible as a pattern of stress fringes.[57] These stress fringes can be converted to stress values via the stress-optical rule.[58, 59]

The most commonly used run modes are:

- Oscillatory. In this mode the upper and lower pistons are lowered and raised together in an oscillatory motion. The overall volume of sample in the barrels remains constant and the sample is transferred through the test section.

- Compression. In this mode the pistons are moved towards each other, the upper descending and the lower ascending. If used with a contraction geometry this will compress the sample. If used with the cross-slot geometry this will force the polymer out of the test section into the side barrels.

- Extrusion. In this mode a single piston is extended so as to force the sample from one barrel into the other via the test section.

The MPR is a good tool for measuring and visualising complex polymer flows such as extrudate swell. The availability of multiple accessories and fixtures mean it is versatile, but also that geometries are not perfectly sealed. This means leaks can occur at high pressure and/or if the test section is not adequately sealed. Overall, as long as the section is sealed properly the MPR will provide a good wasy of measuring extrudate swell.

Chapter 3

Experimental and Computational

The subsequent chapters all use the same experimental apparatus, computational program and theoretical basis. The experimental set-up used for linear, non-linear and processing experiments is described in Section 3.1. The parameters used within *flowSolve* and RepTate are discussed in Section 3.2 before the constitutive equations used are given in Section 3.3.

3.1 Experimental Methods

3.1.1 Material Characterisation

Before extrudate swell can be predicted the polymers used must be properly characterised from both a structural and rheological standpoint. Gel Permeation Chromatography (GPC) characterisations were performed using a Viscotek TDA 302 instrument with a triple detection system.[1] This consisted of refractive index, viscosity and right angle light scattering (RALS) detectors. Combined together, these techniques can produce an estimate of the Mw distribution of a polymer sample. To analyse the distributions the metrics used are the *Weight* Average Molecular Weight, (M_w), *Number* Average Molecular Weight, (M_n) and dispersity (Đ) values.

[1] GPCs were performed by Jon Millican at Durham University

$$
\begin{aligned}
M_w &= \frac{\sum N(M) M^2}{\sum N(M) M} \\
M_n &= \frac{\sum N(M) M}{\sum N(M)} \\
Đ &= M_w / M_n
\end{aligned}
\tag{3.1}
$$

M is the molar mass of the chain and $N(M)$ is the number of polymers with a specific mass M. In general, the M_w value rather than M_n is used in this work as this better describes the large effect that high molecular weight chains have on the molecular weight distribution and thus on the rheological properties of the melt.

Rheological tests were performed using a TA Instruments HR2 rotational rheometer. Two separate geometries were used to measure the linear and non-linear response of the polymer: the plate-plate rheometer and the Sentmanat extensional rheometer (SER)[60] attachment. These are described in the following sections.

3.1.2 Plate-Plate Rheometry

The samples used in these experiments are melt pressed into a 1 mm thick, 25 mm diameter disk at 200 °C for approximately 30 minutes. This produces a homogeneous sample which can be placed on a rheometer plate. The basic set-up of the plate-plate rheometer is shown in Fig 3.1.

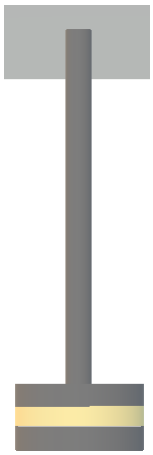

Figure 3.1: A diagram of a plate-plate rheometer

The sample is placed on a lower plate. An upper plate is lowered onto the sample so the sample applies an axial force onto the rheometer head. This axial force is allowed to

decay away until approximately zero. This ensures the rheometer head is in contact with the sample at all points and that the sample is fully relaxed before the test is started. The head is then oscillated at a specific amplitude and frequency so as to impose an oscillatory strain on the sample. The strain applied will follow the form:

$$\gamma(t) = \gamma_0 \sin(\omega t) \tag{3.2}$$

where γ is the strain at time t, γ_0 is the strain amplitude of the oscillation and ω is the oscillation frequency. The stress in the sample as a result of this strain is measured using the force transducer in the rheometer head. For a small enough strain amplitude the resulting stress waveform can be approximated to the form:

$$\sigma(t) = \gamma_0(G' \sin(\omega t) + G'' \cos(\omega t)) \tag{3.3}$$

For significantly high strain amplitudes terms of order γ_0^3 may become relevant as the non-linear regime is entered; however for all the work here a strain amplitude is chosen so the non-linear viscoelastic regime is not entered. The storage and loss moduli, G' and G'' correspond to the magnitudes of the in-phase (sine) and out of phase (cosine) components respectively. For a purely elastic material G'' will be negligible and the material response will be in-phase with the applied strain. For a viscous liquid G' will be zero and the material response will be entirely out of phase with the applied strain. The polymeric materials studied in this work will be viscoelastic, having a response somewhere between these two extremes as shown in Fig 3.2.

The traditional way of plotting these data is not as the raw waveform, but as a plot in the frequency domain, shown in Fig 3.3.

There are three distinct regions observable in this graph, labelled 1, 2 and 3. Region 1 defines the low frequency or long time response. Here, G'' is above G' and the polymer behaves like a viscous liquid. In this regime, the polymer chains have the ability to relax the imposed stress by reptation motion and have fully relaxed via local Rouse motion. At higher frequencies G' and G'' cross over with G' beginning to plateau. The inverse of this crossover frequency is approximately the reptation time, τ_d. This is the linear viscoelastic region. Here, the polymer chains are unable to relax via reptation but are still able to relax via local Rouse motion. Region 3 is a glassy regime where polymer chains cannot relax from the imposed deformation. The second crossover in G'/G'' which occurs here is at the (inverse) entanglement time, τ_e. A second way of plotting the data is the plot of

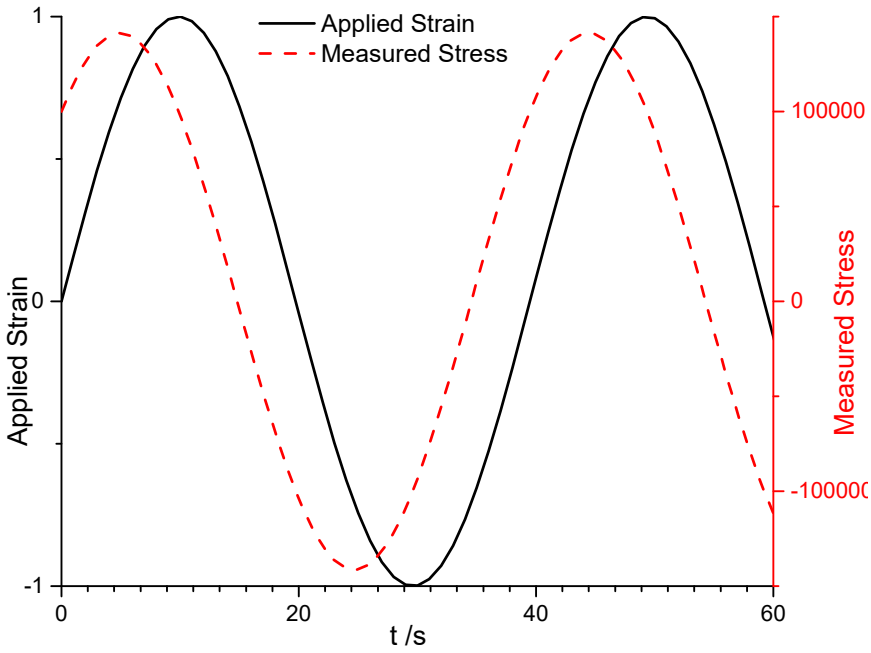

Figure 3.2: Stress response during a sinusoidal strain at a strain amplitude of 1

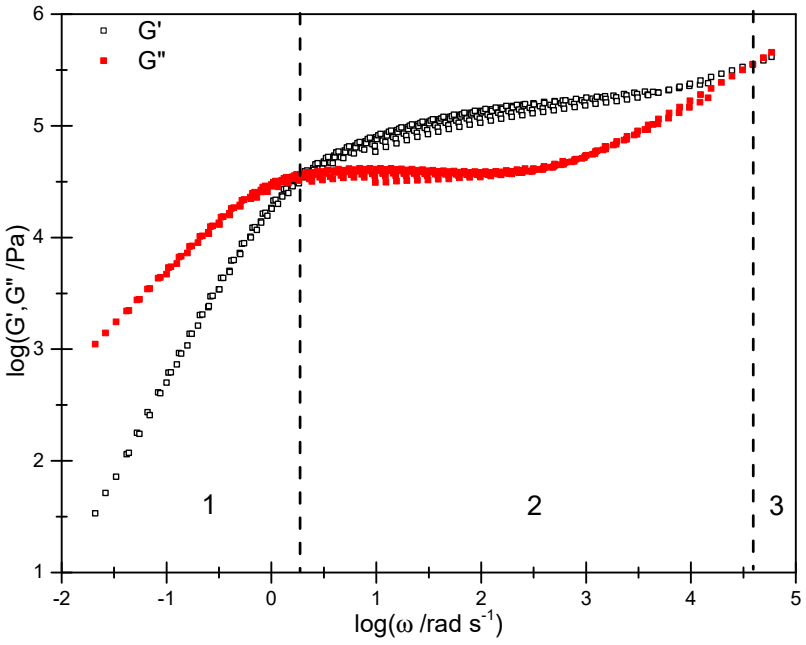

Figure 3.3: G' and G'' as a function of angular frequency for a polystyrene sample

complex viscosity η^* vs frequency. The complex viscosity is defined as:

$$\eta^*(\omega) = \frac{\sqrt{G'^2 + G''^2}}{\omega} \tag{3.4}$$

To characterise the polymers used here, the first test performed is an amplitude sweep. The strain amplitude γ_0 is varied at a constant oscillation frequency of 1 rad s^{-1} to ensure the test parameters fall within the linear regime of the samples. An example amplitude sweep is shown in Figure 3.4.

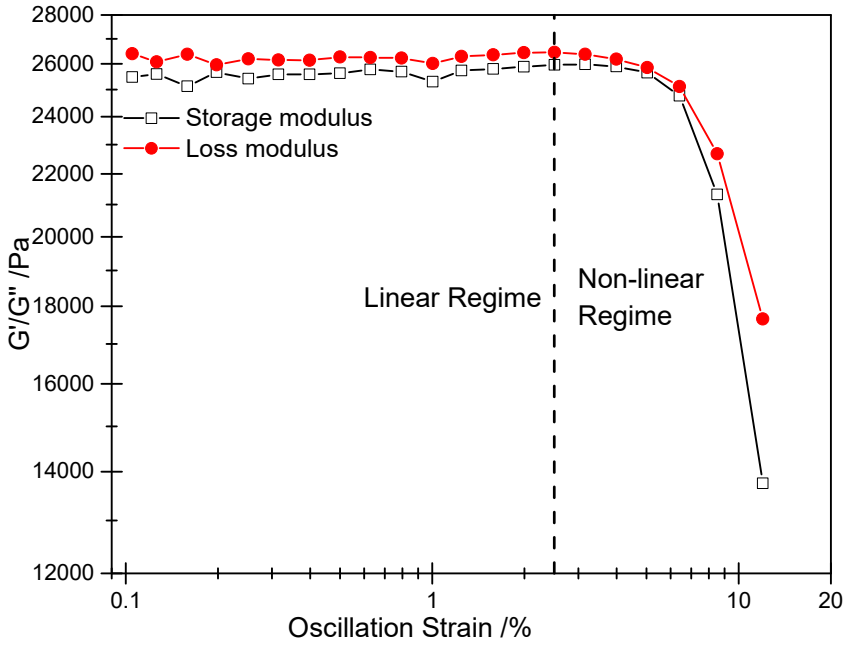

Figure 3.4: G' and G'' as a function of strain amplitude during an amplitude sweep at 1 rad s^{-1}.

The linear regime where the storage and loss moduli are amplitude independent. The non-linear regime (including Mid Amplitude Oscillatory Shear (MAOS) and Large Amplitude Oscillatory Shear (LAOS) regimes) occurs where G' and G'' drop off at increasing amplitude. For almost all polymers used in this work a 1% strain is used as it is well within the linear regime. Secondly, a frequency sweep (at 1% strain) is performed. The frequency range used is 0.1-600 rad s^{-1}. The lower limit is short enough to capture the low frequency response of the samples but long enough to limit the taken to run an experiment. The high frequency limit is approximately the upper limit of the instrument. Temperature control of the samples is achieved using an environmental test chamber (ETC) attachment to the rheometer. Compressed air is used as the purge gas

for polystyrene samples whereas nitrogen is used for polyethylenes to prevent oxidation of the samples during the test.

3.1.3 SER rheometry

The SER is a way of producing a uniaxial extensional deformation in a sample.[60] This allows measurement of the transient extensional viscosity of a polymer. The geometry consists of two counter-rotating drums attached to the rotating rheometer bearing, shown in Figure 3.5. The polymer sample is held in place by two clips attached to the drums. When the drums rotate the sample is extended uniaxially.

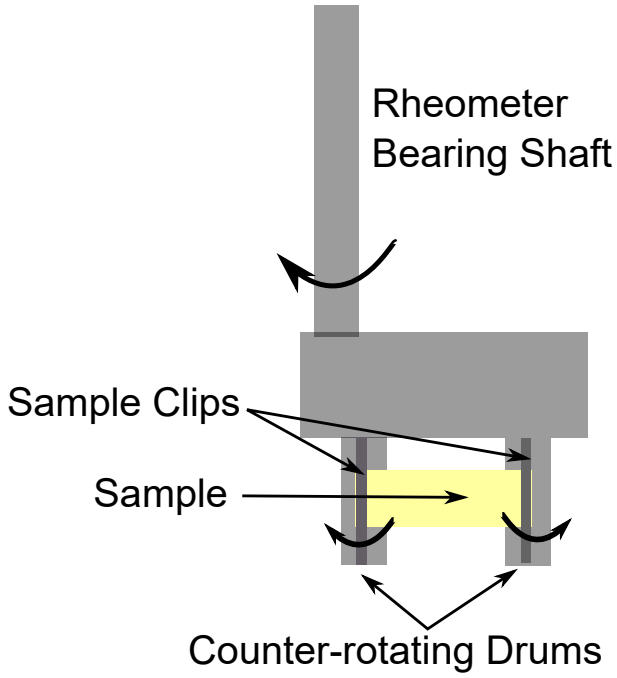

Figure 3.5: A schematic diagram of the SER geometry

The technique is prone to problems; if the clips are over-tightened around the sample it is prone to breakage at the clips. If they are not tightened enough, the polymer will simply slip out of a clip. Deformities in the sample are liable to cause breakage or necking and thus very large extensional viscosities. The parameters for the SER are given in units of Hencky strain, ϵ. This is defined as:

$$\epsilon = \log(l/l_0) \tag{3.5}$$

l is the length of the sample and l_0 its length when loaded. A maximum Hencky strain of 3.8 can be achieved before the sample clips have rotated 180° and the sample wraps around upon itself. A controlled strain rate is applied to the sample by rotating the bearing at a controlled rate and the resulting extensional stress is measured via the torque transducer in the rheometer head. Normally this stress is divided by the strain rate to give an extensional viscosity (formally a 'transient extensional stress growth coefficient'). If the viscosity grows as a function of increasing strain rate the sample is said to be extension hardening. In this work polymers for the SER are melt pressed into a 20 mm long by 10 mm wide by 1 mm thick strip. The sample is placed between the preheated SER clips and allowed to equilibrate to the test temperature. A pre-stretch is applied to the sample for 10 s at a Hencky rate of 10^{-3} s^{-1}. The test is then performed, stretching the sample at the test rate to a Hencky strain of 3.8. Each test is performed at least twice to ensure reliable results are obtained and at the highest strain rates, where the sample is especially prone to breakages, multiple repeats are performed. Typical strain rates achievable for these polystyrene samples range from 0.1 s^{-1} to 60 s^{-1}.

3.1.4 Extrusion Experiments

The two geometries used within the MPR are both capillary extruders. The 5:2 extruder consists of two MPR pieces of equal length with a semicircular hole cut in the end of each. These are screwed tight within the test section and thus a circular capillary is formed. The 5:1 geometry has one test piece longer than the other with the capillary drilled all the way through the longer piece. The 'single hole' setup is preferred as it ensures that a perfectly cylindrical capillary is always formed regardless of how tightly the test pieces are screwed together. The semicircular setup requires additional work to ensure that the test pieces meet exactly and the correct geometry die is formed. The overall geometry is shown in Figure 3.6 and the test pieces are shown in Figure 3.7.

The test section is viewed using a camera fitted with a circular polariser set-up. At the beginning of a test the capillary is blocked via a spare piston placed into the bottom chamber. The test section and upper barrel are then filled with polymer and left to melt at the extrusion temperature. After approximately 30 minutes the sample is compressed via the upper piston and the chamber re-filled with polymer then left to equilibrate. During a test the upper piston is lowered at a constant rate and the extrudate observed and recorded through the quartz windows. The wall shear rate within the capillary test section is calculated using Equation 3.6. This is an approximation for a Newtonian fluid

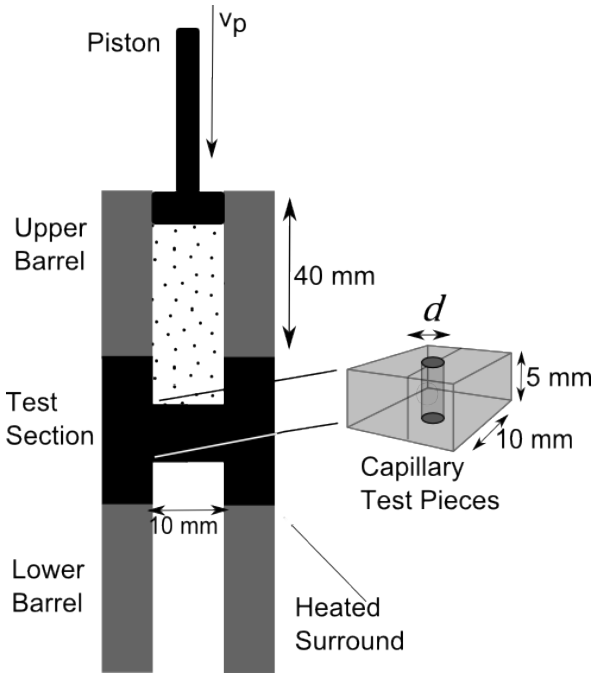

Figure 3.6: A diagram of the MPR setup used for capillary extrusion

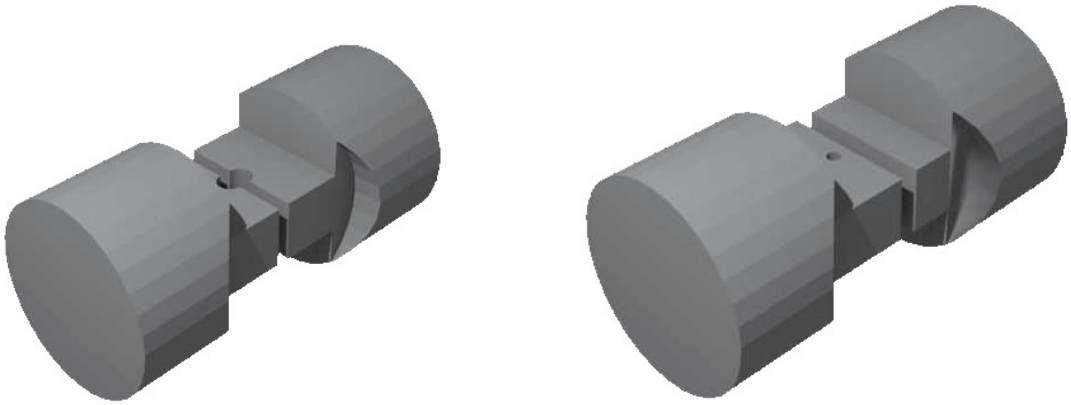

Figure 3.7: The 5:2 (L) and 5:1 (R) capillary test pieces used within the MPR

and its validity is discussed further in Section 4.2.2.

$$\begin{aligned} \dot{\gamma}_w &= \frac{4Q}{\pi r_{\text{cap}}^3} \\ Q &= \pi r_p^2 v_p \end{aligned} \tag{3.6}$$

Q is the volume flux into the test section, r_{cap} is the radius of the capillary, r_p is radius of the upper piston (5 mm) and v_p is the upper piston extension speed. Rouse and reptation

Weissenberg numbers for the flow are:

$$W_R = \tau_R \cdot \dot{\gamma}_w$$
$$W_d = \tau_d \cdot \dot{\gamma}_w \tag{3.7}$$

For each sample, a series of piston speeds are chosen so as to span a range of Rouse Weissenberg numbers above and below 1. The minimum speed possible is 0.001 mm s^{-1} and the maximum speed usefully reached is ∼10 mm s^{-1}.

The extrudate is visible in the lower portion of the test section of the MPR as a dark region (indicating polymer) on the light background (indicating free space). The diameter of the extrudate is measured using the freely available imageJ software.[2] An approximate error in the extrudate swell measurements can be obtained by focussing the camera on the surface of the quartz window or the test pieces rather than on the extrudate and measuring the change in extrudate diameter upon changing the focus.

3.2 Material Modelling

For the following sections, the software used is the RepTate program.[3] This was originally developed in Leeds as part of the Microscale Polymer Processing (μPP) program and is designed for analysis of rheological, and molecular weight distribution data amongst other features. A newer version is under development using the Python programming language and is used extensively in the latter chapters of this thesis.[4]

3.2.1 Molecular Weight Discretisation

Once the molecular weight distribution is obtained via GPC it must be converted into a form that a simulation package can work with. This is done via discretisation, i.e. splitting the continuous distribution into discrete fractions. The aim of discretisation is that when the weight and fractions of each discrete 'bin' are inputted into Equation 3.1 that the same M_w value is obtained as before the discretisation. To begin with the molecular weight distribution is discretised using the RepTate program. The GPC trace is read in and split into a number of equal width intervals (in log space). The area of the rectangular bin is equal to the integral under the GPC trace over the same M_w range. Each bin is

[2]This software is available at https://imagej.nih.gov/ij/index.html
[3]This software can be found at RepTate.com.
[4]This can be found at https://reptate.readthedocs.io/ amongst other places.

then parametrised by a weight average bin molecular weight:

$$M_{w,i} = \frac{\sum w_j \cdot M_j}{\sum w_j} \tag{3.8}$$

and a fraction, ϕ_i which is the area of the bin. These obey $\sum_i \phi_i$=1. A typical discretisation in this work involves splitting into 10 bins. An example of this is shown in Figure 3.8.

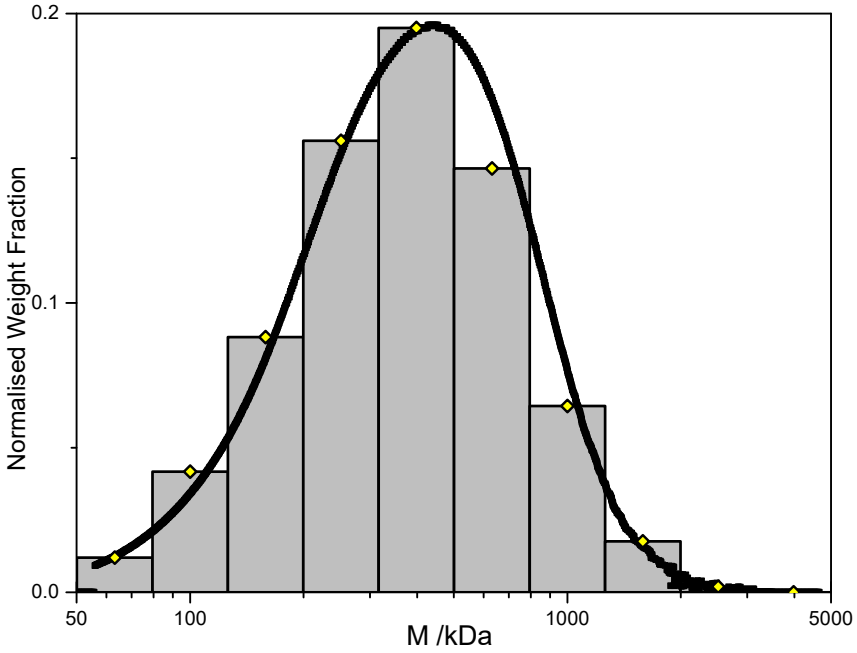

Figure 3.8: A 10 bin molecular weight discretisation for polystyrene PS350. The bin molecular weight is given by the yellow diamond on the edge of each bin.

3.2.2 WLF shifting

It is not possible to measure the whole viscoelastic spectrum in Figure 3.3 at a single temperature in a single experiment. (Although certain methods such as *i-Rheo*[61] attempt to do this) The high frequency limit is set by the accuracy of the rheometer used. In the case of the HR2 rheometer, this is approximately 600 rad s^{-1}. The low frequency limit is set by the lower limit of the rheometer transducer and, more importantly, the patience of the operator, in this case order 10^2 s. Here, the procedure of time-temperature (TTS) shifting is used. The basic principle is simple; As increasing temperature speeds up the relaxation processes of a polymer sample, increasing temperature therefore shifts these relaxation processes to a higher frequency. Crucially, all chain relaxation processes scale by the

same amount, meaning TTS is valid in all parts of the linear and non-linear response of a polymer sample. Given knowledge of how the frequency response varies with temperature a specific frequency at one temperature can be shifted to a higher frequency at a higher temperature. Here the Williams-Landau-Ferry (WLF) equations [62] are described:

$$\begin{aligned} \omega(T_0) &= a_T \omega(T) \\ G(T_0) &= G(T)/b_T \\ \log_{10} a_T &= \frac{-C_1(T - T_0)}{T + C_2} \\ b_T &= \frac{(\rho_0 - TC_3 \cdot 10^{-3})(T)}{(\rho_0 - T_0 C_3 \cdot 10^{-3})(T_0)} \end{aligned} \tag{3.9}$$

a_T is the horizontal shift factor and b_T is the vertical shift factor at a temperature, T. C_1, C_2 and C_3 are material constants and ρ_0 is the density of the material at a temperature, T_0. When applied to several sets of frequency sweep data from a rheometer as in Figure 3.9 a master curve is obtained at a specific temperature.

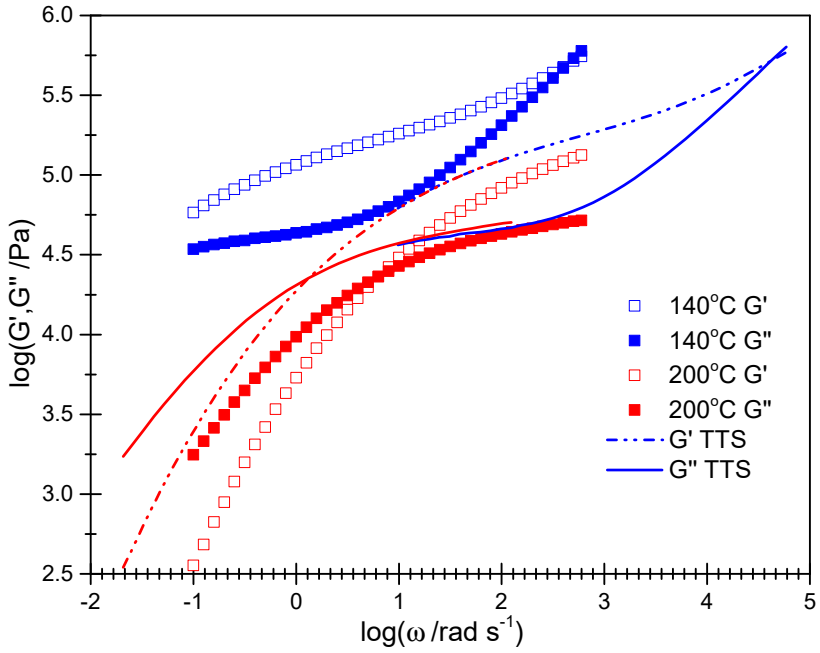

Figure 3.9: TTS shifting of frequency sweep data using RepTate. The points show the raw data at 140 °C and 200 °C and the lines show the TTS shift to 180 °C.

3.2.3 Maxwell Mode Fitting

Once a master curve is obtained at our chosen temperature it is necessary to fit the data using a linear viscoelastic theory so as to obtain a discrete set of parameters to use for a flow simulation. One theory for modelling viscoelasticity is the Maxwell model. The Maxwell model describes the viscoelasticity of the polymer in terms of a spring and dashpot in series., shown in Figure 3.10. The spring describes the elastic (solid) response of the

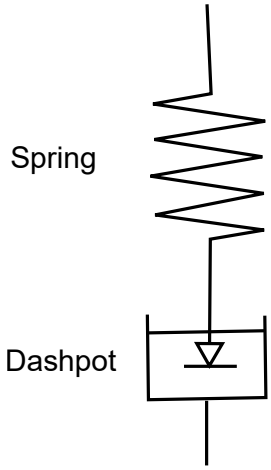

Figure 3.10: A schematic of the Maxwell model for polymer viscoelasticity

material and can be described using the storage modulus, whereas the dashpot describes the viscous (liquid) response of the material and can be described by the loss modulus. The stress/strain response functions for a spring and dashpot model give the following equation for a single Maxwell mode:

$$G(t) = G_0 e^{-t/\tau_d} \tag{3.10}$$

where $G(t)$ is the stress at time t and G_0 is the initial stress (modulus) of the mode. In the case of a oscillatory frequency sweep experiment, the frequency response due to a Maxwell mode is given by:

$$\begin{aligned} G'(\omega) &= G_i \frac{(\omega\tau_i)^2}{1+(\omega\tau_i)^2} \\ G''(\omega) &= G_i \frac{\omega\tau_i}{1+(\omega\tau_i)^2} \end{aligned} \tag{3.11}$$

G_i is the modulus and τ_i is the relaxation time of the mode. If the terminal time, τ_d is used as the relaxation time the prediction shown in Figure 3.11 is obtained.

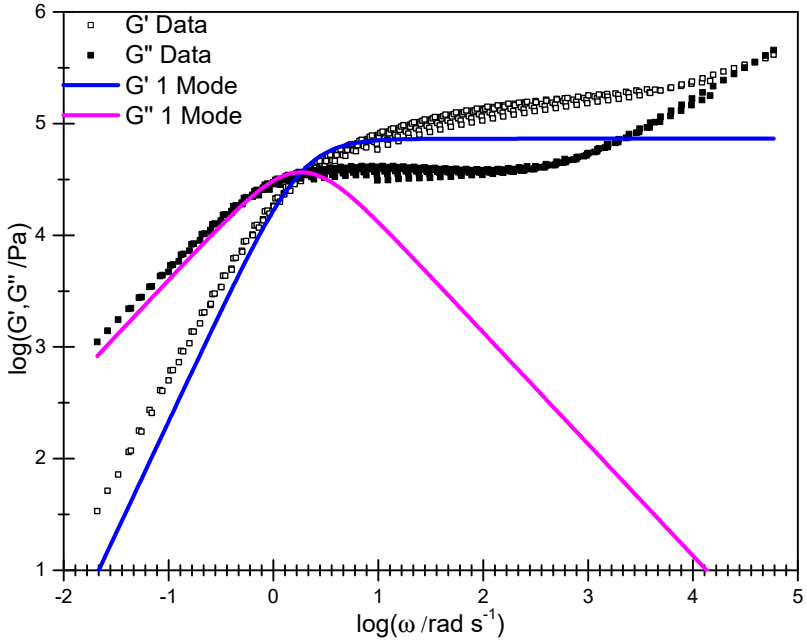

Figure 3.11: A single mode Maxwell mode prediction (lines) of the linear viscoelastic spectrum (dots) for a monodisperse polystyrene melt

A reasonably good fit is obtained for the low frequency rheology using a single Maxwell mode. The high frequency rheology is very poorly predicted, with G' showing a perfect plateau rather than a slight increase and G'' dropping rapidly. A spectrum of Maxwell modes is needed to model the rheology of real materials. A summation of many single exponentials can produce a good fit to the linear rheology over the whole frequency range for all the polymeric materials used in this thesis. In this work, 10 modes are used so as to have approximately 2 modes per decade of rheological data. The modes are always equally distributed in log space but the exact positions of each mode are varied by altering the maximum and minimum frequencies. As a starting value, the minimum frequency $\omega_{\min}$ is equal to the crossover frequency and the $\omega_{\max}$ is equal to the frequency of the highest experimental data point. The difference between the calculated and experimental moduli is minimised using the RepTate minimisation function.

3.2.4 *flowSolve*

The *flowSolve* package described in Section 2.3 is used For the extrudate swell simulations. This section describes the simulation input parameters. These parameters are listed in

a text 'input file' with file extension .fsinp. An example .fsinp input file is given in Appendix A. The geometry data simply describes the geometry given in Figure 2.10. This 5:2 capillary is used in the majority of *flowSolve* simulations except where otherwise stated to use a higher $l:d$. Given that the geometries in *flowSolve* are chosen to match the MPR, the wall shear rate within the capillary is still calculated using Equation 3.6, above. Q here is the volume flux across the flow entry line, v_p the flow entry velocity, and r_p is the radius of the input line. The $fastfactor$ for each simulation is 2, meaning that any element that relaxes faster than 0.01 times the simulation timescale is fast. The max_{len} value used for this geometry is 0.3, chosen as a compromise between simulation speed and accuracy. The effect of changing the mesh size is discussed in Chapter 4. Mesh refinement regions are defined at the die entry and exit corners as these points are expected to have particularly large deformation gradients and thus changes in stress. These regions reduce the max_{len} by 1/2, meaning the number of triangles is much greater and thus the simulation can more accurately capture the mesh deformation at these points. The simulations all include gravity acting normally along the extruder length. The density of the polymers is assumed to be 1 g cm^{-3} for this purpose. The surface tension is set at 30 mN m^{-1} here as in [63] for polystyrene at 180 °C.

Output files for the simulation are produced every 0.1 strain units. For an extrusion using the 5:2 capillary the flow will have reached the end of the extruder at 0.2 strain units. In general, a maximum run time of 2 strain units is more than sufficient for the simulation to have reached a steady state flow. 'Steady state' flow is defined as the point where the maximum diameter of the extrudate is constant with time. Within the *flowSolve* package it is possible to output the profile of the extrudate as a function of both time and distance. Given the mirror line at the centre of the geometry (at coordinate x=0) the diameter of the extrudate at a distance below the extruder y is taken as $2x(y)$ and the B value as x_{max}, the maximum x value reached along the whole profile. An example plot of x_{max} vs time is shown in Figure 3.12. The maximum simulation time possible using the computational resources available is 3 days wall-clock time. Few simulations require a run time longer than this but those that do are restarted from a checkpoint file outputted at the end of the time-limit. A variety of constitutive equations are used within *flowSolve* and are described in the next section.

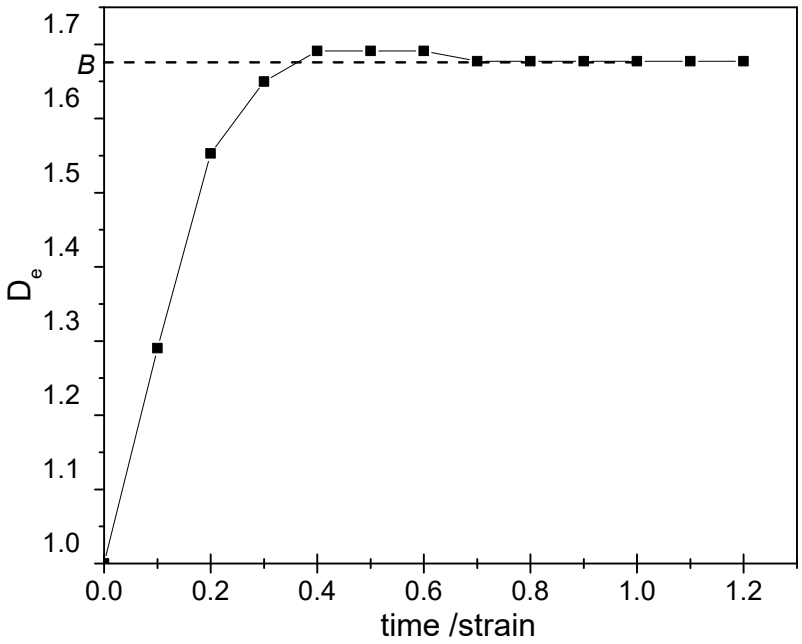

Figure 3.12: Definition of the B value using a graph of extrudate radius versus time for PS281 using the Rolie-Poly model. The B value occurs where the extrudate radius becomes constant with time.

3.3 Description of The Constitutive Equations Used

This section describes the parametrisation of the constitutive equations used within *flowSolve*. Firstly the linear theory for fitting linear-rheological data is described, followed by the non-linear constitutive equations and the friction reduction modifications to them.

3.3.1 Linear Theory

The simplest way of extracting non-linear parameters out of the rheological data is using the linear theory of Likhtman-McLeish. [64] For a chain with $Z = \frac{M_w}{M_e}$ entanglements the Rouse and reptation timescales are:

$$\begin{aligned} \tau_R &= Z^2 \tau_e \\ \tau_d &= 3Z^3 \tau_e \left(1 - \frac{2C_1}{\sqrt{Z}} + \frac{C_2}{Z} + \frac{C_3}{Z^{3/2}}\right) \end{aligned} \tag{3.12}$$

The factors are fitted to numerical data: C_1=1.69, C_2=4.17 and C_3=-1.55.[64]

The relaxation modulus for our sample is calculated as a function of time (or frequency) using the formula.

$$G(t) = \frac{4}{5}\mu(t)R(t) + \frac{1}{5Z}\sum_{p=1}^{Z-1}\exp\left(-\frac{p^2 t}{\tau_R}\right) + \frac{1}{Z}\sum_{p=Z}^{N}\exp\left(-\frac{2p^2 t}{\tau_R}\right) \tag{3.13}$$

The final two terms describe Rouse motion within the tube. In the first term, $\mu(t)$ describes contour length and reptative relaxation processes within the tube and $R(t)$ describes constraint release motion at short times via $R(t) = 1 - \frac{1.8}{Z}\frac{c_\nu t}{\tau_e}$. The term c_ν describes the amount of constraint release present in the theory. For fitting the theory in RepTate c_ν=0.1. Setting this value to 0 would mean no constraint release. RepTate does not solve this equation every time, rather relying on a series of pre-calculated predictions for a range of c_ν and Z values and adjusting for the entanglement time and entanglement modulus, G_e. The plateau modulus should be $G_0 = \frac{4}{5}G_e$.[65]

In a similar way to fitting the linear data the non-linear data is fit with a constitutive equation to describe its flow under shear or extension. Two tube theory based constitutive equations are used, the Rolie-Poly and Pom-Pom equation sets.

3.3.2 Rolie-Poly

In Chapters 4 to 6 the multi-mode finitely extensible Rolie-Poly Equations (Equations 2.14-2.17) are used for monodisperse fits. A monodisperse polymer is assumed to have a single stretching Rolie-Poly element, a variable number of non-stretching elements and at least 1 solvent element. The timescales for the stretching element are taken from the linear theory fit in Section 3.3.1. The finite extensibility, $\lambda_{\max}$ is calculated using the formula:[66, 67]

$$\lambda_{\max} = 0.82\sqrt{\frac{2M_e/M_{\text{mon}}}{C_\infty}} \tag{3.14}$$

The C_∞ of polystyrene is 9.85 as stated in Section 2.2 and [27]. Using the monomer weight of 104 g mol^{-1} and entanglement molecular weight of 16.5 a $\lambda_{\max}$ value of 4.7 is obtained. For consistency with [66] a value of 5 is used here.

3.3.3 Rolie-Double-Poly Parameters

The RDP equation from Section 2.24 is parametrised using a set of discretised molecular weight bins from Section 3.2.1. Each M_w value is divided by the M_e of 16.5 for polystyrene from the RepTate materials database to obtain a value for Z. The relaxation times are

calculated by using a slightly modified version of the Likhtman-McLeish equations:

$$\begin{aligned} \tau_d &= 3Z^3\tau_e \cdot CR \\ \tau_R &= Z^2\tau_e \\ CR &= 1 - \frac{3.38}{\sqrt{Z_{\text{eff}}}} + \frac{4.17}{Z_{\text{eff}}} - \frac{1.55}{Z_{\text{eff}}^{3/2}} \\ Z_{\text{eff}} &= \frac{Z}{\phi_{\text{dil}}} \end{aligned} \tag{3.15}$$

ϕ_{dil} is not the same as the fraction ϕ_i, rather is calculated iteratively by considering the relative dilutive effect of each other molecular weight fraction j on the fraction of interest, i:

$$\begin{aligned} \phi_{\text{dil},i} &= \sum_{j}^{n} \phi_j \\ \tau_{R,i}^{\text{eff}} &= \frac{Z^2\tau_e}{\phi_{\text{dil}}} \end{aligned} \tag{3.16}$$

the index j is the highest value of j such that $\tau_{R,i}^{\text{eff}} < \tau_{d,j}$. A test chain is diluted by a shorter chain if the longest relaxation time of that chain is shorter than the shortest relaxation time of the the test chain. Starting at fraction i=1 and assuming ϕ_{dil}=1, Equation 3.16 is solved for every subsequent fraction in ascending order. The τ_R value from Equation 3.15 are used rather than the effective Rouse time. The overall effect of this dilution is that the reptation time of a molecular weight fraction is increased when diluted by lower molecular weight chains but the Rouse time is left unaffected. This is because the effective dilution of the Rouse time is included in the RDP equation set. A solvent viscosity is worked out using the $lastfast$ or $fastfactor$ terms as previously. In this case the viscosity is given by:

$$\mu = \sum_{i=1}^{lastfast} G_0\tau_{d,i}\left(1-\phi_i\right) \tag{3.17}$$

This RDP equation set is used in Chapters 5 and 6 for simulation of polymer melts of a variety of dispersities.

3.3.4 Pom-Pom Parametrisation

The Pom-Pom equation used in Equations 2.25 to 2.28 are used for simulation of branched polymer melts in Chapter 7. The Pom-Pom parameters are fitted to extensional data in

RepTate using the extensional module. Firstly, the data is fitted to a series of Maxwell modes as in Section 3.2.3 and the data converted into a set of Pom-Pom elements with a G, τ_b, $ratio = \frac{\tau_d}{\tau_R}$, and q value each. The default q is 1 and the default $ratio$ is 2. The q values for all elements are then minimised followed by the ratio for each element to obtain a best-fit to the extensional data. The elements are then exported into a *flowSolve* .fsinp file. The same scheme is used for the XPP model[5] where the original set of Pom-Pom elements are used as initial parameters in the minimisation. In this work the anisotropy α is taken to be 0 in which case the XPP orientation is similar in form to the Pom-Pom orientation.

3.3.5 Reduction in Monomeric Friction Coefficient

For the Rolie-Poly equation sets above an extension developed for the first time in this work is monomeric friction reduction. The underlying physics behind this are discussed in Section 4.4. At high chain orientation values the monomeric friction ζ from Equation 2.8 is reduced, thus reducing τ_e and by extension τ_d and τ_R. The monomeric friction reduction factor, ζ_f is defined:

$$\tau_e = \zeta_f \cdot \tau_e \tag{3.18}$$

ζ_f will be 1 at slow deformation rates and will decrease towards 0 at very high deformation rates. For a spectrum of n Rolie-Poly elements each with an Auxiliary tensor, $\mathbf{A}$ there is an average tube orientation $\overline{\mathbf{S}}$ and stretch $\overline{\lambda}$:

$$\begin{aligned} \overline{\mathbf{A}} &= \frac{\sum_{i=1}^{n} \mathbf{A}_i}{n} \\ \overline{\lambda} &= \sqrt{\mathrm{trace}\left(\overline{\mathbf{A}}\right)/3} \\ \overline{\mathbf{S}} &= \frac{\overline{\mathbf{A}}}{\mathrm{trace}\left(\overline{\mathbf{A}}\right)} \end{aligned} \tag{3.19}$$

This average tube orientation is used approximate a monomeric order parameter S:

$$\begin{aligned} S &= \left(\frac{\overline{\lambda}}{\lambda_{\max}}\right)^2 \left(\overline{S}_{xx} - \overline{S}_{yy}\right) \Big| \; S_{xx} > S_{yy} \\ S &= \left(\frac{\overline{\lambda}}{\lambda_{\max}}\right)^2 \left(\overline{S}_{yy} - \overline{S}_{xx}\right) \Big| \; S_{yy} > S_{xx} \end{aligned} \tag{3.20}$$

[5]The XPP model is not included within the original RepTate program therefore the newer open-source version is edited to include it in this work

The tensorial representation of S is dropped here in favour of a single, direction independent, monomeric orientation in the primary flow direction. It may be more correct to define a monomeric orientation tensor and thus a friction reduction tensor but this is not performed here for simplicity. From the monomeric order parameter the friction reduction coefficient uses a form similar to that in [68]:

$$\begin{aligned} \zeta_f &= \zeta_{\text{min}} + (1 - \zeta_{\text{min}}) \left(S/S_c\right)^{-1.25} \Big| S > S_c \\ \zeta_f &= 1 \Big| S < S_c \end{aligned} \tag{3.21}$$

The ζ_{min} value is the minimal value that the friction can be reduced to. This avoids the monomeric friction unphysically reducing to 0 under highly stretching flows. S_c is the critical orientation parameter at which the friction begins to reduce from the non-equilibrium value. This model is used for monodisperse polymers in Chapter 4. In the case of the polydisperse simulations in Chapter 6 where different chains contribute significantly different amounts to the overall orientation, Equation 3.19 is replaced by Equation 3.22:

$$\overline{\mathbf{A}} = \sum_{i=1}^{n} \phi_i \mathbf{A}_i \tag{3.22}$$

Chapter 4

Extrudate Swell of Monodisperse Samples

In this chapter the simplest system of a nearly monodisperse melt is addressed. In Section 4.1 the characterisation of the melts is described including GPC and rheological fitting. In Section 4.2 the results from the fitted parameters are described as are the relative effects of simulation and constitutive parameters on the speed, stability and results of the simulations. In Section 4.3 the simulation results are compared to experimental data and the differences between the two explained. In Section 4.4 the Rolie-Poly model is extended using a friction reduction model to give an improved fit to experimental data. Much of the work in this chapter has been published in [36].

Work on monodisperse polymers is often difficult to perform, due to the difficulty of synthesising large quantities of well defined, monodisperse materials. Polydisperse samples are easy to synthesise in bulk, however rheological features may be broadened out or hidden by the many relaxation processes present. The monodisperse sample PS281 used in this work derives from its use in [35], where use of monodisperse polymer allowed direct comparison to molecular theory. Similarly, the monodisperse melts used here were synthesised for use in [37] for comparison to simulation results.

4.1 Characterisation

4.1.1 GPC

All samples were synthesised by living anionic polymerisation and are approximately monodisperse. GPC data were obtained on a variety of the samples used. Figure 4.1

shows the raw and processed GPC data for PS281 and summary data for all the molecular weights studied in this work are given in Table 4.1.

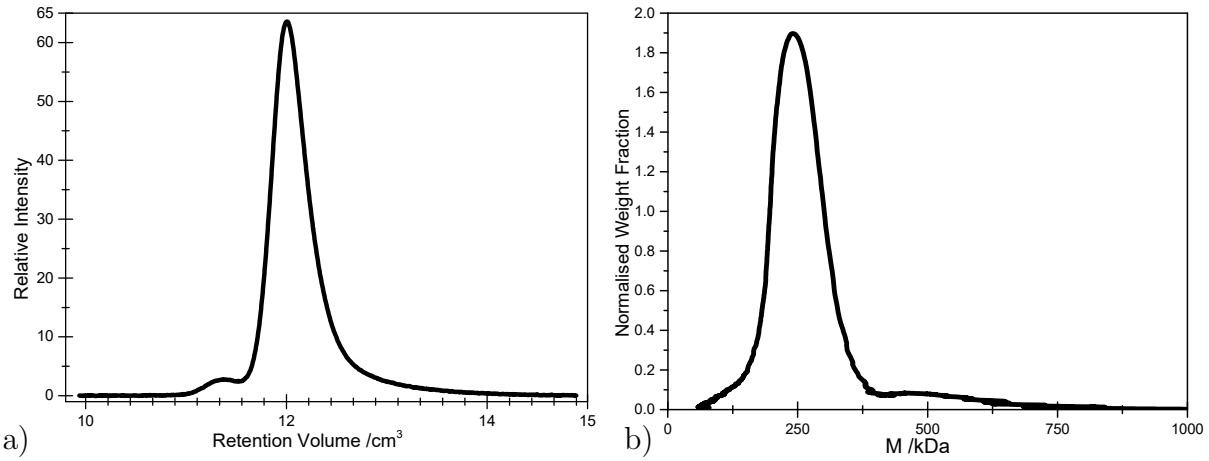

Figure 4.1: GPC traces for the monodisperse polymer PS281. a) shows the Raw data from the GPC and b) shows the data converted into molecular weight units.

Table 4.1: Summary Molecular weight data for the monodisperse polystyrenes used in this chapter.

Sample	M_n/kDa	M_w/kDa	Đ
PS100	99.5	99.7	1.04
PS281	250	281	1.13
PS400	436	460	1.05

The sample PS281 is deuterated due to its previous use in a neutron experiment. It contains a small blended amount of the hydrogenated equivalent polymer, resulting in a slightly higher overall dispersity than each individual fraction. The calibration used for the GPC is for a hydrogenated polystyrene, therefore the molecular weight given is that of a hydrogenated polystyrene with the same volume as the deuterated sample.

4.1.2 Rheology

Frequency sweep data for PS100, 281 and 400 are shown in Figure 4.2. As expected for similar samples the entanglement time (as identified from the second crossover in the rheological data) is approximately (but not exactly) independent of molecular weight (approximately 10^4 rad s^{-1}) but the low frequency crossover decreases with increasing molecular weight. The TTS parameters are given in Appendix B. The fit of the data to

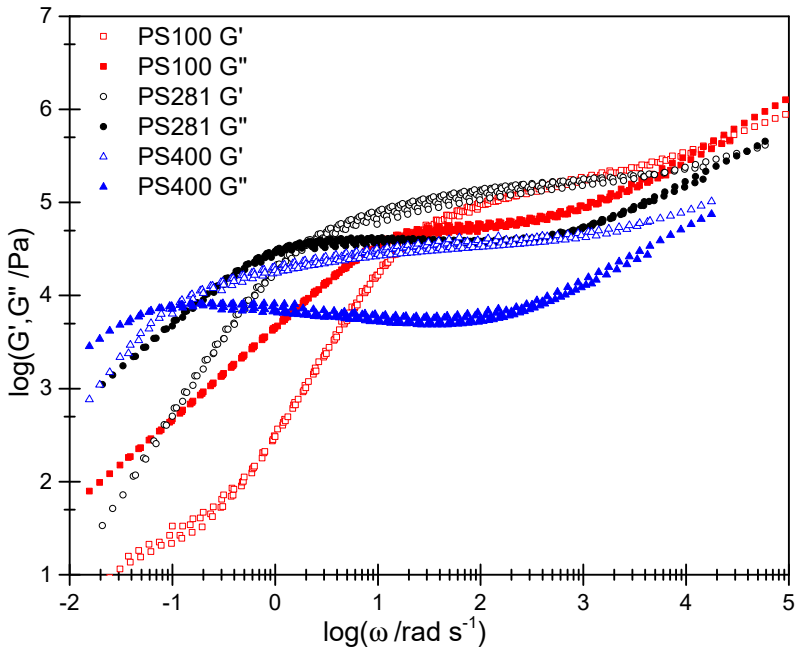

Figure 4.2: Linear rheological data for PS100,PS281 and PS400 TTS shifted to 180 °C.

the Maxwell mode theory and Likhtman-McLeish theory as described in Section 3.2 are shown in Figure 4.3.

Both theories capture the low frequency response of the polymer accurately, and give good predictions of the linear rheology up to frequencies of approximately 10^4 rad s^{-1}. From the basis of these fits it is not possible to predict the linear or non-linear response above shear rates of 10^4 s^{-1}. In very few cases does this work go above 10^3 s^{-1} therefore these fits should be adequate. An improved Maxwell mode fit could be obtained by increasing the ω_{max} value although this is not necessary here. Fitting parameters for all the samples are shown in Table 4.2.

Table 4.2: Likhtman-McLeish fitting parameters for monodisperse polystyrenes at 180 °C.

	τ_e/s	G_e /Pa	τ_d /s	τ_R /s
PS100	0.000369	2.26×10^5	0.0871	0.0179
PS281	0.000222	2.18×10^5	0.765	0.0470
PS400	0.000413	48294	11.0	0.293

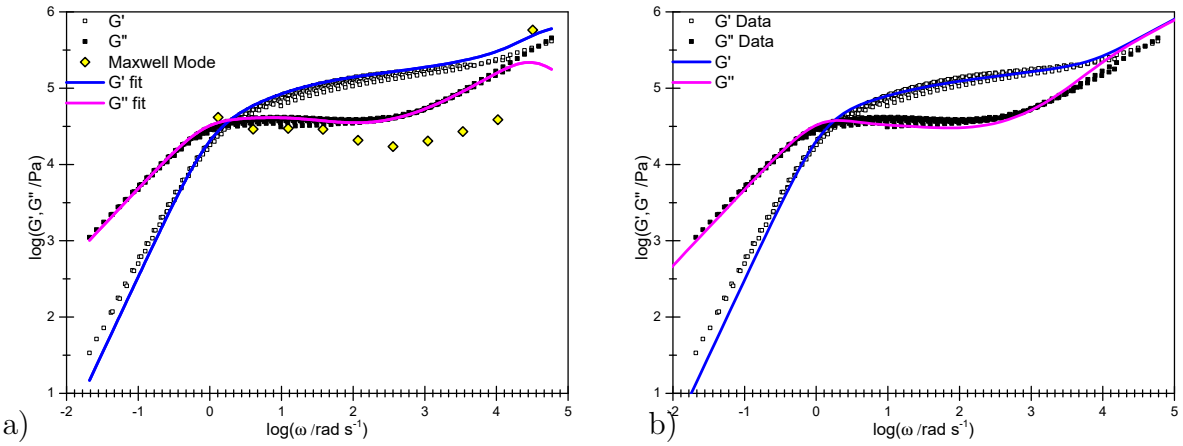

Figure 4.3: Linear rheological fits to PS281 at 180 °C. a) shows the Maxwell modes and the resulting prediction. b) shows the Likhtman-McLeish theory best fit.

Using a single stretch time should be accurate for these monodisperse melts; as all chains should relax at roughly the same rate and at these flow rates the chain stretch should all be carried by the slowest Rouse mode of the chain. Using multiple stretch times may be more accurate but the aim of this chapter is to predict extrudate swell without using any non-linear fitting. The full list of Rolie-Poly elements used for PS281 are shown in Table 4.3. Fits for the other samples are given in Appendix C. The single stretch time is associated with the slowest Maxwell mode, which is set to have the terminal reptation time shown in Table 4.2.

Table 4.3: Rolie-Poly elements for PS281 used in *flowSolve* simulations at 180 °C.

Modulus /Pa	τ_d /s	τ_R /s
41501	0.765	0.0470
28985	0.249	-
29687	0.0809	-
28932	0.0263	-
20742	0.00855	-
17121	0.00278	-
20243	0.000904	-
26977	0.000294	-
38626	9.56×10^{-5}	-
577151	3.11×10^{-5}	-

A first test of these parameters before they can be be used for flow simulation is by simulation of the much simpler uniaxial extensional flow. Results from the SER and

Rolie-Poly predictions from RepTate are shown in Figure 4.4.

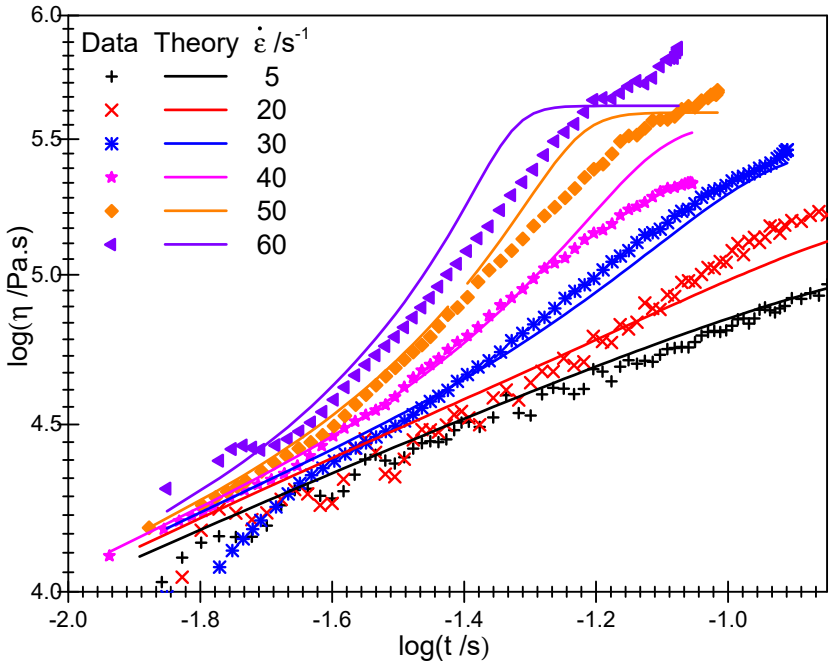

Figure 4.4: SER extensional data for PS281 and the Rolie-Poly model fit using non-linear parameters from Table 4.2.

There is an increase in viscosity with extension time (i.e. Hencky strain). At the longest time a steady state plateau is reached. This is only partially visible for the highest rates, as for the lower rates the plateau will only be reached at a strain above the limit of the SER. The plateau is a result of the finite extensibility of the polymer chains (and the $\lambda_{\max}$ term in the Rolie-Poly model). The simple one mode fit does a good job at fitting the strain hardening of PS281. For 40 s^{-1} and 50 s^{-1} the extensional viscosity is slightly over-predicted. It is not possible to measure higher stretching rates for these samples at this temperature due to sample breakage within the SER. The onset of extension hardening is correctly predicted (30 s^{-1} corresponding to W_R=1.4) and good predictions are obtained up to $W_R \approx 3$. Higher Weissenberg numbers are reached in the flow simulations, although the extensional fits show that the Rolie-Poly parameter are reasonable.

4.2 Simulations

In this section the results from *flowSolve* simulations using the Rolie-Poly equation are described. The effects of varying rheological parameters, geometry, shear rate and mesh

size are discussed and used to describe an optimum set of simulation parameters for comparison with experiments.

4.2.1 Extrudate geometry

Figure 4.5 shows the progression of triangles through a simulation of PS281 at W_R=4.7.

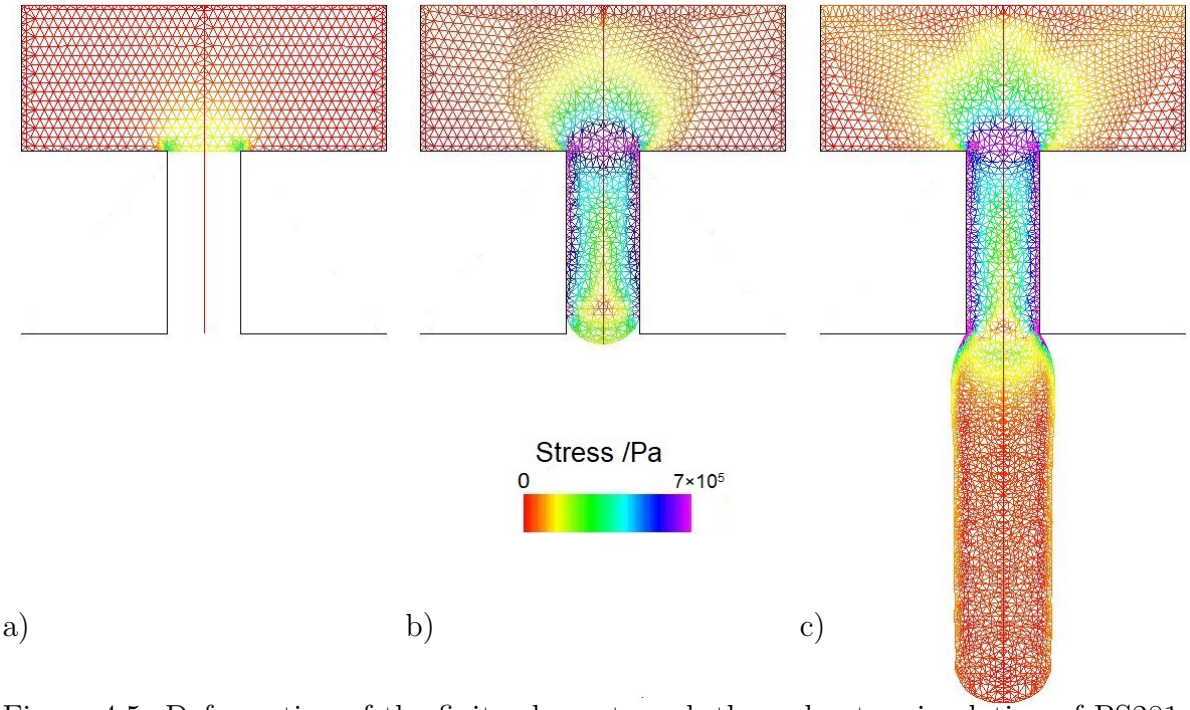

Figure 4.5: Deformation of the finite element mesh throughout a simulation of PS281 at W_R=4.7. The colours indicate the normal stress difference across a triangle. a) shows t=0, b) shows t_{strain}=2, and c) shows t_{strain}=1.2.

At the beginning of a simulation, the mesh is regular, but as the simulation continues triangles become more distorted. By the end of a run most of the triangles in the entry well are deformed, except a small number in the corners of the well where there is a small recirculating flow region. The extrudate shows three regions:

1. An initial expansion out of the die due to stress relaxation at the die exit.

2. A slight contraction after the maximum diameter.

3. A long steady state region.

4.2.2 Molecular Weight

The molecular weight enters the simulations via the ratio of relaxation times $\frac{\tau_d}{\tau_R}$ in the slowest element (which is approximately $3Z$). The data obtained from extrusion simulations for these polymers are described in Figure 4.6. Several similar diagrams are

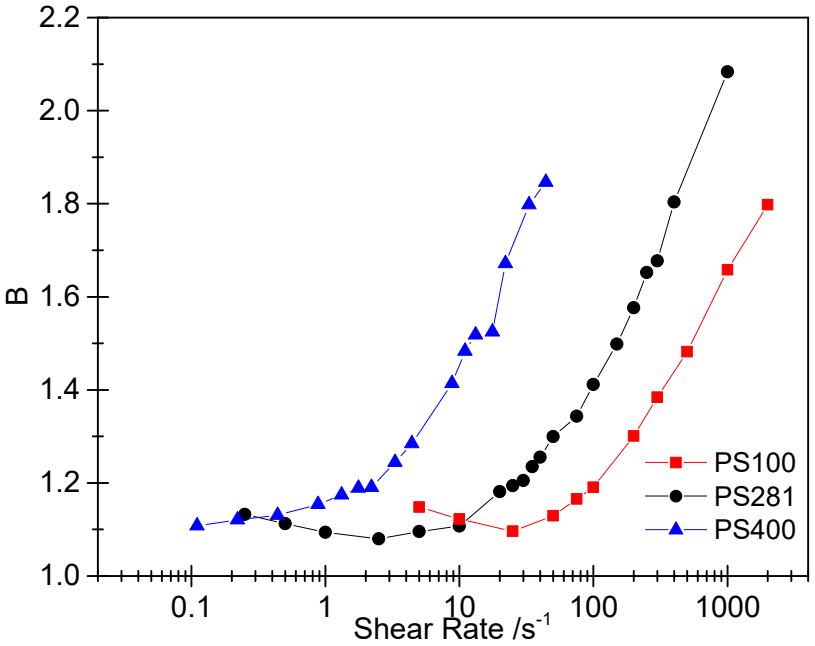

Figure 4.6: Extrusion data versus shear rate for PS100, PS281 and PS400 at 180 °C.

described in this work, so it is worth describing in detail here. On the vertical axis the B value $\frac{D_e}{d}$ defined in Sections 2.1 and 3.2.4 is shown. On the horizontal axis the flow input speed and thus wall shear rate $\dot{\gamma}_w$ increases. A log scale is used so as to more clearly separate the data points and differences between them. The individual points are specific simulation runs. These points are joined by lines to indicate an overall trend and to distinguish the simulation predictions from the experimental data points which is included on later graphs. The shear rate ranges are chosen to correspond to specific Weissenberg numbers rather than a constant shear rate range, hence the shifting in shear rate range at different molecular weights. Overall the trend with increasing shear rate is:

- A small decrease at low shear rates. This is most noticeable for PS100 but is not seen for PS400 as a low enough shear rate is not simulated.

- A small increase or plateau at intermediate shear rate.

- A rapid, continuous increase at high shear rate.

For these polymers the lowest swelling ratio seen (in the middle region) is slightly less than 1.1, roughly agreeing with previous work for the Newtonian swelling ratios. At a constant shear rate the swelling increases with increasing molecular weight although this may not apply at the lowest shear rates for each sample. For example, the B value at the lowest shear rate for PS100 is above that for PS281 at the same shear rate. Given the curves show the same shear rate dependence, but at different absolute values it makes sense to normalise to give a molecular weight independence. Three possibilities exist: The swelling could be controlled by reptation relaxation, the rate of which increases with Z^3. The swelling could be controlled by the rate of chain stretch relaxation which increases with Z^2. There is also the possibility that neither of these effects matter and the swelling simply increases with Z. Normalising by τ_d, by τ_R or by Z will reveal if any such scaling exists. Figure 4.7 shows the data above normalised by Weissenberg numbers:

$$\begin{aligned} W_d &= \dot{\gamma}_w \tau_d \\ W_R &= \dot{\gamma}_w \tau_R \end{aligned} \tag{4.1}$$

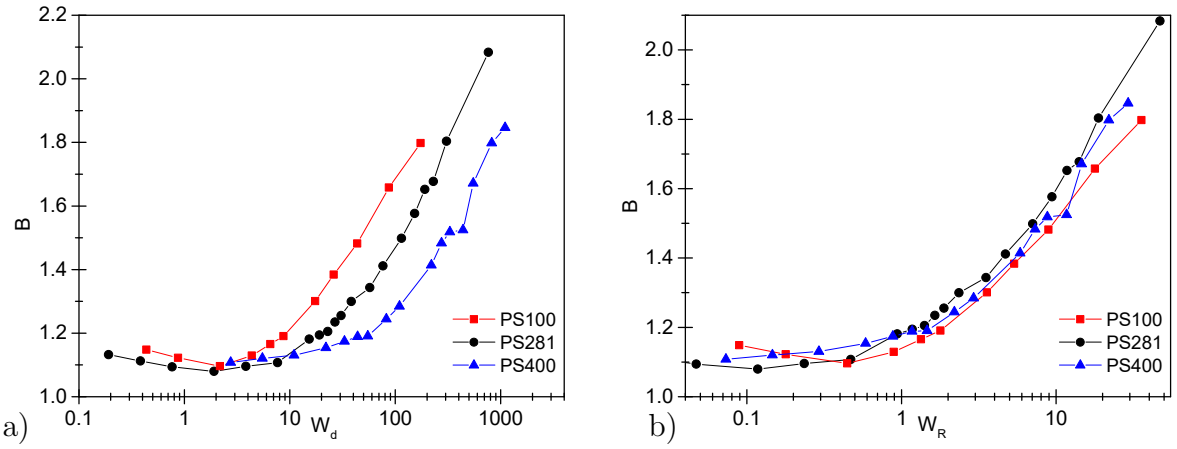

Figure 4.7: Simulated extrusion data for PS281 normalised by a) reptation Weissenberg number and b) Rouse Weissenberg number.

Multiplication by Z gives a poor agreement and is not shown. The data superimpose well versus W_R but not with W_d. The superposition versus W_R means that of the spectrum of Rolie-Poly elements used in the simulation, the only one that makes a significant difference to the swelling is the slowest, and the timescale that matters is the stretch

relaxation time. Below W_R=1 the data do not superimpose well, with the minimum B value occurring at different points for each molecular weight. This minimum and the low shear swelling ratios approximately superimpose versus reptation Weissenberg number. The low shear swelling ratios are therefore a chain orientation controlled phenomenon and the high shear ratios are chain stretch controlled. The rapid swelling for all samples starts at $W_R \approx$1. The decrease at low shear rates is the first evidence of non-linearity in the flow. As the reptation Weissenberg number is approached the polymer begins to shear thin slightly and thus flows out of the die slightly faster, reducing the swelling. At slower speeds any stress built up at the die exit will have fully relaxed instantly, leading to the Newtonian result.

The timescale parameters used in the above figures are fitted to rheology at 180 °C, resulting in a simulation effectively carried out at 180 °C. Once the timescale and shear rate are converted to a Weissenberg number the temperature becomes irrelevant. Extrudate swell at one shear rate and temperature is equivalent to extrudate swell at a higher temperature and higher shear rate provided the Weissenberg number is constant. This was tested by running additional sets of simulations at 200 °C and renormalising by the TTS shifted relaxation times. The results match those in Figure 4.7 closely and are shown in Figure B.1 in the Appendix.

4.2.3 Non-Newtonian Shear Rates

The shear rates reported previously used Equation 3.6 for Newtonian melts. This assumes that the velocity profile across the capillary is parabolic. In reality, however, as polymer melts shear thin their viscosity will vary across a capillary and thus the exact velocity profile will not be perfectly parabolic. A traditional way for correcting for this effect is using a Rabinowitsch correction:[69, 70]

$$\dot{\gamma}_w = \frac{1}{4}\dot{\gamma}_a \left(3 + \frac{d\log(\dot{\gamma}_a)}{d\log(\sigma_r)}\right) \tag{4.2}$$

which calculates the true wall shear rate from the a plot of the apparent (Newtonian) shear rate $\dot{\gamma}_a$ versus the wall shear stress σ_r, calculated from the pressure drop across the capillary. This correction requires accurate measurements for pressure drops across the MPR capillary, which are difficult to obtain within an extrusion experiment. It is possible to obtain true wall shear rates from a *flowSolve* simulation. Results for $\dot{\gamma}_a$ vs simulated shear are shown in Figure 4.8.

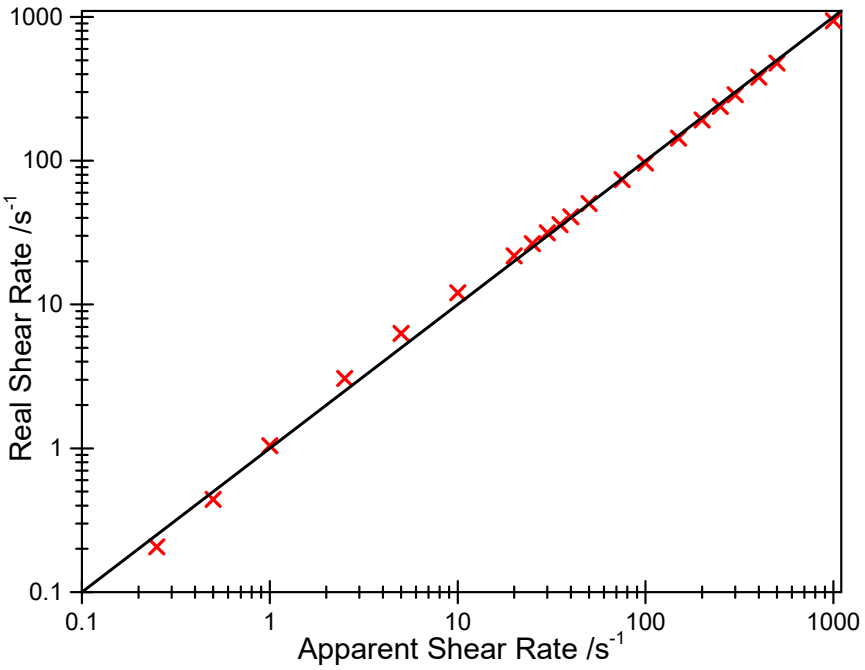

Figure 4.8: Apparent wall shear rate against simulated wall shear rates within *flowSolve* for PS281. The straight line indicates $\dot{\gamma}_w = \dot{\gamma}_a$.

The real shear rates are very close to the apparent shear rates. At the highest shear rates the deviation is most significant ($\dot{\gamma}_w = 939$ at $\dot{\gamma}_a = 1000$) but this is almost negligible on a logarithmic scale. It is therefore reasonable to keep using apparent shear rates to calculate the Weissenberg numbers in this work.

4.2.4 Effect of Finite Extensibility

The results in Figure 4.7 include a $\lambda_{\max}$ of 5. The effect of removing the finite extensibility (FE) and using the infinitely extensible Rolie-Poly equation are given in Figure 4.9.

FE appears to start to reduce the swelling ratios above $W_R \approx 5$ with a larger effect at higher Weissenberg number. As expected there is no observable effect below $W_R = 1$ as chain stretch values are much lower than the finite extensibility.

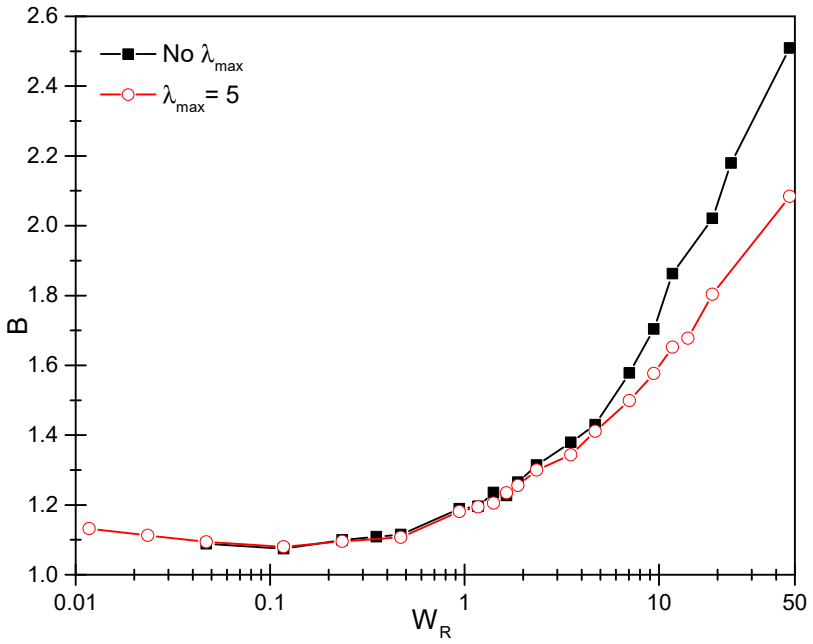

Figure 4.9: Results of the Rolie-Poly simulations for PS281 with a FE of 5 and without FE

4.2.5 Chain Stretch Profiles

The benefit of using a molecular constitutive equation is that the values of molecular parameters such as chain stretch and orientation can be calculated as a function of both distance along the extruder and from the centre-line. Given that the above results confirm that chain stretch is a dominant factor in control of extrudate swell then it makes sense to observe where the chain stretch occurs during the extrusion. At first, chains become stretched by the wall shear within the extruder in the extrusion direction. At the flow outlet the chains relax back and expand perpendicular to the flow direction, causing extrudate swell. Figure 4.10 shows the evolution of chain stretch along the extruder at a point in time where the flow has reached a steady state. On the vertical axis is the chain stretch value where λ=1 is the unstretched state. The horizontal axis shows the distance along the extruder at which the chain stretch occurs. Below 0 mm is the flow inside the entry well. 0 to 5 mm is the flow within the extruder and >5 mm is the free space after the die exit. The effect of finite extensibility (FE) is clear here, the stress built up at the die entry is vastly higher without FE and much of this extra stretch has not relaxed away by the die exit. This extra chain stretch at the die exit will result in a larger extrudate swell.

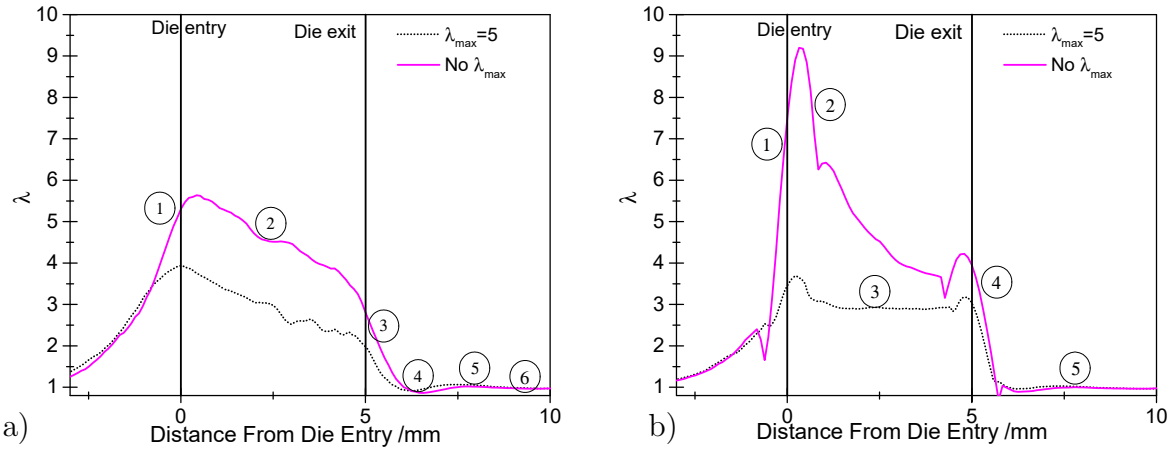

Figure 4.10: Simulated chain stretch values for PS281 at a Rouse Weissenberg number of 19 with and without finite extensibility, a) at the extruder centre line and b) at the extruder wall. The numbers refer to the regions in the list below.

Similarly, Figure 4.11 shows the stretch along the extruder for different flow speeds.

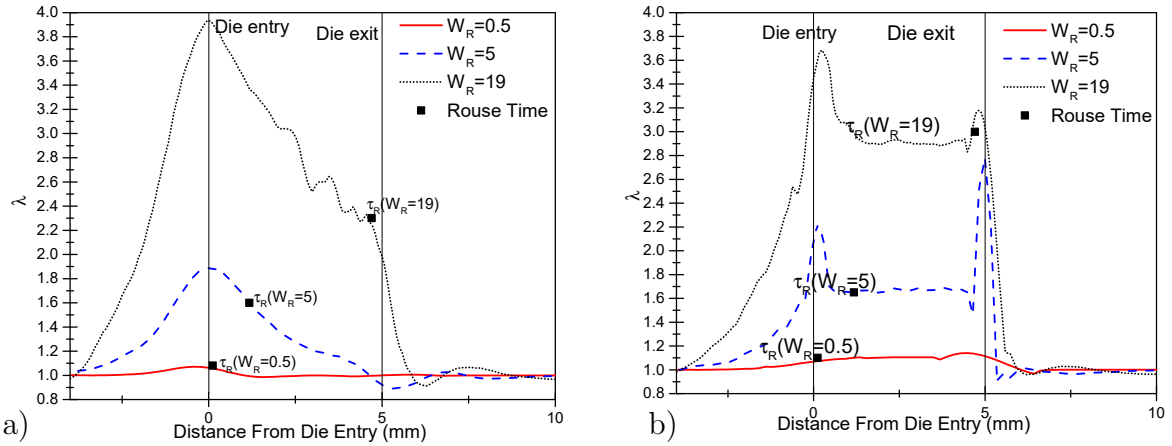

Figure 4.11: Chain stretch values along the extruder for PS281 at three different Rouse Weissenberg numbers. The points labelled τ_R show the distance the flow will have travelled in the Rouse time at each flow speed.

The chain stretch at the die wall and at the die centre line show different profiles:

- **Centre line (Figure 4.10 a)).**

  1. A steady increase in chain stretch towards the die entry, reaching a broad peak at the die entry contraction.

2. A steady decrease in chain stretch along the die, reaching 1 at the lowest rates (i.e. complete relaxation).
3. A rapid decrease in stretch immediately after the die exit as removal of the boundary wall allows fast relaxation.
4. A small dip below 1 after the die exit. This is the reversing flow after the die exit. As the flow swells outwards it contracts backwards slightly, meaning that chains contract below their equilibrium stretch.
5. A small peak after the die exit caused by orientation of chains perpendicular to the flow direction. As the flow swells outwards, the material at the centre-line is stretched slightly by this flow. Figure 4.12 shows the components of the Rolie-Poly **A** tensor along the die.

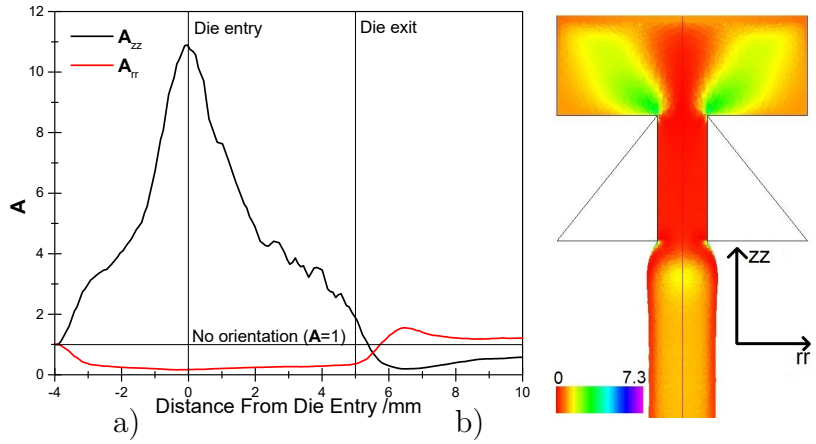

Figure 4.12: a) Rolie-Poly orientation components at the extruder centre line for PS281 at $W_R = 5$ parallel to (zz) and perpendicular to (rr) the centre-line of the extruder. b) shows the rr orientation spatially.

Chains are stretched in the zz direction within the die, corresponding to stretch in the flow direction. After the die exit, orientation decreases significantly in the zz direction and increases slightly in rr, corresponding to a small overall stretch. This is the cause of the small decrease in extrudate diameter after the maximum swell value. Relaxation of stress in rr causes a slight expansion of the extrudate in zz, reducing the extrudate diameter

6. A long steady state stretch of approximately 1. The lack of stretch relaxation means there is no significant change in extrudate diameter after this point.

- **Die Wall (Figure 4.10 b))**

1. A steady increase in chain stretch towards the die entry, reaching a sharp peak at the die entry corner.
2. Fast relaxation of stretch after the die entry corner. The higher the stretch at the die entry the longer this relaxation will take to reach the steady-state value. Without finite extensibility as in Figure 4.10 a) the stress may not have relaxed by the die exit.
3. A region of steady-state stretch at the die wall. At this point the rate of relaxation is equal to the rate of deformation at the die wall.
4. A sharp peak at the die exit caused by the large extensional pull-off at the exit corner singularity. This is especially noticeable for W_R=2 in Figure 4.11
5. Rapid relaxation of stretch after the die exit.

Figure 4.11 also shows the average distance that the flow will have travelled within the Rouse time. This is defined as $\frac{v_{\text{inp}} r^2_{\text{entry}}}{r^2_{\text{cap}}} \cdot \tau_R$. Up to a W_R of about 19 the residence time within this die is greater than the Rouse time of PS281. This does not of course mean that all stretch could have relaxed, rather indicating that the flow within the die has roughly reached steady state as a function of distance. The flow speed within the die varies with distance across the die (0 at the wall to $\sim 2v_{\text{cap}}$ at the centre line). We can define a Rouse Deborah number for the flow at a radius r:

$$D_R(r) = \frac{\tau_R}{l/V(r)} \tag{4.3}$$

where the radius r is the distance from the centre-line of the die divided by the die radius, $D_R(r)$ is the Deborah number at radius r, l is the die length, and $V(r)$ is the flow velocity at radius r. At W_R=19 $D_R(r)>1$ for $r<0.66$. This means that the stretch within a distance of 0.34 mm of the die wall has had time to relax via Rouse motion within the die. This radius decreases with decreasing W_R until $W_R<10$ where the residence time for the material at the centre line is longer than the Rouse time. The radius for reptation at the flow rates in Figure 4.11 is closer to the wall than the diameter of a single simulation triangle and cannot be resolved. Therefore chain orientation at the initial contraction is not relaxed before the die exit. Figure 4.11 b) also highlights the importance of considering the die exit, in contrast to early theories for extrudate swell such as the theory of Tanner described in Section 2.1. There is a significant chain stretch peak at the die exit above the steady state which much be relaxed during swelling. Given chain stretch is the dominant

factor in swelling this extra stretch at the exit corner will have a significant effect on the swelling.

4.2.6 Mesh size and Calculation Convergence

The max_{len} value of 0.3 used in the above simulation results gives stable results and will run the simulations in hours-days, which is an acceptable timescale. It is also necessary to check if the results are accurate. A very small mesh will be the most true to reality, but will take a long time to run. Figure 4.13 shows the effect of changing mesh size on the simulations.

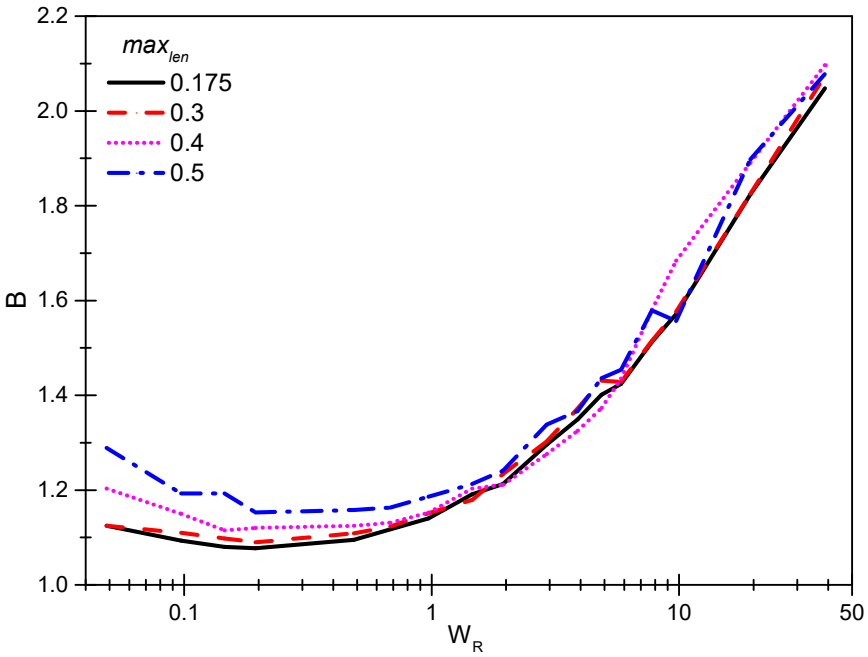

Figure 4.13: Extrudate swell values for PS281 at using different max_{len} values. The larger the max_{len} value, the coarser the mesh.

Reducing the max_{len} below 0.3 has little effect on the simulation, therefore the max_{len} of 0.175 is not used. The larger mesh sizes begin to increase the swelling ratios, particularly at low flow speeds. Using a max_{len} of 0.5 results in a significantly increased extrudate swell at low shear rates. In addition, given a capillary of diameter 1 mm will only have 2-3 triangles across, meaning the differences in flow velocities and stress values across the capillary cannot be resolved, making this coarse mesh unfavourable.

4.2.7 Effect of Free-Surface Parameters on Simulation Results

The stress and stretch at the die wall have a large effect on the swelling ratios but parameters such as gravity and surface tension may also have an effect. In general, the surface tension is set to 30 mN m^{-1} and gravity is used. Both of these factors were removed in turn, followed by removal of both surface tension and gravity. This has no observable effect on the results at either high or low shear rates. The lack of dependence on gravity can be explained using the relative forces on the melt. The plateau modulus of PS281 is approximately 1.7E5 Pa. Assuming this stress is applied over the area of the die exit, the downwards force required to overcome this is ∼0.53 N. This corresponds to 50 g of polymer or an extrudate volume of ∼50 cm^{-3}. This is not reached within these simulations and thus gravity has no visible effect.

Increasing gravity is not physical, this would be similar, but not equivalent, to decreasing the viscosity of the sample, whether by using a lower molecular weight polymer or increasing the temperature. Although gravity and surface tension are not strong effects on these polystyrenes under the experimental conditions of this work they may still have an effect in different systems.

4.2.8 Wall Slip

Within the previous simulations, any free-surface points which touch the capillary wall remain fixed there for the remainder of the simulation, meaning a zero velocity at the capillary wall. Adding a slip length term s to the wall shifts the line of zero velocity beyond the wall by s mm[1] and allows wall points to move downwards with the flow and eventually off the wall at the die exit corner. The effect of increasing slip length is shown in Figure 4.14.

As slip length s increases the extrudate swell decreases. Above s=1 there is no significant change in results upon changing slip length. At these slip lengths the velocity across the capillary is effectively unaffected by the presence of the boundary wall and thus the chain stretch also remains approximately the same. At the highest slip lengths the Newtonian limit for swelling reduces from 1.1 to approximately 1. This is because the wall slip has removed the velocity gradient at the die exit. Adding a fixed slip length is not physically realistic. In reality, wall slip will increase with increasing speed. This is not implemented directly within *flowSolve*, although if wall slip is present at the highest speeds, the swelling ratios may change from the s=0 curve to the s=10 curve.

[1]The s values are given in reduced units, but correspond exactly to mm in these simulations.

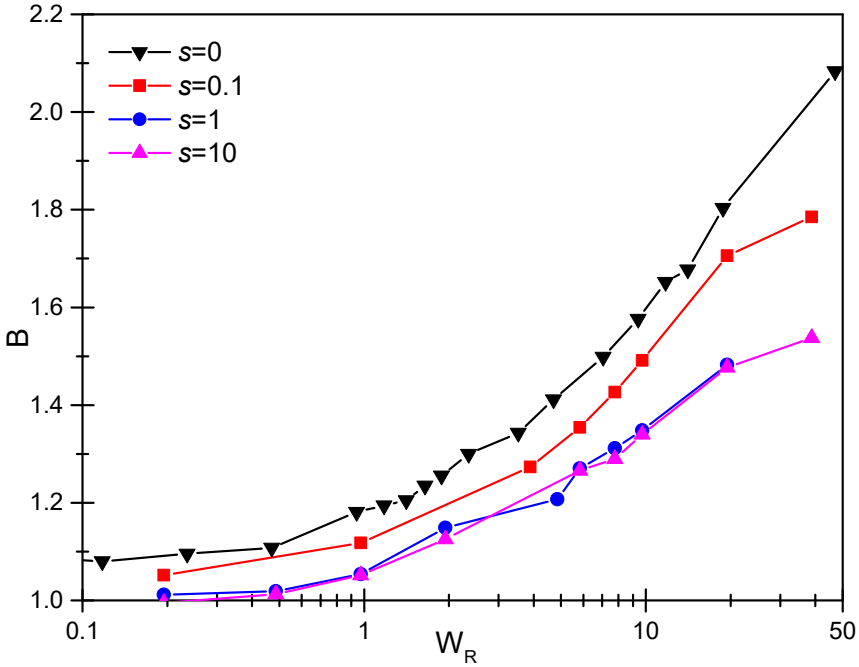

Figure 4.14: Effect of changing slip length on extrudate swell simulations of PS281. Slip lengths of 0 (no slip) and s=0.1, 1 and 10 (increasing slip) relative to the die diameter of 2 mm are used.

4.2.9 Effect of Extruder Geometry

The extruder length to diameter ($l:d$) ratio is often changed in industrial processes and has been the subject of significant previous work. In Section 4.2.5 it was shown that the chain stretch along the die wall is constant for a long period before the die exit even at high Weissenberg numbers but the stretch at the die centre line, in general, has not relaxed by the die exit. Changing the $l:d$ ratio will affect the centre line stretch and may therefore affect the extrudate swell. Figure 4.15 describes the simulated effect of changing the $l:d$ ratio on extrudate swell. This is done by altering the die length (2 mm, 5 mm, 10 mm and 20 mm dies are used) but also by narrowing the die to give a 5:1 capillary.

There is almost no effect of $l:d$ ratio on swelling. All the 2 mm diameter dies have approximately the same swelling ratios even at high Weissenberg number. The 5:1 die exhibits a slightly lower swelling ratio at high W_R but the same swelling ratios at lower W_R. To explain this the chain stretch along the die can be considered. Figure 4.16 shows the chain stretch along the die. b) shows that the peak in stretch after the die exit is not dependent upon the stretch relaxed at the exit line, as it is constant in position and magnitude for all die lengths. The swelling ratio must be dependent upon the stretch at

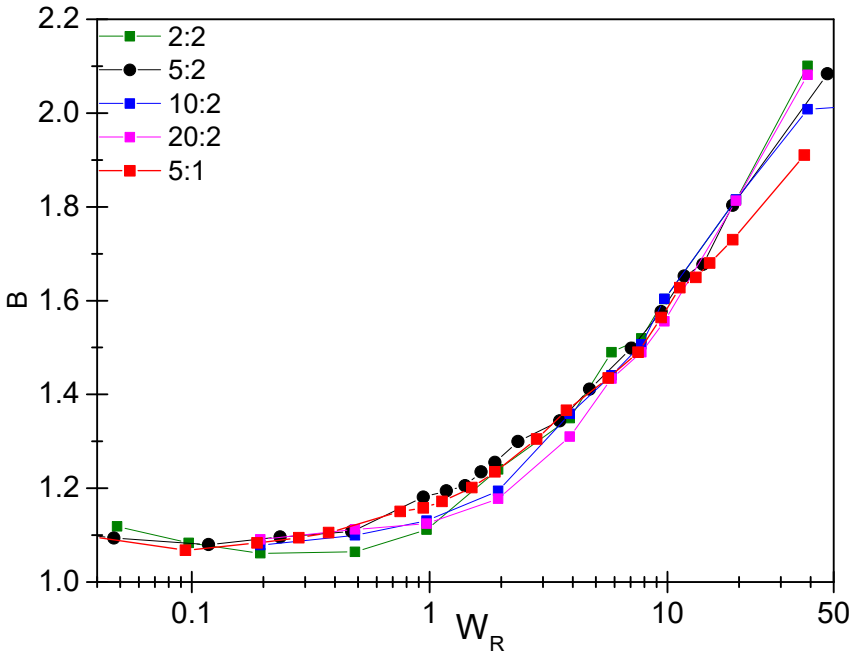

Figure 4.15: Simulated Swelling ratios for PS281 at different $l:d$ ratios

the die wall for these samples. The B value for all samples in Figure 4.16 a) - c) is the same and so is the magnitude of the steady-state chain stretch plateau. However, the amount of chain stretch to be relaxed at the die exit varies significantly, $\lambda \approx 3$ for $l:d$=1 but $\lambda \approx 1.5$ for $l:d$=10. The chain stretch plateau at the die wall is slightly lower for the 5:1 capillary, which results in the prediction for a slightly reduced extrudate swell.

In some previous studies the effect of slanting the die entry (to reduce the entry contraction stress) has been investigated. For the 5:2 geometry here this has no effect, as the stress state along the die wall has reached steady state regardless of the entry stress built up. Another possibility is removing the sharp corner at the die exit by rounding the exit corner. This is shown in Figure 4.17. Rather than removing the die exit singularity, rounding the die corner moves it up the die slightly. Swelling after this point then causes the flow to stick to the wall along the curve, at a higher radius than that of the original die. This effectively moves the extensional pull-off outwards, increasing the B values observed. This increase is greater for the higher flow speeds and means it is not possible to investigate the effect of removing the die exit corner.

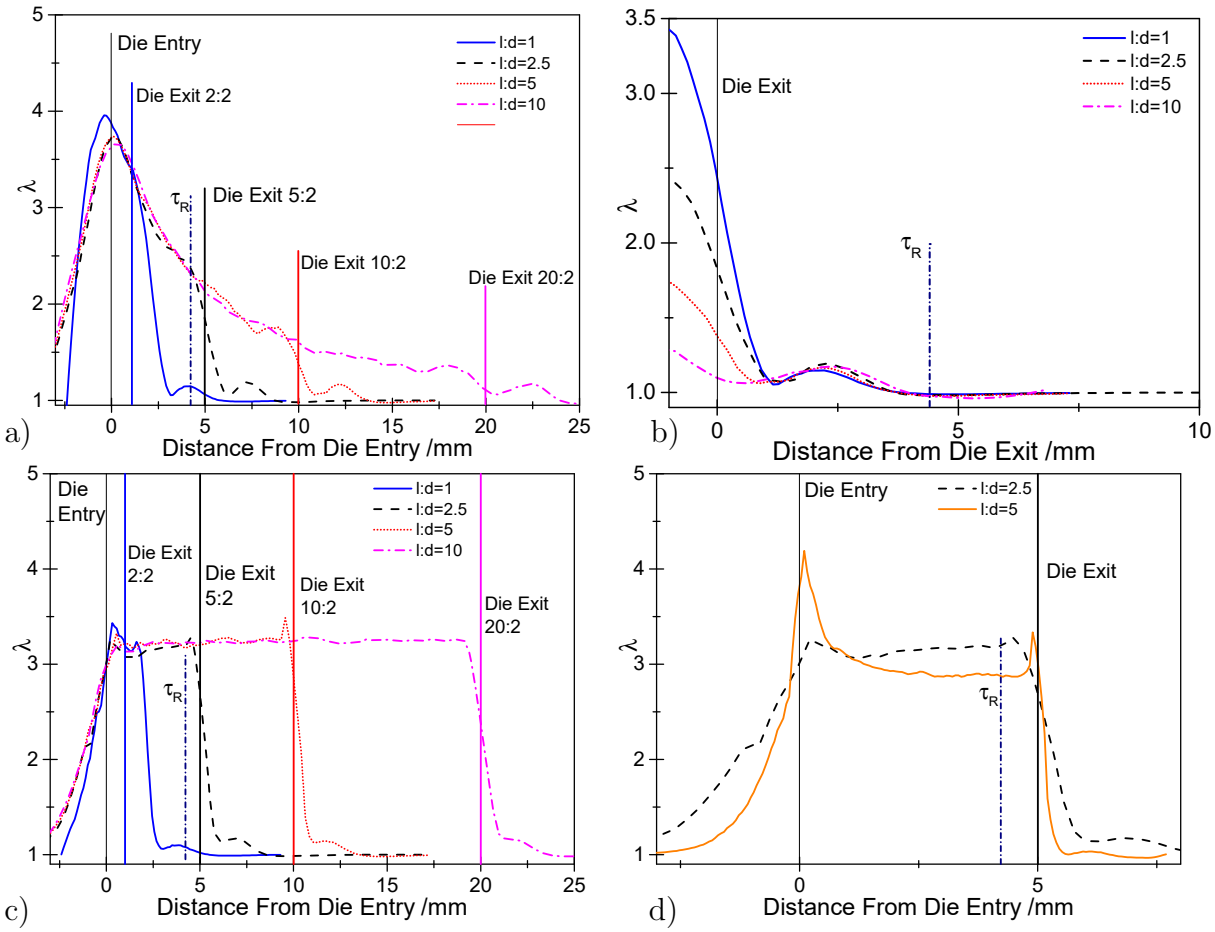

Figure 4.16: Chain stretch values at W_R=19 for a 2 mm diameter and l length capillary. a) shows stretch along the capillary centre-line b) shows after the die exit c) shows stretch along the capillary wall for d=2. d) shows stretch along the capillary wall for l=5 and variable l.

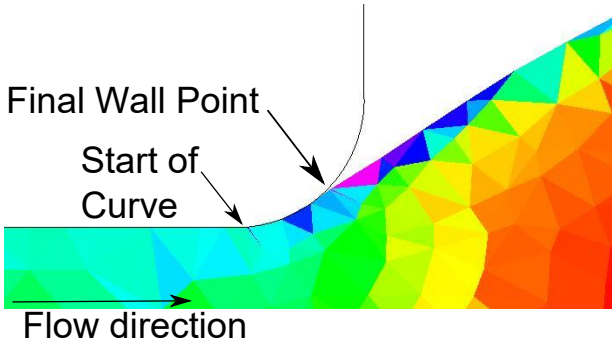

Figure 4.17: Diagram showing a rounded die exit corner. Triangle colours show chain stretch for PS281 at W_R=19.

4.2.10 Predictions of Extrudate Profiles and Die Exit Angles

In Section 2.1 one limitation of previous theories for predicting B values was that they cannot predict the profile of the extrudate, only a maximum value. *flowSolve* is capable of predicting the extrudate profile as a function of both time and distance. Regardless of Weissenberg number (flow speed) the extrudate initially expands rapidly before reaching a steady state. (Figure 4.18).

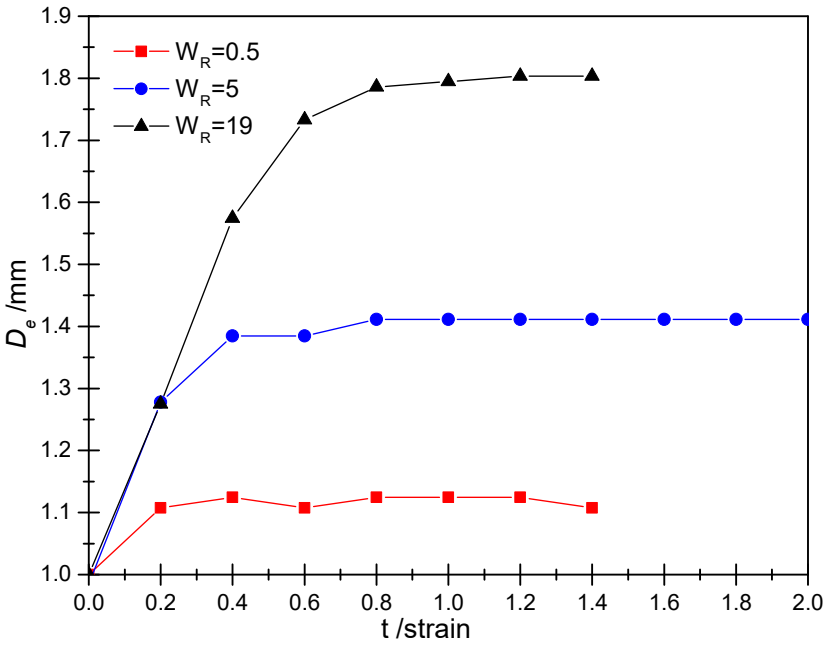

Figure 4.18: Extrudate profiles as a function of reduced time for PS281 at increasing Weissenberg number. The colours match those in Figure 4.11.

As speed increases, the strain time required to reach steady state increases. The initial rate of expansion out of the die is constant regardless of Weissenberg number. This is due to the scaling by v_{inp} used in the definition of strain time. The factor that varies is the point at which the increase slows and steady state is reached. For W_R=0.5 this happens almost instantaneously. In real time units the fastest flows reach steady state in well under a second, therefore in practical extrusion flows it will not be necessary to wait for the flow to reach steady state except at the slowest speeds where steady state is achieved in a few seconds.

Considering a steady state flow as in Figure 4.19 two useful measures are the distance beyond the die exit at which the maximum swell occurs and the die exit angle. The maximum swelling distance (D_B) is the distance below the die exit at which the extrudate

first reaches its maximum value. The die exit angle θ is contained between the wall below the die exit, the fixed die exit corner point and the first free surface point below the exit.

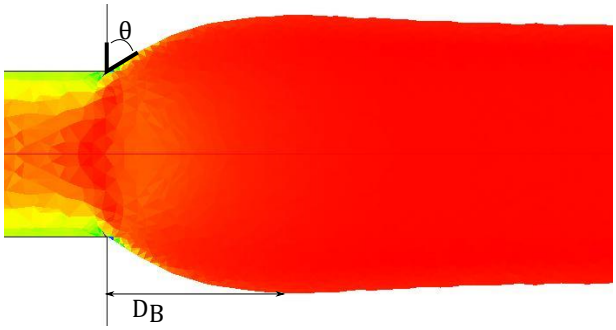

Figure 4.19: A view of the flow below the die exit, showing downstream flow phenomena.

Figure 4.20 shows the value of D_B in a similar way to B against Weissenberg number.

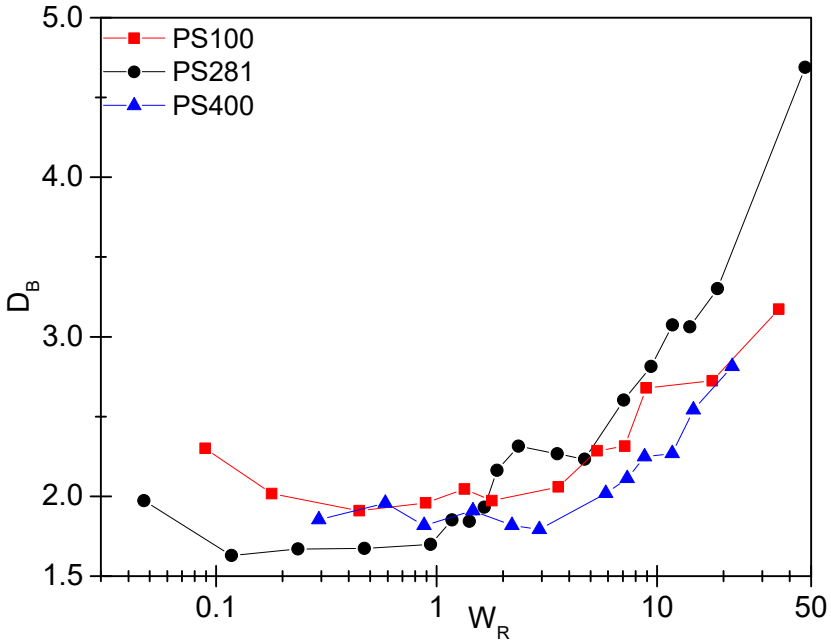

Figure 4.20: Downstream distance to the point of maximum swell for monodisperse polymers at 180 °C against Rouse Weissenberg number

The D_B values for different molecular weights do not superimpose versus Weissenberg number as well as the B values do, and the increase is much less smooth. The overall trend is the same as for B values, i.e. that there is a decrease with increasing W_R at low W_R, followed by a rapid increase at higher W_R. These distances do not correspond to the

Rouse distances defined previously, the slowest speeds have D_B of over 1.5 mm whereas the chain stretch will decay on a scale of 0.003 mm. Similarly chain orientation will decay on a timescale of 0.1 mm. This may be due to the fact that the flow takes many times the Rouse time to fully relax all stretch built up at the die exit and thus reach the maximum swell. Figure 4.21 shows predictions for the angle of flow exit from the die.

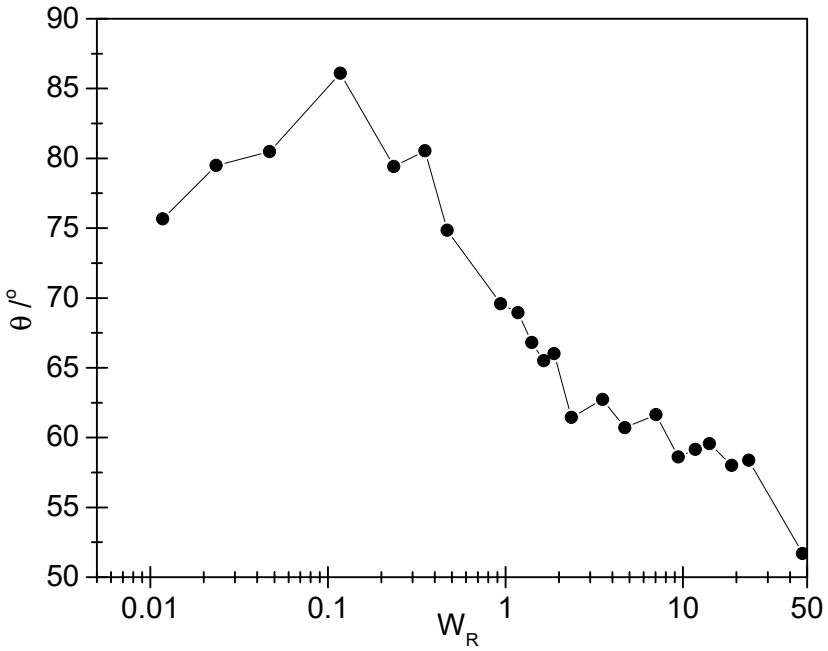

Figure 4.21: Simulated instantaneous die exit angles for PS281

θ=0° would mean the polymer expanding laterally along the bottom of the die and 90° would mean either no swell or a significantly delayed swell. The maximum exit angle corresponds to the minimum B value at approximately W_d=1. In this case the extrudate exhibits almost no swell immediately after the die exit, rather exhibiting a very small delayed swell. As the flow speed increases the exit angle decreases. The B values also increase here, meaning that the flow is swelling for a much longer straight-line distance for these higher speeds.

Overall, *flowSolve* provides a good way of investigating the factors affecting extrudate swell, as well as providing detailed information about the evolution of the extrudate as a function of time and distance. It therefore has the potential for being useful for predicting practical extrusion flows. First, the simulation results must match the experimental data.

4.3 Experimental Results

Experiments were performed in the MPR at the same shear rates as those simulated within *flowSolve*. This allows direct comparison between theory and experiment. Still images from the MPR are shown in Figure 4.22.

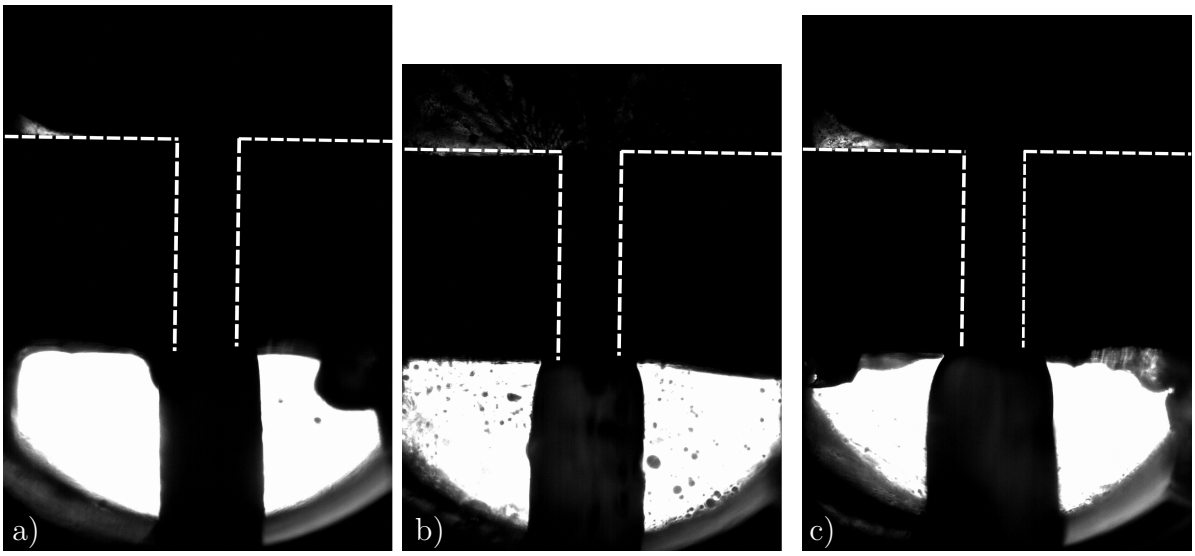

Figure 4.22: Images taken during extrusion within the MPR for PS281 at W_R= a) 0.5, b) 5 and c) 19

There is no visibility within the top section for these samples due to particulates picked up in previous experiments and some degradation during these experiments. Analogously to Figure 4.7 for simulations, Figure 4.23 shows experimental results for extrudate swell at different molecular weights. Similar to the *flowSolve* predictions the MPR extrusion data superimpose well with W_R. This confirms the lack of molecular weight dependence stated in the previous section. The predictions of extrude swell match experimental data very well for both molecular weights up to $W_R \approx 7$. There is insufficient data from the MPR at low shear rates to completely confirm the low-shear upturn seen at low speeds in the experimental predictions. Although the lowest shear rate point for PS281 has a B value greater than the next lowest, as predicted by *flowSolve*, the same can be said for PS400, which is not predicted. The experimental data at high Weissenberg number is over-predicted by *flowSolve*. At approximately a W_R of 7 the rate of increase in swelling with shear decreases slightly, causing the swelling ratios to become lower than the predictions. After this, the experimental data appear to increase at approximately the same rate as the simulated data, albeit shifted down by a constant factor or upwards in

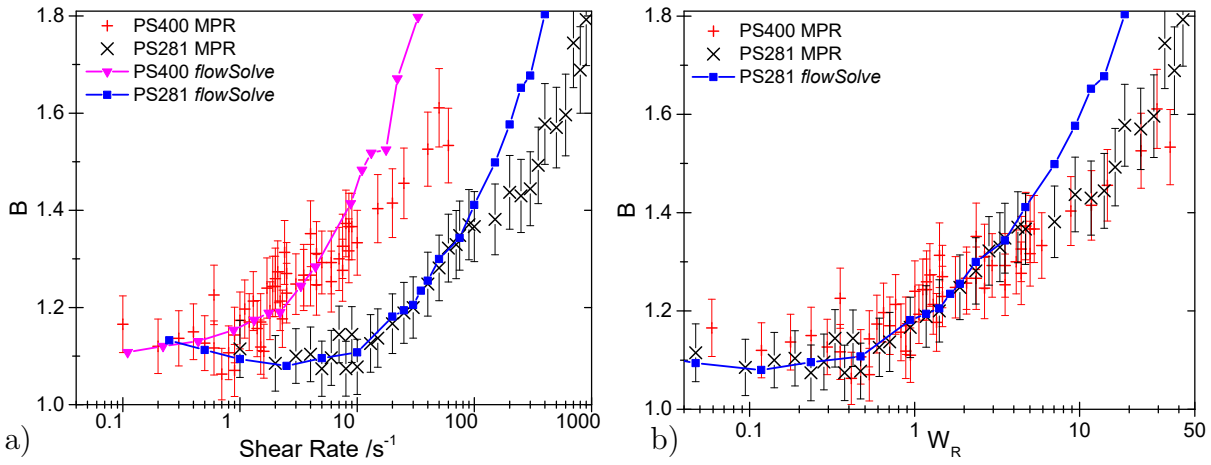

Figure 4.23: Experimental data and theoretical predictions for PS281 at 180 °C. a) versus shear rate and b) versus W_R. The prediction for PS400 is removed in b) due to the superposition with PS281. Error bars are taken as the difference between swell values measured using the camera in and out of focus.

Weissenberg number.

One possible reason for this difference is that this is caused by leakage within the MPR. At higher speeds the geometries can leak slightly, and this may cause a drop in shear rates, flow pressures and thus swelling ratios. This seems unlikely however, as the drop-off occurs at roughly the same point in W_R for PS281 and PS400 but almost an order of magnitude different in shear rate. Leakage/failure within the MPR should occur at roughly the same shear rate for the two samples, especially given the similar viscosities. Pressure differences within the MPR are also different. For PS400 the pressure drop at W_R=5 is 40 bar. For PS281 it is 20 bar. The differences in pressure drop mean that it is unlikely that the MPR is losing sample at the same rate; therefore the difference should be due to another factor. Section 4.4 explores the hypothesis that the difference is associated with reduction of monomeric friction coefficient during regions of high chain stretch within the die.

Quantitative comparison of the extrudate profiles from the MPR is difficult, as it is not possible to resolve detail in the immediate vicinity of the die exit point from the images in Figure 4.22. The polymer extrudate and the steel of the die wall look the same in the black and white image. A qualitative comparison is shown in Figure 4.24.

The predicted profiles qualitatively match the experimental profiles, with the majority of swelling occurring at the die exit followed by a roughly constant region. A more quantitative comparison is shown in Figure 4.25.

The profile at long distances is predicted well for W_R=0.5 and 5. The swell near the

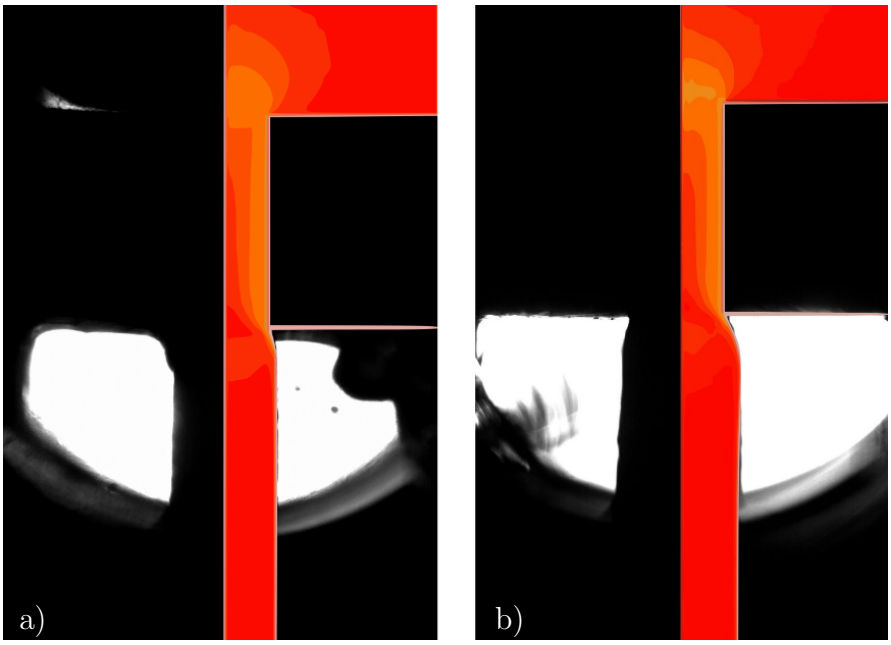

Figure 4.24: A comparison of extrudate profiles of PS281 at a) W_R=1 and b) W_R=5 from *flowSolve* (right) and the MPR (left)

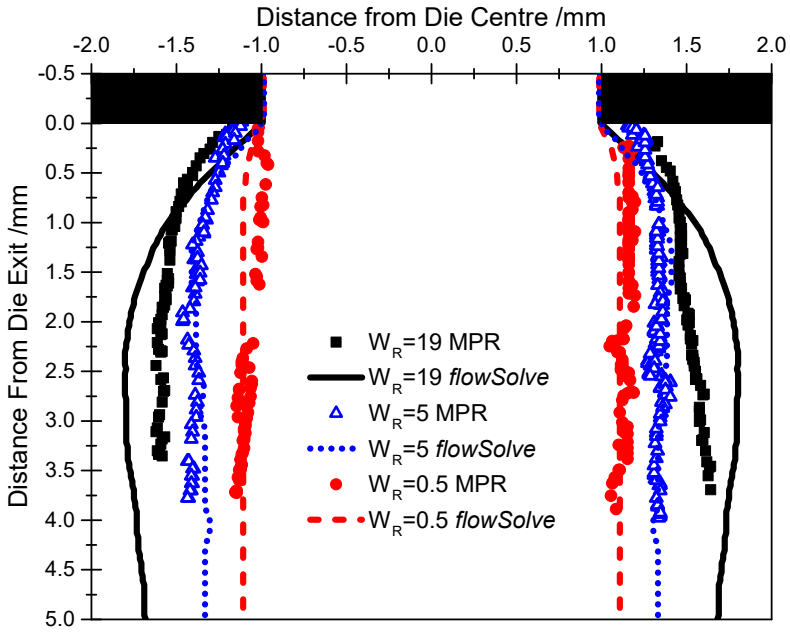

Figure 4.25: Comparison of the extrudate profile from theory and experiments at increasing Weissenberg numbers. The flow direction is in negative y and the die spans $-1 < x < 1$. The points are pixels traced from the images of the extrudate from the MPR and the lines are *flowSolve* predictions at the same speed.

die exit is not correctly predicted, as the experimental extrudate swell appears to start ∼0.2 mm outside the die exit. This is due to the lack of resolution in the region of the die exit. At W_R=19 the swelling at long distance is over-predicted, and the angle of swelling out of the die is also over-predicted. This may be due to the over-prediction of chain stretch at the exit, which will cause swelling to be too rapid.

4.3.1 The effect of $l:d$ Ratio on Experimental Extrudate Sswell

Data from the 5:1 capillary are shown in Figure 4.26.

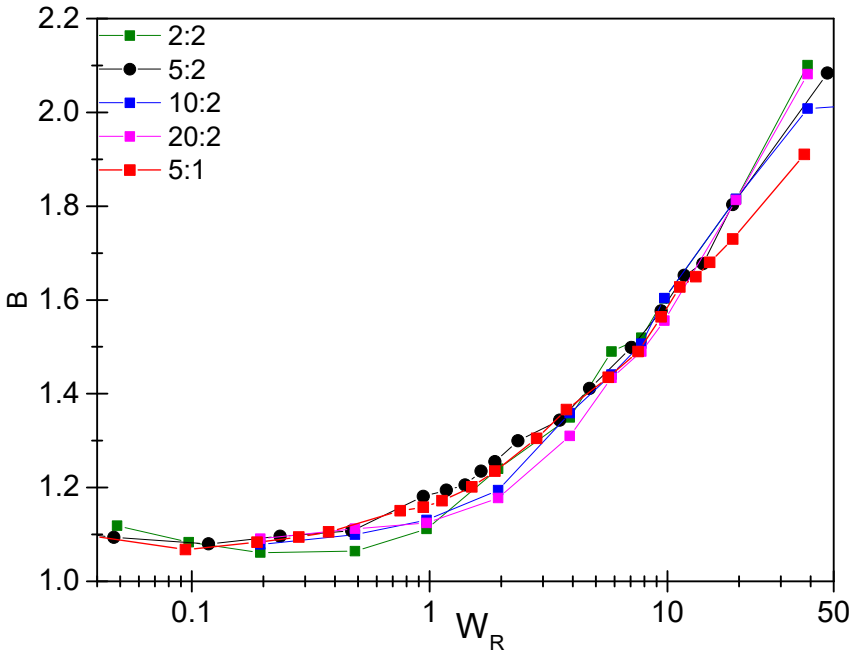

Figure 4.26: Simulated and experimental swelling ratios for PS281 in both the 5:1 and 5:2 capillaries

The 5:1 capillary data, as predicted, matches the previous data well up to the limits of the apparatus. Although, theoretically, the maximum Weissenberg number achievable for the narrower capillary should be higher due to the higher shear rates within a narrower capillary at constant v_p this is not the case in practice. At the highest shear rates the leakage around the geometry is significant relative to the flow through the capillary. This limits the maximum shear rate and the number of high shear rate runs which can be usefully performed. It is not possible to check the prediction of lower swelling ratios above $W_R \approx$10 as insufficient data points are obtained here. There is no difference outside of error between the data for the two capillaries when normalised by Weissenberg

number. This provides further support for the idea that the disagreement in swelling ratios between theory and experiment occurs due to a constitutive problem rather than due to an experimental problem, as it is independent of both molecular weight and geometry.

4.3.2 Comparison to Previous Theory

The monodisperse results can now be compared to the previous theory of Tanner from Equation 2.2 [3, 4]. To do this, the normal stress difference must be calculated. This is performed via the Laun approximation [71]:

$$N_1(\dot{\gamma}) \approx 2G'(\omega)\left(1+\left(\frac{G'(\omega)}{G''(\omega)}\right)^2\right)^{0.7} \tag{4.4}$$

This is an approximation, but should serve to provide a rough predicted extrudate swell. The results obtained are shown in Figure 4.27.

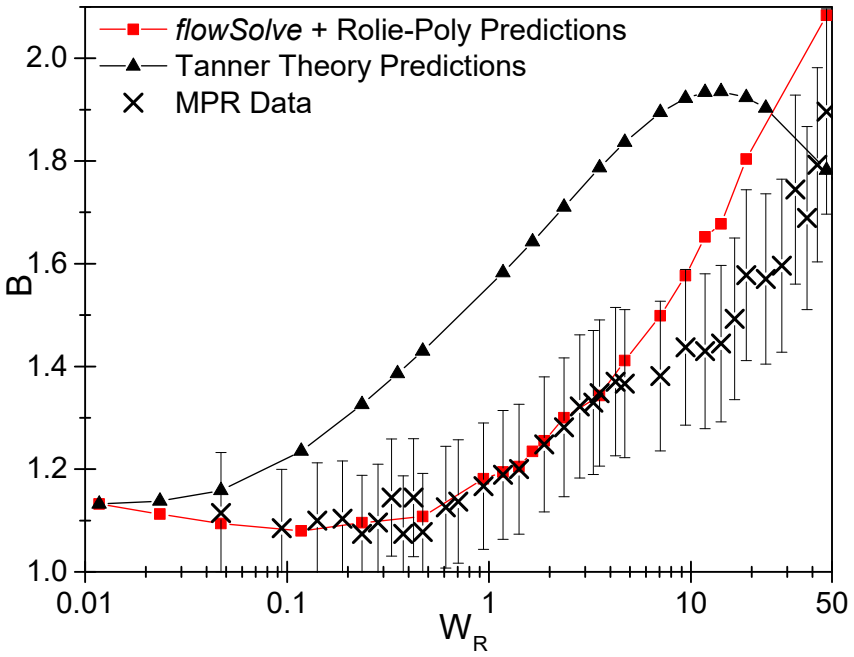

Figure 4.27: The predictions of the extrudate swell equation of Tanner and comparison to experimental extrusion data for PS281 from the MPR 5:2 capillary.

The Tanner theory consistently over-estimates the extrudate swell, and is unable to predict swelling at high shear rates, due to N_1 starting to drop off at these high rates. This may be due to the use of a single normal stress value rather than the full stress tensor

used in the constitutive models described in this work. Considering a full stress tensor is especially important in the region around the die exit corner where the flow changes direction.

4.4 Friction Reduction Extension to Rolie-Poly

4.4.1 Background

Equation 2.7 first defined a monomeric friction coefficient ζ to scale the timescales for molecular motions of an individual polymer chain. For a very slow flow it is reasonable to treat ζ as constant with flow speed. However, under highly stretching and orienting flow in an entangled polymer melt this assumption is no longer valid. Instead, ζ is dependent on the environment of individual chain Kuhn segments,which becomes anisotropic when chains are highly stretched. When Kuhn segments on a chain are aligned by a flow they exert a smaller frictional force on Kuhn segments on neighbouring chains.[72] This means that neighbouring chains can move past one another more easily than if they were randomly oriented with each other.

The effect of monomeric friction reduction increases with polymers with a low finite extensibility, i.e. stiff chains or those with a low number of monomers per entanglement. This is due to the greater Kuhn segment alignment which occurs at a low chain stretch. Polystyrene, with a $\lambda_{\max}$ of 5 and low Rouse time is especially likely to require friction reduction for accurate simulation at high flow rates. Yaoita *et al* [73] performed simulations of polystyrene melts under extensional flows. They replaced the constant friction with a variable friction which is a function of a stretch-orientation factor. This factor is a combination of chain stretch and orientation. One definition is given in Equation 4.5. They fitted extensional flow data to a complex empirical equation and found that there was a lower critical value of the stretch-orientation factor of 0.14 at which the friction reduction began. Yaoita used this fitted parameter within PCN (Primitive Chain Network)-FENE simulations incorporating these friction reduction equations. They found that without the friction reduction, simulations over-predicted start-up extensional viscosities, but gave good agreement when friction reduction is included. The effect is especially visible for higher molecular weight polystyrenes where the extension hardening is significant. Ianniruberto [68], in an alternative model, kept the critical order parameter S_c but replaced the complex equation of Yaoita [73] with a much simpler power law form for stretching in

the xx (or uniaxial stretching) direction:

$$\begin{aligned} \frac{\zeta}{\zeta_0} &= \left(\frac{S}{S_c}\right)^{-1.25} \Bigg| \; S \geq S_c \\ \frac{\zeta}{\zeta_0} &= 1 \qquad\qquad\quad \Bigg| \; S < S_c \\ S &= \left(\frac{\overline{\lambda}}{\lambda_{\max}}\right)^2 \left(\overline{S}_{xx} - \overline{S}_{yy}\right) \end{aligned} \tag{4.5}$$

Initially, these equations were based upon empirical fitting of rheological data. Ianniruberto *et al* also performed molecular dynamics simulations on polystyrene oligomers to simulate polymers under extensional flow.[68] They measured the diffusion coefficient of a test chain at different levels of oligomer alignment and thus related this to the monomeric friction. They found an increase in diffusion (decrease in friction) at a critical value, 0.063, of Kuhn segment alignment. This is not the same as the previous critical value of 0.14, possibly due to the slightly different system used. Mead *et al* [74] have developed an approach to friction-reduction in the case of general polydispersity, taking as a starting point the form in Equation 4.6.

$$\frac{\zeta}{\zeta_0} = 0.02239(S_{\text{kuhn}})^{-1.65}$$

The Kuhn segment alignment is related to the overall tube alignment by:

$$\begin{aligned} S_{\text{kuhn}} &= (1 - \frac{3}{5}l^2 + \frac{1}{5}l^4 + \frac{1}{5}l^6)S_{tube} \\ l &= \frac{\lambda}{\lambda_{\max}} \end{aligned} \tag{4.6}$$

This is approximately the same form as in Equation 4.5 except with a more complicated term for the finite extensibility function. Both are approximations to the finite extensibility function $F(\lambda)$ from Equation 2.13. Mead *et al* extended this work to create a slip-link based toy model to predict the behaviour of polydisperse melts under shear and extensional flow.[75, 76]. For a polydisperse system, rather than using a single chain orientation for all polymers, they used a coupled form for the overall orientation:

$$\frac{\zeta}{\zeta_0} = 0.02239 \left(\sqrt{(\mathbf{S}_{\text{Kuhn},i}) : \sum_j \phi_j \mathbf{S}_{\text{Kuhn},j}}\right)^{-1.64} \tag{4.7}$$

As in Section 3.3.3, ϕ_i and ϕ_j are the volume fractions of chains i and j respectively.

These various theories all follow the general form of a power-law decrease in friction with an increase in monomer orientation. This monomer orientation is related to the chain stretch/finite extensibility and tube orientation in the flow direction. All these functions allow for a decrease in monomeric friction (and thus polymer relaxation times) that approaches 0 at high monomer orientation. For the purposes of flow simulation this seems unphysical. For example, at a die exit corner where polymer chains are very highly stretched, relaxation will not proceed infinitely quickly, rather should reach a constant value based upon easy it is for oriented chains to flow past each other. In the following section the formulae described in Section 3.3.5 incorporating a non-zero friction at high orientation are used.

4.4.2 Extrudate Swell Results with Monomeric Friction Reduction

Extrudate swell simulation results using monomeric friction reduction are shown in Figure 4.28. Three sets of friction reduction parameters are shown with varying values of S_c and $\zeta_{\min}$.

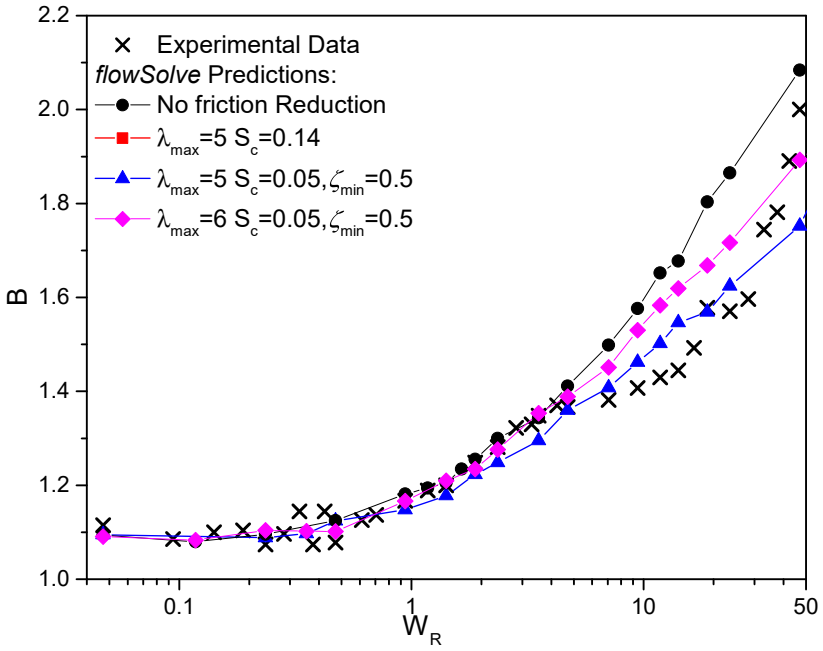

Figure 4.28: Effect of monomeric friction reduction on *flowSolve* predictions of extrudate swell for PS281 using the single stretching mode Rolie-Poly equation and a $\lambda_{\max}$ of 5.

The simulations with S_c=0.14 are chosen to match the previous simulations of Yaoita [73]. These simulations agree with the standard simulations up to W_R=7 before the B values plateau at higher W_R. The plateau in B does not correspond to the observed discontinuity in the experimental data, rather occurring at higher B and higher W_R. This can be solved by decreasing the value of S_c to 0.1. However, this value of S_c results in a plateau in B values (not shown on the plot) and thus an underestimation in swelling ratios. The decrease in relaxation times at high shear rates causes the chain stretch/orientation built up to be roughly constant with increasing shear rate, thus resulting in constant extrudate swell. This is solved using the $\zeta_{\min}$ term. This causes a limited reduction in relaxation times at high shear, thus still allowing additional stretch to be built up, and allowing for an increase in extrudate swell. The parameters used in Figure 4.28 of S_c=0.05 and $\zeta_{\min}$=0.5 are fitted to the experimental data, so as to deviate from the full-friction model at the correct point and by the correct magnitude. The parameters of S_c=0.0235

and ζ_{min}=0.819 are fitted to the SER data which will be shown in Figure 4.30. This latter parameter set is not unique, almost identical extrudate swell (and SER) predictions results can be obtained using λ_{max}=6, S_c=0.05 and ζ_{min}=0.5. In this work the value of λ_{max} is kept at 5 for consistency. The effect of the two parameters on friction reduction is shown in Figure 4.29.

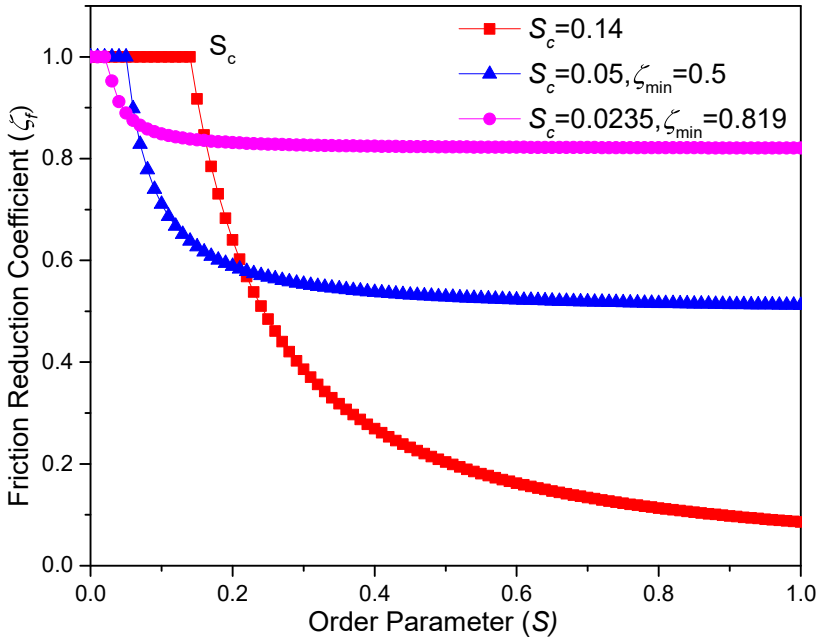

Figure 4.29: Effect of the tube order parameter S on the monomeric friction reduction coefficient and thus the scaling of relaxation times. 1 equals no friction reduction and thus relaxation times equal to their equilibrium value and 0 would mean relaxation times of 0.

The fitted parameters result in friction reduction at low order parameters, leading to the earlier onset in reduction in extrudate swell predictions than that for S_c=0.14. The lower value of S_c increases the friction reduction at low rates, but adding an ζ_{min} term limits this, especially at higher rates. However, the friction at order parameters above ~0.2 is significantly higher, limiting the effect of friction reduction at high Weissenberg number. Friction reduction does not only affect the flow simulations, it also has an effect on uniaxial extension. The SER data from Figure 4.4 are shown alongside predictions with reduced friction in Figure 4.30.

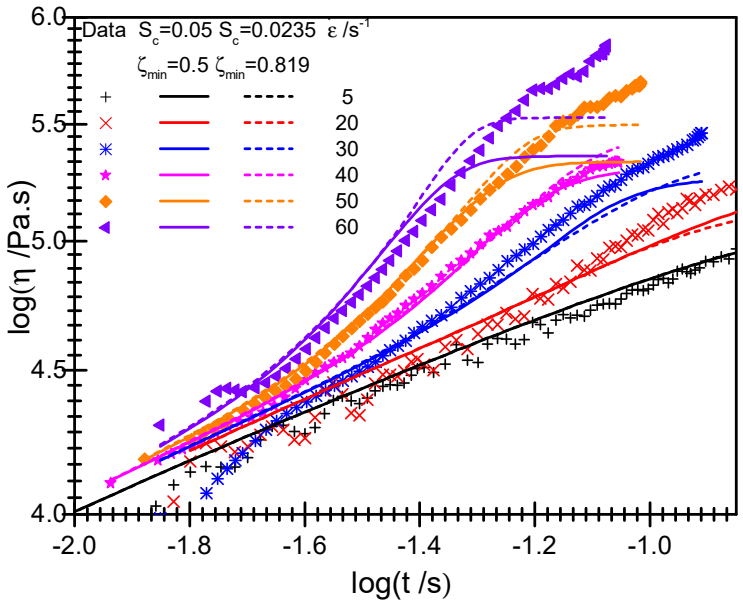

Figure 4.30: SER data for PS281 and predictions for the Rolie-Poly equation with S_c = 0.05 and $\zeta_{\min}$=0.5.

At 30 s^{-1} using friction reduction has little effect on the extensional prediction except at the longer times at which point the reduced friction causes a slight under prediction in extensional viscosity. At 40 s^{-1} the predictions fit the data well up to the limit of the SER data. At higher speeds, friction reduction results in a low steady state plateau which is not seen in the SER data. Thus at long times (high strains) the extensional viscosity is under-predicted. The parameters S_c=0.05 and $\zeta_{\min}$=0.5 which gave good results for the extrudate swell produce a greatly under-predicted steady-state viscosity. The parameters S_c=0.0235 and $\zeta_{\min}$=0.819 give a better fit the extensional data better but do not adequately reduce B values at high Weissenberg number. The current model for friction reduction, therefore, is not able to produce accurate predictions for both extrudate swell and uniaxial extension of PS281. Parameters which produce a good fit to extrusion data under-predict the steady-state extensional viscosity at high extension rates. Parameters which improve the fit to uniaxial extensional data over-predict the extrudate swell at high Weissenberg number. Further work is required here to produce a theory which will fit both data sets simultaneously with the same parameter set. In this work, the parameter set which best fits the extrudate swell is used but we note that the model does not correctly predict the extensional viscosities in this case.

As the friction reduction coefficient ζ_f is a constitutive parameter like λ it can be plotted spatially along the extruder. ζ_f is shown spatially in Figure 4.31 and the effect of this on chain stretch is shown in Figure 4.32.

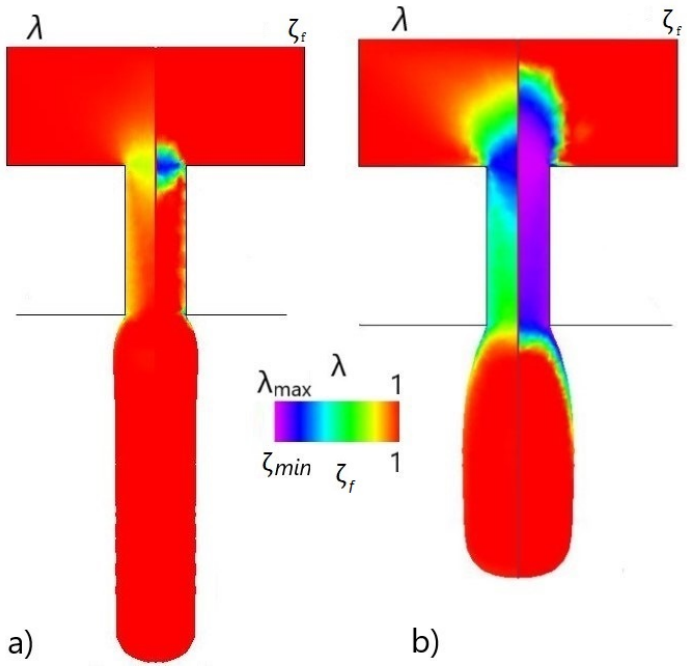

Figure 4.31: Friction reduction coefficient ζ_f (right half of each sub-figure) and chain stretch (left half of each sub-figure) along the extruder for PS281 with S_c=0.05 and ζ_{min}=0.5. In a) W_R=4.7 and b) W_R=47.

ζ_f changes in the same positions as λ. At the die entry, as chain stretch increases, the friction reduces rapidly. At the capillary wall where stretch has plateaued the friction also has a constant value, which will range from 1 at the lowest rates to ζ_{min} at the highest rates. Friction reduction has almost no effect on chain stretch for low Weissenberg numbers, leading to the lack of effect on swelling ratios. At higher Weissenberg number, the stretch is consistently lowered by friction reduction, reducing both the chain stretch at the die entry and exit by approximately 0.7. This reduction in chain stretch causes the significant reduction in extrudate swell seen on Figure 4.28. A comparison of the profiles from the MPR and friction-reduced simulations is shown in Figure 4.33.

In this figure, the maximum diameter reached by the extrudate (and thus the B value) is approximately correct, as for the data in Figure 4.28. However, the profile is not predicted correctly. The maximum swelling in the MPR occurs closer to the die exit than predicted. This may be due to experimental errors, such as the polymer sticking to the ceiling of the bottom section, or may be due to a constitutive issue.

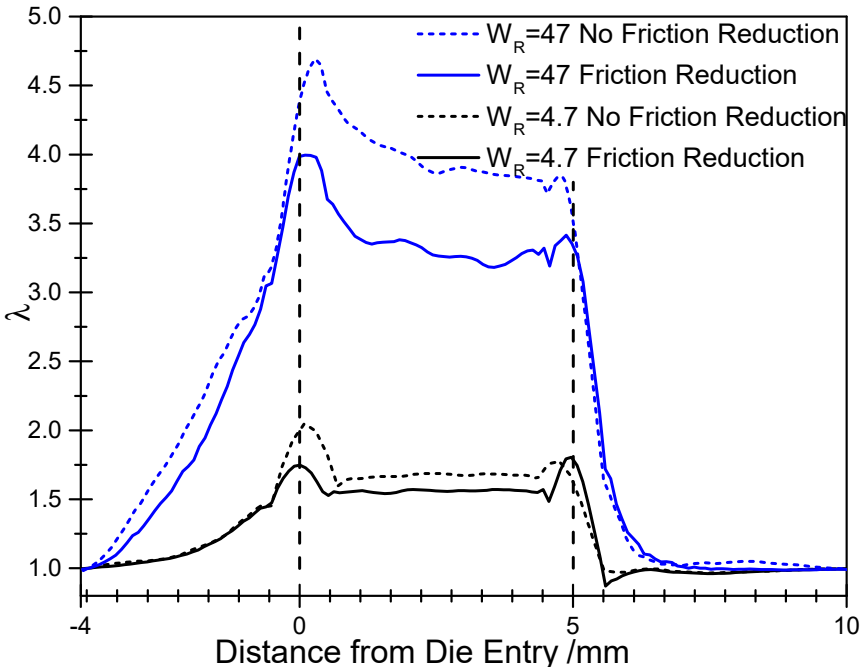

Figure 4.32: Chain stretch values along the extruder for PS281 with and without friction reduction at Weissenberg numbers to match Figure 4.31.

Figure 4.33: MPR data and *flowSolve* prediction with reduced friction for PS281 at W_R=19.

4.5 Polydisperse Rolie-Poly used for a Near-Monodisperse System

A first test of the accuracy of the polydisperse Rolie-Double-Poly theory introduced in Section 3.3.3, and used in the next chapter, is whether or not it matches the experimental data for a nearly-monodisperse sample. Of course, for a truly monodisperse sample such a move would be inapplicable as there would be a single molecular weight peak, which could not be coupled with another fraction as required. However PS281 is not completely monodisperse, so a set of 9 Rolie-Poly elements can be calculated, as shown in Table D.1 in Appendix D.

4.5.1 Extrudate Swell Results

Figure 4.34 shows the results from the RDP theory overlaid on the experimental MPR data

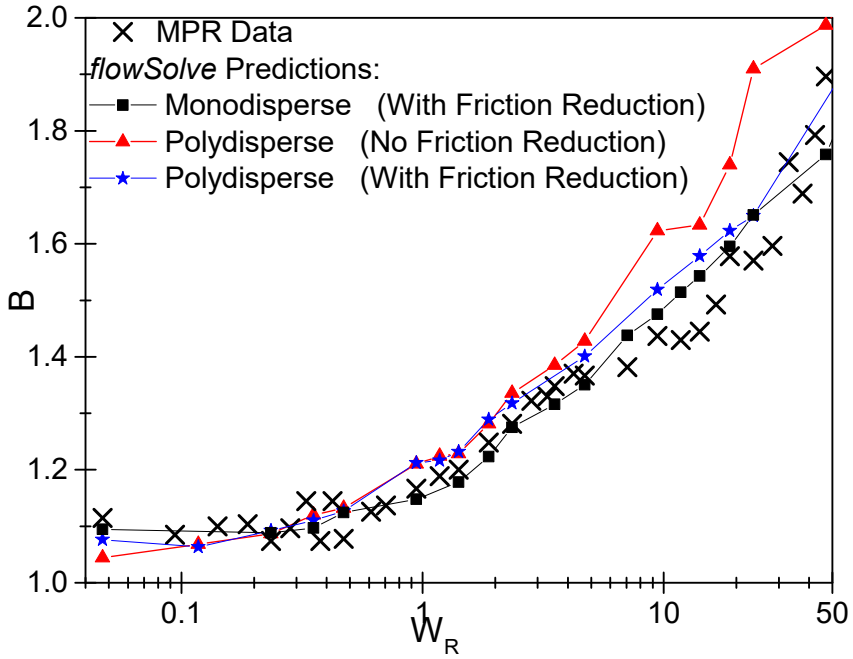

Figure 4.34: Monodisperse and RDP predictions for PS281 with and without friction reduction

The RDP simulations predict roughly the same swelling ratios as the monodisperse ones and also match the experimental data up to $W_R \sim 7$. Incorporating friction reduction with the same parameters used previously also gives improved predictions above this point. The

agreement with previous simulations and experimental data means that the RDP model can be used with confidence for the polydisperse samples used in later chapters.

4.5.2 Extensional Fits

A fit to the SER data for PS281 is shown in Figure 4.35.

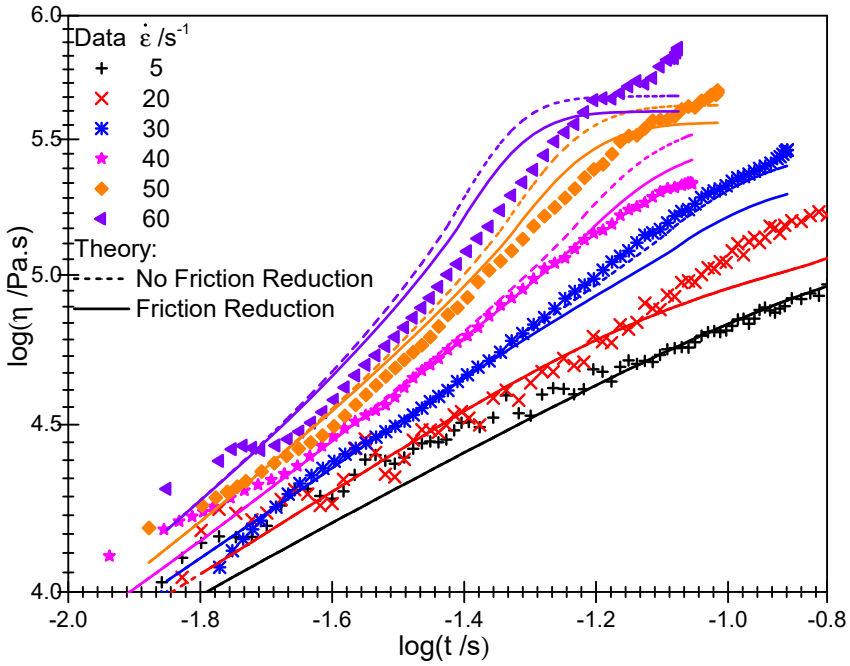

Figure 4.35: Rolie-Double-Poly predictions with(—) and without (- - -) friction reduction for PS281 under uniaxial extension.

The standard RDP fit acts similarly to the monodisperse Rolie-Poly fit from Figure 4.4. The data at 30 s^{-1} are fitted well but the extensional viscosities are over-predicted at higher rates. At the lowest rate the exact extensional viscosities are not correctly predicted at short times but seem to improve at higher strains and strain rates. This is in line with the simulations of Boudara where the linear prediction of the RDP model was incorrect. [40] The predictions incorporating friction reduction (S_c=0.05 and $\zeta_{\min}$=0.5) produce a plateau at high strain that is not seen in the data although the viscosity at which this plateau occurs is higher than for the single-mode prediction. The under-prediction in extensional viscosity at higher Hencky rates is therefore smaller when using the RDP equations.

4.6 Concluding Remarks

The use of monodisperse melts has allowed investigation of various factors affecting extrudate swell. The most important factor is Rouse Weissenberg number. Where the shear rate for an extrusion experiment is non-dimensionalised by the Rouse relaxation time of the polymer the effect of molecular weight can be removed, resulting in a master curve for polystyrene. The approximate Newtonian swelling ratio observed and predicted is 1.1, in agreement with previous work. This is followed by an increase in swelling at $W_R \approx 1$. The scaling by W_R means that extrudate swell is also temperature independent when rates are non-dimensionalised in this way. Extrudate swell is therefore a chain stretch controlled phenomenon, the greater the stretch to be relaxed at the die exit the greater the extrudate swell. Surface tension and gravity have no significant effect on these simulations as at these dimensions and under isothermal conditions they are calculated to have no effect on the experimental extrusions. Die $l:d$ ratio has very little effect on extrudate swell as the chain stretch at the die wall reaches a steady state value close to the die entry. This means that die entry effects have effectively decayed away and there is little effect of increasing the die length. At the very highest speeds the extrudate swell is slightly reduced for a long, narrow capillary in simulations although there is little evidence to support this experimentally.

Experimental data can be obtained for these samples within the MPR up to Rouse Weissenberg numbers of $\sim$50. This value appears to be the practical limit of the MPR for samples of this viscosity. Simulations using the standard Rolie-Poly model with a single stretching element match the experimental data up to W_R=5$-$7. Above this point the experimental data are consistently lower than the simulations predict. The extrudate swell continues to increase albeit at a lower B value than the simulations predict. One possible constitutive reason for this disagreement is a flow-induced reduction in monomeric friction at high shear rates. Where chains are significantly stretched by shear at the die wall and extension at the die exit the frictional force on the chain monomers on each other is decreased, causing a reduction in relaxation times. The faster relaxation reduces chain stretch and thus reduces extrudate swell. A novel method of introducing friction reduction in the Rolie-Poly equation has been developed and used to provide improved predictions of extrudate swell at high shear, qualitatively capturing the trend of the data up to $W_R \approx 50$. Results do not match quantitatively at every point, this may be due to geometry factors such as wall slip, which is known to occur at high rates or due to some additional physics not yet considered. Friction reduction slightly improves fitting to uniaxial extensional

data at low rates but the predictions still deviate significantly at high extension rates and strains. Friction reduction parameters which fit the uniaxial extensional data do not adequately fit the extrudate swell data, but fitting to the extrudate swell data produces a under-prediction in extensional viscosity at high strain rates. This implies that there is some additional physics to consider.

The Rolie-Double-Poly model can also be used for this sample, as it is not quite monodisperse and thus has multiple molecular weight fractions which can be used as a series of Rolie-Double-Poly elements. This model produces comparable results to the standard Rolie-Poly model in extrudate swell but the effect of friction reduction on predictions for uniaxial extension is much smaller. The Rolie-Double-Poly model thus does a better, but not perfect, job at reconciling the two measurement types.

Chapter 5

Differences in Extrudate Swell for Bidisperse Blends

This chapter extends the previous work on a monodisperse system to a more complicated system; an approximately bimodal blend. The differences in extrudate swell upon introducing a second molecular weight peak into the molecular weight distribution are described and the reasons for this based on the tube model are described. Different methods for accounting for these differences are introduced, both within the Rolie-Poly and Rolie-Double-Poly models.

5.1 Previous Work on Bidisperse Blends

A full molecularly aware linear theory for monodisperse polymers has existed for many years.[64] but a similar theory for bidisperse or polydisperse melts is less well developed. The theory of 'double reptation' is commonly used to describe the effect of blending different molecular weights. We consider a blend containing two chains short and long which are entangled with themselves and each other. Either chain can independently reptate to relieve the entanglement and thus relax stress imposed upon the chain. Once an entanglement is relieved by reptation of one chain it relieves an entanglement on the other chain as well. Given that the total polymeric stress is proportional to the fraction of surviving entanglements on each chain the stress can be described as:

$$\sigma = G_0 \cdot P(t)^2 \tag{5.1}$$

$P(t)$ is the tube survival probability, i.e. the probability at time t that a section of tube has not had its constraints relaxed via reptation. It is a weighted sum of the single exponential relaxations of each component in the bimodal blend:

$$P(t) = \phi_s e^{-t/2\tau_s} + \phi_l e^{-t/2\tau_l} \tag{5.2}$$

ϕ_s is the volume fraction of short chains in the blend and ϕ_l is the volume fraction of long chains. This theory gives qualitatively correct linear predictions for bidisperse blends but a simple 2 mode prediction will produce far sharper features than you will observe in reality. Multiple modes corresponding to individual weight fractions must be incorporated to accurately predict real systems. This can be done by replacing the two terms in Equation 5.2 with a sum over a series of fractions. For non-linear flows, it is not as simple as treating relaxations as a series of single exponentials and a constitutive equation of the form of the Rolie-Poly equation must be used to model the flow as a function of time. This requires a closer look at the tube theory of a bidisperse melt.

A test chain is constrained in tubes formed by both long and short chains. Short chains will relax faster than longer ones due to their shorter reptative contour length and higher relative frequency of chain ends. Longer chains will relax slower due to slower reptation and constraint release. The overall extension hardening and stress relaxation behaviour is thus governed by relaxation of the long chains. The mechanisms by which these long chains can relax are described by considering different tubes for each chain. Two tubes are described in Figure 5.1; A 'fat' tube made up of entanglements with long chains and a 'thin' tube made up of entanglements with both long and short chains.

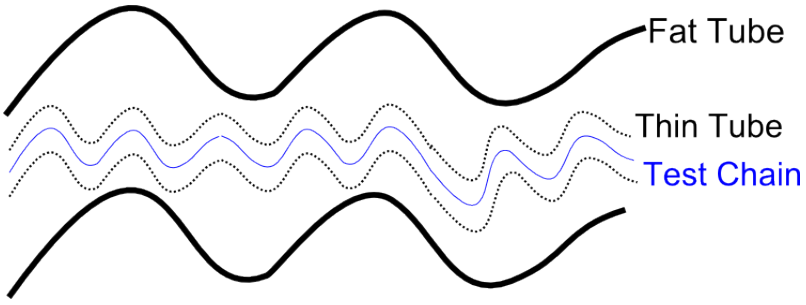

Figure 5.1: A diagram of the two tube model for a bidisperse melt

The test chain can relax via reptation along the thin tube but also via constraint release (CR) events of the thin tube. These CR events allow the thin tube to explore the fat tube and thus relax backbone stretch. The rate of stretch relaxation in the fat tube is

therefore dependent on how fast the thin tube can relax within the fat tube. This process will be slightly slower than the bare Rouse time for the long chain in the fat tube. In effect, dilution with short chains increases the diameter of the fat tube and increases the time taken for the long chains to fully explore the constraining fat tube. The relaxation times of a long chain are therefore increased by the presence of short chains. It can be shown [77] that the stretch relaxation time is increased according to

$$\tau_{R,l,\text{eff}} = \frac{\tau_{R,l}}{\phi_l} \tag{5.3}$$

The effective stretch time $\tau_{R,l,\text{eff}}$ is therefore increased by the addition of short chains. A small volume fraction of very long chains will have an effective stretch time which is very significantly increased above the equilibrium Rouse time. Which relaxation processes are important at a particular time is dependent upon the exact ratios of CR Rouse to reptative motion of the short chain as well as the relaxation time of the long chain.[78, 79] This is described schematically in the Viovy diagram (Figure 5.2).

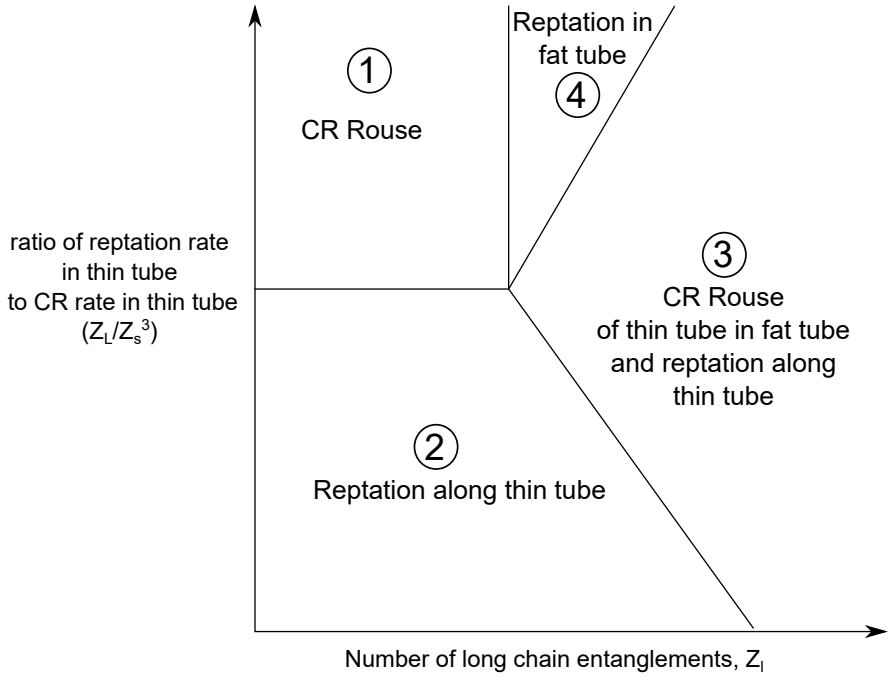

Figure 5.2: A Viovy diagram describing the relaxation processes available to a long chain in a blend of long and short chains.[78]

At the left hand side of the diagram long chains are effectively unentangled with each other and thus their terminal relaxation time depends upon which is slower, reptation along the thin tube (region 2 on the diagram) or constraint release of the thin tube

(region 1 on the diagram). If the long chains are entangled (on the right hand side of the diagram) then the terminal time depends upon whether reptation of long chains (4) or CR motion of the thin tube in the fat tube (3) is the limiting relaxation mechanism. Read *et al* [80] recently added multiple lines onto this graph depicting the effects of thin tube CLF motions upon relaxation in the fat tube and whether the Rouse or reptation motions are accelerated by dilution. In particular, region 3 is split into regions where CLF of the thin tube do not affect the fat tube (bottom right of the diagram) and regions where the fat tube is dilated and the resulting chain relaxation times are enhanced (centre and top right of the diagram). The bidisperse Rolie-Poly equations discussed in equation 2.2.3 do approximately contain the enhanced stretch relaxation time shown in Equation 5.3. The $\tau_{R,l}$ increase does not occur directly, rather as a consequence of the multiplication by ϕ in Equation 2.19. At small values of λ_l, i.e. $\lambda_l \ll 2$ the stretch time is effectively renormalised by ϕ_l. At higher values of λ the stretch time is not renormalised and takes its equilibrium value.

5.2 Characterisation

The polymer used here is labelled P627-S, which is its designation from Polymer-Source.[1] This sample was synthesised using living anionic polymerisation in THF at -78 °C. The GPC trace for P627S is shown in Figure 5.3. The monodisperse sample PS281 is shown

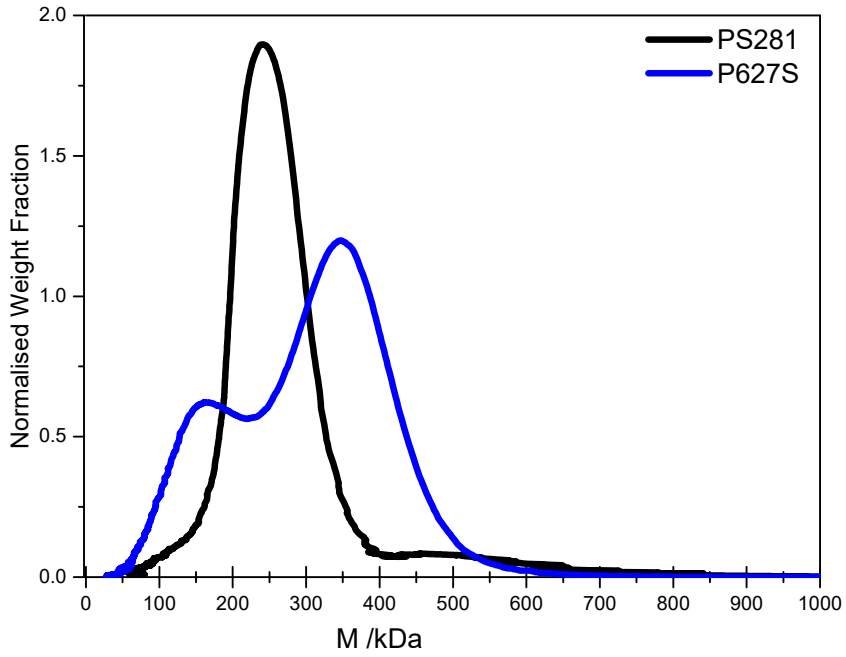

Figure 5.3: GPC data for the bidisperse sample P627-S alongside monodisperse PS281 for comparison.

to highlight the differences between the molecular weight distributions between the two samples. The M_w values are similar in each case and differences in the rheology will be mostly due to the effect of polydispersity. Two clear peaks are present in the GPC trace. The two peaks were fit to two distinct Gaussian peaks using the Origin 'fitpeaks' function This gives a weight fraction associated with each fraction as shown in Table 5.1.

Table 5.1: Molecular weight data for bidisperse P627-S

	M_n/kDa	M_w/kDa	Đ	ϕ
Lower Peak	140	160	1.15	0.37
Higher Peak	329	340	1.03	0.63
Average	198	252	1.27	1

[1]PolymerSource, Quebec, Canada

An initial attempt to simulate this polymer assumes the sample is made up of two separate, monodisperse peaks and uses linear theory to calculate a Rouse time for each molecular weight fraction. These fractions are given in Table 5.2.

Table 5.2: Rolie-Poly element data for bidisperse P627-S.

Molecular Weight/kDa	ϕ	τ_d /s	τ_R /s
160	0.37	0.926	0.0361
340	0.63	4.43	0.163

When normalising by these timescales in order to calculate W_R and W_d we assume that the longest relaxation time (340 kDa) is the most important one and thus use these timescales to calculate Weissenberg numbers.

The linear rheological response is modelled by a series of Maxwell modes for a monodisperse simulation in Figure 5.4.

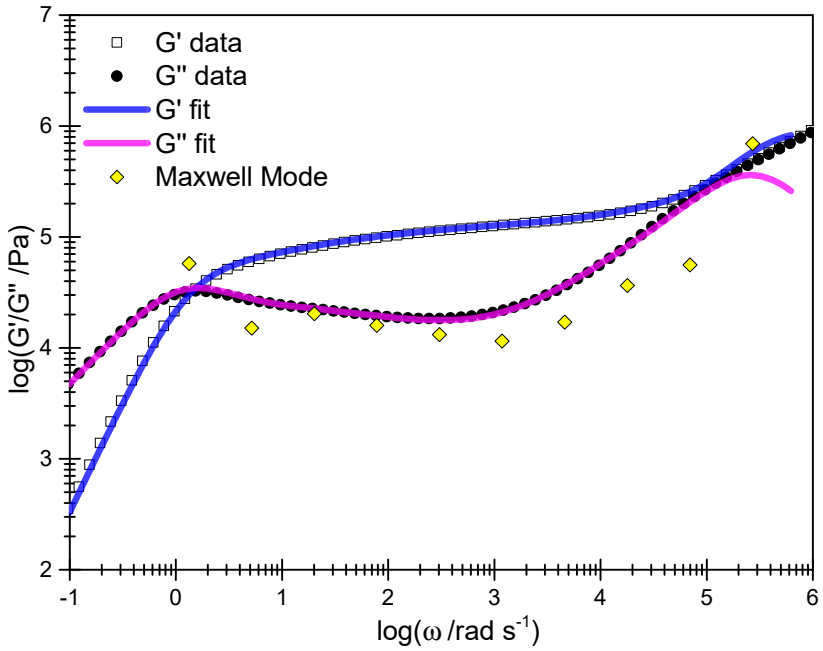

Figure 5.4: Linear rheological data (points) and Maxwell mode predictions (lines) for P627S. The Maxwell modes are shown as yellow diamonds.

The lowest frequency element is assigned the τ_d and $\tau_{R,l}$ from Table 5.2 for the monodisperse simulation. For a bidisperse simulation, consistent with the increased stretch time upon dilution discussed in [77], the higher weight element is diluted by the lower one,

increasing the Rouse time for the 340 kDa fraction in Table 5.2 from 0.163 s to 0.259 s using Equation 5.3. The increased $\tau_{R,l}$ is assigned to the highest Maxwell mode for the bidisperse simulation and the remaining Maxwell modes are a best fit to the linear data.

If we treat the blend P627-S as a purely bidisperse melt of 340 and 160 kDa chains as in Table 5.2 we would not expect stretch time enhancement of 340 kDa chains by dilution with 160 kDa chains according to the modified Viovy diagram in [80] as the two peaks are not significantly separated in molecular weight. However, Figure 5.3 shows that the sample is not two distinct peaks rather consists of two broad, polydisperse peaks. Stretch time enhancement is expected of the highest molecular weight chains and some of the intermediate chains by the very shortest chains. This will lead to a slight enhancement in the average stretch relaxation time of the whole melt.

5.3 Results from Experiments and Simulations

The results of maximum swelling ratios from MPR experiments are given alongside the predictions from Table 5.2 in Figure 5.5. This figure shows that treating the bidisperse blend as a monodisperse peak is not an acceptable way of modelling the extrudate swell. We see that experimentally at low W_R there is an increased swelling over that predicted from the monodisperse simulation, rather than a sharp increase at W_R=1. The hypothesis here is that this is due to the effect of the increased Rouse time with dilution. Figure 5.5 also contains a second set of predictions for extrudate swell using the increased Rouse time discussed in Section 5.2. This model gives a slightly better prediction at low W_R than using an uncorrected Rouse time, however still underestimates swelling, especially at W_R>1. The basic physics of an increased Rouse time is therefore qualitatively correct although work is needed for quantitative predictions.

Next, the use of the bidisperse theory from equations 2.21 and 2.20 is considered. The problem with using this theory is not constitutive, rather is *flowSolve* related. In a normal simulation with a spectrum of Maxwell modes a number of the fastest modes are used provide a solvent viscosity. In the bidisperse case we cannot do this (as there are only two modes) and therefore a solvent viscosity must be otherwise defined. A first guess at this comes from the full Maxwell mode fit in Figure 5.4. The solvent viscosity is calculated via

$$\sum_{i=1}^{lastfast} G_i \tau_i$$

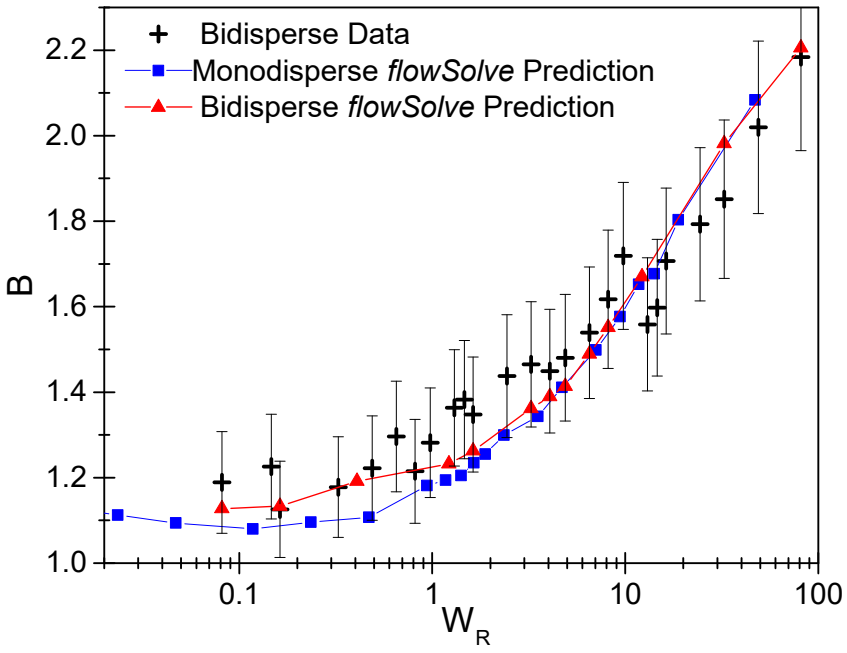

Figure 5.5: MPR data and *flowSolve* predictions for P627S at 180 °C. Results are shown from simulations using a single stretching element (monodisperse) and a single stretching element with an increased Rouse time (bidisperse).

where $lastfast$ in this case is 7, corresponding to the seven highest frequency modes of Figure 5.4. At a v_{inp} of 1 mm s^{-1} the solvent viscosity is 5100 Pa·s. If we change the viscosity input even slightly from this value then we see a significant shift in the swelling ratios observed. If the viscosity is too high then the simulations will fail to run and if the viscosity is too low then swelling will decrease significantly. In order to remove viscosity as a free parameter and instead calculate it during the simulations *flowSolve* is run in a conventional multimode fashion by using the full polydisperse theory. In this theory, the shortest chains can be effectively treated as solvent to the longer chains and thus a solvent viscosity can be defined by summing over these chains. The M_w distribution in Figure 5.3 is discretised and converted into the series of Rouse and reptation times shown in Table 5.3. The results for this model versus the SER extensional data are shown in Fig 5.6.

The SER data correctly predicts the onset of extension hardening for for P627S, which seems promising for the prediction of low W_R extrudate swell. If swelling first occurs at the onset of chain stretch within the extruder then correctly predicting the onset of extension hardening due to chain stretch should give good predictions for the onset of swelling. The *flowSolve* predictions for P627S are given in Figure 5.7.

Table 5.3: Discretised molecular weight distribution and associated Rolie-Poly timescales for P627S.

Element Index	Molecular Weight /kDa	ϕ	τ_d /s	τ_R /s
1	75	0.0195	0.00935	0.00795
2	107	0.0621	0.0348	0.0162
3	147	0.127	0.112	0.0304
3	183	0.081	0.250	0.0472
4	208	0.0549	0.398	0.0611
6	234	0.0684	0.600	0.0770
7	267	0.0676	0.959	0.100
8	323	0.146	1.87	0.148
9	401	0.216	3.90	0.227
10	479	0.121	7.12	0.324
11	563	0.0318	12.1	0.448
12	675	0.00618	22.0	0.643

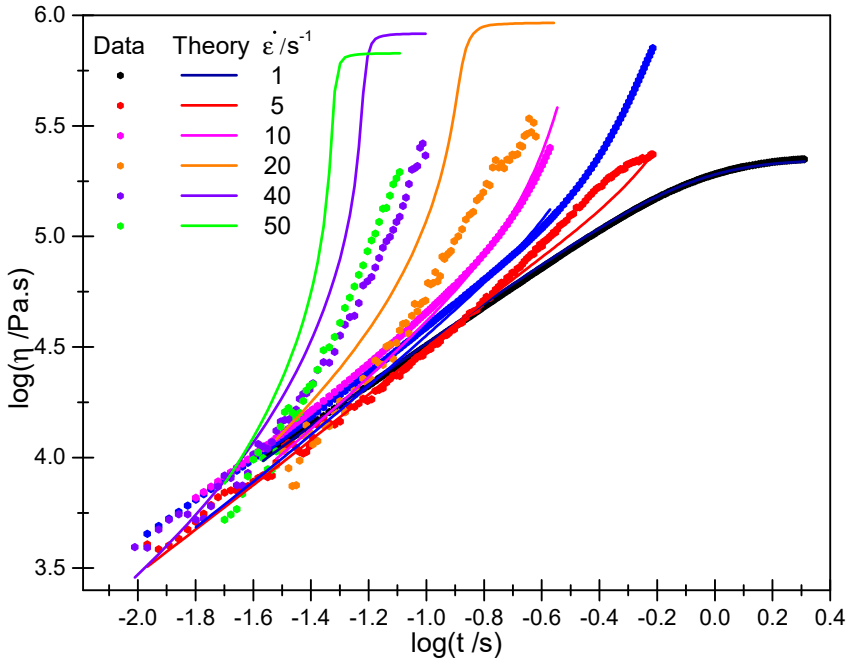

Figure 5.6: SER extensional data (points) and predictions of the Rolie-Double-Poly blends theory (lines) at 180 °C for P627-S.

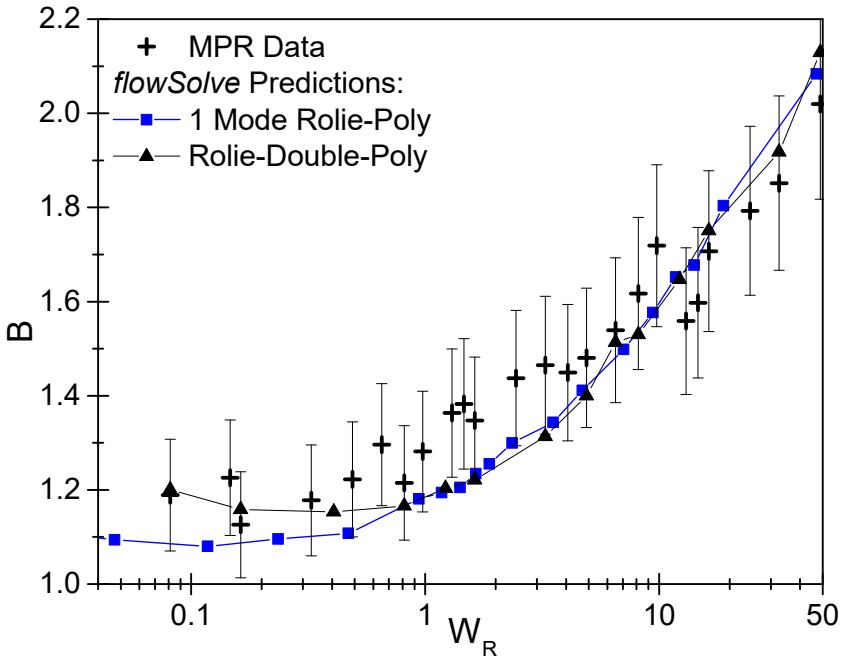

Figure 5.7: RDP predictions for P627-S using the data from Table 5.3 alongside MPR extrusion data.

The polydisperse prediction fits almost perfectly to the monodisperse prediction, except at the lowest Weissenberg numbers where the swelling plateaus above the Newtonian value of 1.1 and then increases with decreasing W_R. Although these predictions are slightly better than the monodisperse case, they are worse than the results coming from increasing the Rouse time by the weight fraction as in Figure 5.5. This may be because the increased Rouse time from the polydisperse model only occurs at low chain stretch values. If we consider the extrusion at $W_R \approx 1$ the chain stretch in elements 11 and 12 is over 2.5. This is over the criterion for Rouse time reduction of $\lambda < 2$ discussed in Section 2.2.3. The stretch values along the extruder for different elements are shown in Figure 5.8. The polydisperse model does account for the significant stretching of high molecular weight chains at even intermediate Weissenberg numbers, however this does not translate to the increased swelling ratios observed in the MPR. This may be due to the lack of an effective Rouse time increase for the highest modes or to inadequate weighting of these higher molecular weight elements towards the stress.

To help distinguish between these effects, Figure 5.9 shows the stretch in the high molecular weight peak for the three theories. This figure shows that the increased Rouse time gives a greatly increased steady state wall stretch, accounting for the increased swelling ratios. However, the polydisperse model has a much lower steady state stretch

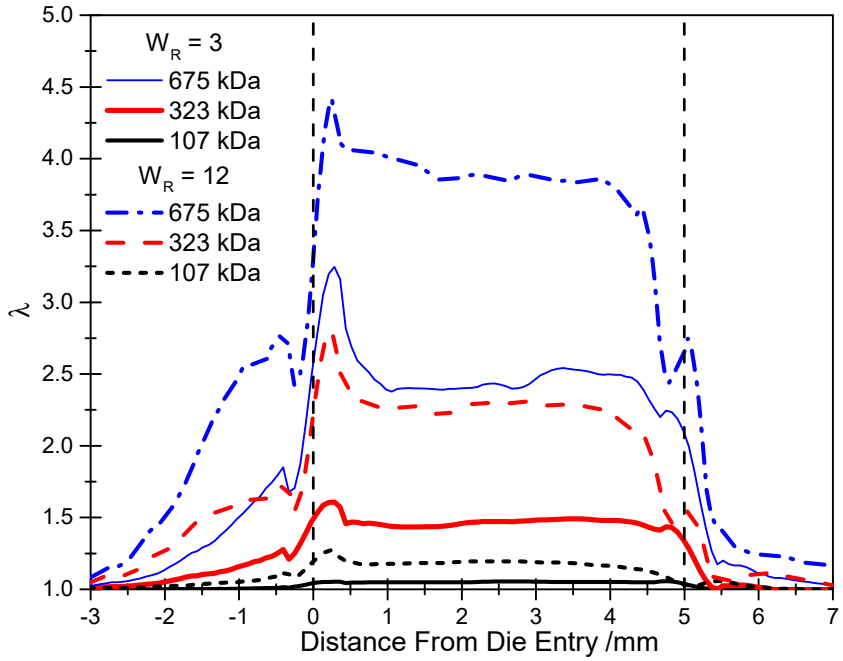

Figure 5.8: Chain stretch values across the MPR extruder for $W_R = 3$(—) and 12(- - -) for the elements in Table 5.2.

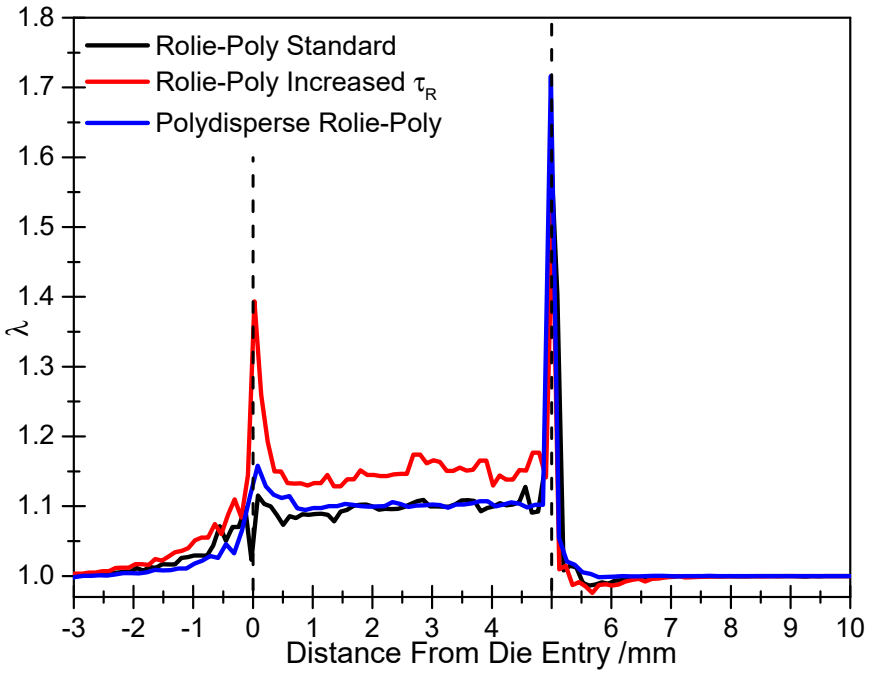

Figure 5.9: Chain Stretch values along the extruder at $W_R = 0.4$ for the single stretching mode in the monodisperse Rolie-Poly equation with and without stretch time increase as well as the stretch in element 9 of the Rolie Double Poly prediction.

than this, with almost no change compared to the monodisperse case. Therefore, although high molecular weight fractions are significantly stretched, causing some swelling, the unchanged stretch of the fraction with the largest weighting means that the effect of the polydisperse model on extrudate swell predictions is small.

5.4 Concluding Remarks

In conclusion, even a slightly polydisperse system like a bidisperse polymer shows significantly different swelling ratios than the monodisperse case. Considering dilution of the high molecular weight chains in a blend is important for predicting the low Weissenberg number extrudate swelling of such a sample, which is significantly increased from the monodisperse case. Increasing the Rouse time of the diluted high molecular weight chains gives an improved prediction of swelling ratios but use of the Rolie-Double-Poly equation set does not give a significant improvement here. This is due to the increase in effective Rouse time occurring only at low chain stretch values, thus only increasing extrudate swell at the lowest Weissenberg numbers. At higher chain stretch values, Rouse times are not increased and thus the extrudate swell values are not significantly different from the monodisperse case.

Chapter 6

Polydisperse Polymers

6.1 Previous work

Various authors have investigated the effect of polydispersity on extrudate swell. This is generally due to the ease of obtaining such materials cheaply and in large quantities. Graessley *et al* [81] considered extrudate swell as a function of shear stress for high and low dispersity polystyrenes. They found that narrow dispersity polymers begin to exhibit swelling at a much higher shear stress (flow speed) than broad dispersity samples and that at a given dispersity the swelling ratios increased significantly as a function of molecular weight. They did find that, at low shear rates, all polymers exhibit the same Newtonian plateau of 1.1 in B. Similarly, in [82] it was found that polypropylene with a broad MWD has a greatly increased extrudate swell especially at high deformation rates. Later studies have found that using a single dispersity value is a poor way of predicting whether a sample will have a high extrudate swell value. For example, in [83] the higher moments of the distribution $M_z = \frac{N(M)M^3}{N(M)M^2}$ and M_{z+1} were used to compare different samples. The justification for doing this was that this moment more accurately captured the effect of the high molecular weight tail on the extrudate swell. These higher moments were converted into an overall polydispersity parameter, P_J where $P_J = \frac{M_z}{M_w}\left(\frac{M_{z+1}}{M_z}\right)^2$. There was an increase in swelling with increased P_J but no such simple dependence upon M_w. In [83] a decrease in swelling at the highest molecular weight was observed but attributed to a decrease in P_J. It was found in [84] that extrudate swell does not necessarily increase with M_w and that simple measures for polydispersity do not adequately predict the trends in extrudate swell. Mendelson *et al* [84] showed that the highest molecular weight fractions in a polydisperse melt greatly influence the extrudate swell, and hypothesised that these

fractions alter the ability of lower molecular weight fractions to contribute to the overall stress.

In this chapter the dependence of extrudate swell on molecular weight and molecular weight distribution is investigated by extending the chain-stretch based approaches used for monodisperse systems. To start with, some mildly polydisperse systems are analysed using *flowSolve*, MPR and capillary rheometrical approaches to characterise the swelling behaviour of these samples. Finally, some significantly polydisperse polyethylenes are tested to determine the influence of molecular weight distribution and in particular high molecular weight fractions on the swelling ratio. Much of the work in Section 6.2 is published in Journal of Rheology as [85].

6.2 Moderately Polydisperse Commercial Polystyrenes

6.2.1 Characterisation

Two polymers are used here, both obtained from Sigma-Aldrich. They are labelled PS350 (Aldrich product code: 441147/MKBS6136V) and PS192 (Aldrich product code 430102/MKCD4385) and described in Table 6.1 and Fig 6.1.

Table 6.1: Summary Molecular Weight and average timescale data at 180°C for Aldrich Polystyrenes.

Sample Code	M_w /kDa	M_n /kDa	Đ	τ_d /s	τ_R /s
PS350	349	116	3.01	5.59	0.170
PS192	192	100	1.92	0.37	0.030

As usual, TTS master curves can be obtained for the samples as shown in Fig 6.2.

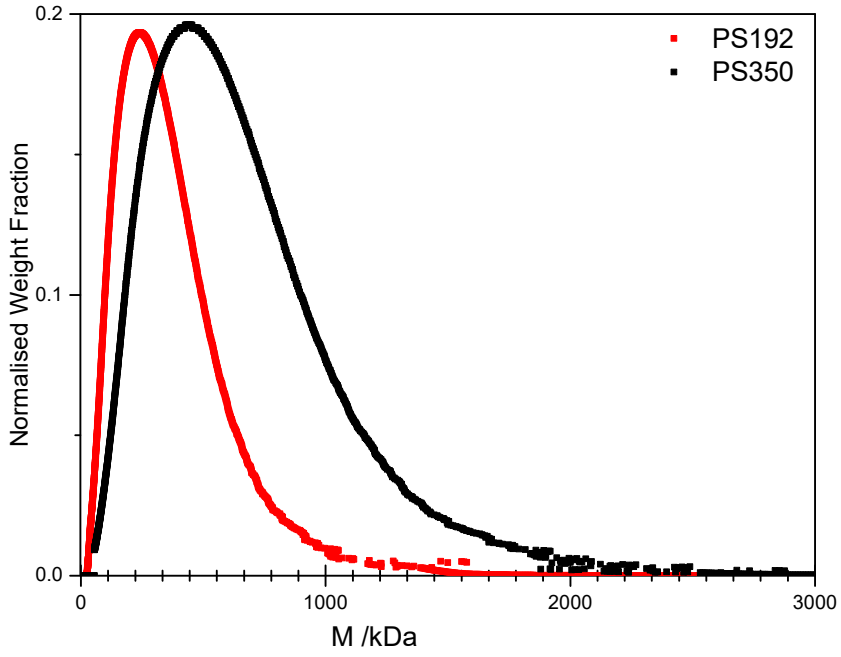

Figure 6.1: GPC Data for Aldrich Polystyrenes

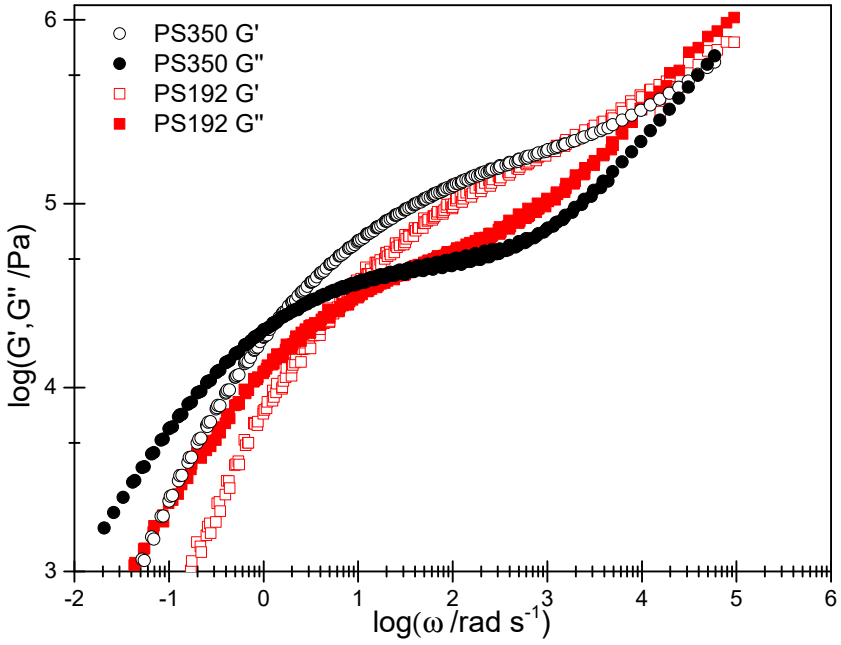

Figure 6.2: Linear rheological data for PS350 and PS192 at 180 °C.

Neither of these polymers fit well to a monodisperse Likhtman-McLeish model, which is to be expected as they contain a wide variety of relaxation times which are not taken account for within the single mode theory. It is convenient for normalising the data to obtain an average Rouse time for the melt, therefore the M_e and τ_e are used from the monodisperse data in Chapter 4 and thus τ_d and τ_R are calculated for a monodisperse melt with the same M_w as the polydisperse sample. These are shown in Table 6.1.

Using the single monodisperse Rouse time and a spectrum of Maxwell modes as previously shown for monodisperse polymers in Figure 4.4 gives uniaxial extensional viscosity predictions shown as unbroken lines in Figure 6.3.

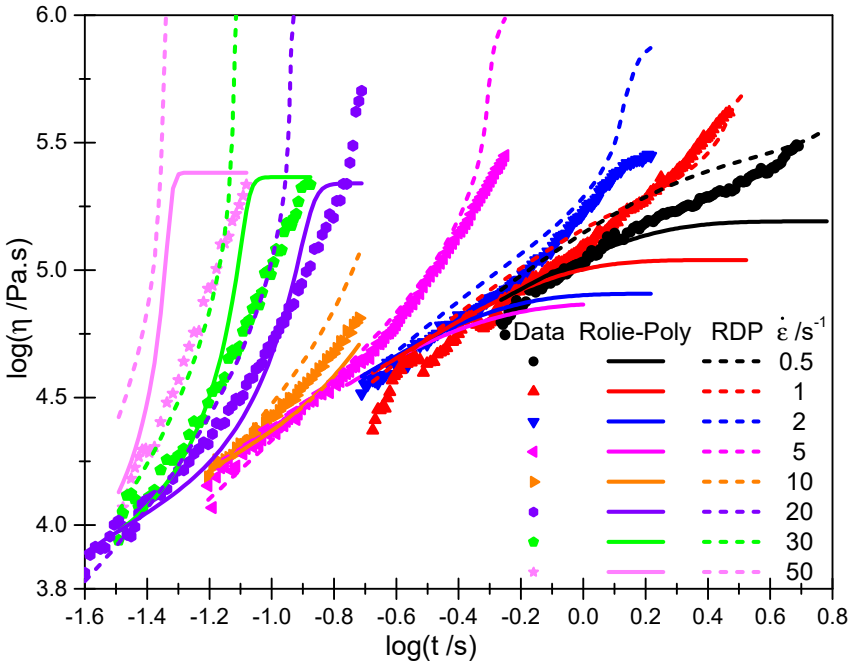

Figure 6.3: SER extensional rheometry data (points), single mode Rolie-Poly predictions (—) and RDP Predictions (- - -) for PS350 at 180 °C.

Strain hardening is predicted by Rolie-Poly for the highest shear rates but the onset of strain hardening at approximately 1-2 s^{-1} observed is not at all predicted using standard Rolie-Poly. This could be due to the stretch time enhancement observed in the previous chapter or due to stretching of higher molecular weight chains not yet accounted for. To obtain better predictions the method from Section 2.2.4 and Figure 3.8 described by Boudara was used to describe a spectrum of relaxation times.[40] The Rolie-Poly element data are shown in Table 6.2.

A first test of these Rolie-Poly elements is how well the uniaxial extensional predictions

Table 6.2: Rolie-Double-Poly element data for PS350 and PS192 at 180 °C.

Element	PS350				PS192			
	M_w /kDa	ϕ	τ_d /s	τ_R /s	M_w /kDa	ϕ	τ_d /s	τ_R /s
1	63	0.0166	0.0119	0.00414	40	0.0212	0.000590	0.00117
2	100	0.0573	0.188	0.0104	62	0.0536	0.00246	0.00284
3	158	0.122	0.219	0.0261	97	0.124	0.0125	0.00689
4	251	0.216	1.14	0.0656	155	0.241	0.0709	0.0176
5	398	0.270	5.59	0.165	242	0.244	0.349	0.0431
6	631	0.203	25.4	0.414	359	0.183	1.36	0.0946
7	1000	0.0890	112	1.04	522	0.106	4.76	0.200
8	1580	0.0244	478	2.61	789	0.0254	18.2	0.457
9	2510	0.00271	1880	6.56	1200	0.00298	70.3	1.06
10	3980	5.48×10^{-5}	8440	16.5	1830	7.50×10^{-5}	254	2.45

fit SER data. Uniaxial extensional predictions using these elements are shown as the dashed lines in Figure 6.3. The RDP model correctly predicts the onset of strain hardening at 1 s^{-1}. Above this point, the predictions correctly predict the level of strain hardening at first but then significantly over-predict the extensional viscosities at the highest strains. Above ∼10 s^{-1} the model increasingly over-predicts the extensional viscosities even at the lowest strains. The correct prediction for the onset of strain hardening show promise for prediction of extrudate swell at low shear rates as swelling is a chain stretch driven phenomenon. At higher rates it may be expected from the SER data that the extrudate swell is over-predicted and a modification such as friction reduction will once again be required.

6.2.2 Extrusion Through a Slit Geometry

The initial experiments performed within the MPR used the pre-existing slit geometries. The geometry shown in Figure 6.4 is used to extrude through. As previously, the upper chamber is filled with polymer and the lower chamber is empty. The entire apparatus is heated to 180 °C. Two examples of extrusion using this setup are shown in Figure 6.5.

The advantage to this method over using a capillary is that it is possible to visualise the flow within the channel. In Figure 6.5 a) several stress fringes can be observed within the channel as well as a significant tightening of the fringes around the die entry singularity, indicating an increase in stress at this point. There is some distortion of the fringes at the extruder exit points, showing some increase in stress here although the resolution of the

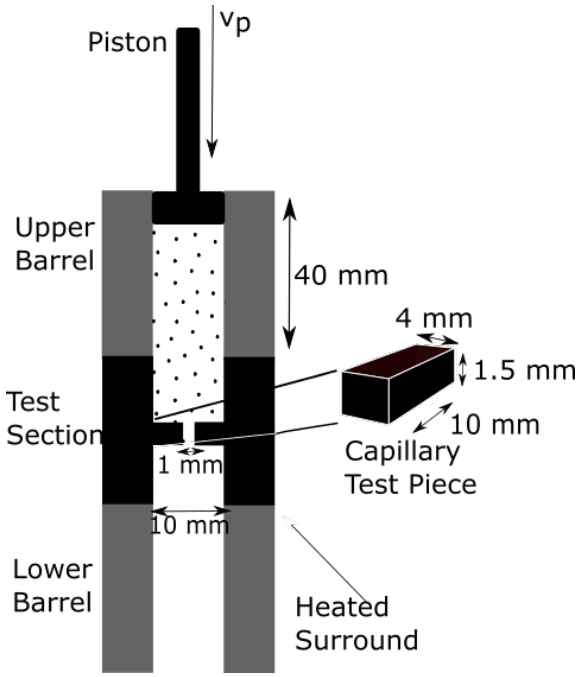

Figure 6.4: A schematic diagram of the MPR slit test section

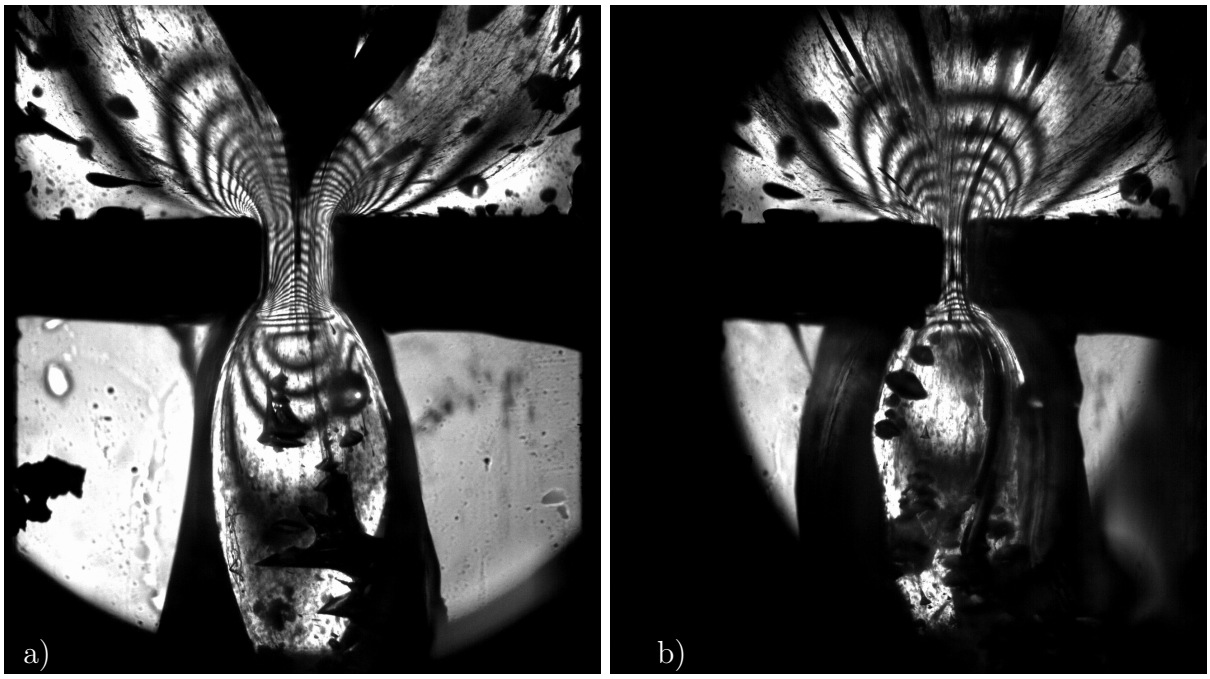

Figure 6.5: Extrudate swell profile within the MPR slit section at a) v_p =0.1 mm s^{-1} and b) 1 mm s^{-1} respectively.

image is too low to work out what form this takes. The disadvantage of this method is that the magnitude of the extrudate swell is almost impossible to measure accurately. In Figure 6.5 b) there are two regions below the extruder: There is a bright field image where the polymer has emerged from the extruder in a full 10 mm deep strip. This allows the polarised light to pass through. There is also a dark field region where the polymer has stuck to the quartz windows at either the front or the back and thus does not allow the light to pass through. These two regions make it difficult to decide unambiguously where the edges of the extrudate are and thus make accurately obtaining a B value difficult. A second problem is that the extrudate is constrained by the quartz windows and is not free to swell equally in all directions. Although swelling can occur parallel to the windows it cannot occur perpendicular to (through) them and the results obtained do not accurately match the simulated geometry which assumes no constraints in any direction. The polymer can also stick to the windows and slowly expand outwards to coat them, both obscuring the viewable area and pulling the extruded polymer out of the free-flowing shape.

By measuring the diameter of the bright field region it is still possible to obtain results for swelling ratios for PS350 in a planar contraction, as shown in Figure 6.6. The data points obtained are shown alongside the *flowSolve* predictions using a planar geometry.

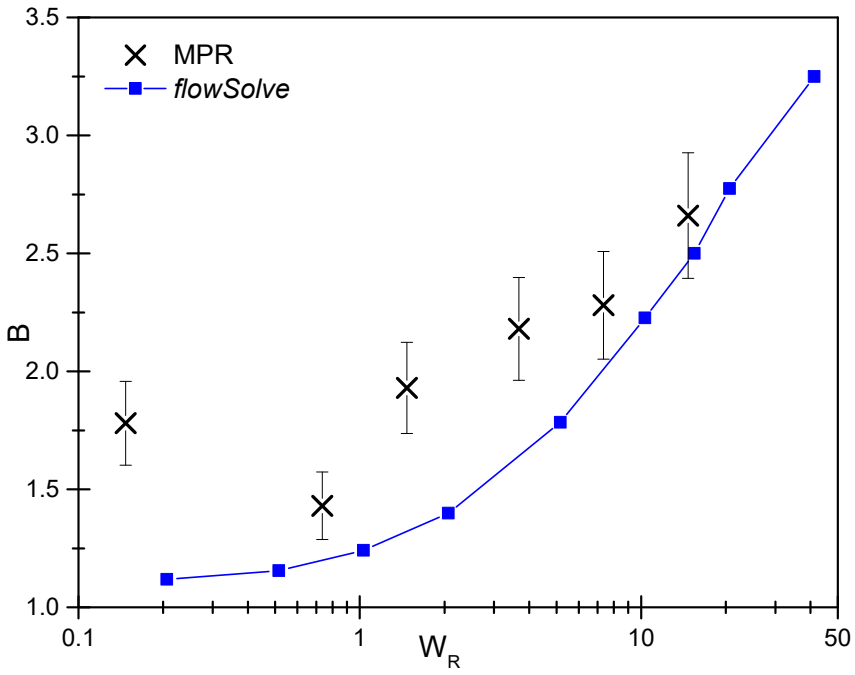

Figure 6.6: Predicted swelling ratios and experimental results for planar extrusion of PS350 at 180 °C. W_R is calculated using the Rouse time from Table 6.1

The MPR data show a general increase above W_R=1 although the values of 1.5-2.5 obtained are far higher than expected for polystyrene. There is a very large increase in apparent extrudate swell at low shear, which is due to the extrudate sticking to the glass windows and spreading out along them for the long time periods possible during slow flow speeds. This geometry is not used any further. If a slit die is required this could be machined in a similar way to the capillary die where the polymer does not touch the glass windows.

6.2.3 Extrusion Through a Capillary Die

Here, the 5:2 capillary described in Section 3.1.4 is used once more. Results from the MPR in this geometry for PS350 are shown in Figure 6.7.

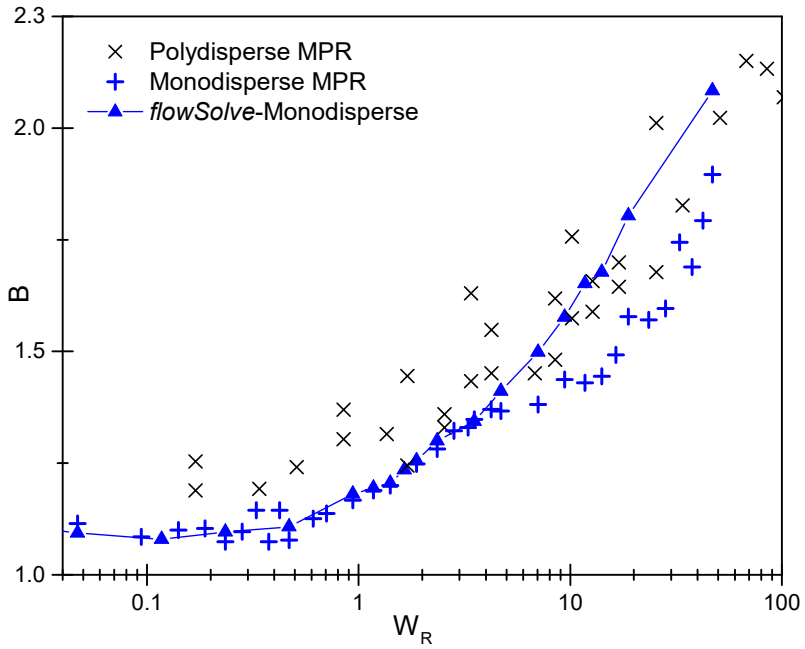

Figure 6.7: Polydisperse MPR measurements for PS350 alongside the MPR measurements for monodisperse PS281. Monodisperse *flowSolve* predictions using the parameters from Table 6.1 for PS350 are given as a line and symbol plot.

The polydisperse polymer has a much higher extrudate swell than the monodisperse one, even when normalised by Rouse time and plotted against Weissenberg number. This is due to the polydispersity of the sample. Table 6.2 shows that 31.8% of PS350 has a Rouse relaxation time higher than the monodisperse value of 0.17 from Table 6.1. Combined with the effective increase in stretch time of these elements upon dilution, the high molecular

weight chains are significantly stretched even when W_R is below 1. This chain stretch causes extrudate swell at lower rates than expected using a simple monodisperse prediction.

A better way of predicting extrudate swell is by using the full Rolie-Double-Poly (RDP) model. (Equation 2.24 and [41]) These results are shown in Figure 6.8. Without

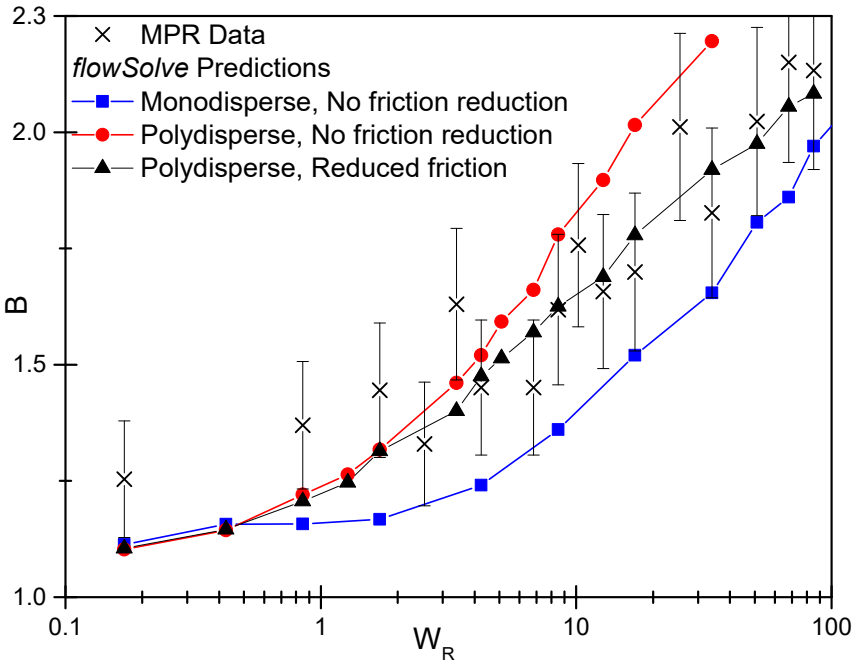

Figure 6.8: Polydisperse Rolie-Poly predictions for PS350 both with and without reduction of monomeric friction compared to the MPR extrusion data at 180 °C.

monomeric friction reduction the predictions correctly predict the onset point of swelling, and give reasonable predictions at low W_R. However, at high W_R the predicted swelling ratios are higher than the observed values. In this work this difference is attributed to the reduction in monomeric friction at high deformation rates used in Section 4.4. Including monomeric friction reduction with S_c=0.05 and ζ_{min}=0.5 gives very good predictions up to the limits of the MPR for this sample at $W_R \approx 100$. Comparisons of the extrudate profile between theory and experiment are shown in Figure 6.9. The profiles appear consistent within the viewing window. For the higher rate it is more difficult to compare as the predicted point of maximum diameter is further away from the die exit. The extrudate contained within the viewable area matches the theory predictions well. The RDP and friction reduction models have not been used previously in these kinds of simulations but nevertheless produce good predictions for extrudate swell.

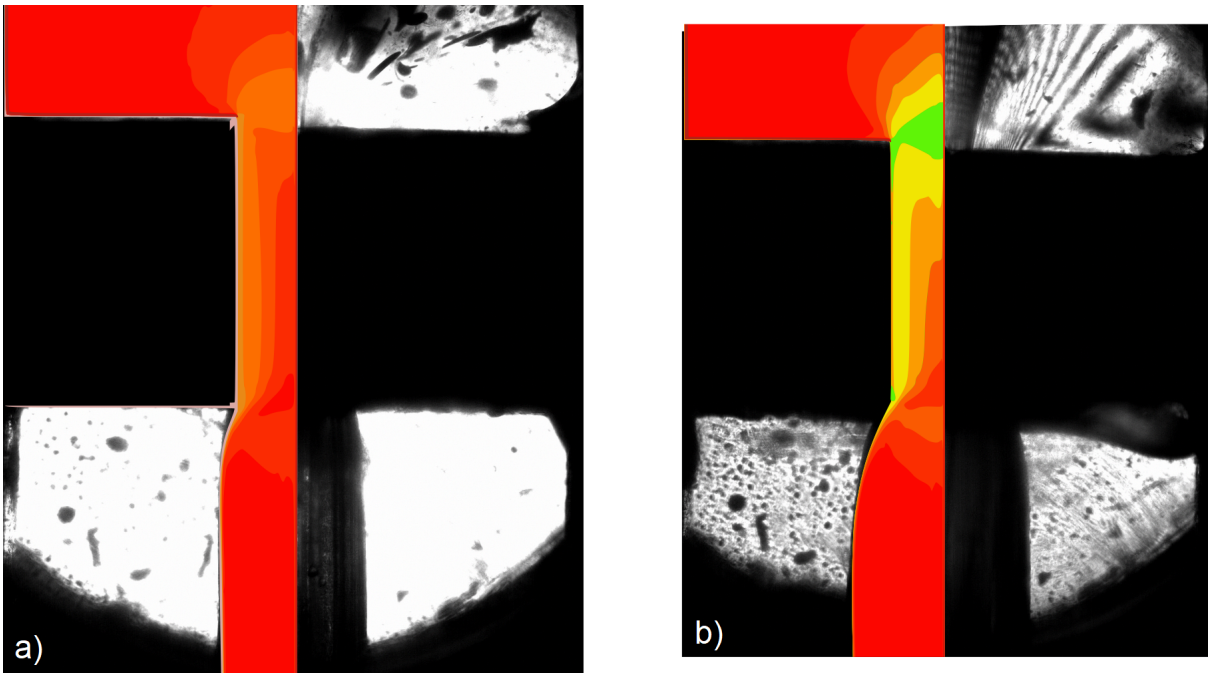

Figure 6.9: *flowSolve* and MPR extrusion profiles for extrusion experiments of PS350 at a) W_R=1.7 and b) 17.

If the stretching in the single stretching element of the one mode simulation of PS350 is compared to the roughly equivalent element (element 5) of the polydisperse simulation (Figure 6.10) it can be seen that the chain stretch at the die wall is slightly higher for the monodisperse simulation. There is no additional stretch or stretch time enhancement for these 398 kDa chains, in fact the dilution results in a reduced overall stretch. The additional swelling observed is therefore due to additional stretching of high molecular weight chains rather than enhancement of the stretch time of lower M_w chains.

Data for PS192 are compared with PS350 in Figure 6.11. These data are limited to lower W_R due to the lower range of accessible piston speeds of the MPR. The slightly lower viscosity of PS192 and the higher piston speed result in increased leakage around the test section and a lower maximum W_R. This effectively limits the maximum piston speed of the MPR. The data for PS192 match up well with those from PS350, meaning that the universality with molecular weight for monodisperse polymers still holds for mildly polydisperse systems of comparable molecular weight distributions. The polydisperse predictions also match up well for this molecular weight. There is a slight overestimation at higher shear rates, although this is within experimental error.

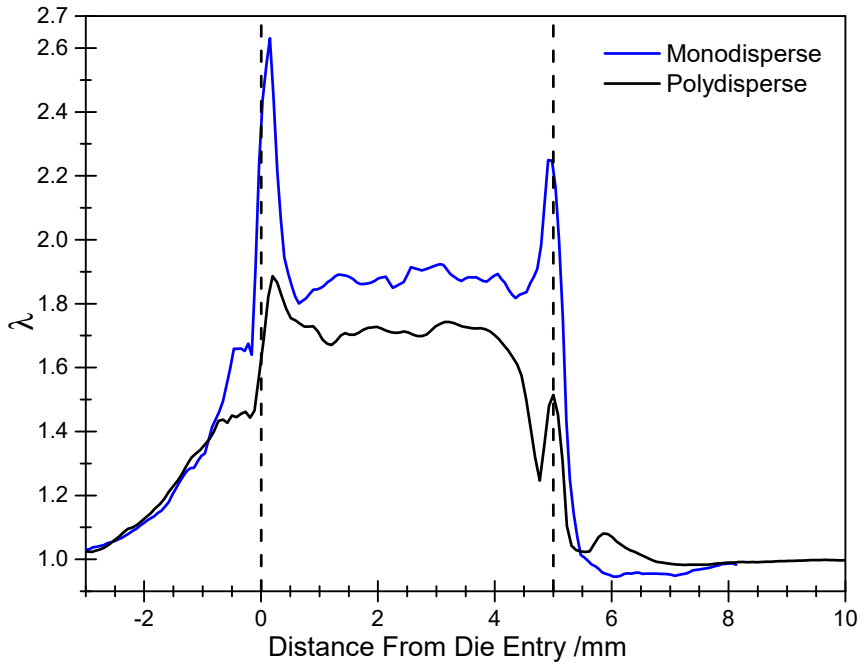

Figure 6.10: Chain stretch at the die wall of the single stretching element in the monodisperse simulations and element 5 in the polydisperse simulations of PS350 at W_R=4.

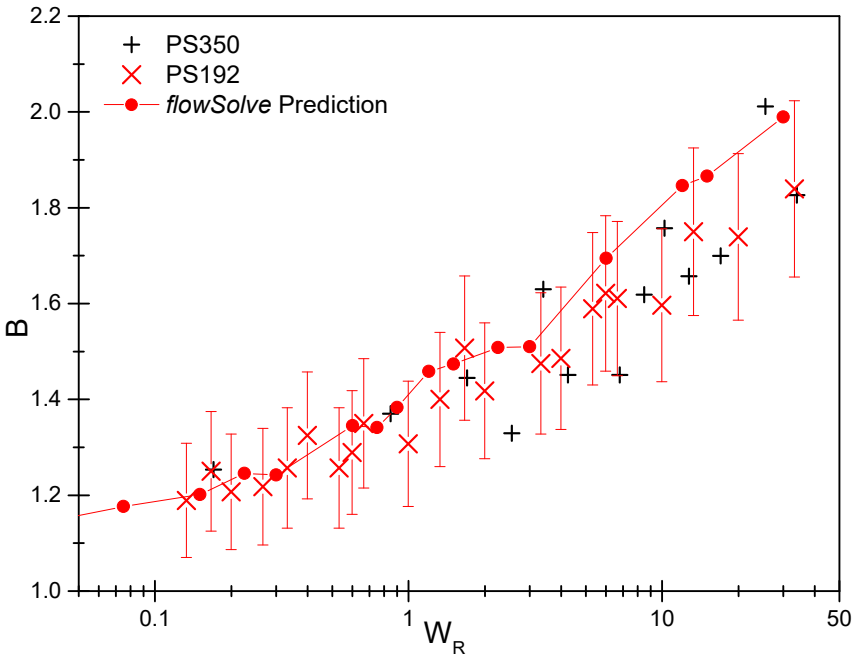

Figure 6.11: Experimental Data and *flowSolve* predictions for PS192 including friction reduction as well as experimental data for PS350.

6.2.4 Comparison to Previous Theory

Similarly to the monodisperse sample in Section 4.3.2, the simulated and experimental data are compared to the predictions of Equation 2.2 in Figure 6.12.

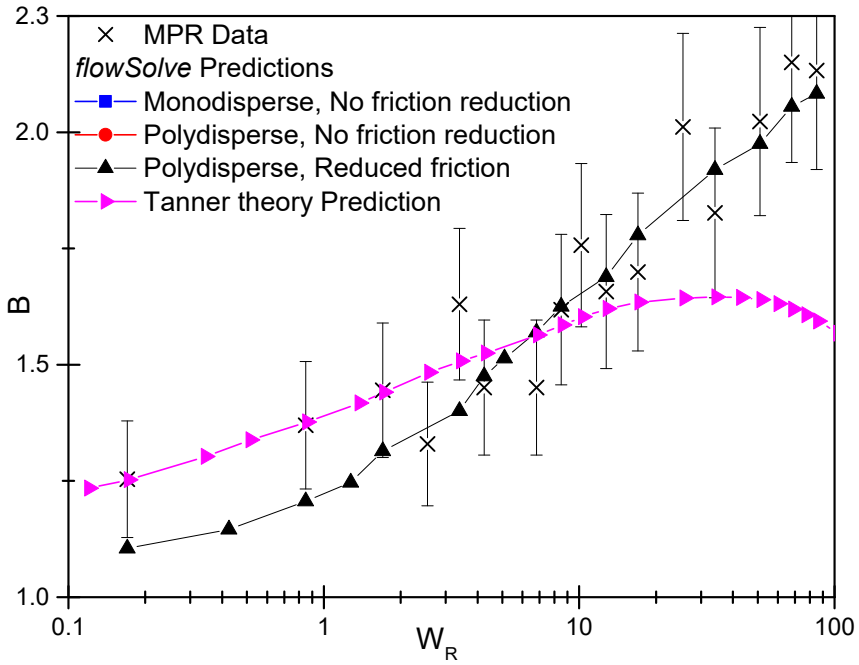

Figure 6.12: Comparison of the predictions of Equation 2.2 to the MPR extrusion data and *flowSolve* predictions of PS350.

Conversely to the monodisperse case, the increased swelling of these samples at low shear is correctly predicted by the Tanner theory, and a good agreement with experimental data is seen up to $W_R \approx 10$. Above this point, the first normal stress difference reaches a maximum and extrudate swell is under-predicted.

From these results it is easy to see why this equation and descriptions of extrudate swell in terms of normal stress differences are so commonly used. Good predictions for extrudate swell are seen over a wide range of shear rates with almost no understanding of the underlying molecular physics. An understanding of the physics is still needed for predicting extrudate swell at high shear rates where the normal stress approach fails.

6.3 Capillary Rheometry Measurements

Thus far all experiments have been performed isothermally within the MPR. The disadvantage of the bright field measurements obtainable here is that it is difficult to visualise any turbulence or elastic instabilities in the flow and it is impossible to visualise the flow after it has travelled more than 5 mm downstream. Both as a check of the MPR swelling ratios and as a way of studying swelling over a larger distance a capillary rheometer is now used for measurements of extrudate swell. This can only be performed on the polydisperse polymers due to the large amount required for a test. An extrusion test uses approximately 500 g of polymer, which is more than the sum weight of all the monodisperse polymers used in the previous chapters.

6.3.1 Experimental

The equipment used was a Rosand RH7 capillary rheometer at Intertek, Wilton, UK.[1] A 1 mm diameter, 20 mm length extruder was used. Shear rates were calculated as for the MPR albeit with a Rabinowitsch correction applied to account for the non-Newtonian nature of the material. This uses a plot of log flow rate vs shear stress to calculate a correction factor n for the polymer. Video images of the extrudate were acquired for all speeds using a standard digital camera. B values were obtained by measuring the diameter of the extrudate with a set of calipers once cooled. Multiple measurements were taken along the length of the extrudate and an average value taken to obtain a B value. For the MPR measurements, each extrusion was performed individually, whereas for the capillary measurements all shear rates were done in a continuous experiment consisting of discrete shear rates. Pressure readings were obtained from a transducer in the top chamber and the extrusion continued until steady state pressure was achieved. After this point the shear rate was increased. At the highest rates steady state would not be reached before the pressure limit in the upper chamber was reached and thus the experiment terminated. After each shear rate run completed the extrudate was cut at the die exit so as to eliminate the effect of gravity. The conditions used are shown in Table 6.3.

Some additional measurements were performed on a Rosand RH2000 capillary rheometer with a 24:1.5 capillary but also an orifice (0.25:1.5) die. The measurements were performed by Carl Reynolds at the University of Stellenbosch. This system is fitted with a laser micrometer to measure the swelling ratios over time as the polymer emerges

[1] Further information can be found at http://www.intertek.com/analytical-laboratories/wilton/ (accessed 20/11/18)

Table 6.3: Experimental conditions used for capillary extrusion of PS350. Successful runs are marked with a y. The conditions which cause an over-pressure failure are marked with an 'f'. Speeds greater than this cannot be run.

$\dot{\gamma}$/ s^{-1}	30	60	150	300	600	1500	3000	6000	15000
220 °C	y	y	y	y	y	y	y	y	f
190 °C	y	y	y	y	y	y	y	y	f
175 °C	y	y	y	y	y	f			
160 °C	y	y	y	y	f				

from the die. In this case the B value is taken as the diameter achieved at steady state, similarly to the definition used for the simulations.

The idea of a shear viscosity map as a way of describing a polymer processing experiment is introduced here.[2] Once the linear rheology is fitted using a set of Maxwell modes, $\eta^*(\omega)$ can be obtained for the polymer using Equation 3.10. Assuming the Cox-Merz rule applies [86] and $\eta^*(\omega) = \eta(\dot{\gamma})$ the viscosity response as a function of shear rate is obtained. Using the pre-defined WLF parameters the viscosity is shifted to obtain $\eta(\dot{\gamma})(T)$. The resulting contour plots are shown in Figure 6.13 for PS350 and B.2 in the Appendix for PS192. Included on the plot are the inverse Rouse and reptation times and the positions of the experimental conditions used. It is not generally possible to process the polystyrenes above τ_e, therefore few points exist to the right of the blue τ_e curve on Figure 6.13. The runs that are performed in this region are turbulent and generally cause a high pressure trip on the rheometer.

6.3.2 Results

To verify that the Cox-Merz rule indeed applies for these polymers a graph of viscosity vs deformation rate is included for the Aldrich polymers in Figure 6.14. The viscosities from shear and oscillatory measurements match up well and the trends with increasing shear rate are the same as those with increasing frequency. The Cox-Merz rule can be stated to apply for these systems.

[2]We acknowledge Dr Ian Robinson for the idea of presenting the data in this way and for linking the processing behaviours to the parameters on the shear map.

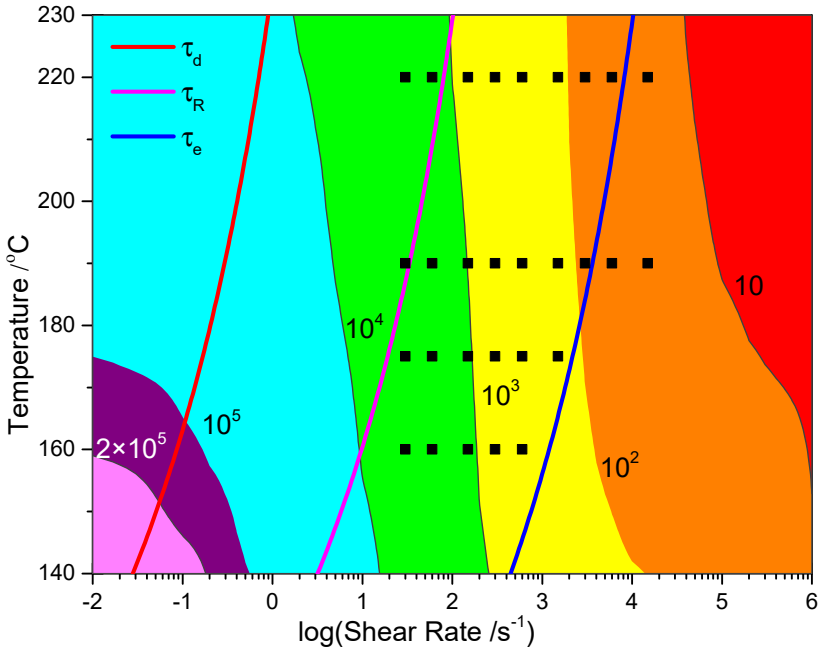

Figure 6.13: Shear viscosity vs shear rate and temperature for PS350. The contours are labelled with viscosity in units of Pa.s

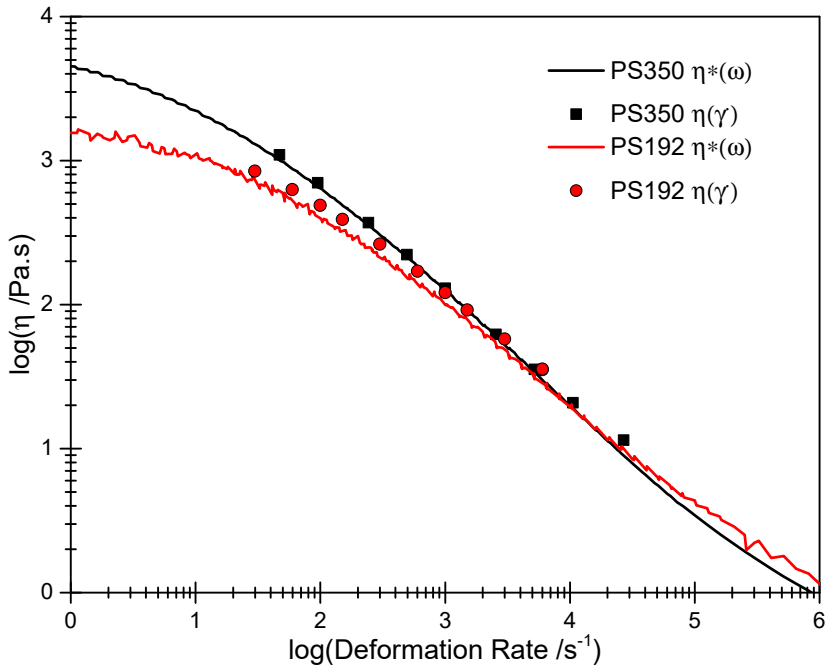

Figure 6.14: Plot of complex viscosity vs angular frequency (lines) from the rheometer and shear viscosity vs wall shear rate (points) from the capillary rheometer. All data is shifted to 220 °C.

The results from the temperature ramp for PS350 and PS192 are shown in Figure 6.15. a) shows the decrease in extrudate swell with increasing temperature at constant

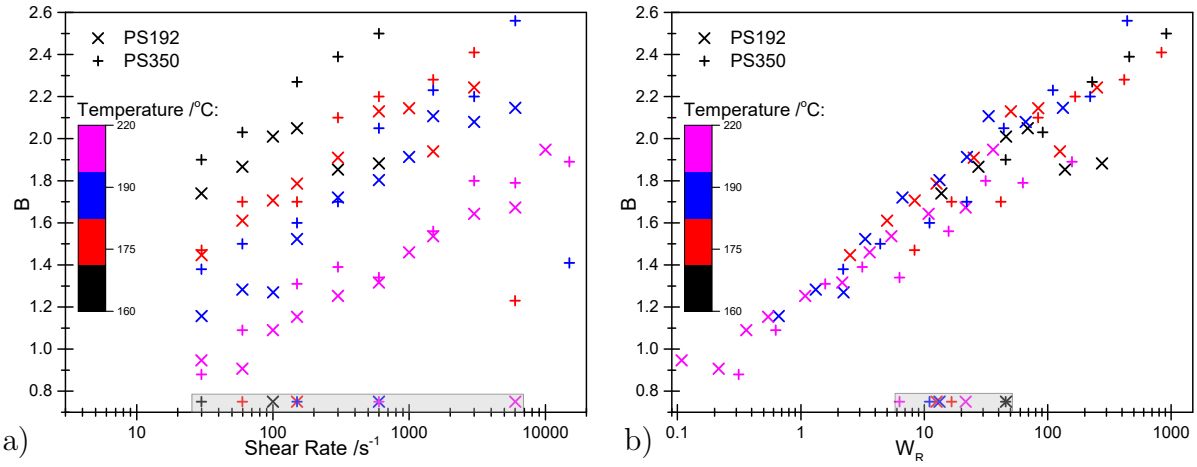

Figure 6.15: Extrudate swell data for PS192 and PS350 at the 4 capillary extrusion temperatures. a) shows raw data versus shear rate and b) shows data vs Rouse Weissenberg number. The symbols in the grey box indicate the speed at which the flow becomes unsteady for each set of conditions.

shear rate. This is to be expected as the relaxation times of the material decrease with increasing temperature. As for the monodisperse case, the higher molecular weight sample has the higher extrudate swell. This effect is minimal, partially due to polydispersity smoothing out the differences and partially due to the relative similarity in molecular weight compared to the monodisperse case. At the highest shear rates the swelling ratios fall significantly where gross melt fracture has occurred. b) shows the superposition versus Rouse Weissenberg number. This reinforces the ability to not only shift extrudate swell by molecular weight, but also TTS shift it, even during non-isothermal extrusion. To compare these data to results from the MPR, a matching MPR capillary geometry is used. An exactly matching capillary is not available but the 5:1 capillary provides the same capillary diameter. The only differences may possibly arise at the highest speeds where entry stress has not relaxed by the end of the 5 mm capillary but would have relaxed by the end of a 20 mm capillary. It is possible to simulate the 20:1 capillary in *flowSolve*, therefore the simulation results can be additionally shown in Figure 6.16.

The MPR data shows two main differences to the capillary rheometry measurements:

1. The capillary rheometry gives swelling ratios below 1, i.e. contraction out of the die whereas the MPR measurements level off at 1.1. This is due to the effect of

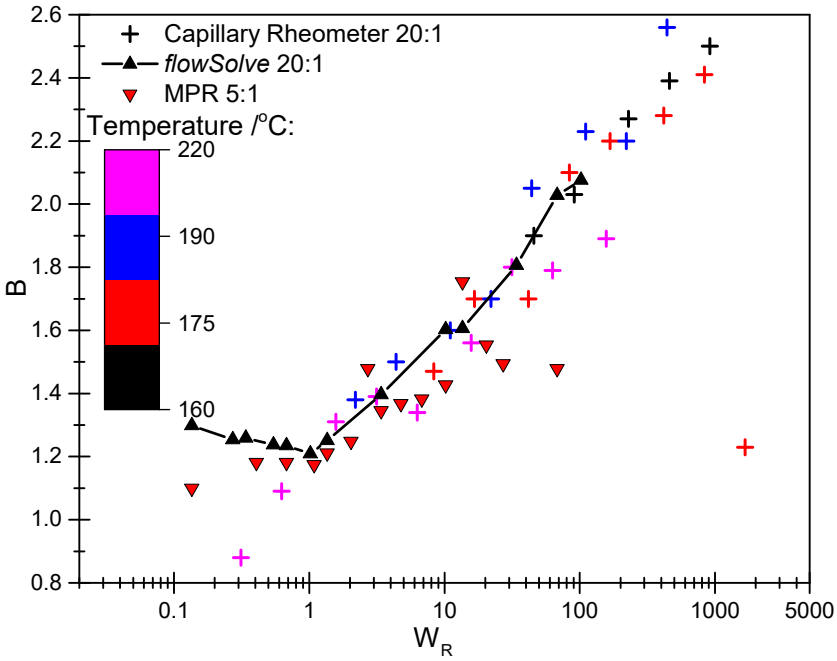

Figure 6.16: Comparison of data obtained from capillary rheometer measurements, MPR measurements and *flowSolve* simulations for Aldrich PS350.

gravity on the extrudate. The extrudate could extend almost a metre below the die exit, compared to the MPR where it could extend centimetres below the die exit. As a large weight of extrudate is suspended from a 1 mm diameter capillary, the extrudate thins at the die exit.

2. The MPR B values start to plateau or drop off at high shear much earlier than the capillary measurements. This is due to the significant leakage out of the MPR at the highest rates. For the narrow capillary the pressure on the capillary is high enough that the polymer starts to preferentially leak around the edges of the test section. This makes achieving the desired shear rate difficult. It may also result in the MPR data not having reached steady state flow before the viewing window is obscured by polymer.

The *flowSolve* B values roughly match the capillary measurements up to $W_R \sim 10$. Above this point the B values from the MPR start to plateau whereas those from capillary rheometry do not. These results are an encouraging sign that the results obtained from the MPR (at least at low to medium Weissenberg numbers) in previous chapters are reliable, as swelling ratios from the MPR can be reproduced with a different machine and geometry. These results can be compared to those taken on the RH2000 capillary

rheometer.[3] Results from the capillary die are consistent with the previous capillary measurements using a narrower capillary. The orifice die has a diameter of 1.5 mm but a length of 0.25 mm meaning that wall shear is almost irrelevant and the stress state at the exit comes mainly from the stress built up at the die entry. Results for this orifice die and the longer 16:1 contraction are shown in Figure 6.17 in which the orifice die gives a significantly increased extrudate swell compared to the capillary.

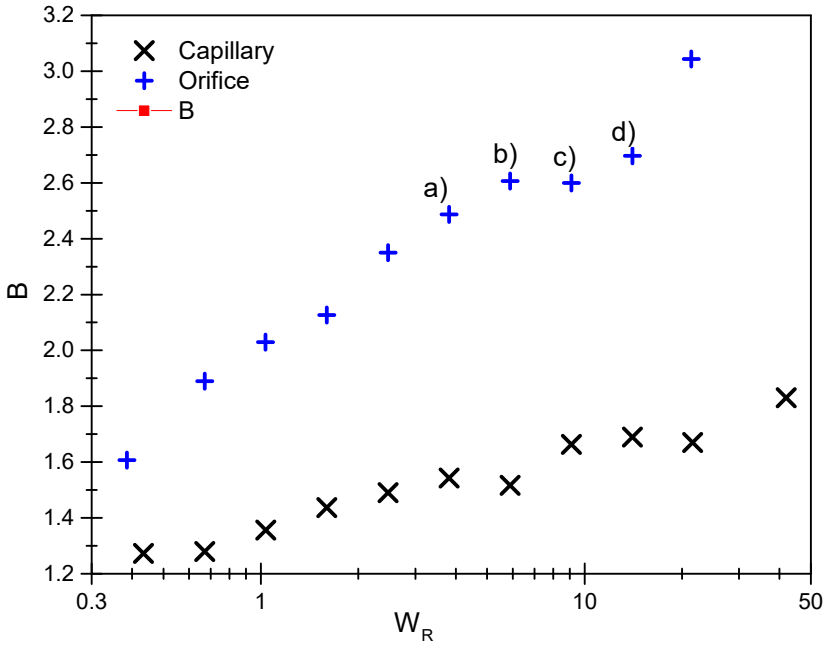

Figure 6.17: Capillary rheology results at 170 °C for PS350 using a 16:1 capillary and a 1:6 orifice die. The letters refer to the extrudate images in Figure 6.18.

At low shear rates the extrudate swell is increased by ∼0.2, increasing to over 1.4 by the highest rates. This difference is approximately the contribution to extrudate swell from the entry effects only.

6.3.3 Extrusion Instabilities in Capillary Rheometry

Thus far it has been assumed that the extrudate is a cylindrical column and once a steady state has been reached this column remains roughly constant in time. In this section the instabilities that occur at high rates are considered. The advantage of using the capillary rheometer for this analysis are twofold:

[3]These experiments were performed by Carl Reynolds at the University of Stellenbosch

1. The length of extrudate which can be observed is much longer. Several centimetres can be seen below the capillary die exit whereas only 5 mm can be seen below the MPR die exit.

2. The maximum length of an extrusion run is greater. For unsteady flows the bottom chamber of the MPR can become filled with polymer and/or the view through the windows can become obscured. In capillary rheometry this is not a problem and the evolution of the instabilities with time can be observed.

Two types of instability are seen: Shark-skinning and melt fracture. Shark-skinning is the formation of small waves on the extrudate surface, where the flow is steady but the surface of the extrudate is no longer smooth. This is shown in Figure 6.18 b).

At speeds above this point, the extrudate no longer leaves the die steadily as in Figure 6.19 a), rather oscillating from side-to-side during extrusion.(Figure 6.19 b)) As speed increases, the extrudate wrinkles and shrivels up (Figure 6.19 c)), with the magnitude of oscillations on the extrudate surface approaching the extrudate radius. This has occurred by Figure 6.18 d). We define the onset of instability as the point at which the extrudate has become shark-skinned. This is the limit of practical processability. The boxed points at the bottom of Figure 6.15, above, show the point at which instabilities occur for PS192 and PS350. There is no superposition at all versus shear rate, with instabilities occurring over two orders of magnitude. Superposition is better versus W_R, where instabilities occur around $W_R \approx 10$ but there is still a large spread in the data. Partially this could be due to the few, discrete data points used. Given the large difference between points, an instability could occur very close to a low shear rate point and not be detected until a much higher shear rate. The values are therefore only a rough indicator of where instabilities occur. We can say that the safe limit for processability of these samples is $W_R \approx 1$. Above this point there is an increasing likelihood of shark-skinning, and by $W_R \approx 10$ the sample will almost certainly show an instability. Crucially, looking at the shear viscosity map in Figure 6.13, the onset point of turbulence does not correspond to a constant shear viscosity. If stable flow is required at a high flow rate the temperature must be increased so as to ensure $W_R < 1$. This results in a decrease in the shear viscosity which may cause other problems in processing. A balance must be struck between speed and viscosity requirements whilst ensuring no turbulence occurs.

The results from the orifice die show that the onset of unstable flow is not dependent on the die length. At W_R=5.9 in Figure 6.18 the flow becomes unsteady. This occurs at the same flow speed in the 16:1 (24:1.5) capillary die and is approximately the same as

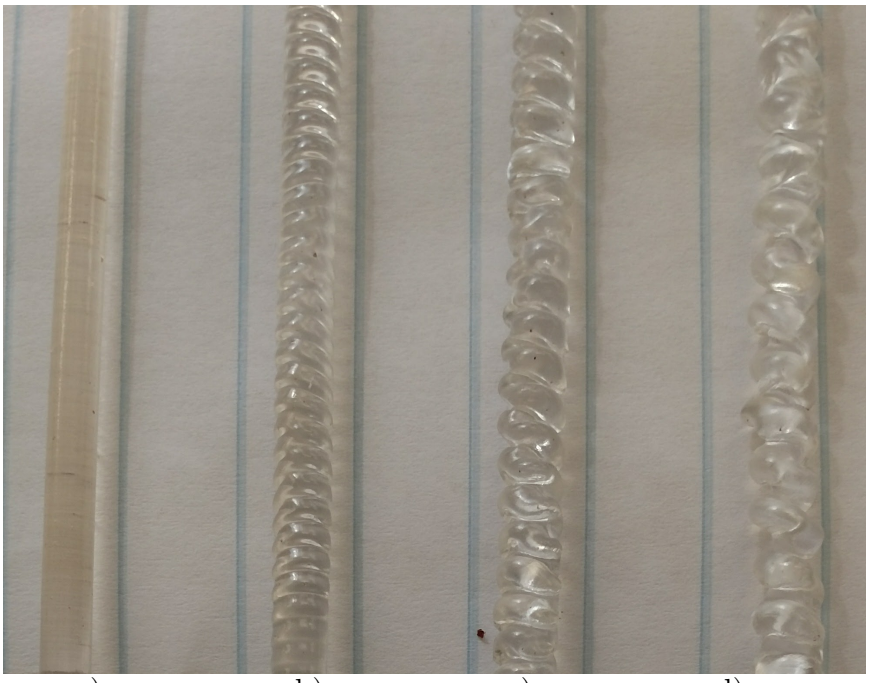

a) b) c) d)

Figure 6.18: Images of the extrudate from capillary rheometry measurements using the orifice die at the University of Stellenbosch. The shear rate increases left to right and the runs a)-d) are labelled on Figure 6.17.

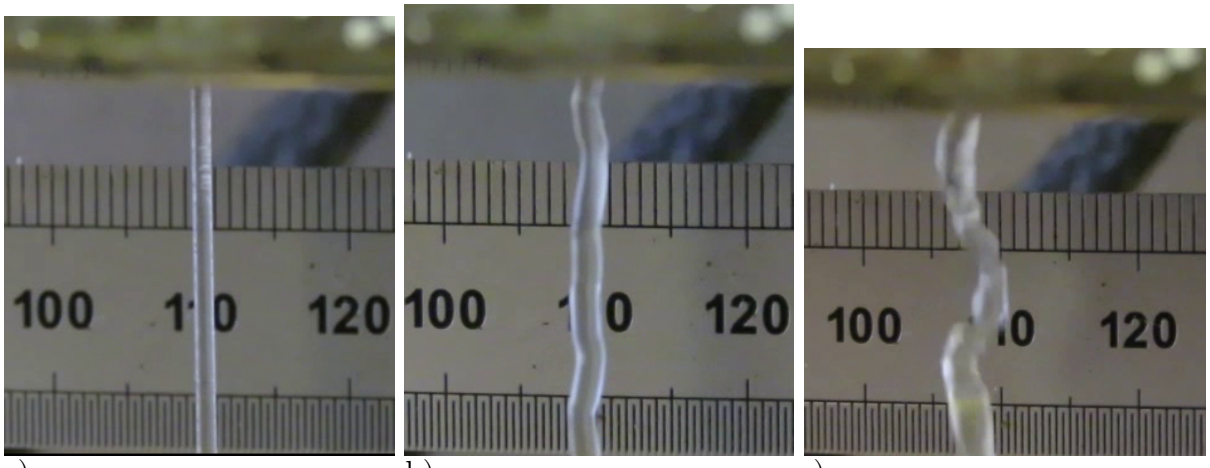

a) b) c)

Figure 6.19: Images of the extrudate during a capillary rheometry measurement for PS350 at 175 °C. Shear rates are a) 30 s^{-1}, b) 60 $s^{-1}$and c) 3000 s^{-1}.

the onset of turbulence in the 20:1 capillary for PS350. This indicates that the cause of turbulence is not shear at the capillary wall, as there is none present in the orifice die. If turbulence is caused by a die entry effect it does not differ as the die length increases, the instability instead travelling as part of the steady state flow within the capillary. The other option is that this is a die exit effect, being caused by the increase in orientation/stretch at the die exit corner. A hypothesis is that this is due to the chain stretch at the edge of the extrudate. Figure 6.20 shows that most of the significant stretch within the die relaxes immediately at the exit corner, causing swelling.

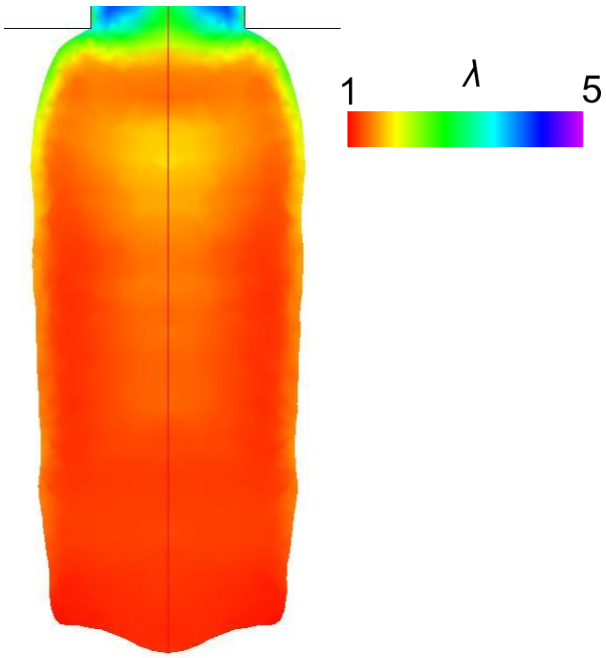

Figure 6.20: Simulated chain stretch after the die exit in element 6 for PS350 is a 20:1 capillary geometry at W_R=15.

A significant portion at the edge of the extrudate remains stretched for a long way below the die exit. This chain stretch may relax and cause the edge of the extrudate to deform. A few such small deformations can be seen in Figure 6.20. The temperature gradient along the extrudate during capillary extrusion may cause differences in relaxation rates along the extrudate, exacerbating the issue. Further study is needed to examine if this is indeed the cause of extrudate instabilities. In particular, these *flowSolve* simulations do not capture flow instabilities, so study is needed to see if this can be included. One issue which must be overcome is the cylindrical symmetry within *flowSolve*. This symmetry does not allow for asymmetric changes in the directions of flow such as those seem in practical extrusion.

flowSolve therefore cannot capture the full complexity of a 3 dimensional flow.

6.4 Highly Polydisperse Polyethylenes

In order to test the Rolie-Double-Poly model rigorously some more complex systems than these Aldrich polymers must be used, namely very polydisperse systems. In this section, several highly polydisperse polyethylenes are analysed and extrudate swell simulated.

6.4.1 Characterisation

DOW Chemical has provided a series of five polydisperse polyethylenes with broad molecular weight distributions, as shown in Figure 6.21 and Table 6.4:

Table 6.4: Molecular weight distribution parameters from GPC for the 5 DOW samples.

Sample	M_n /kDa	M_w/kDa	Đ
DOW-A	14	228	16.5
DOW-B	12	126	10.5
DOW-C	13	197	15.3
DOW-D	10	221	21.8
DOW-E	12	176	14.6

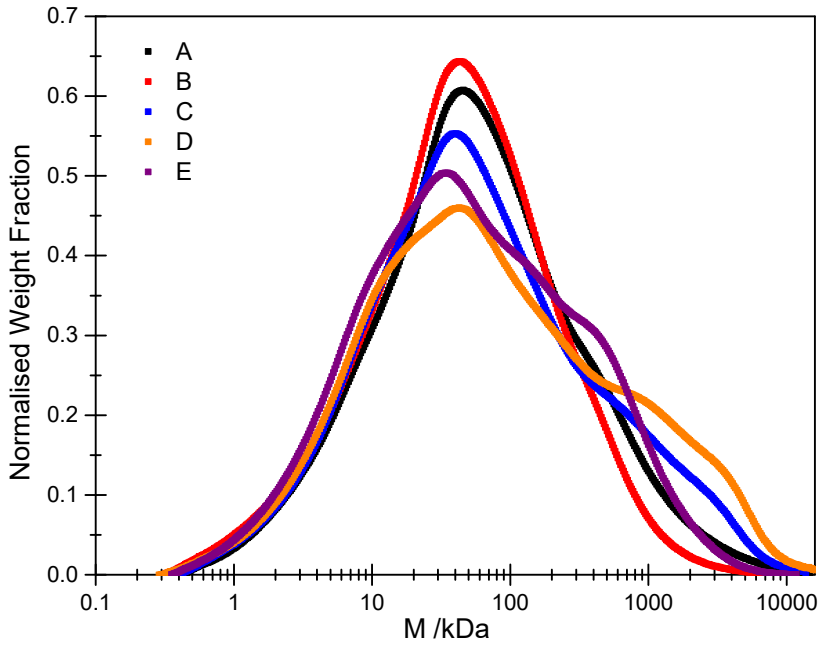

Figure 6.21: GPC data for polydisperse DOW Polyethylenes A, B, C, D and E. The colours are the same as in Table 6.4.

These samples are quite significantly more polydisperse than the Aldrich samples discussed previously and many do not have symmetric molecular weight distributions. In particular, DOW-D and E have large 'bumps' in the distribution at high M. Industrially, extrudate swell decreases A to E. As usual for *flowSolve* simulations, the distribution is discretised into 12 bins and converted into a series of Rouse and reptation times. For the most polydisperse samples more bins would be ideal, but internal memory limitations within *flowSolve* make having more than 12 Rolie-Poly elements difficult especially within the polydisperse theory. It is not now as simple as taking a value of τ_e from the linear rheology. The HR2 rheometer can obtain frequencies of order 10^3 rad s^{-1} but the entanglement time of polyethylene is of order 10^8-10^9 rad s^{-1} [87] and therefore the data obtained cannot come close to the correct frequency. In addition, polyethylene has a very weak temperature dependence upon viscosity so TTS cannot be used to any great effect here. Low temperatures cannot be used as TTS is not valid at, or close to, the melting temperature. We therefore perform frequency sweeps at 140, 150 and 160 °C and from 0.1 to 600 rad s^{-1} then TTS shift to 150 °C. These sweeps are shown in Figure 6.22.

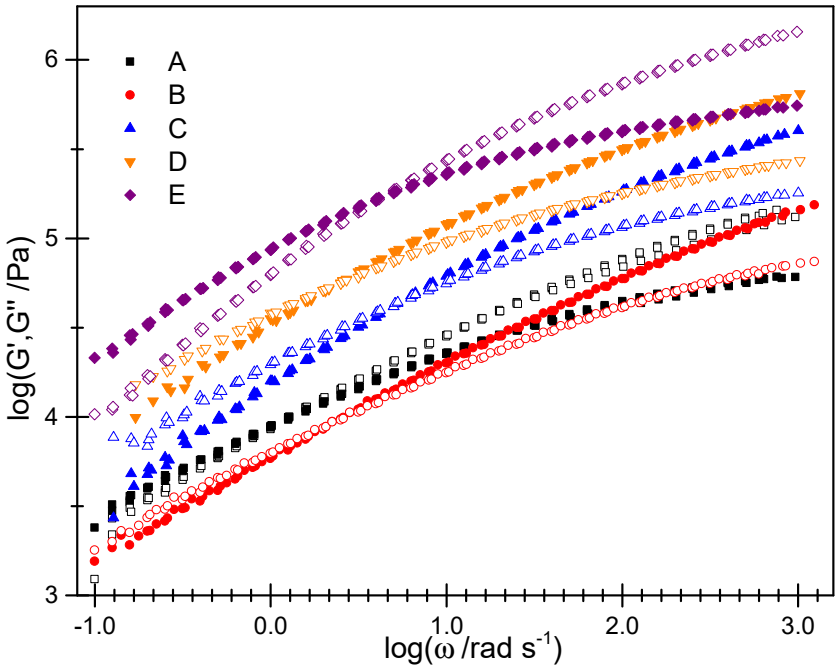

Figure 6.22: Linear rheological data for DOW A-E. G' are open symbols and G'' are closed symbols. Moduli are shifted vertically by 0.25 log units per file to aid viewing.

The moduli for the samples are very similar, although DOW-B has a lower modulus than the other samples by approximately 10 kPa. The crossover times are very similar for all 5 samples with no systematic change observed between along the series. The rheology was then fitted using the double reptation theory within RepTate to obtain an estimate for τ_e, M_e and G_e for each sample. The parameters obtained for DOW-A are shown in Table 6.5 and parameters for the other samples are shown in Appendix D.

In practice, elements 1 and 2 in Table 6.5 have timescales far too short to be resolved by *flowSolve* for any tractable *timestep* and are ignored. For systems this polydisperse it is not correct to normalise by the peak relaxation time. The average reptation and Rouse relaxation times from Equation 6.1 are used to calculate Weissenberg numbers.

$$\overline{\tau} = \sum_{i=1}^{n} \tau_i \phi_i \tag{6.1}$$

The resulting average relaxation times are shown in Table 6.6.

Table 6.5: Rolie-Double-Poly element data for DOW-A.

Element	M_w /kDa	ϕ	τ_d /s	τ_R /s
1	3	0.0380	3.78×10^{-8}	7.03×10^{-8}
2	6	0.0720	4.85×10^{-7}	3.06×10^{-7}
3	13	0.114	7.38×10^{-6}	1.34×10^{-6}
4	27	0.170	9.85×10^{-5}	5.95×10^{-5}
5	56	0.196	0.00108	2.50×10^{-5}
6	116	0.158	0.0113	0.000108
7	243	0.109	0.114	0.000470
8	509	0.0748	1.13	0.00207
9	1.06×10^3	0.0404	10.7	0.00892
10	2.22×10^3	0.0186	101	0.0392
11	4.62×10^3	0.00742	924	0.17
12	8.68×10^3	0.00151	6310	0.600

Table 6.6: Average relaxation times for DOW A-E at 150 °C.

Sample	$\overline{\tau_d}$ /s	$\overline{\tau_R}$ /s
A	18.8	3.49×10^{-3}
B	10.1	2.29×10^{-3}
C	2.54	4.96×10^{-4}
D	0.781	2.63×10^{-4}
E	1.76	3.99×10^{-4}

The timescales here are much shorter than those in Section 6.2 due to the lower entanglement time of polyethylene as opposed to polystyrene. On average chains are oriented but only the very highest molecular weight chains are stretched at flow rates accessible within the MPR The average relaxation times show a small decrease A-B, then a large drop B-C but little change C-E. It might be expected from this that A and B will behave differently to C-E but differences may be small within the two groups.

6.4.2 Results and Discussion

Extensional Rheology fit

SER data for DOW-A,B and E are shown in Figure 6.23.

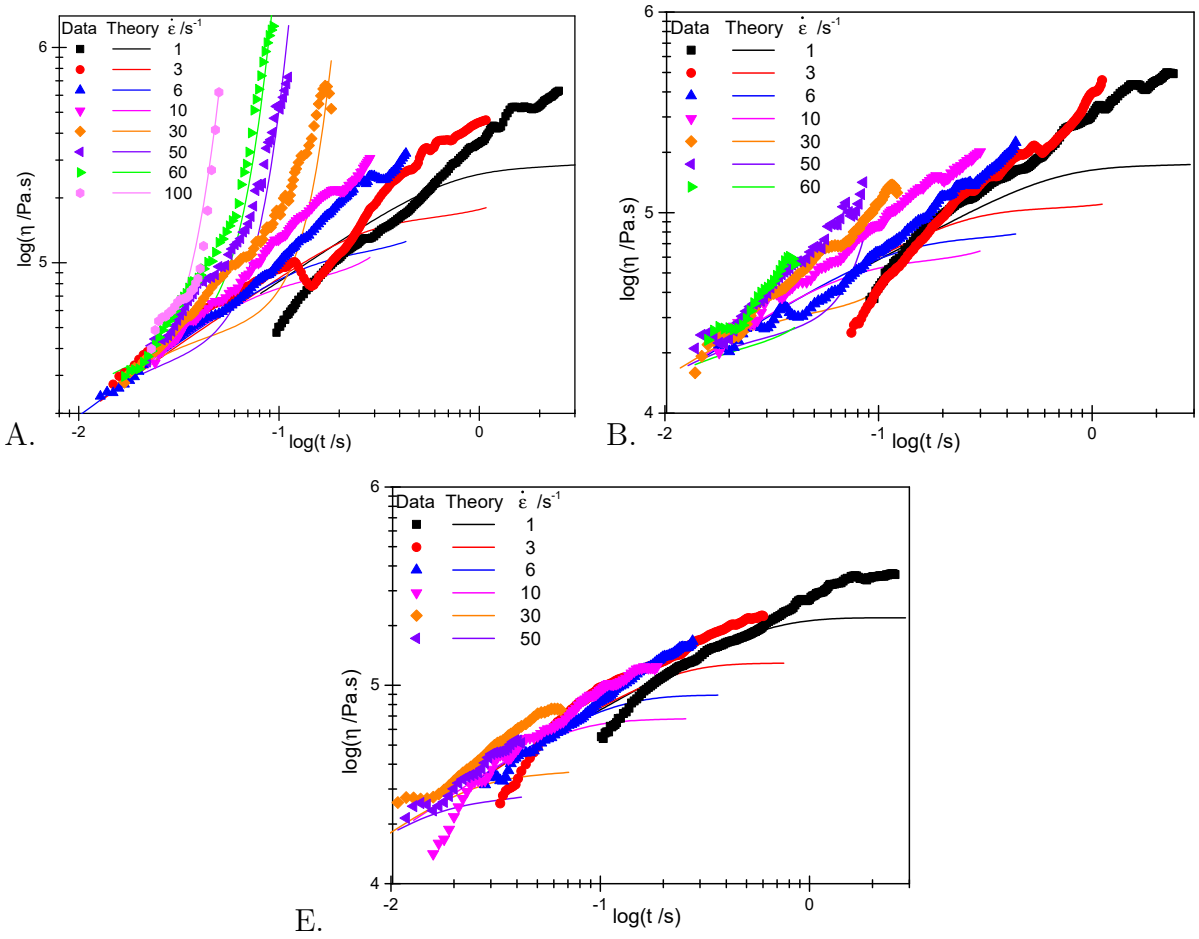

Figure 6.23: SER data (points) and RDP predictions (lines) for DOW-A, B and E at 150 °C.

The predictions for DOW-A at the highest rates are reasonable; the onset of strain hardening is correctly predicted and the viscosities are roughly correct. The linear prediction at low rates is poor here however, consistently under-predicting the viscosities. Predictions for DOW-B are poor; although strain hardening is correctly predicted at 50 s^{-1} the viscosity is lower than observed. Predictions for DOW-E are better; the linear envelope is roughly correct and the lack of strain hardening at the accessible strain rates is correctly predicted.

Extrusion Data

Results from the MPR are shown in Figure 6.24.

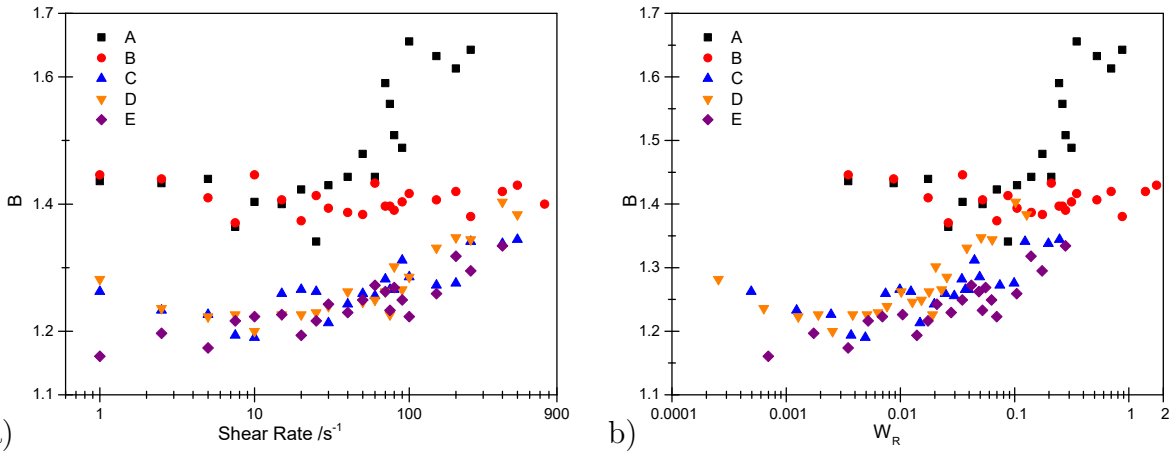

Figure 6.24: MPR extrusion data for DOW A-E at 150 °C. The colour key is the same as for the previous tables. a) shows the data vs shear rate and b) shows normalisation by $\overline{\tau_R}$.

The expected trend in extrudate swell A-C is seen, i.e. a decrease in swelling at constant shear rate. No differences are seen C-E within the error in the MPR measurements. It is difficult to claim superposition versus W_R here. Some superposition is seen between the data sets at $W_R \approx 0.1$ but the low shear rate data from A and B do not fit onto this curve and the high shear rate data for DOW-B shows no noticeable increase with W_R. All samples except E show a small decrease in extrudate swell with increasing shear rate from 1 s^{-1} up to approximately 10 s^{-1}. This is the onset of shear thinning causing a drop-off in swelling, as for the monodisperse case. DOW-A has an initial B value of 1.4 then gives a small increase in swelling from 10-90 s^{-1} before giving a very large jump at 90-100 s^{-1}. DOW-B starts at the same value as DOW-A but shows no increase within the experimental window. DOW C-E start much lower, at $B \approx 1.2$ before swelling increases gradually until the highest speed. Several interesting features can be observed from these data:

- For no samples do B values reach the Newtonian plateau of 1.1 observed for polystyrene in the previous sections. In particular, the low shear swelling from DOW-A is not the same as the high shear swelling from DOW-E despite the fact that not even the highest molecular weight fraction has exceeded $W_R = 1$ at this point. This indicates that there is another factor causing swelling in these systems that is not present in the later systems or the earlier polystyrenes. This may be due

to the presence of some long chain branching in the polyethylenes which has been introduced at some point in its synthesis.

- DOW-B shows no change in swelling within the MPR. This can be explained from the molecular weight distribution. Although DOW-B has a higher $\overline{\tau_R}$ than DOW-C it has a significantly lower weight fraction above 10^3 kDa. (0.013 for DOW-B compared to 0.10 for DOW-C). The polymer chains above this point are stretched at high shear rates in the MPR and thus cause swelling. A low fraction of these chains results in a low extrudate swell.

- Despite the fact that C,D and E have different molecular weight distributions at high weights they have the same extrudate swell. It seems therefore that so long as there is a large enough fraction of high molecular weight polymer the overall distribution does not greatly matter.

MPR extrudate profiles are shown in Figure 6.25. Here the large difference between the samples at this high shear rate can be seen.

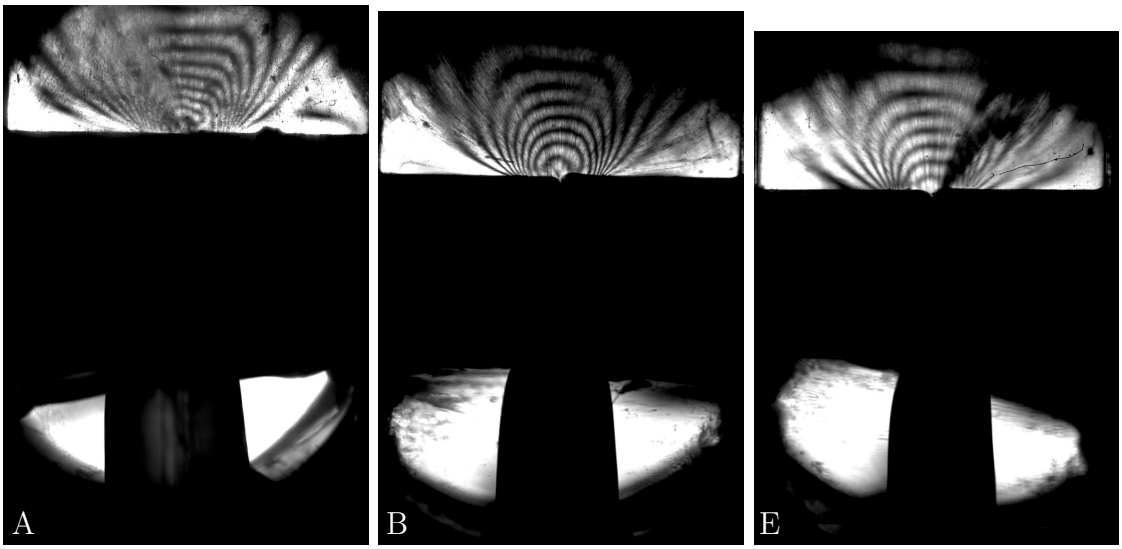

Figure 6.25: Images obtained from the MPR at a shear rate of 200 s^{-1} for DOW-A, B and E.

These polymers can now be simulated using the discretised element data from Table 6.5 and Appendix D. The data from these simulations for A, B and E are shown in Figure 6.26 a).

It is not possible currently to obtain predictions for the lowest shear rates. These rates require very low *timestep* values to run successfully and thus will not run on an accessible

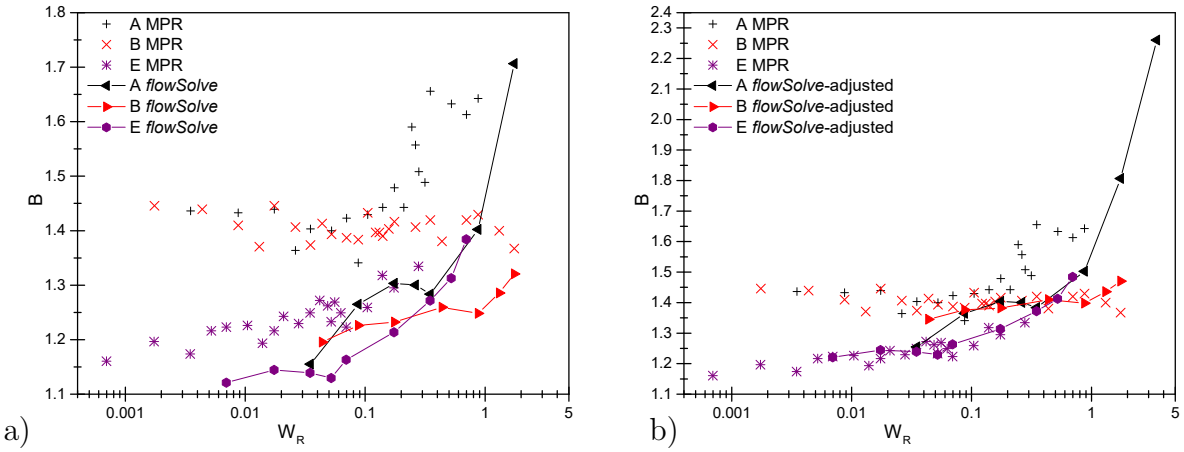

Figure 6.26: MPR and *flowSolve* data for DOW A, B and E. a) shows the raw swelling ratios and b) shows the values increased by 0.1 to match the experiments.

time frame. In all cases, the simulations underpredict the B values. If the simulated B values are corrected by +0.1 then the data in Figure 6.26 b) are obtained.

The simulations qualitatively predict the trends of the data here. For DOW-A the sudden rapid increase of swelling is predicted, albeit shifted to higher W_R. For DOW-B the lack of any increase in swelling is captured until the highest rates, where the MPR data is least certain. The magnitude and position of the increase in swelling for DOW-C, D and E are correctly predicted. We can justify the increase in swelling from DOW-A to E by examining the chain stretch along the extruder. Figure 6.27 a) shows the chain stretch in the highest element for each sample at the slowest speed simulated (0.1 mm s^{-1}). The figure shows that there is very little stretch at the wall for any sample. This is to be expected, as the stretch Weissenberg numbers for these speeds are only just greater than 1. More noticeable is the peak in stretch at the die exit. This peak contributes a very small amount to the overall polymeric stress due to the low weight fraction of the element but the chain stretch still serves to increase the extrudate swell above the Newtonian value. A plot of chain stretch at constant Weissenberg number (Figure 6.27 b)) shows that, unlike the trend observed experimentally, the weighting of each element is important. The swelling decreases A>B>E at this W_R. DOW-B has much higher chain stretch in element 12 but given the very low weighting of this element this does not translate to an increased swelling ratio. DOW-A has a high weighting, therefore the highest swelling ratio, despite the slightly lower chain stretch. DOW-E has a low weighting and the lowest stretch leading to the lowest extrudate swell.

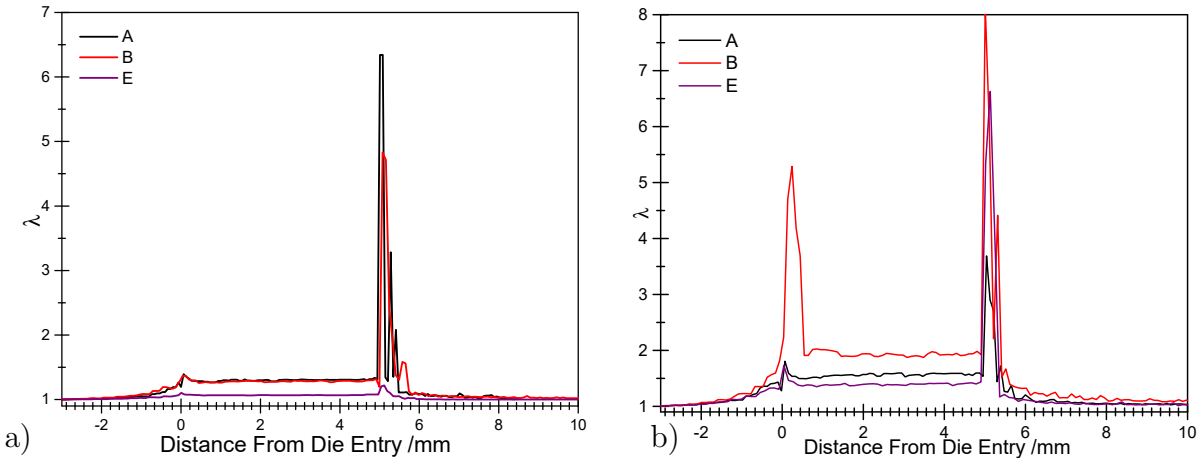

Figure 6.27: Chain stretch in the highest Rolie-Poly element for samples A, B and E at a) v_p=0.1 mm s^{-1}and b) W_R=0.1.

The RDP model is accurately predicting the onset of the chain stretching which causes extrudate swell but it fails to predict accurately the increased low shear swelling ratios, instead predicting the same low shear plateau of 1.1 predicted for polystyrenes. This is either because of additional chemistry which is altering the swelling ratios of these samples or due to the equation insufficiently capturing the contribution of the high molecular weight elements to the overall stress.

Industrial Extrusion

The MPR results can be roughly compared to data on industrial instruments obtained by DOW.[4] A capillary rheometer was used with a 10 mm long and 2 mm wide die. The identical die width allows for easy comparison with MPR measurements. The data are plotted as hollow symbols in Figure 6.28.

The DOW measurements do not superimpose perfectly against molecular weight. DOW A-D fall onto a single curve with Weissenberg number but data for DOW-E are significantly lower than the rest of the data when normalised. The data from the DOW measurements are consistently much higher than those taken from the MPR. The reason for this comes from the profile of the extrudate as a function of distance. The data from the MPR are taken 3-4 mm below the die exit. As shown in section 4.2.1 for polystyrenes this is sufficient to see constant flow as a function of distance and all the swelling occurs just below the die exit. For polyethylenes this is not the case, as shown in Figure 6.29.

[4]Measurements from Sylvie Vervoort at DOW Terneuzen

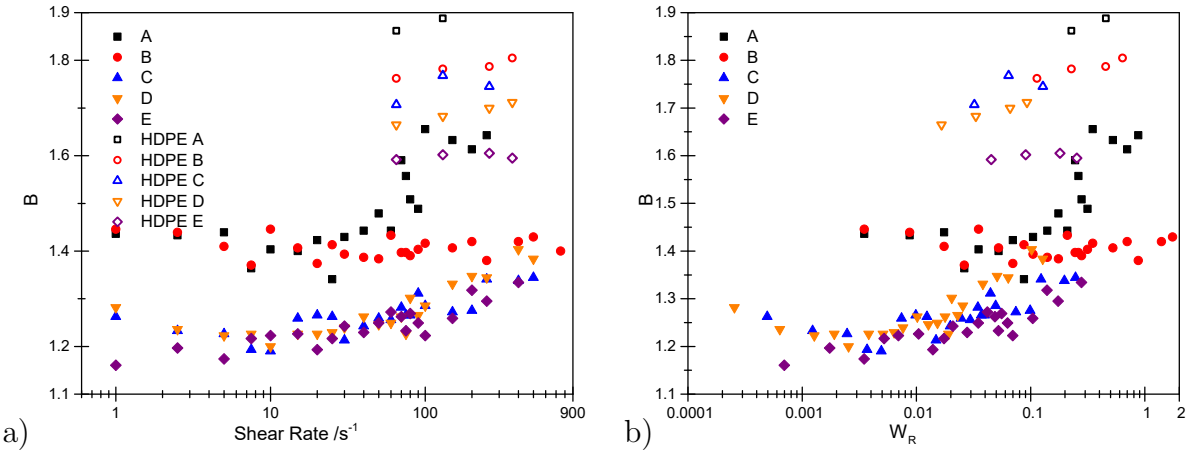

Figure 6.28: Extrusion data from the MPR (solid symbols) and using a DOW extruder (open symbols) and taking measurements 5 cm below the die exit. a) shows data vs shear rate and b) vs Rouse Weissenberg number.

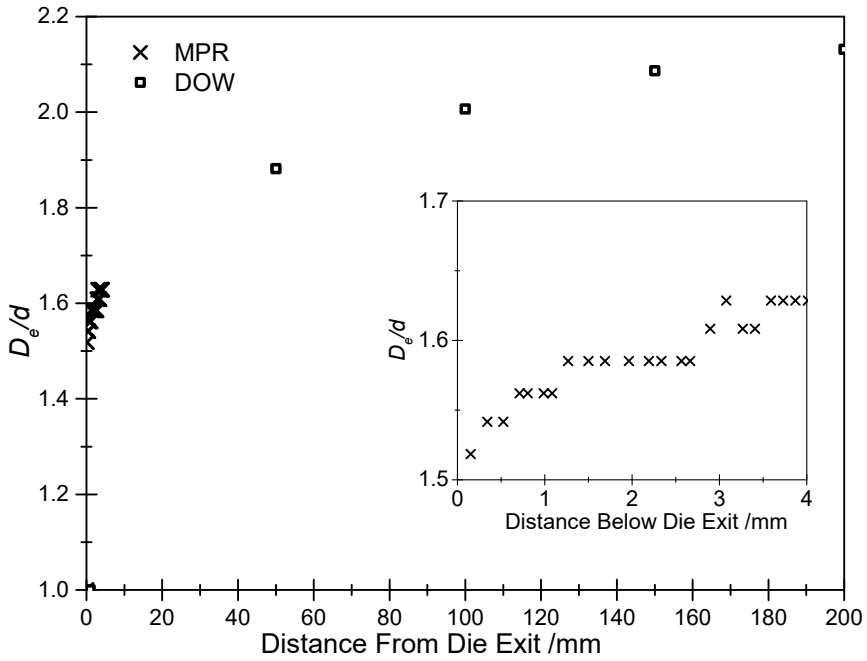

Figure 6.29: Extrudate diameter as a function of distance below the extruder for DOW-A at 130 s^{-1}. Open symbols are DOW measurements and the crosses are traced from the MPR profile. The inset shows a zoom in of the MPR data.

The extrudate continues swelling as a function of distance up to 50 cm below the die exit. There is very significant swelling between the 4 mm limit of the MPR and the first 5 cm measurement from DOW. It does seem that a large amount of swelling occurs

immediately after the die exit, but to measure the maximum die swell ratio it is necessary to measure significantly further below the die. Due to the time required to continue a simulation this far it is not possible to directly compare these experimental profiles with simulated ones from *flowSolve*. It is still possible to simulate the extrudate for several millimetres below the die exit however. Figure 6.30 shows the simulated chain stretch below the die exit extending into free space.

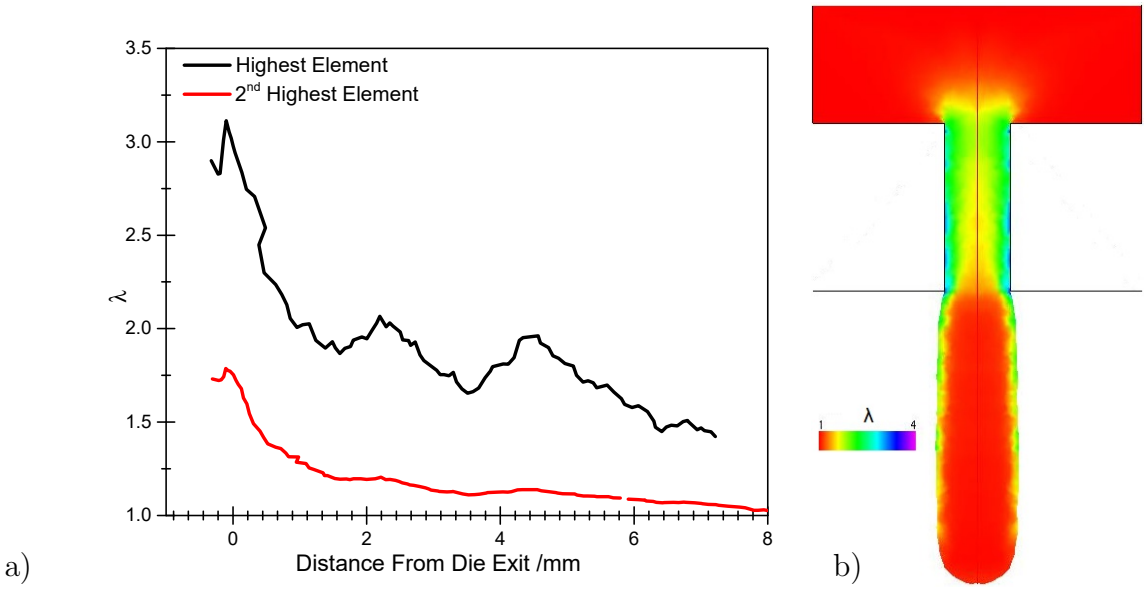

Figure 6.30: Simulated chain stretch below the die for DOW-A at $W_R \approx 0.5$. a) shows the chain stretch values in the highest and second highest Rolie-Poly elements in Table 6.5 and b) shows an image of the stretch in the highest element.

The highest molecular weight chains remain stretched for these samples for a significant distance below the die exit. The resulting stretch relaxation causes the extrudate to continue to expand outwards slightly for a significant distance below the die, causing the profiles seen in Figure 6.29.

6.5 Concluding Remarks

Polydispersity vastly complicates the issue of extrudate swell. A slight increase in polydispersity increases extrudate swell at a specific Weissenberg number although at very high dispersities this is no longer true. An important factor is the presence of a high molecular weight fraction which increases swelling ratios at a low *average* Weissenberg number. The form of this peak does not seem to matter as long as it contains a high enough weight fraction. It is difficult therefore to look at a molecular weight distribution and pick which one has the highest extrudate swell as different molecular weight fractions will become important at different shear rates. *flowSolve*, combined with the polydisperse Rolie–Double-Poly model, is capable of predicting extrudate swell for mildly polydisperse systems under different flow geometries. For highly polydisperse polyethylenes it is possible to predict roughly the onset of increased swelling with increasing shear rate although the magnitude of extrudate swell is consistently under-predicted.

A capillary rheometer is another useful tool for measuring the extrudate swell of industrial materials. The advantage of this method is that it allows visualisation of the flow downstream of the die, in particular visualisation of flow instabilities. These instabilities are important in flow processing but are not captured by *flowSolve*. A hypothesis is that they are a chain stretch induced phenomenon, occurring where the flow rate exceeds the Rouse Weissenberg number. If this is the case then understanding of the molecular weight distribution and its effect on the polymeric relaxation times is very important for understanding of not only extrudate swell but flow instabilities. Looking at the downstream flow is also important for polyethylene samples which appear to reach a maximum swelling ratio centimetres rather than millimetres below a die exit. The flow within the MPR cannot be seen this far below the die exit, therefore a terminal extrudate swell value cannot be obtained from MPR experiments.

Overall, MPR measurements have been shown to be consistent with capillary rheometer measurements for moderately polydisperse samples. Some differences at low and high shear rates have been observed but reasons for these have been identified and evaluated.

Chapter 7

Extrusion of Branched Polymers

7.1 Introduction

The work thus far has focussed on linear polymers. In general however, many industrial samples will, either deliberately or as unwanted products of synthesis and processing, have some long chain branching. Simulation of the rheology of these branched samples is therefore necessary to understand and predict extrudate swell for an arbitrary industrial sample. This chapter focusses on the simulation of rheology and extrudate swell for various branched samples. In Section 7.1.1 previous work on extrudate swell for branched samples is discussed and in Section 7.1.2 previous work on the branched samples used in this work is described. In Section 7.2 the physical and rheological properties of these samples are described. In Section 7.3 long chain branched polyethylenes are simulated using the Pom-Pom and XPP equation sets within *flowSolve* and the extrudate swell data compared to extrusion experiments within the MPR.

7.1.1 Effect of Long chain Branching on Rheological Properties

Long chain branching increases the shear viscosity of a polymer melt. In [88] narrow dispersity polyethylenes with controlled branching densities were studied, and a large increase in viscosity was seen above approximately 0.2 LCB/10,000C (Long Chain Branches per 10,000 Carbon atoms). Doubling the LCB density resulted in a sixfold increase in the shear viscosity. This corresponded to (on average) 1 LCB for every 6 polymer chains. A very small amount of branching can therefore have a larger effect on the rheology of a melt. Although extrudate swell is governed by polymer relaxation times rather than viscosity, it seems reasonable that small numbers of branches will have

a similarly large effect on swelling ratios. Hamielec *et al* [89] found that for short $l:d$ ratios there was a large increase in extrudate swell with increasing branching number. For an orifice die extrudate swell at a shear rate of 600 s^{-1} increased from ~ 2.5 to ~ 3.5 with branching number increasing from 2 to 4 LCB/1000C. The effect was much smaller for a long die, only increasing by 0.2 over the same range. They therefore concluded that the increase in swelling with branching is primarily a flow entry effect.

7.1.2 Long chain Branched Polyethylenes

Two series of polyethylenes are studied in this work, the CM series of low density polyethylenes and the HDB series of high density polyethylenes. The CM1, 2, 3 series is a set of low density polyethylenes synthesised by DOW chemical using a metallocene catalyst to control the branching density. CM1 is linear and CM3 has 0.099 LCB/1000C. The dependence of melt viscosity on dilution of polymer melts with a squalane solvent was previously used to determine the LCB density of the melts. Even low levels of branching were found to have a significant effect on the viscosity of the melts and solutions.[90] CM1 has been used as a low molecular weight polyethylene for comparison to branched melts in cross-slot and slit flow.[91] These polyethylenes have been used in cross-slot flow for measurements of steady-state and transient extensional viscosities.[92]

The HDB series of polyethylenes was also synthesised at DOW chemical also using a metallocene catalyst to achieve controlled levels of chain branching. They were characterised in [93] both rheologically and using GPC. This series is fairly lightly branched, with 0.26 LCB/1000C for HDB1 and 0.8 LCB/1000C for HDB4. As with previous work, in [93] and [94] it was found that zero shear viscosity increased with increasing long chain branching. Additional samples were later added to the series, going up to HDB7. [95] The well-defined nature of these melts has proved useful for simulation and analysis of the effect of branching on flow in various flow geometries.[96, 49, 97] The highest levels of chain branching resulted in the formation of 'W cusps' in cross-slot flow [49]. These melts are generally simulated using the multi-mode Pom-Pom model [43] for non-linear response but their linear response has been predicted accurately using the BOB (Branch-On-Branch) theory for branched systems.[95]

Work on these well-defined branched polymers is thus common for understanding their behaviour in basic extensional, shear and cross-slot flow. In this work their behaviour under a process flow is described via extrudate swell measurements.

7.2 Characterisation

Three types of polyethylene are analysed here; The CM series of LDPEs, the HDB series of HDPEs and the highly branched LDPE Lupolen LD1840H.[1] Summary data of these samples are shown in Table 7.1.[98]

Table 7.1: Summary molecular weight and branching data for the polyethylenes studied in this chapter.

Sample Code	M_w /kDa	Đ	LCB/1000C	b_n
CM1	104	2.07	∼0	∼0
CM2	83	2.21	0.032	0.190
CM3	80	2.20	0.099	0.566
LD1840H	240	9	6	23
HDB1	77	2.13	0.026	0.067
HDB2	82	2.20	0.037	0.099
HDB3	86	2.23	0.042	0.116
HDB4	96	2.45	0.080	0.224
HDB5	79	2.42	0.090	0.21
HDB6	68	2.69	0.188	0.34
HDB7	70	3.07	0.332	0.54

The branching number b_n is the number of branches per chain. Rheological characterisations for each sample are given at 150 °C. This include the linear rheology and SER data.

[1] Information on LD1840H can be found at https://www.lyondellbasell.com/en/polymers/p/Purell-PE-1840H/441ffe15-592c-4a93-bd1a-af8b13ba49fb (accessed 08/11/18)

7.2.1 CM Series of Lightly Branched LDPEs

Linear rheology for the CM series is shown in Figure 7.1.

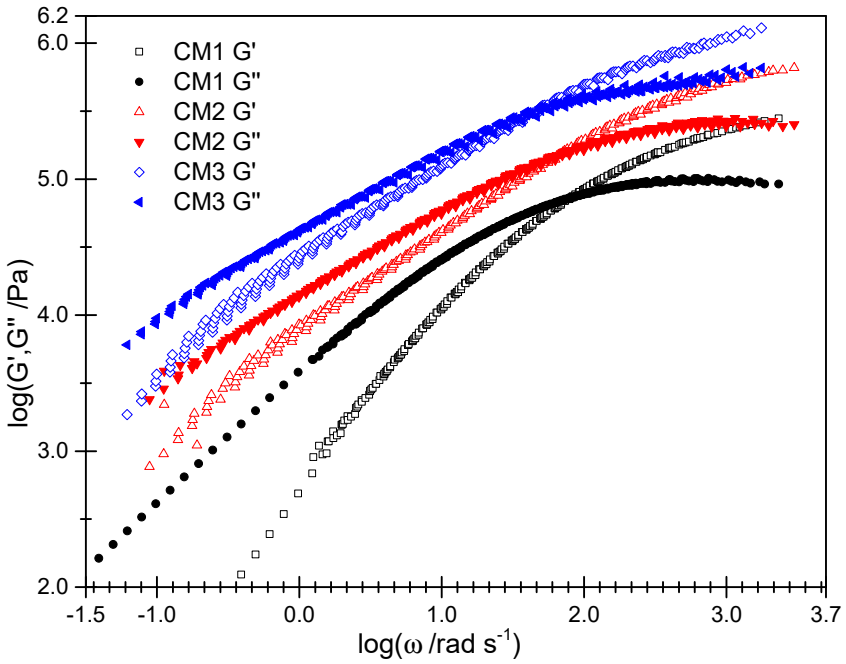

Figure 7.1: Linear rheological data for the CM series of polyethylenes at 150 °C. For clarity, CM1 is shifted vertically by -0.5 and CM3 is shifted vertically by +0.5 log units.

The three samples have approximately the same crossover modulus and there is a small decrease in crossover frequency with an increase in branching. The Maxwell mode fits for these rheology data are shown in Appendix C. Extensional rheology from the SER is shown in Figure 7.2. The overal modulus of CM2 is higher than that for CM3 but CM3 strain hardens at lower rates. CM3 shows some strain hardening at a Hencky rate of 1 $s^{-1}$where CM2 does not. At higher rates, the magnitude of the strain hardening is almost the same for both samples Data for CM1 are not shown as this sample exhibits no strain hardening.

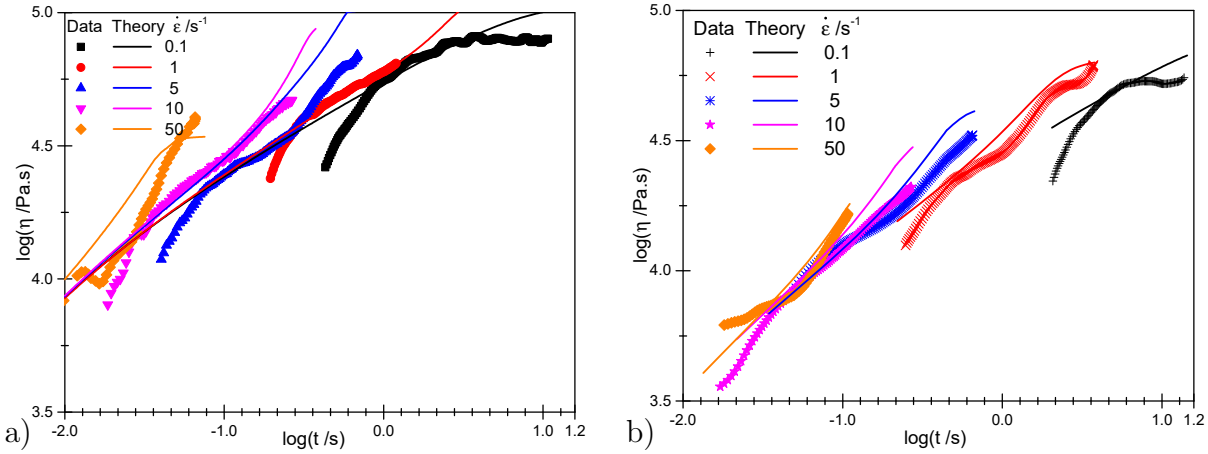

Figure 7.2: Transient uniaxial extensional data for a) CM2 and b) CM3. The lines show the Pom-Pom prediction using the parameters in C.2.

7.2.2 HDB Series of Lightly Branched HDPEs

Linear rheological data at 150 °C are shown in Figure 7.3. In this case a Van-Gurp-Palmen plot [99, 100] is used to highlight differences between the samples, as they would appear very similar in the standard view of modulus versus frequency. This shows phase angle δ versus complex modulus G^*. The larger the degree of long chain branching the lower the phase angle.[101] This plot therefore shows the increasing level of branching down the HDB series. Linear CM1 is shown for comparison. This sample is the least elastic, therefore has the highest phase angle. The extensional data for HDB1 and HDB7 are shown in Figure 7.4. The sample HDB1 exhibits little to no strain hardening. HDB7 shows some strain hardening at extension rates above ~0.3 s^{-1}. HDB7 also has a significantly higher viscosity at low extension rates.

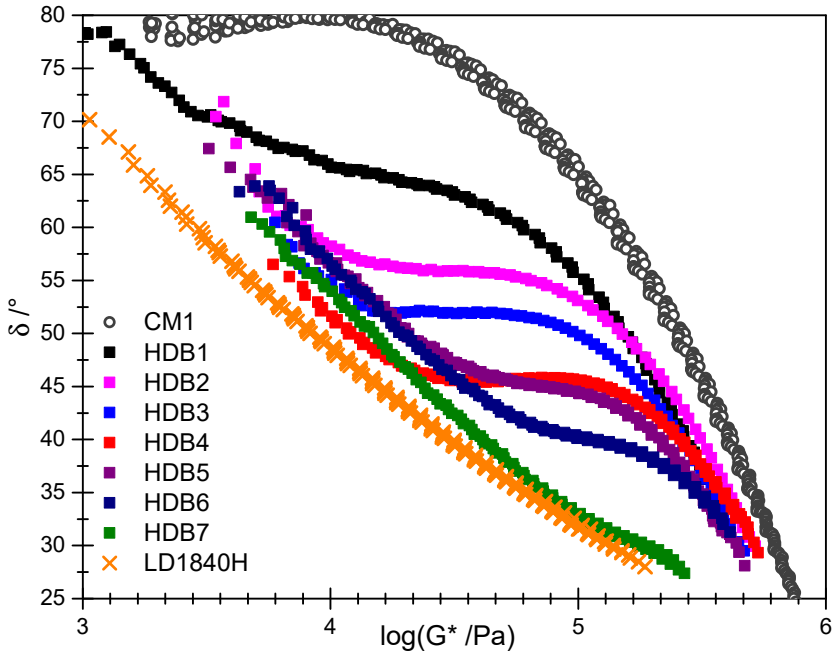

Figure 7.3: Phase angle versus complex modulus for linear CM1, branched HDB1-7 and highly branched Lupolen LD1840H.

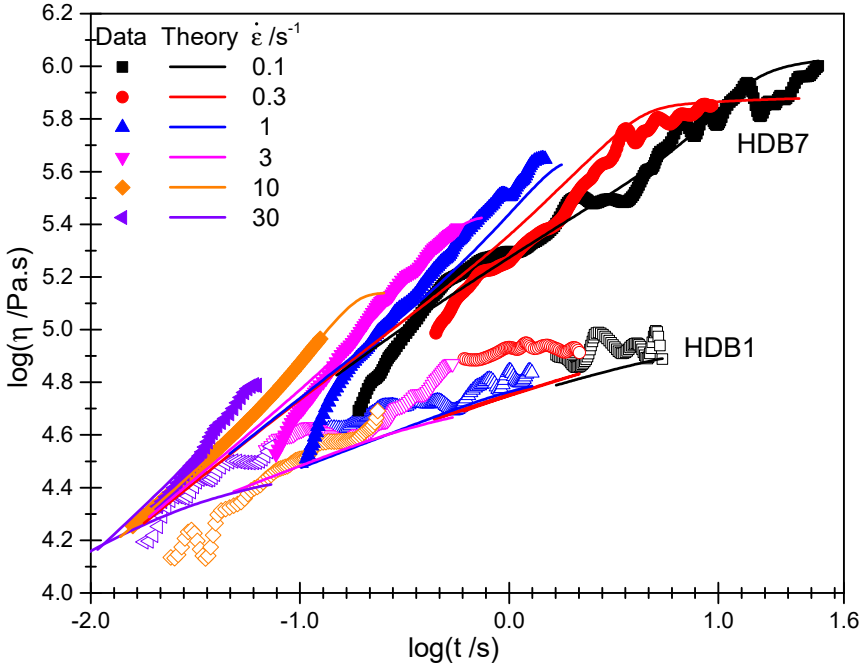

Figure 7.4: Uniaxial extensional data for HDB1 and HDB7. The open symbols are HDB1 and the closed symbols are HDB7. Fits to the XPP model are shown as lines.

7.2.3 Highly Branched Polyethylene

The linear data for LD1840H are shown on Figure 7.3. This sample is the most highly branched, so has the lowest phase angle. The plateau modulus of this sample is similar to the HDB series, and the crossover frequency is similar to HDB7. The crossover frequencies are summarised in Table 7.2.

Table 7.2: Crossover frequencies and times for the polyethylenes studied in this chapter at 150 °C.

Sample	ω /rad s^{-1}	τ_d /s
HDB1	276	0.0036
HDB2	151	0.0066
HDB3	124	0.0081
HDB4	31.5	0.032
HDB5	19.9	0.050
HDB6	4.04	0.25
HDB7	1.64	0.61
CM1	78.1	0.013
CM2	59.7	0.017
CM3	40.1	0.025
LD1840H	1.77	0.56

The crossover time is used as an average relaxation time and is used for calculation of a reptation Weissenberg number, W_d. This Weissenberg number will not normalise for non-linear behaviour such as extrudate swell but allow removal of the effect of differences in the linear rheology to highlight differences in non-linear response.

The linear response of this sample is not very different to the linear response of the previous samples. The same is not true for the non-linear response. LD1840H strain hardens much more significantly than all of the HDB and CM series. This is due to the significant chain branching (Figure 7.5). The Linear Viscoelastic Envelopes for CM and HDB series polyethylenes are shown on the graph to illustrate that all the samples differ both in terms of steady state viscosities and the levels of strain hardening. LD1840H strain hardens at rates as low as 0.5 s^{-1} whereas the CM and HDB samples did not strain harden until above 10 s^{-1}. The linear prediction for extensional viscosity is lower than for the CM and HDB samples but the strain hardening is much greater.

The Pom-Pom and XPP *ratio* and q parameters are obtained by fitting in RepTate. These parameters are summarised in Appendix C and are used in the following section.

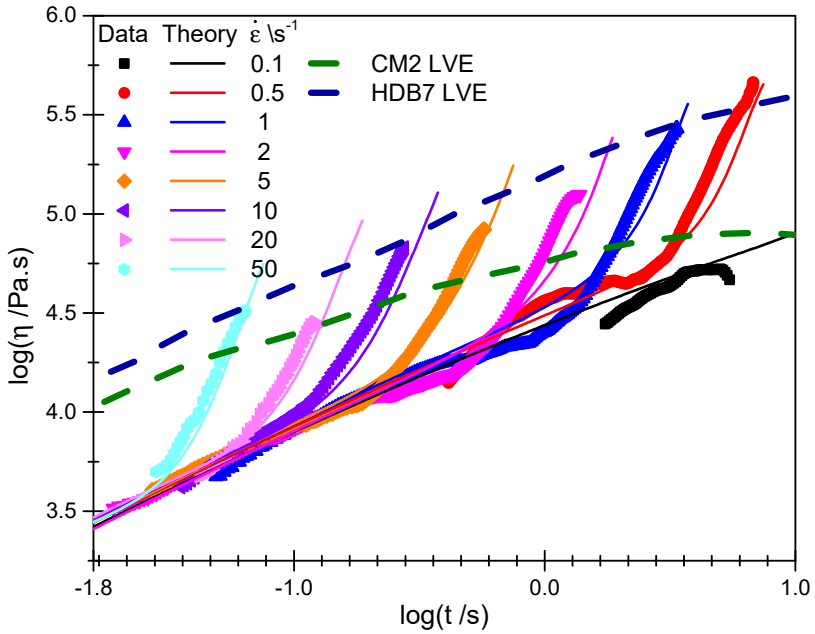

Figure 7.5: Uniaxial extensional data for Lupolen LD1840H. Linear viscoelastic envelopes are shown for CM2 and HDB7 for comparison. Extensional fits using the XPP model are shown as lines on the data.

7.3 Results and Discussion

The samples analysed in the previous section have varying levels of long chain branching and thus significantly different behaviour in uniaxial extension. The frequency response for all samples is similar and thus the Maxwell mode fits for these samples are similar. This section investigates whether the differences in extensional response translate into differences in extrudate swell. In this section the experimental and theoretical extrudate results are shown. Simulations are presented for the Pom-Pom and XPP models and compared to MPR extrudate swell data for each series of polyethylenes. Finally, all the experimental data sets are compared to highlight the effect of long chain branching on extrudate swell.

7.3.1 Extrusion of the CM Series of Branched LDPEs

The MPR data for the CM series are shown versus reptation Weissenberg number in Figure 7.6. The Weissenberg numbers are calculated using the timescales in Table 7.2. For CM1 the predictions using the set of Maxwell modes from Table C.2 but the non-stretch Rolie-Poly equation are also shown. If the same timescales which were

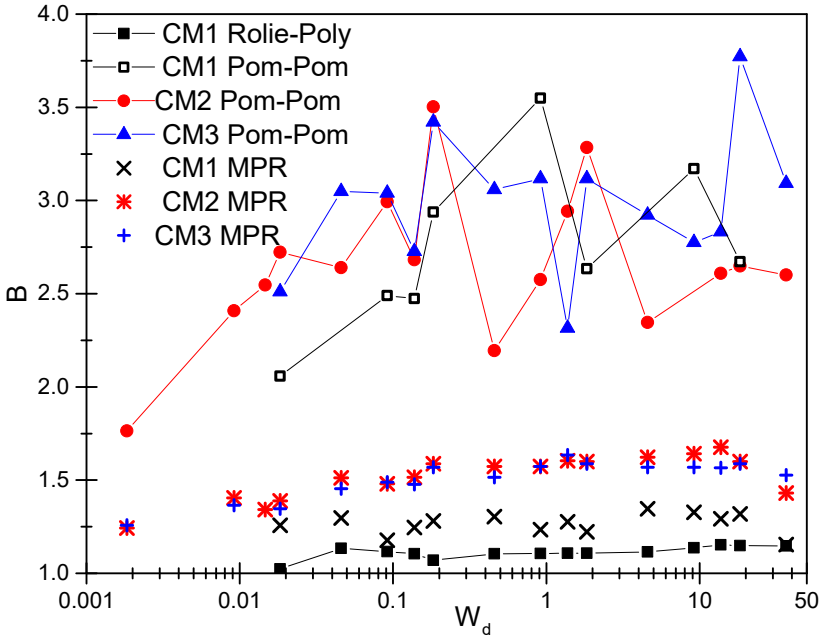

Figure 7.6: Pom-Pom predictions (points and lines) and MPR extrusion data (points) for the CM series of polyethylenes at 150 °C.

found for the DOW polyethylenes in Section 6.4.1 are used the 104 kDa chains of CM1 would be expected to have a Rouse relaxation time of order 10^{-6} s. It is safe to assume they are non-stretching on the shear rates up to 1000 s^{-1} used here. Similarly to the previous polyethylenes the Rolie-Poly equation slightly under-predicts the extrudate swell. Whereas Rolie-Poly predicts the usual 1.1, the polyethylenes swell by ~ 1.2 under Newtonian flow. The Pom-Pom predictions are much worse, however. The swelling ratios are greatly over-predicted and the results are slightly inconsistent with increasing Weissenberg number. These differences between simulation runs are due to inconsistencies and instabilities on the surface of the extrudate. An example of this is shown in Figure 7.7.

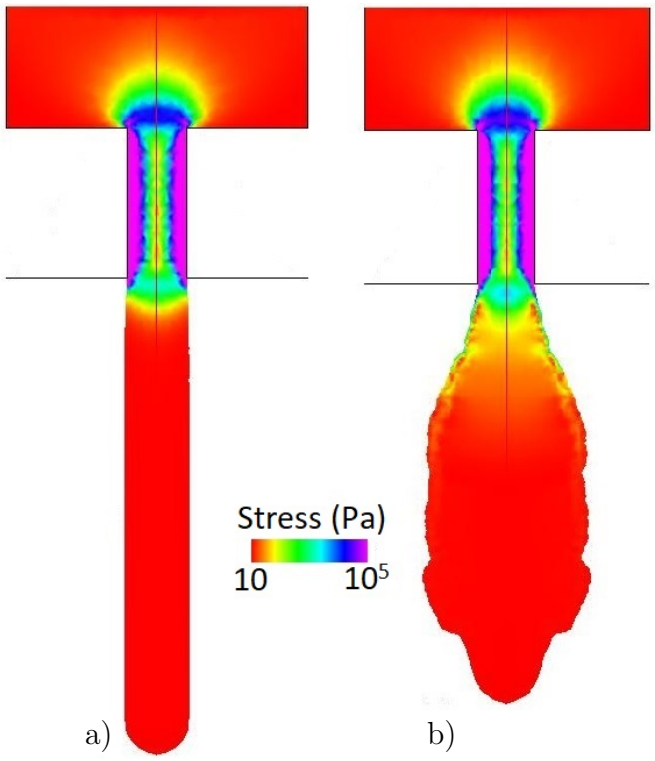

Figure 7.7: Simulated images of the extrudate for CM1 at $W_d = 0.018$. with a) Rolie-Poly and b) Pom-Pom using an identical set of Maxwell modes.

The Rolie-Poly simulations all give smooth extrudate surfaces, with an increase to a maximum then a steady state flow. The Pom-Pom simulations do not do this, rather the edge of the extrudate is jagged and varies significantly both spatially and with simulation run time. This appears to be caused by the stress at the free-surface line of the simulations. For Rolie-Poly the stress relaxes quickly at the die exit, but for Pom-Pom the stress barely relaxes at the die exit, rather relaxing very slowly with distance. In particular, the Pom-Pom orientation becomes extremely large at the die exit. Considering the rr component of the Pom-Pom auxiliary tensor $\mathbf{A}$ (perpendicular to the flow direction), $A_{rr} \approx 50$ at the die entry and ≈ 0.4 at the die wall. At the die exit, however, A_{rr} becomes of order 10^{19}. This causes the extrudate to expand randomly in response to fluctuations in this orientation. To avoid this occurring, the XPP model introduced in Section 2.2.6 is used in this chapter. This model used the $\mathbf{S}$ tensor for evolution of orientation, which is limited to unit trace and cannot become large at the die exit corner. Results for these samples with the XPP model are shown in Figure 7.8.

The XPP model produces more reasonable predictions for extrudate swell, especially at low shear rates. Up to $W_d \approx 0.3$ the simulations accurately match the experimental

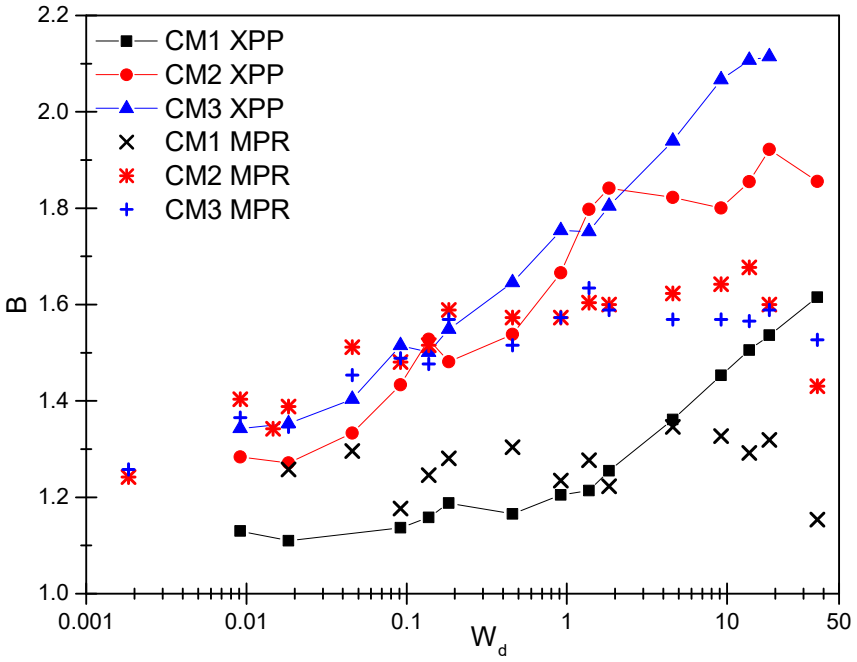

Figure 7.8: MPR extrusion data for the CM polyethylenes and simulation results from the XPP model.

data for CM2 and 3. Simulations for CM2 and 3 predict that extrudate swell ratios increase significantly above W_d=1. The over-prediction of stress is a known problem with the XPP model,[102] although ordinarily attributed to the fact that the chain stretch is unbounded. The unbounded chain stretch improves computational stability, but reduces agreement with experimental data. Figure 7.9 compares the three theories used for linear CM1. Similarly to Rolie-Poly, the XPP data for CM1 are slightly underestimated. The high shear rate predictions are also poor. Even without any stretch times the predicted extrudate swell increases above W_d=1. The data show no increase, due to the lack of any chain stretch. One possible reason for the disagreement is the difference in measurement conditions. As in previous chapters, the B value used is the maximum swelling ratio reached in the simulation. However the experimental values are taken at 5 mm below the die exit. For the quickly swelling polystyrenes this is not a problem, but in this section, as for the polyethylenes in Section 6.4, it has an effect. Figure 7.10 shows the simulated extrudate swell 5 mm below the die exit point. The fits here are slightly improved. For CM2, the high Weissenberg number swelling ratios are reasonably well predicted but this is countered with an underestimation at low shear rates. The overestimation for CM3 is also slightly reduced. The predictions for CM1 are not improved, giving the same overestimation at high shear rates and underestimation at low shear rates.

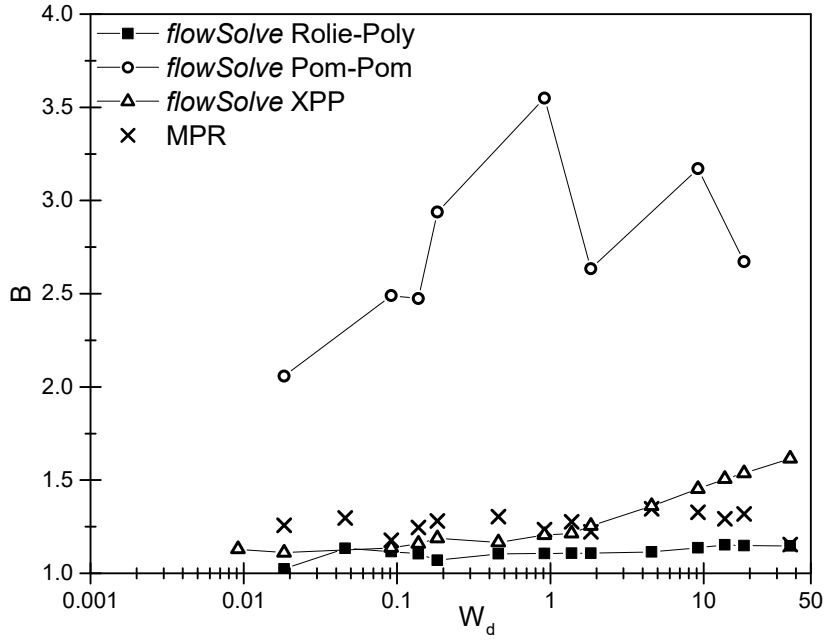

Figure 7.9: MPR extrusion data for CM1 and simulation results from the Rolie-Poly, Pom-Pom and XPP models.

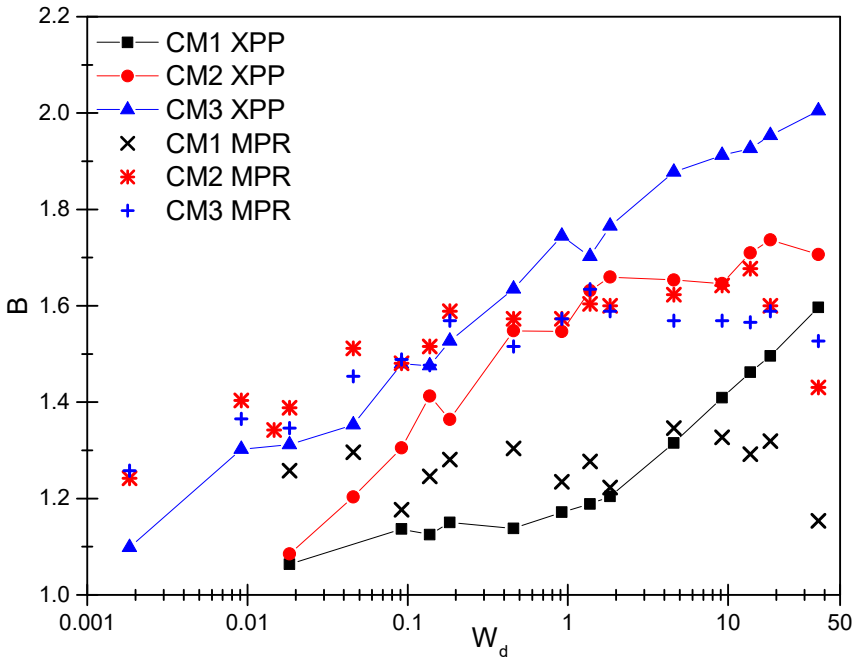

Figure 7.10: MPR extrusion data for the CM polyethylenes and XPP predictions for the extrudate swell at 5 mm below the die exit.

7.3.2 Extrusion of a Highly Branched Sample

The swelling ratios for LD1840H at the same temperature and using the same shear rates are shown in Figure 7.11.

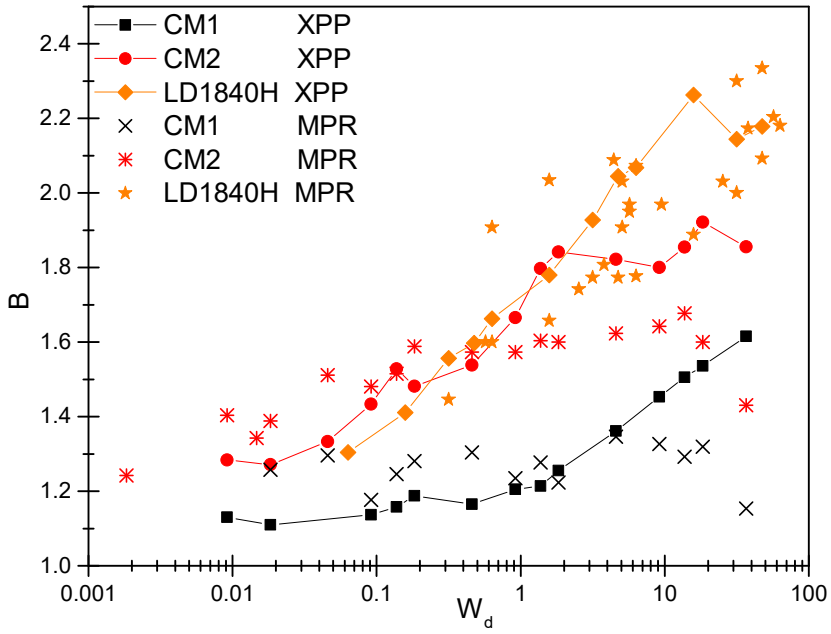

Figure 7.11: Extrusion data for the LD1840H and the associated XPP predictions at 150 °C. The CM data are shown for comparison. The open and closed symbols show data taken from the same sample in separate MPR runs.

This sample shows a much greater increase in swelling with shear rate than the CM series. Although the swelling starts at a similar point, the maximum swelling reached is above 2.3. This value is similar to the maximum swell observed for the monodisperse polystyrenes. The XPP prediction here is good, predicting both the low and high shear swelling ratios within error. There is large scatter in the data for this sample, possibly due to degradation of the sample within the MPR. To check for this effect all samples are tested rheologically before and after a run in the MPR. Linear rheology for LD1840H is shown in Figure 7.12. The sample has degraded slightly in the MPR. Under a nitrogen atmosphere the only change is a slight drop in the moduli. However, when the frequency sweep is performed in air, the storage modulus increases at low frequency so that no crossover is observed (except at the first temperature run used). This degradation may be the cause some of the inconsistencies in the B values measured.

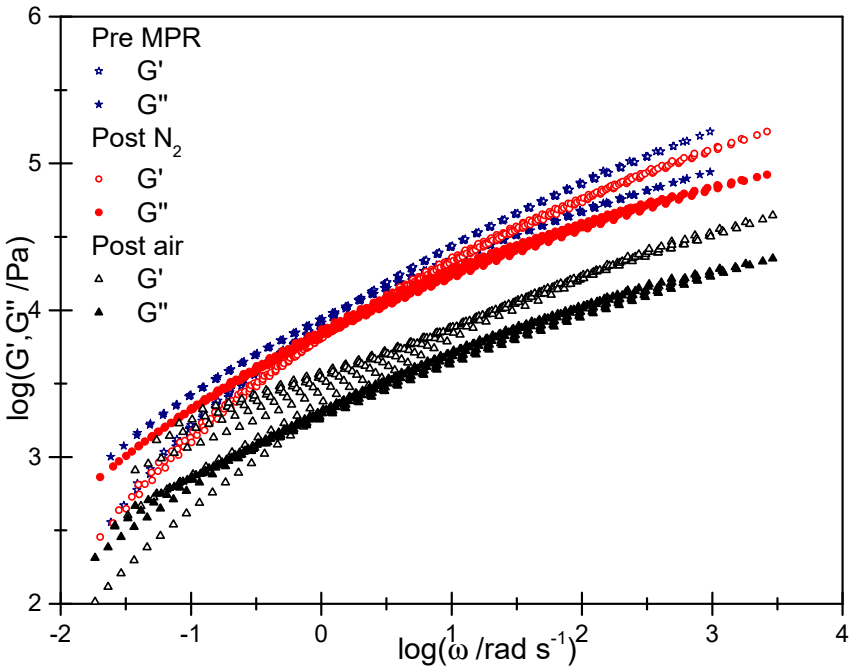

Figure 7.12: Linear rheological data for LD1840H at 150 °C before and after an extrusion run in the MPR. Rheology runs in both an air and nitrogen atmosphere are shown.

7.3.3 Extrusion of the HDB Series of Branched HDPEs

Results from the HDB polyethylenes are shown in Figure 7.13.

The MPR data for all the HDB samples superimpose well. There is a small decrease in swelling at low speeds, followed by a similar small increase at higher rates. Similarly to the CM polyethylenes there is very little dependence of swelling upon shear rate.

The simulations do not match the experiments accurately. Firstly, although the simulations show a general upwards trend with increasing shear rate, there are large dips at specific shear rates for all samples. These dips are caused by the assignment of solvent modes in the simulation. As stated in Section 2.3 any elements faster than 10^2 faster than the inverse shear rate are defined as solvent. When increasing in shear rate a Pom-Pom element from Table C.3 is moved from the solvent to being fully resolved. This causes a dip in solvent viscosity and thus in extrudate swell. Secondly, the simulations under-predict swelling ratios at low shear rates. This implies that there are some slow relaxation modes in the material which are not accounted for in the Pom-Pom fit. Thirdly, although the simulations for HDB2 and HDB6 predict roughly the same swelling ratios (which match experiments), the predictions do not match for HDB1 and HDB7. The simulations predict differences in extrudate swell between the samples which do not occur in practice.

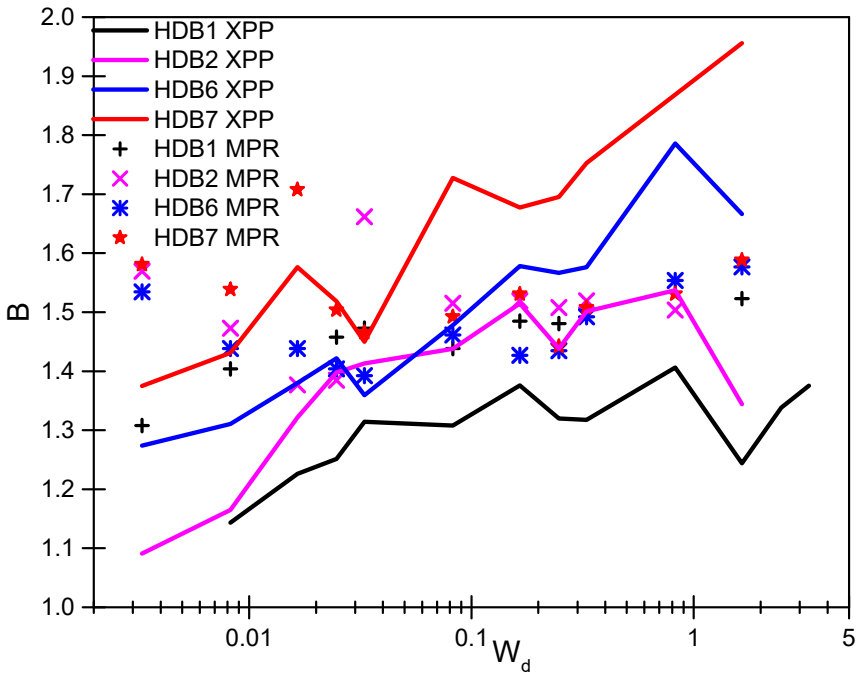

Figure 7.13: MPR B values (points) for HDBs 1, 2, 6 and 7 alongside XPP predictions at 5 mm below the die exit (lines).

Although there is a significant increase in strain hardening in uniaxial extension (evident in Figure 7.4) this does not correspond to an increase in extrudate swell. Lastly, the extrudate swell is over-predicted at high shear rates. Although fast modes are required to fit the extensional data they cause a poor fit to extrudate swell data at higher rates. This over-prediction may also be a failure of the XPP model at high shear rates. As for CM1, the XPP model predicts an increase in chain orientation at high shear rates, leading to extrudate swell, even if the chain stretch λ is limited to $\lambda < q$.

The HDB extrusion data are compared with the data for the CM samples and LD1840H in Figure 7.14. There are three types of polymer studied here: The linear polyethylene, where the extrudate swell starts at approximately B=1.2 at low shear and does not change significantly with increasing shear rate. There are the lightly branched polymers, where swelling starts at ∼1.4 and increases very slightly with shear rate. Finally, there is the highly branched polyethylene which also starts at ∼1.4 at low shear rates and increases very significantly at high shear rates. Images from the MPR for each series are shown in Figure 7.15. In this figure, a small increase in swelling is seen from moving from the linear to lightly branched sample (from a) to b)). This is contrasted with the very large increase from the lightly branched to highly branched sample (b) to c)).

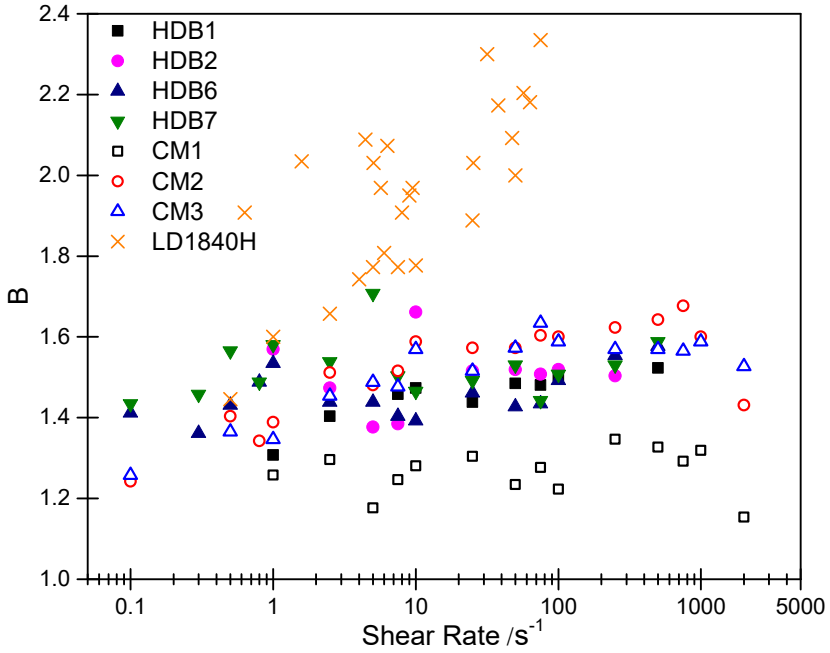

Figure 7.14: Experimental B values versus shear rate for all the polyethylenes studied in this chapter.

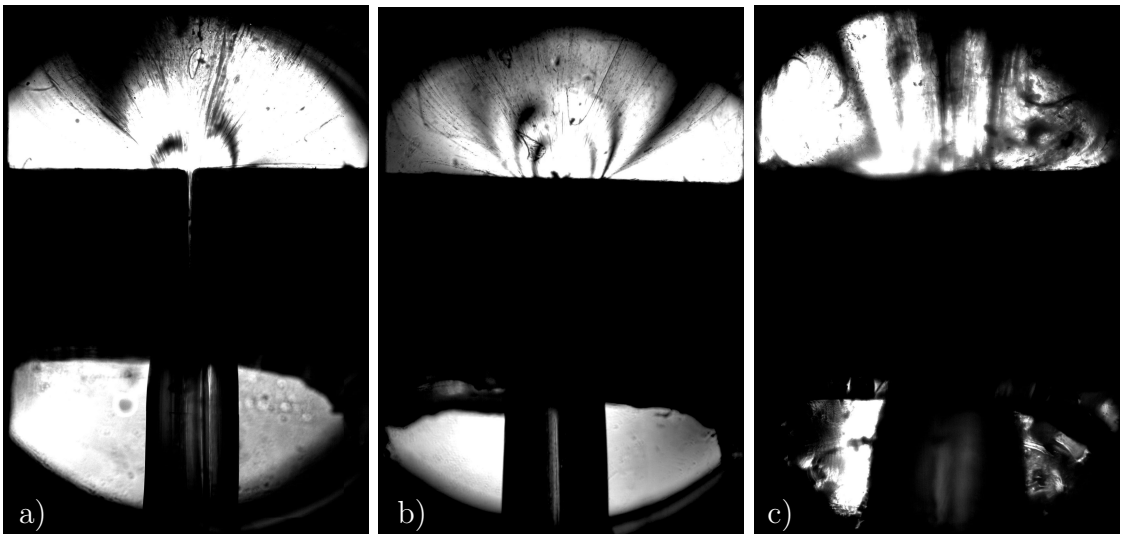

Figure 7.15: MPR extrusion images at a shear rate of 50 s^{-1} for a) CM1, b) HDB6 and c) LD1840H.

It seems that extrudate swell is very weakly dependent on branching density for lightly branched polymers, as long as there is a small amount of branching. Very highly branched polymers which strain harden significantly at low rates exhibit increased extrudate swell. Similarly to the linear polymers, the extrudate swell is dependent more on the onset point of strain hardening than on its magnitude at high rates. The extrudate of a sample which barely strain hardens at low rates extrudate swells little, regardless of the level of branching and the associated increase in strain hardening at the highest rates. At present, none of the constitutive models presented in this work are able to capture fully this extrudate swell behaviour whilst also adequately predicting the uniaxial extensional data.

7.4 Concluding Remarks

Simulation of extrudate swell is much more difficult for branched polymers than for linear samples. The XPP and Pom-Pom equation sets have flaws which mean that their use in free-surface extrusion flows is non-ideal. The Pom-Pom model exhibits a numerical instability at the die exit corner which means that results in free-surface flow cannot be trusted whereas the XPP model tends to over-predict extensional stress and thus extrudate swell. It is roughly possible to predict the effect of chain branching on extrudate swell using *flowSolve* and the XPP model. The differences between linear, lightly branched and highly branched samples are clearly predicted. However, small differences between lightly branched samples are predicted which are not observed in experimental data. There are multiple other extensions and alterations to the Pom-Pom model which could be investigated for the purpose of obtaining accurate simulations of extrudate swell of these branched melts.

MPR results show that even a small level of long chain branching results in an increase in the extrudate swell compared to a linear sample. Moderate increases in the level of branching (where chains have on average no more than one branch point) give no further change in experimentally observed extrudate swell. This is despite the increased strain hardening observed in uniaxial extensional flow. Highly branched polymers have much higher extrudate swell, especially at high shear rates.

Chapter 8

Conclusions and Future Work

8.1 Conclusions

In this work, extrudate swell for a number of polystyrenes and polyethylenes were measured experimentally and predicted using fluid dynamics simulations.

The fluid dynamics software used was *flowSolve*. This software was ideal for simulating extrudate swell as it allowed not only the free-surface extrusion flow to be modelled but allowed extraction of molecular constitutive parameters, such as chain stretch, both spatially and as a function of time. A major advantage of *flowSolve* for this work was the ability to edit the source code. New constitutive equations and extensions to existing equations have been coded in in this work, and bugs fixed as they occurred.

Extrudate swell B values were simulated at a variety of shear rates and molecular weights. For monodisperse polystyrenes there is a large increase in swelling ratio with increasing shear rate with the largest increase occurring at shear rates above a Rouse Weissenberg number of 1. Conversion of shear rates to Rouse Weissenberg numbers removes the molecular weight dependence of extrudate swell. This implies that extrudate swell is primarily a chain stretch controlled phenomenon. Chain stretch was computed during the simulations and plotted versus distance along the extruder, showing the relative effects of the die entry, continuous shear at the die wall and the die exit. For medium to long dies the die entry has little effect upon the observed swelling ratios, rather the extrudate swell depends upon the shear at the die wall and the rapid extension at the die exit corner.

Extrusion experiments were performed in a Multi-Pass Rheometer (MPR) using a pair of newly designed extrusion geometries. A range of shear rates were chosen so as to match

the *flowSolve* simulations and to provide a good comparison between experiment and theory. For a range of near-monodisperse polystyrenes a good agreement was observed between experiment and theory up to a Rouse Weissenberg number of 7. Above this point the simulated B values were greater than those observed in the MPR. This difference was attributed to the reduction in monomeric friction which occurs for polymers at high extension rates. A novel model for friction reduction was developed and incorporated into the Rolie-Poly equation within *flowSolve*. Using a critical order parameter of 0.05 and a minimum friction of 0.5 resulted in an improved fit to the experimental data at high Weissenberg number. Using the same parameters for prediction of uniaxial extensional viscosities resulted in an under-prediction in extensional viscosities at the highest extensional rates. There is, therefore, a disconnect between the improved fits to extrudate swell data and the poor fit to uniaxial extensional data. This may be due to the many complicating factors involved in an extrusion flow which smooth out some of the rheological differences between theories or possibly due to some physics not yet considered. Friction reduction has only recently been established as a relevant factor under high shear rate flow, so no universally accepted method for accounting for it yet exists. Future work on this phenomenon may result in a form for the friction reduction which gives a good fit to both uniaxial extension and flow simulation.

The new Rolie-Double-Poly (RDP) model of Boudara *et al* was used in the simulation of approximately bidisperse and polydisperse polystyrenes. This model correctly predicted extrudate swell at high Weissenberg number when combined with friction reduction. It slightly under-predicted the swelling ratios at low Weissenberg numbers where stretch time enhancement of high molecular weight chains by dilution with shorter chains is relevant. Use of the standard Rolie-Poly equation with an artificially increased stretch time to account for this effect resulted in an improved fit to swelling data at approximately W_R=1. The RDP model does a poorer job of prediction the extrudate swell of significantly polydisperse polyethylenes. Although the model qualitatively predicts the onset of extrudate swell correctly it fails quantitatively to predict the magnitude of the swelling. The highly polydisperse polyethylenes do not experimentally exhibit the Newtonian low shear plateau of 1.1 that the polystyrenes do, rather swelling at the low shear limit of the MPR seems to be sample dependent. The extrudate swell is significantly molecular weight distribution dependent, samples with a low fraction of high molecular weight chains show only a small increase in swelling ratio with shear rate.

A variety of polyethylenes with well controlled long chain branching were also studied. It was found that a small amount of branching increases the swelling ratios versus the

linear case, even with less than 1 long chain branch per ten chains. Branching also causes a small increase in extrudate swell with increasing shear rate which is not seen for a linear polyethylene at these molecular weights. A moderate increase in long chain branching (up to 1 branch on average per chain) gives no discernible effect on the extrudate swell but a large increase in long chain branching (many branches per chain) gives significantly increased swelling ratios especially at high shear rates. Simulation of these melts with the Pom-Pom model was not possible due to numerical instabilities at the die exit corner. The XPP model was thus used to simulate these melts. The differences between unbranched, branched and highly branched samples are correctly predicted by *flowSolve* but the exact quantitative extrudate swell values are over-predicted at the highest shear rates. One complicating factor for polyethylenes is the distance below the die exit at which the maximum swelling ratio occurs. For polystyrenes this maximum is within the viewable area of the MPR but for polyethylenes it is far below this point. It is thus not possible to measure the maximum swell experimentally, only the swelling at a certain distance below the die exit. Some differences between the branched polyethylenes may be lost because of this.

Overall, the greatest success in simulation of extrudate swell was for monodisperse and slightly polydisperse polystyrenes. In this case good predictions could be obtained up to high Weissenberg number. Simulation of polyethylene proved more difficult. For both linear, polydisperse and branched polyethylenes, *flowSolve* incorrectly predicted the low-shear extrudate swell to be 1.1, whereas it was higher for all polyethylenes studies. This meant that although some qualitative agreement with MPR data could be obtained qualitative predictions of extrudate swell were lacking. When it comes to practical processing, rheological differences between samples can be removed by normalising by Rouse Weissenberg number but the same cannot be said about chemical differences.

8.2 Future Work

Future work on this project would focus on the modelling of the polydisperse and branched systems and on the friction reduction modification. In this work, a good fit was obtained for slightly polydisperse polystyrenes but not for highly polydisperse polyethylenes. It would be interesting, therefore, to investigate some highly polydisperse polystyrenes to see if good predictions can be obtained for these systems. This may provide an insight into whether the differences observed for polyethylene are due to branching, polydispersity or due to some other chemical factor. It would also allow analysis of how versatile the

RDP theory is towards increasing polydispersity or if there is a point where discretisation of the molecular weight distribution into (up to) 12 bins is no longer appropriate.

In terms of long chain branching, some branched samples with branching numbers greater than 1 could be measured. This will determine if there is a branching density at which a sudden, significant increase in extrudate swell is observed, or if there is a gradual increase from slightly to highly branched polyethylenes. Alterations to the computational scheme of *flowSolve* or use of another fluid dynamics package may allow the use of the standard Pom-Pom equation set rather than XPP. This could avoid the overestimation in extrudate swell at high shear seen with XPP whilst avoiding the current issues with Pom-Pom within *flowSolve*. Experimentally, a capillary rheometer could be useful for measurement of these polyethylenes. The ability to measure extrudate swell far below a die exit is necessary for these samples. Their crystallinity means that care must be taken to make the extrusion as isothermal as possible so as to obtain an accurate measure of the isothermal extrudate swell far below the die exit.

The friction reduction proposed in this work is a single, isotropic term. In a 2D or 3D flow simulation a better way of modelling friction reduction would be to develop a tensorial representation of the friction reduction coefficient, and thus different relaxation times parallel and perpendicular to the flow direction. To justify further the use of friction reduction a different polymer chemistry should be used. If a similar over-prediction in extrudate swell occurs at high Weissenberg number this should allow extraction of an S_c and ζ_{min} for this polymer. A different polymer chemistry will have a different λ_{max} and thus the magnitude of friction reduction should be different. If a fit can be obtained for a different polymer then this will further justify the use of the friction reduction equations used in this work.

Appendix A

Example *flowSolve* Input File

#flowSolve input

#param global
title Example *flowSolve* file for PS281
tmax 3 Maximum simulation time. All values in strain time
tstep 0.0001 Time step
tdump 0.1 Outputting a results file
tchk 0.1 Outputting a restart file
ulength 1 1 mm = 1 *flowSolve* unit
invel 1 v_p in mm s^{-1}.
density 1 Density used for gravity
axial 1 Mirror line cylindrical symmetry
gravity 1 Gravity on at 9.8 m s^{-2}
surface 30 Surface tension term
constit roliepoly Rolie Poly equation

#param constitutive Constitutive parameters for each Rolie-Poly element
modulus 232333 25045.6 13762 13118.3 13762 15888.9 15145.7 16668.6 16668.6 39479.1
taud 0.00028 0.00073 0.00193 0.00509 0.01346 0.03558 0.09406 0.24865 0.6573 1.73758
tauR 0.04703
lambdaMax 5
beta 0.5
delta -0.5
lastFast 7 The first non-solvent mode (or fastfactor)

firstStretch 10 The first Rolie-Poly stretch
Sc 0.05 Critical orientation for friction reduction
fmin 0.5 ζ_{min} for friction reduction

#shape outline Outline of shape filled with polymer-upper well
Start 0 -1
Type Mirror
Line 0 3
Type Entry
Line 5 3
Type Bound
Line 5 -1
Line 1 -1
Pressure 0 No pressure applied from atmosphere onto free surface
Type Free
Close

#param refine
maxlen 0.3 Maximum triangle length
lenFact 0.5 Reduction of maxlen in refinement regions
lenFact2 0.5

#shape refine Refinement box at entry corner
Start 1.25 -0.75
Line 0.75 -0.75
Line 0.75 -1.25
Line 1.25 -1.25
Close

#shape refine2 Refinement box at exit corner
Start 1.25 -5.75
Line 1.25 -6.25
Line 0.75 -6.25
Line 0.75 -5.75
Close

#shape walls Extra wall shape not filled with polymer to represent extruder
Start 1 -1
Type Bound
Line 1 -6
Line 5 -6
Close

#end

Appendix B

Temperature Shifting

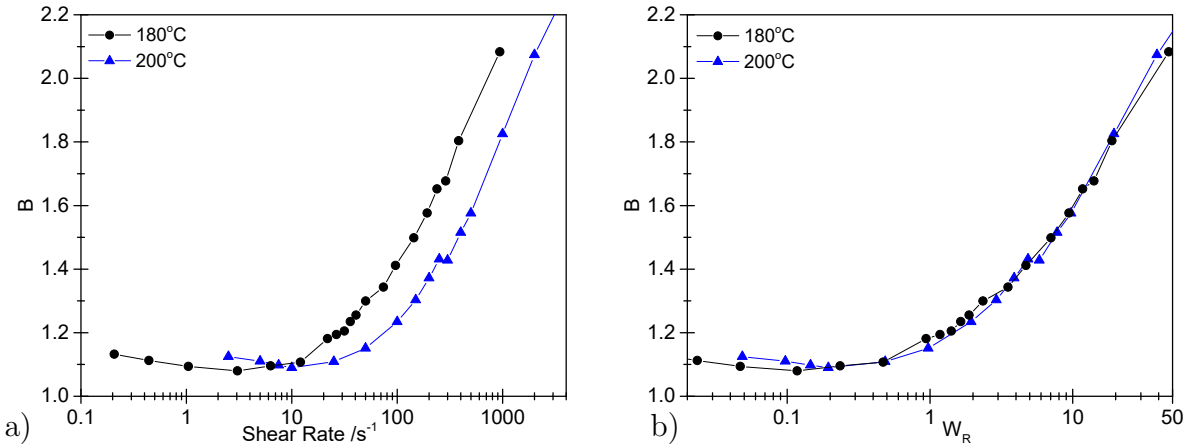

Figure B.1: Extrudate swell predictions at 180 °C and 200 °C. a) shows the reduction in swelling with increasing temperature at constant shear rate and b) shows the temperature independence versus Weissenberg number.

Table B.1: WLF shift parameters for the polystyrenes studied at 180 °C.

Sample	C1	C2	C3
PS100	7.63	-11	10
PS281	6.43	-11	16
PS400	7.64	-11	10
P627-S	7.63	-11	10
PS192	5	-50	0.69
PS350	6.55	-8.4	0.69

Table B.2: WLF shift parameters for the polyethylenes studied in Chapters 6 and 7 at 150 °C.

Sample	C1	C2	C3
DOW-A	2.9	150	0.61
DOW-B	4.41	150	0.61
DOW-C	3.12	150	0.61
DOW-D	3.25	150	0.61
DOW-E	3.02	150	0.61
CM1	4.98	345	0.1
CM2	3.07	150	0.3
CM3	3	170	0.6
LD1840H	13	480	-10
HDB1	4	199	2
HDB2	4	199	0.61
HDB3	4	190	0.61
HDB4	4	199	2
HDB5	4	199	1.7
HDB6	4	199	1.9
HDB7	4	200	2.6

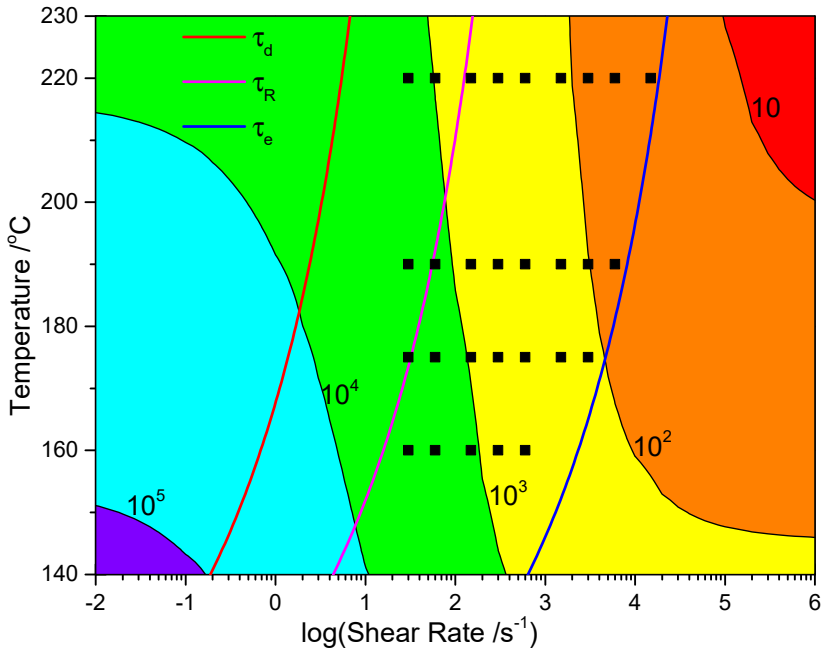

Figure B.2: Shear viscosity vs shear rate and temperature for PS192. The contours are labelled with viscosity in units of Pa.s

Appendix C

Rolie-Poly and Pom-Pom Element Fits

Table C.1: Rolie-Poly elements for monodisperse polymers PS100 and 400. PS281 is shown in Section 4.1.2.

PS100			PS400		
Modulus /Pa	τ_d /s	τ_R /s	Modulus /Pa	τ_d /s	τ_R /s
46587	0.0871	0.0179	12398	11.0	0.293
26639	0.0273		7067	2.16	
35700	0.00965		6865	0.427	
37652	0.00342		5617	0.0844	
39711	0.00121		4730	0.0167	
59147	0.000430		4955	0.00329	
88245	0.000150		10203	0.000649	
104540	5.00×10^{-5}		31934	0.000128	
160220	2.00×10^{-5}		76626	2.53×10^{-5}	
1.88×10^{6}	1.00×10^{-5}		536362	5×10^{-6}	

Table C.2: Pom-Pom elements for the CM series of polyethylenes and the highly branched sample LD1840H at 150 °C.

	CM1				CM2			
Element	Modulus /Pa	τ_b /s	q	*ratio*	Modulus /Pa	τ_b /s	q	*ratio*
1	324041	0.00501	1	–	88330	0.0132	1	–
2	137478	0.0109	1	–	35687	0.0297	1	–
3	72140	0.0236	1	–	424142	0.0670	1	–
4	39857	0.0512	1	–	12841	0.151	1	–
5	16199	0.111	1	–	7588	0.340	1	–
6	5775	0.241	1	–	5057	0.766	1	–
7	914	0.523	1	–	2107	1.725	2	4
8	312	1.134	1	–	1219	3.88	3	4
9	55	2.46	1	–	683	8.50	3	5
10	25	5.34	1	–	243	19.7	3	5
11	15	11.6	1	–	88	44.4	4	5
12	13	25.1	1	–	29	100	7	5
	CM3				LD1840H			
Element	Modulus /Pa	τ_b /s	q	*ratio*	Modulus /Pa	τ_b /s	q	*ratio*
1	247540	0.00631	1	–	96151	0.00089	1	–
2	41955	0.0187	1	–	20531	0.00282	1	–
3	20340	0.0557	1	–	25442	0.00892	1	–
4	12961	0.165	1	–	15455	0.0282	1	–
5	6873	0.491	1	–	9900	0.0891	1	–
6	38413	1.46	1	–	6890	0.281	1	–
7	1431	4.33	8	5	3544	0.889	5	5
8	347	12.9	8	5	2255	2.81	9	5
9	135	38.2	8	5	1046	8.88	6	5
10	13	113	12	4	512	28.1	10	1
11	1	337	20	4				
12	0.04	1000	25	4				

Table C.3: Pom-Pom elements for the HDB series of polyethylenes at 150 °C.

	HDB1				HDB2			
Element	Modulus /Pa	τ_b /s	q	*ratio*	Modulus /Pa	τ_b /s	q	*ratio*
1	164673	0.000138	1	–	241871	0.000152	1	–
2	292406	0.000679	1	–	326023	0.000735	1	–
3	166719	0.00334	1	–	222867	0.00356	1	–
4	52167	0.0165	1	–	78431	0.0172	1	–
5	11534	0.0810	1	–	24178	0.0833	3	4
6	3908	0.399	1	–	7302	0.403	2	5
7	1225	1.97	1	–	5283	1.95	2	5
8	126	9.68	2	2	300	9.44	2	5
	HDB3				HDB4			
Element	Modulus /Pa	τ_b /s	q	*ratio*	Modulus /Pa	τ_b /s	q	*ratio*
1	336216	0.000692	1	–	501187	0.000126	1	–
2	165020	0.00267	1	–	294974	0.000703	1	–
3	90982	0.0103	1	–	243279	0.00392	1	–
4	34804	0.0399	1	–	97071	0.0219	1	–
5	14397	0.154	2	5	32940	0.122	1	–
6	8167	0.596	5	5	15530	0.680	2	5
7	2799	2.302	2	5	7350	3.79	2	5
8	1949	8.90	2	5	3053	21.2	1	5
	HDB5				HDB6			
Element	Modulus /Pa	τ_b /s	q	*ratio*	Modulus /Pa	τ_b /s	q	*ratio*
1	378428	0.000243	1	–	357635	0.000135	1	–
2	236289	0.001276	1	–	277171	0.000717	1	–
3	155399	0.0067	1	–	144780	0.00381	1	–
4	56641	0.0352	1	–	61761	0.0202	1	–
5	24971	0.185	2	5	31625	0.108	1	–
6	12230	0.969	1	2	16212	0.571	4	5
7	4830	5.09	3	5	6099	3.03	2	5
8	802	26.7	2	5	1754	16.1	2	5
	HDB7							
Element	Modulus /Pa	τ_b /s	q	*ratio*				
1	218754	0.000384	1	–				
2	100689	0.00179	1	–				
3	61150	0.00830	1	–				
4	39841	0.0386	1	–				
5	23619	0.180	2	5				
6	12613	0.835	2	4				
7	4920	3.89	2	3				
8	1970	18.1	5	4				

Appendix D

Rolie-Double-Poly data tables

Table D.1: Rolie-Double-Poly Elements for PS281 at 180 °C used in Section 4.5. The plateau modulus is 2E5 Pa.

Element index	M_w /kDa	ϕ	τ_d /s	τ_R /s
1	126	0.000182	0.0175	0.00597
2	158	0.0121	0.366	0.0150
3	200	0.156	0.515	0.0377
4	251	0.7561	2.58	0.0946
5	316	0.0559	12.3	0.238
6	398	0.0135	51.8	0.796
7	501	0.00104	140	8.14
8	631	0.000423	215	144
9	794	0.000664	1189	339

Table D.2: Rolie-Double-Poly elements for DOW-B

Element	M_w /kDa	ϕ	τ_d /s	τ_R /s
1	2	0.0321	4.85×10^{-8}	9.06×10^{-8}
2	4	0.0592	6.50×10^{-7}	4.04×10^{-7}
3	9	0.101	1.03×10^{-5}	1.81×10^{-6}
4	20	0.155	0.000137	8.01×10^{-6}
5	41	0.205	0.00153	3.42×10^{-5}
6	86	0.182	0.0163	0.000149
7	179	0.125	0.163	0.000648
8	374	0.0749	1.62	0.00285
9	773	0.0331	15.0	0.0121
10	1.62×10^3	0.0102	141	0.0532
11	3.35×10^3	0.00262	1270	0.229
12	6.82×10^3	0.000442	10700	0.945

Table D.3: Rolie-Double-Poly elements for DOW-C

Element	M_w /kDa	ϕ	τ_d /s	τ_R /s
1	5	0.0612	8.17×10^{-9}	1.17×10^{-8}
2	10	0.103	9.99×10^{-8}	4.64×10^{-8}
3	20	0.141	1.25×10^{-6}	1.85×10^{-7}
4	39	0.171	1.29×10^{-5}	7.16×10^{-7}
5	76	0.152	0.000121	2.75×10^{-6}
6	150	0.115	0.00109	1.08×10^{-5}
7	304	0.0840	0.00993	4.44×10^{-5}
8	614	0.0670	0.0891	0.000182
9	1.22×10^3	0.0504	0.725	0.000714
10	2.41×10^3	0.0346	5.78	0.00280
11	4.55×10^3	0.0155	39.8	0.00998
12	9.69×10^3	0.00420	400	0.0453

Table D.4: Rolie-Double-Poly elements for DOW-D

Element	M_w /kDa	ϕ	τ_d /s	τ_R /s
1	7	0.0871	3.38×10^{-9}	6.77×10^{-9}
2	14	0.124	3.22×10^{-8}	2.60×10^{-8}
3	27	0.143	4.02×10^{-7}	1.02×10^{-7}
4	53	0.147	4.54×10^{-6}	4.05×10^{-7}
5	107	0.123	4.72×10^{-5}	1.62×10^{-6}
6	213	0.0100	0.000445	6.46×10^{-6}
7	427	0.0815	0.00402	2.59×10^{-5}
8	853	0.0725	0.0346	0.000104
9	1.69×10^{3}	0.0591	0.290	0.000406
10	3.32×10^{3}	0.0428	2.31	0.00157
11	6.20×10^{3}	0.0166	15.3	0.00547
12	1.23×10^{4}	0.00329	124	0.0215

Table D.5: Rolie-Double-Poly elements for DOW-E

Element	M_w /kDa	ϕ	τ_d /s	τ_R /s
1	2	0.0392	5.64×10^{-9}	9.10×10^{-9}
2	5	0.0780	8.00×10^{-8}	4.01×10^{-8}
3	11	0.123	1.13×10^{-6}	1.71×10^{-7}
4	22	0.153	1.40×10^{-5}	7.32×10^{-7}
5	45	0.160	0.000157	3.15×10^{-6}
6	96	0.136	0.001713	1.40×10^{-5}
7	200	0.117	0.017051	6.09×10^{-5}
8	416	0.0987	0.165836	0.000264
9	849	0.0625	1.47148	0.00110
10	1.75×10^{3}	0.0255	13.2906	0.00468
11	3.51×10^{3}	0.00662	108.384	0.0188
12	6.81×10^{3}	0.000726	817.435	0.0708

Bibliography

[1] Bagley, E.B., and Duffey, H.J. Recoverable shear strain and the Barus effect in polymer extrusion. T. Soc. Rheol. **14**, 545–553 (1970).

[2] Nakajima, N., and Shida, M. Viscoelastic behavior of polyethylene in capillary flow expressed with three material functions. T. Soc. Rheol. **10**, 299–316 (1966).

[3] Tanner, R.I. A theory of die-swell. J. Polym. Sci A2 **8**, 2067–2078 (1970).

[4] Tanner, R.I. A theory of die-swell revisited. J. Non-Newtonian Fluid Mech. **129**, 85–87 (2005).

[5] Huang, D.C., and White, J.L. Extrudate swell from slit and capillary dies: An experimental and theoretical study. Polym. Eng. Sci. **19**, 609–616 (1979).

[6] Tanner, R.I. A new inelastic theory of extrudate swell. J. Non-Newtonian Fluid Mech. **6**, 289–302 (1980).

[7] Al-Muslimawi, A., Tamaddon-Jahromi, H.R., and Webster, M.F. Simulation of viscoelastic and viscoelastoplastic die-swell flows. J. Non-Newtonian Fluid Mech. **191**, 45–56 (2013).

[8] Guillet, J., and Seriai, M. Quantitative evaluation of extrudate swell from viscoelastic properties of polystyrene. Rheol. Acta **30**, 540–548 (1991).

[9] Seriai, M., Guillet, J., and Carrot, C. A simple model to predict extrudate swell of polystyrene and linear polyethylenes. Rheol. Acta **32**, 532–538 (1993).

[10] Sun, J., Phan-Thien, N., and Tanner, R. Extrudate swell through an orifice die. Rheol. Acta **35**, 1–12 (1996).

[11] Liang, J.Z. Estimation of die-swell ratio for polymer melts from exit pressure drop data. Polym. Test. **20**, 29–31 (2000).

[12] Liang, J.Z. A relationship between extrudate swell ratio and entry stored elastic strain energy during die flow of tyre compounds. Polym. Test. **23**, 441–446 (2004).

[13] Meng, L., Wu, D., He, X., and Zhuang, J. Visualization experiments on extrudate swell behavior at the microscale. P. I. Mech. Eng. N. J. Nano. **229**, 34–40 (2015).

[14] Georgiou, G.C., Papanastasiou, T.C., and Wilkes, J.O. Laminar Newtonian jets at high Reynolds number and high surface tension. AIChE J. **34**, 1559–1562 (1988).

[15] Delvaux, V., and Crochet, M.J. Numerical simulation of delayed die swell. Rheol. Acta **29**, 1–10 (1990).

[16] Konaganti, V.K., Ansari, M., Mitsoulis, E., and Hatzikiriakos, S.G. Extrudate swell of a high-density polyethylene melt: Ii. modeling using integral and differential constitutive equations. J. Non-Newtonian Fluid Mech. **225**, 94–105 (2015).

[17] Kim, J.H., and Lyu, M.Y. Predictions of flow behaviors and entrance pressure drop characteristics of a rubber compound in a capillary die using various rheological models. Polym. Eng. Sci. **54**, 2441–2448 (2014).

[18] Ganvir, V., Lele, A., Thaokar, R., and Gautham, B.P. Prediction of extrudate swell in polymer melt extrusion using an Arbitrary Lagrangian Eulerian (ALE) based finite element method. J. Non-Newtonian Fluid Mech. **156**, 21–28 (2009).

[19] Ganvir, V., Gautham, B.P., Pol, H., Bhamla, M.S., Sclesi, L., Thaokar, R., Lele, A., and Mackley, M. Extrudate swell of linear and branched polyethylenes: ALE simulations and comparison with experiments. J. Non-Newtonian Fluid Mech. **166**, 12–24 (2011).

[20] Utracki, L.A., Bakerdjian, Z., and Kamal, M.R. A method for the measurement of the true die swell of polymer melts. J. Appl. Polym. Sci. **19**, 481–501 (1975).

[21] Behzadfar, E., Ansari, M., Konaganti, V.K., and Hatzikiriakos, S.G. Extrudate swell of HDPE melts: I. experimental. J. Non-Newtonian Fluid Mech. (2015).

[22] Koopmans, R.J. Extrudate swell of high density polyethylene. part ii: Time dependency and effects of cooling and sagging. Polym. Eng. Sci. **32**, 1750–1754 (1992).

[23] Anand, J.S., and Bhardwaj, I.S. Die swell behaviour of polypropylene — An experimental investigation. Rheol. Acta **19**, 614–622 (1980).

[24] Yang, B., and Lee, L.J. Effect of die temperature on the flow of polymer melts. part ii: Extrudate swell. Polym. Eng. Sci. **27**, 1088–1094 (1987).

[25] Zhu, Z., and Wang, S.Q. Experimental characterization of extrudate swell behavior of linear polybutadiene. J. Rheol. **48**, 571–589 (2004).

[26] Yang, X., Wang, S.Q., and Chai, C. Extrudate swell behavior of polyethylenes: Capillary flow, wall slip, entry/exit effects and low-temperature anomalies. J. Rheol. **42**, 1075–1094 (1998).

[27] Dealy, J.M., and Larson, R.G. Structure and Rheology of Molten Polymers - From Structure to Flow Behavior and Back Again, (Hanser Publishers, Munich, 2006).

[28] Dealy, J.M., Read, D.J., and Larson, R.G. Structure and Rheology of Molten Polymers - From Structure to Flow Behavior and Back Again, (Hanser Publishers, Munich, 2018), 2 edn.

[29] Doi, M., and Edwards, S.F. The Theory of Polymer Dynamics, (Oxford University Press, 1986).

[30] Milner, S.T., and McLeish, T.C.B. Reptation and contour-length fluctuations in melts of linear polymers. Phys. Rev. Lett. **81**, 725–728 (1998).

[31] Graham, R.S., Likhtman, A.E., McLeish, T.C.B., and Milner, S.T. Microscopic theory of linear, entangled polymer chains under rapid deformation including chain stretch and convective constraint release. J. Rheol. **47**, 1171–1200 (2003).

[32] Likhtman, A.E., and Graham, R.S. Simple constitutive equation for linear polymer melts derived from molecular theory: RoliePoly equation. J. Non-Newtonian Fluid Mech. **114**, 1–12 (2003).

[33] Valette, R., Mackley, M.R., and del Castillo, G.H.F. Matching time dependent pressure driven flows with a Rolie Poly numerical simulation. J. Non-Newtonian Fluid Mech. **136**, 118–125 (2006).

[34] Lord, T.D., Scelsi, L., Hassell, D.G., Mackley, M.R., Embery, J., Auhl, D., Harlen, O.G., Tenchev, R., Jimack, P.K., and Walkley, M.A. The matching of 3D Rolie-Poly viscoelastic numerical simulations with experimental polymer melt flow within a slit and a cross-slot geometry. J. Rheol. **54**, 355–373 (2010).

[35] Bent, J., Hutchings, L.R., Richards, R.W., Gough, T., Spares, R., Coates, P.D., Grillo, I., Harlen, O.G., Read, D.J., Graham, R.S., Likhtman, A.E., Groves, D.J., Nicholson, T.M., and McLeish, T.C.B. Neutron-mapping polymer flow: Scattering, flow visualization, and molecular theory. Science **301**, 1691–1695 (2003).

[36] Robertson, B., Thompson, R.L., McLeish, T.C.B., and Robinson, I. Theoretical prediction and experimental measurement of isothermal extrudate swell of monodisperse and bidisperse polystyrenes. J. Rheol. **61**, 931–945 (2017).

[37] Collis, M.W., Lele, A.K., Mackley, M.R., Graham, R.S., Groves, D.J., Likhtman, A.E., Nicholson, T.M., Harlen, O.G., McLeish, T.C.B., Hutchings, L.R., Fernyhough, C.M., and Young, R.N. Constriction flows of monodisperse linear entangled polymers: Multiscale modeling and flow visualization. J. Rheol. **49**, 501–522 (2005).

[38] Kabanemi, K.K., and Htu, J.F. Nonlinear dynamics and conformational changes of linear entangled polymers using the Rolie-Poly model with an effective maximum contour length. Rheol. Acta **48**, 801–813 (2009).

[39] Kabanemi, K.K., and Htu, J.F. Nonequilibrium stretching dynamics of dilute and entangled linear polymers in extensional flow. J. Non-Newtonian Fluid Mech. **160**, 113 – 121 (2009).

[40] Boudara, V. Supramolecular and entangled polymer materials: rheological models. Thesis, Department of Mathematics, University of Leeds (2017).

[41] Boudara, V.A.H., Peterson, J.D., Leal, L.G., and Read, D.J. Nonlinear rheology of polydisperse blends of entangled linear polymers: Rolie-double-poly models. J. Rheol. **63**, 71–91 (2018).

[42] Bishko, G., McLeish, T.C.B., Harlen, O.G., and Larson, R.G. Theoretical molecular rheology of branched polymers in simple and complex flows: The Pom-Pom model. Phys. Rev. Lett. **79**, 2352–2355 (1997).

[43] McLeish, T.C.B., and Larson, R.G. Molecular constitutive equations for a class of branched polymers: The pom-pom polymer. J. Rheol. **42**, 81–110 (1998).

[44] Blackwell, R.J., McLeish, T.C.B., and Harlen, O.G. Molecular dragstrain coupling in branched polymer melts. J. Rheol. **44**, 121–136 (2000).

[45] Lee, K., Mackley, M., McLeish, T., Nicholson, T., and Harlen, O. Experimental observation and numerical simulation of transient stress fangs within flowing molten polyethylene. J. Rheol. **45**, 1261–1277 (2001).

[46] Inkson, N.J., McLeish, T.C.B., Harlen, O.G., and Groves, D.J. Predicting low density polyethylene melt rheology in elongational and shear flows with pom-pom constitutive equations. J. Rheol. **43**, 873–896 (1999).

[47] Bishko, G. Implementing Molecular Rheology in Complex Flow Fields: a Lagrangian Simulation. Ph.D. thesis, Department of Physics and Applied Mathematics, University of Leeds (1997).

[48] Collis, M.W., and Mackley, M.R. The melt processing of monodisperse and polydisperse polystyrene melts within a slit entry and exit flow. J. Non-Newtonian Fluid Mech. **128**, 29–41 (2005).

[49] Hassell, D.G., Hoyle, D., Auhl, D., Harlen, O., Mackley, M.R., and McLeish, T.C.B. Effect of branching in cross-slot flow: the formation of W cusps. Rheol. Acta **48**, 551–561 (2009).

[50] Verbeeten, W.M.H., Peters, G.W.M., and Baaijens, F.P.T. Differential constitutive equations for polymer melts: The extended PomPom model. J. Rheol. **45**, 823–843 (2001).

[51] Nicholson, T.M., Martyn, M.T., and McLeish, T.C.B. Measurement and modelling of high density polyethylene melt extrudate swell. AIP Conf. Proc **1027**, 231–233 (2008).

[52] Mackley, M.R., Marshall, R.T.J., and Smeulders, J.B.A.F. The multipass rheometer. J. Rheol. **39**, 1293–1309 (1995).

[53] Mackley, M.R., and Hassell, D.G. The multipass rheometer a review. J. Non-Newtonian Fluid Mech. **166**, 421–456 (2011).

[54] Mackley, M.R., Moggridge, G.D., and Saquet, O. Direct experimental evidence for flow induced fibrous polymer crystallisation occurring at a solid/melt interface. Journal of Materials Science **35**, 5247–5253 (2000).

[55] Lele, A., Mackley, M., Galgali, G., and Ramesh, C. In situ rheo-x-ray investigation of flow-induced orientation in layered silicate-syndiotactic polypropylene nanocomposite melt. J. Rheol. **46**, 1091–1110 (2002).

[56] Stasiak, J., Mackley, M.R., Squires, A.M., Castelletto, V., Hamley, I.W., and Moggridge, G.D. Dynamics of shear-induced orientation transitions in block copolymers. Soft Matter **6**, 1941–1947 (2010).

[57] Luap, C., Mller, C., Schweizer, T., and Venerus, D.C. Simultaneous stress and birefringence measurements during uniaxial elongation of polystyrene melts with narrow molecular weight distribution. Rheol. Acta **45**, 83–91 (2005).

[58] Fuller, G. Optical Rheometry of Complex Fluids, (Oxford University Press, 1995).

[59] Reynolds, C., Thompson, R., and McLeish, T. Pressure and shear rate dependence of the viscosity and stress relaxation of polymer melts. J. Rheol. **62**, 631–642 (2018).

[60] Sentmanat, M., Wang, B.N., and McKinley, G.H. Measuring the transient extensional rheology of polyethylene melts using the SER universal testing platform. J. Rheol. **49**, 585–606 (2005).

[61] Tassieri, M., Laurati, M., Curtis, D.J., Auhl, D.W., Coppola, S., Scalfati, A., Hawkins, K., Williams, P.R., and Cooper, J.M. i-Rheo: Measuring the materials' linear viscoelastic properties in a step! J. Rheol. **60**, 649–660 (2016).

[62] Williams, M.L., Landel, R.F., and Ferry, J.D. The temperature dependence of relaxation mechanisms in amorphous polymers and other glass-forming liquids. J. Am. Chem. Soc. **77**, 3701–3707 (1955).

[63] Wu, S. Surface and interfacial tensions of polymer melts. ii. poly(methyl methacrylate), poly(n-butyl methacrylate), and polystyrene. J. Phys. Chem. **74**, 632–638 (1970).

[64] Likhtman, A.E., and McLeish, T.C.B. Quantitative theory for linear dynamics of linear entangled polymers. Macromolecules **35**, 6332–6343 (2002).

[65] Larson, R.G., Sridhar, T., Leal, L.G., McKinley, G.H., Likhtman, A.E., and McLeish, T.C.B. Definitions of entanglement spacing and time constants in the tube model. J. Rheol. **47**, 809–818 (2003).

[66] Roln-Garrido, V.H., Wagner, M.H., Luap, C., and Schweizer, T. Modeling non-Gaussian extensibility effects in elongation of nearly monodisperse polystyrene melts. J. Rheol. **50**, 327–340 (2006).

[67] van Meerveld, J. Validity of the linear stress optical rule in mono-, bi- and polydisperse systems of entangled linear chains. Journal of Non-Newtonian Fluid Mechanics **123**, 259–267 (2004).

[68] Ianniruberto, G. Extensional flows of solutions of entangled polymers confirm reduction of friction coefficient. Macromolecules **48**, 6306–6312 (2015).

[69] Mooney, M. Explicit formulas for slip and fluidity. J. Rheol. **2**, 210–222 (1931).

[70] Rabinowitsch, B. ber die viskositt und elastizitt von solen. Z. Phys. Chem. **145A**, 1 (1929).

[71] Laun, H.M. Prediction of elastic strains of polymer melts in shear and elongation. J. Rheol. **30**, 459–501 (1986).

[72] Ianniruberto, G., Brasiello, A., and Marrucci, G. Simulations of fast shear flows of PS oligomers confirm monomeric friction reduction in fast elongational flows of monodisperse PS melts as indicated by rheooptical data. Macromolecules **45**, 8058–8066 (2012).

[73] Yaoita, T., Isaki, T., Masubuchi, Y., Watanabe, H., Ianniruberto, G., and Marrucci, G. Primitive chain network simulation of elongational flows of entangled linear chains: Stretch/orientation-induced reduction of monomeric friction. Macromolecules **45**, 2773–2782 (2012).

[74] Mead, D.W., Banerjee, N., and Park, J. A constitutive model for entangled polymers incorporating binary entanglement pair dynamics and a configuration dependent friction coefficient. J. Rheol. **59**, 335–363 (2015).

[75] Mead, D.W., Monjezi, S., and Park, J. A constitutive model for entangled polydisperse linear flexible polymers with entanglement dynamics and a configuration dependent friction coefficient. part i: Model derivation. J. Rheol. **62**, 121–134 (2018).

[76] Mead, D.W., Monjezi, S., and Park, J. A constitutive model for entangled polydisperse linear flexible polymers with entanglement dynamics and a configuration dependent friction coefficient. part ii. modeling shear modification following cessation of fast shear flows. J. Rheol. **62**, 135–147 (2018).

[77] Auhl, D., Chambon, P., McLeish, T.C.B., and Read, D.J. Elongational flow of blends of long and short polymers: Effective stretch relaxation time. Phys. Rev. Lett. **103**, 136001 (2009).

[78] Viovy, J.L., Rubinstein, M., and Colby, R.H. Constraint release in polymer melts: tube reorganization versus tube dilation. Macromolecules **24**, 3587–3596 (1991).

[79] Read, D.J., Jagannathan, K., Sukumaran, S.K., and Auhl, D. A full-chain constitutive model for bidisperse blends of linear polymers. J. Rheol. **56**, 823–873 (2012).

[80] Read, D.J., Shivokhin, M.E., and Likhtman, A.E. Contour length fluctuations and constraint release in entangled polymers: Slip-spring simulations and their implications for binary blend rheology. J. Rheol. **62**, 1017–1036 (2018).

[81] Graessley, W.W., Glasscock, S.D., and Crawley, R.L. Die swell in molten polymers. T. Soc. Rheol. **14**, 519–544 (1970).

[82] Minoshima, W., White, J.L., and Spruiell, J.E. Experimental investigations of the influence of molecular weight distribution on melt spinning and extrudate swell characteristics of polypropylene. J. Appl. Polym. Sci. **25**, 287–306 (1980).

[83] den Doelder, C.F.J., and Koopmans, R.J. The effect of molar mass distribution on extrudate swell of linear polymers. J. Non-Newtonian Fluid Mech. **152**, 195–202 (2008).

[84] Mendelson, R.A., and Finger, F.L. High-density polyethylene melt elasticitysome anomalous observations on the effects of molecular structure. J. Appl. Polym. Sci. **19**, 1061–1078 (1975).

[85] Robertson, B., Thompson, R.L., McLeish, T.C.B., and Robinson, I. Polymer extrudate-swell: From monodisperse melts to polydispersity and flow-induced reduction in monomer friction. J. Rheol. **63**, 319–333 (2019).

[86] Cox, W.P., and Merz, E.H. Correlation of dynamic and steady flow viscosities. J. Polym . Sci. **28**, 619–622 (1958).

[87] Szanto, L., Vogt, R., Meier, J., Auhl, D., Van Ruymbeke, E., and Friedrich, C. Entanglement relaxation time of polyethylene melts from high-frequency rheometry in the mega-hertz range. J. Rheol. **61**, 1023–1033 (2017).

[88] Yan, D., Wang, W.J., and Zhu, S. Effect of long chain branching on rheological properties of metallocene polyethylene. Polymer **40**, 1737–1744 (1999).

[89] Hamielec, L.A., and Vlachopoulos, J. Influence of long chain branching on extrudate swell of low-density polyethylenes. J. Appl. Polym. Sci. **28**, 2389–2392 (1983).

[90] Crosby, B.J., Mangnus, M., de Groot, W., Daniels, R., and McLeish, T.C.B. Characterization of long chain branching: Dilution rheology of industrial polyethylenes. J. Rheol. **46**, 401–426 (2002).

[91] Hassell, D.G., Auhl, D., McLeish, T.C.B., and Mackley, M.R. The effect of viscoelasticity on stress fields within polyethylene melt flow for a cross-slot and contraction-expansion slit geometry. Rheol. Acta **47**, 821–834 (2008).

[92] Coventry, K.D., and Mackley, M.R. Cross-slot extensional flow birefringence observations of polymer melts using a multi-pass rheometer. J. Rheol. **52**, 401–415 (2008).

[93] Wood-Adams, P.M., and Dealy, J.M. Using rheological data to determine the branching level in metallocene polyethylenes. Macromolecules **33**, 7481–7488 (2000).

[94] Costeux, S., Wood-Adams, P., and Beigzadeh, D. Molecular structure of metallocene-catalyzed polyethylene: rheologically relevant representation of branching architecture in single catalyst and blended systems. Macromolecules **35**, 2514–2528 (2002).

[95] Das, C., Inkson, N.J., Read, D.J., Kelmanson, M.A., and McLeish, T.C.B. Computational linear rheology of general branch-on-branch polymers. J. Rheol. **50**, 207–234 (2006).

[96] Hoyle, D.M., Auhl, D., Harlen, O.G., Barroso, V.C., Wilhelm, M., and McLeish, T.C.B. Large amplitude oscillatory shear and Fourier transform rheology analysis of branched polymer melts. J. Rheol. **58**, 969–997 (2014).

[97] Auhl, D., Hoyle, D.M., Hassell, D., Lord, T.D., Harlen, O.G., Mackley, M.R., and McLeish, T.C.B. Cross-slot extensional rheometry and the steady-state extensional response of long chain branched polymer melts. J. Rheol. **55**, 875–900 (2011).

[98] Hoyle, D. Constitutive modelling of branched polymer melts in non-linear response. Ph.D. thesis, Department of Mathematics, University of Leeds (2010).

[99] Trinkle, S., and Friedrich, C. Van Gurp-Palmen-plot: a way to characterize polydispersity of linear polymers. Rheol. Acta **40**, 322–328 (2001).

[100] Fleury, G., Schlatter, G., and Muller, R. Non linear rheology for long chain branching characterization, comparison of two methodologies : Fourier transform rheology and relaxation. Rheol. Acta **44**, 174–187 (2004).

[101] Trinkle, S., Walter, P., and Friedrich, C. Van Gurp-Palmen plot ii - classification of long chain branched polymers by their topology. Rheol. Acta **41**, 103–113 (2002).

[102] Inkson, N.J., Phillips, T.N., and van Os, R.G.M. Numerical simulation of flow past a cylinder using models of XPP type. J. Non-Newtonian Fluid Mech. **156**, 7–20 (2009).